SAPIENZA
UNIVERSITÀ DI ROMA

Mathematical models of cell migration and self-organization in embryogenesis

Dipartimento di Scienze di Base ed Applicate per l'Ingegneria

Dottorato di Ricerca in
Modelli e Metodi Matematici per la Tecnologia e la Società – XXVI Ciclo

Candidate

Ezio Di Costanzo
ID number 1379310

Thesis Advisor

Prof. Roberto Natalini, IAC-CNR

A thesis submitted in partial fulfillment of the requirements
for the degree of Doctor of Philosophy in Modelli e Metodi Matematici per
la Tecnologia e la Società

23 May 2014

Thesis defended on 2 October 2014
in front of a Board of Examiners composed by:

Prof. Brunello Tirozzi (chairman)
Prof. Renato Spigler
Prof. Francesco Vaccarino

Mathematical models of cell migration and self-organization in embryogenesis
Ph.D. thesis. Sapienza – University of Rome

This thesis has been typeset by LaTeX and the Sapthesis class.

Author's email: ezio.dicostanzo@sbai.uniroma1.it

Dedicated to my parents

Acknowledgements

I need to thank my advisor prof. Roberto Natalini, that has introduced me to the fascinating field of the Mathematical Biology and has given me confidence during my research period, always showing availability to guide me, even after the greater commitments due to his new position as director of the Istituto per le Applicazioni del Calcolo “M. Picone”, Consiglio Nazionale delle Ricerche.

A special thank to prof. Luigi Preziosi for his collaboration, and for his accurate revision work on my manuscript.

I also thank Dr. Andrea Tosin for useful discussions about some mathematical modelling issues.

I am particularly grateful to the Department SBAI of Sapienza University of Rome, and especially to professors Micol Amar, Fabio Camilli, Maria Rosaria Lancia, and Maria Agostina Vivaldi, with whom I have collaborated fruitfully for my university teaching experience.

Finally, a particular thought goes to my parents, that always lovingly support me during my studies. With them, with my colleagues, and with my professors, I share the satisfaction of this moment.

List of publications

[1] Di Costanzo E, Marasco A (2012) *Approximate analytic solution of Dirichlet's problems for Laplace's equation in planar domains by a perturbation method.* Elsevier-Computers and Mathematics with Applications 63(1):60–67.

[2] Di Costanzo E, Natalini R, Preziosi L (2013) *A hybrid mathematical model for self-organizing cell migration in the zebrafish lateral line.* Journal of Mathematical Biology, in press, DOI: 10.1007/s00285-014-0812-9.

[3] Di Costanzo E, Natalini R (2014) *A hybrid mathematical model of collective motion under alignment and chemotaxis*, in preparation.

[4] Di Costanzo E, Giacomello A, Messina E, Natalini R, Pontrelli G, Twarogowska M (2014) *A discrete in continuous mathematical model for cardiospheres formation in human cardiac stem cells*, in preparation.

Contents

Introduction

In the current scientific research, mathematical biology plays a role of increasing relevance. New and powerful mathematical tools are improving, ever more, their descriptive and predictive capacity in several applications of the real life. By describing a biological system in a quantitative manner, and numerically simulating its behaviour, some properties can be inferred that might not be evident solely on experimental basis. Various reasons have brought, in last years, to a remarkable interest in the field of mathematical biology. Among these, the introduction of advanced experimental technique and the availability of large amount of data, the development of new mathematical tools in the description of complex systems, the enhancement of computer processing capabilities to perform calculations and numerical simulations, the increasing interest in *in silico* experimentation, which represents a potential alternative in human and animal research due to ethical considerations, risk, unreliability for economic reasons or other complications (Deutsch, 2004).

In this thesis we deal with mathematical models for cell migration and self-organization in embryogenesis. Understanding mechanisms regulating collective motion of cells brings important advantages in the resolution of crucial issues related to the growth, development and disease of many organs and tissues (see Chapter 1).

The part of biology which studies the formation and development of the embryo from fertilization until birth is called embryology. Morphogenesis is then the part of embryology which is concerned with the development of patterns and forms. It is well known that although morphogenesis processes are controlled at the genetic scale, genes themselves cannot create the pattern. In general a series of biological mechanisms of self-organization intervene during the early development and the formation of particular biological structures can not be anticipated solely by genetic information (Murray, 2003). This needs to be taken into account in the choice of a suitable mathematical formulation of such phenomena.

The basic theory of the morphogenesis was put forward in a seminal paper by Turing (1952) considering, on the chemical scale, systems of reaction diffusion equations. Turing showed that different diffusion coefficients can generate, under certain circumstances, steady states which are stable in the absence of diffusion and become unstable when it is present. This peculiarity of the reaction diffusion systems, known as Turing instability, can produce spatial inhomogeneous patterns depending on the chemicals and on the geometry of the domain. The chemical theory of the morphogenesis has been extended and applied as a possible mechanism in pattern formation in the animal species, such as in the animal coat of zebra, leopard, or in the butterfly wings, but also during the regeneration or segmentation in some animal embryos (see Murray, 2003 and Section 2.1). The reaction diffusion models, however, do not consider the spatial organization of the cells, while, in the reality, in biological processes the formation of cell aggregates is regulated by the response of cell populations to chemical concentrations in the environment. This behaviour is known as *chemotaxis* and can be described by the so called reaction-diffusion-chemotaxis equations. Chemical chemotaxis models have been widely employed in embryonic pattern formation since the seminal work by Keller and Segel (1970) (see Section 2.2), for instance, in processes of pigmentation pattern, cell colonization (Murray and Myerscough, 1991; Painter et al, 2000; Landman et al, 2003), or in tumor growth (Perumpanani et al, 1996; Owen and Sherratt, 1997).

Clearly, in highly structured multicellular organisms certain processes need to be investigated in more detail on the cellular scale, above all when attraction, adhesion and, more generally, force generation become relevant. This leads to investigate the role that mechanical forces play in the morphogenetic process in combination with chemical effects. In this context, mechanochemical models have been proposed by Oster and Murray and applied to describe, for example, the morphogenesis of internal tissues, as dermis and mesenchyme, or of the external epithelium (see Section 2.3 and Murray, 1983; Oster et al, 1983; Murray and Oster, 1984a; Murray and Oster, 1984b; Maini, 1999). Similar models find applications also in vasculogenesis and dermal wound healing (Murray, 2003).

Other morphogenetic processes, for instance the one described in Chapter 1, can involve only a small number of cells and the behaviour of a single cell is closely influenced by the presence of other units, so that the collective motion in cell migration needs to be investigated (see Sections 2.5–2.7). In general, when a phenomenon takes place at different spatial and/or temporal scales, it can require also different mathematical approaches for their complete description. They can be represented by continuous, discrete or hybrid models, as we will see in Section 2.4.

In the subsequent chapters two main topics will be investigated, which here for convenience will be separately discussed in two parts. Firstly, we will analyze and mathematically model the self-organizing cell migration in the morphogenesis of the lateral line in the zebrafish (*Danio rerio*). In a second part, starting from this model, we will propose, and will study both from the analytical and the numerical point of view, a simpler mathematical model of collective motion under only alignment and chemotaxis effects.

Part I - A mathematical model for self-organizing cells in the zebrafish lateral line

In the first part of this thesis (including the first three chapters) we will study the morphogenetic process involved in the growth and the development of the lateral line in a zebrafish embryo, and we will propose a possible mathematical model about it.

The *lateral line* is a fundamental sensory system, present in fish and amphibians, that extends from the head to the tail along each flank of the individual. It is involved in a large variety of behaviours: to detect movement and vibrations in the surrounding water, for prey detection and predator avoidance, in school swimming and sexual courtship. The main sensory organs of the lateral line are represented by the *neuromasts*, located on the body surface in specific patterns. In particular we deal with the posterior lateral line (PLL), which comprises the neuromasts arranged on the body and on the tail (Ghysen and Chaudière, 2004; Coombs and Netten, 2005), see Figure 0.1. Each neuromast has a rosette-shaped structure with one or two cells in the centre innervated by sensory neurons and surrounding by other support cells.

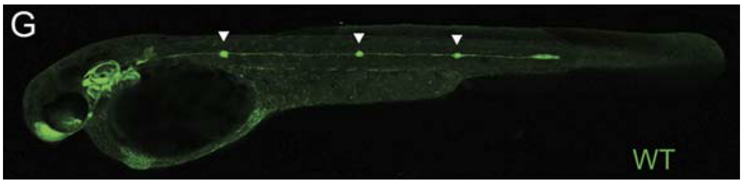

Figure 0.1. The posterior lateral line formation in a zebrafish embryo. An initial group of cells migrate from the head (left) to the tail (right), while neuromasts (green dots) are deposited along the body (source Haas and Gilmour, 2006).

In the current scientific research the function of the lateral line represents a subject of great interest in biology. Many general issues have found a deeper explanation, such as the interactions between multiple signaling pathways and the coordination of cell fate during development, the behaviour of collective motion of cells, the response of an organ to injury and the healing of damaged components (Chitnis et al, 2012).

In the present thesis we follow closely the results obtained in recent biological experiments performed on the zebrafish lateral line system (see Haas and Gilmour, 2006; Nechiporuk and Raible, 2008; Lecaudey et al, 2008, and the further papers Haddon et al, 1998; Itoh and Chitnis, 2001; Draper et al, 2001; Ghysen and Chaudière, 2004; Li et al, 2004; Matsuda and Chitnis, 2010; Sarrazin et al, 2010; Mizoguchi et al, 2011; Sweet et al, 2011). The great interest for this sensory system is motivated by the still not complete understanding of the general mechanism for cells arranging and organization (Lecaudey et al, 2008).

Not only in relation to the lateral line, the zebrafishes hold an important role in scientific research, being useful vertebrate model organisms whose genome is fully sequenced. Particular advantages are due to their regenerative abilities, to robustness and transparency of the embryos (Dahm, 2006). The zebrafish model has been widely tested in many fields of biology: developmental biology, oncology, toxicology, reproductive studies, genetics, neurobiology, stem cell research and regenerative medicine (Xiang et al, 2009; Major and Poss, 2007).

Lateral line formation in the zebrafish is a complex process where embryonic cells are driven by an articulated system of receptor activation, rather than a guidance determined by birth. Experimental observations (Haas and Gilmour, 2006; Sarrazin et al, 2010) have shown an initial elongated group of mesenchymal cells (called *primordium*), in the range 80–100 cells, located in the otic vesicle. In few hours post-fertilization a total migration of the primordium begins from the head to the tail of the embryo at a velocity of about 69 $\mu\mathrm{m\,h}^{-1}$ (Lecaudey et al, 2008). Subsequently, during the migration process a cell transition, occurring in the rear of the migrating group, makes some cells epithelial-like (mesenchymal-epithelial transition) and rosette-shaped structures (proto-neuromasts) begin to emerge. When these cell aggregates become fully mature, they are detached and deposited along the body of the embryo, giving rise to the growth and location of neuromasts (about four or five neuromasts along a flank, see Nechiporuk and Raible, 2008), see Figure 0.2 (a).

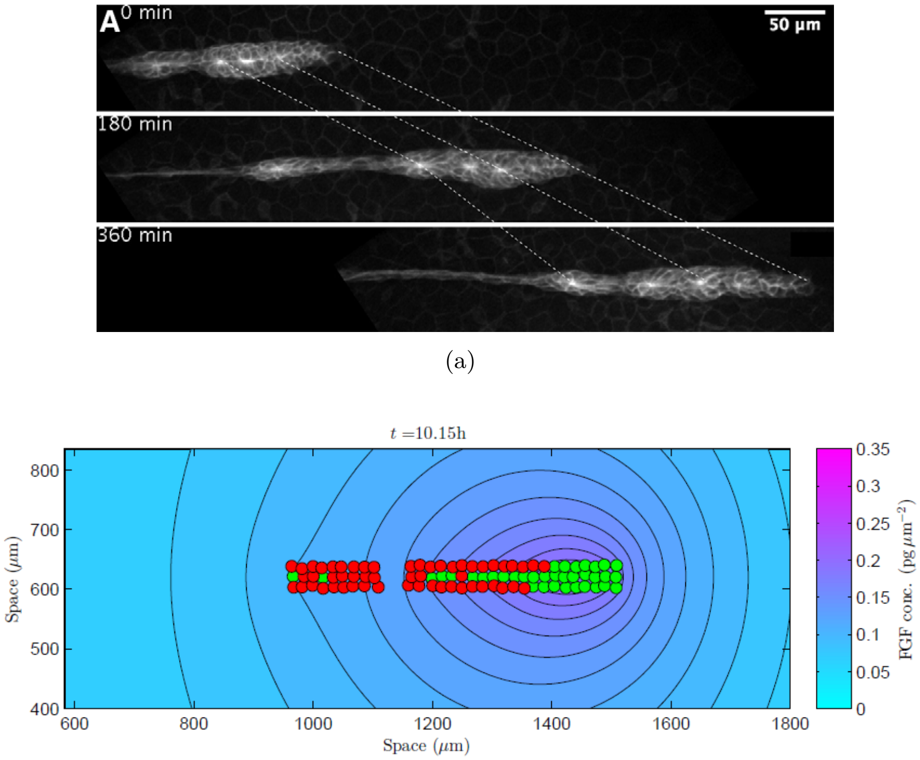

(a)

(b)

Figure 0.2. (a) Image from a time-lapse movie about the migration in the zebrafish posterior lateral line primordium. Leading zone is on the right of the primordium, trailing zone is on the left. Cell migration is to the right while neuromast deposition occurs in the trailing region (source Lecaudey et al, 2008). (b) An example of dynamical simulation of our mathematical model proposed in Chapter 3.

In general we can split the morphogenesis of the zebrafish lateral line primordium in two primary mechanisms: a collective migration, and a neuromast assembly. The first process is regulated by a haptotactic chemokine, called *stromal cell-derived factor-1a* (SDF-1a), expressed by the substratum and detected by the primordium through the receptor CXCR4b (Ghysen and Chaudière, 2004; Haas and Gilmour, 2006). Moreover, the total migration is ensured by a series of cell-cell interactions via mechanical forces, and by a cell-substratum adhesion, both mediated by molecules as cadherins and integrins (see Section 1.3, and also Liu et al, 2003a; Kerstetter et al, 2004; Papusheva and Heisenberg, 2010; Liu et al, 2011; Mertz et al, 2013).

The neuromast formation, in the second stage, is regulated by two main chemotactic factors expressed by the primordium, the *fibroblast growth factors* FGF3-FGF10, and by their receptors FGFRs. Two prevalent experimental observations are shown in Lecaudey et al (2008): firstly, FGF3 and FGF10 are substantially equivalent, demonstrating a robustness of the system; secondly, FGF signal and its receptor are mutually exclusive. In particular FGF3-FGF10 are broadly expressed in the leading region of the primordium and focused in one or two cells in the centre of the rosettes in the trailing region, on the other hand FGFR is expressed in the trailing region except the FGF sources. The first observation suggests us take into account, in our mathematical model, only a single growth factor that we will name FGF. The second observation let us then divide the cell population in two kinds: *leader* cells that produce FGF signal and *follower* cells that, activating the receptor FGFR, do non produce any signal. At the beginning, the primordium contains only leader cells, afterwards, a process of differentiation on the backside makes some cells follower-like (corresponding to the mesenchymal-epithelial transition), except one or two cells located in the centre. The follower cells are then driven toward the FGF sources to form rosette-shaped aggregates (the future neuromasts), that subsequently are detached during the migration. Hence a new rosette is generated in a cyclic process (see Section 1.4).

Finally, the concomitant mechanisms that ensure the leader-to-follower transition in the trailing region can be represented by three conditions: a low level of SDF-1a (Ghysen and Chaudière, 2004), a high level of FGF (Lecaudey et al, 2008) and an influence of *lateral inhibition* (Haddon et al, 1998; Itoh and Chitnis, 2001; Hart et al, 2003; Matsuda and Chitnis, 2010; Mizoguchi et al, 2011; Sweet et al, 2011). This last condition involves a common phenomenon in embryology, that here can be read as follows: a cell that adopts the follower fate inhibits its immediate neighboring cells from doing likewise. This mechanism, for which still remain some unresolved issues (Chitnis et al, 2012), will be translate in our mathematical formulation counting the number of cells surrounding a given cell, and considering the leader-to-follower transition favored by a low number of neighboring cells. In this way a central leader will be more inhibited to become follower, while a cell at the edge of the primordium will be more likely to undergo the transition (see Section 1.5).

In Chapter 3 we will propose a mathematical model for the above discussed morphogenesis process. As we will see, our model will be consistent with the biological observations if we consider chemical effects concomitant with other cell mechanisms, as lateral inhibition, alignment, damping, adhesion-repulsion effects. Taking into account the low number of cells involved, we will adopt a hybrid discrete in continuous model, where cells are treated as discrete entities moving in a continuous space, and chemical signals, at molecular level, are described by continuous variables (see Section 2.4). On the chemical scale we will adopt diffusion and chemotaxis equations (see Sections 2.1–2.2), while on the cellular scale typical effects of collective dynamics will be taken into account (see Sections 2.5–2.7). Although the cell will be discrete points (coincident with their centres), we will recover their shape through suitable detection radii and, for simplicity, we will suppose circular cell shapes. In our mathematical formulation we will follow two objectives. Firstly, we would like to obtain a minimal model which is able to describe the total cell migration, the formation and the detachment of the neuromasts, in the spatial and temporal scale of the experimental observations. Secondly, we will require the existence and stability of the rosette structures characterizing the neuromasts, as stationary solutions of the system. As we will see, this will provide restrictions on the range of some parameter of the model, fixing their values or their suitable ratios. Other parameters, used in the numerical simulations, will be obtained from biological literature or by a numerical data fitting. In our analysis we will consider the 2D case, because collective motion takes place in an environment confined to essentially two dimensions due to the flattened morphology of the primordium (see Chapter 1).

From a mathematical point of view, on cell scale our model is based on a second order dynamic equation in the form

$$\ddot{\mathbf{X}}_i = \mathbf{F}(t, \mathbf{X}, \dot{\mathbf{X}}, u, \nabla u) - \mu \dot{\mathbf{X}}_i,$$

where $\mathbf{X}_i \in \Omega \subset \mathbb{R}^2$, $i = 1, \dots, N_{\text{tot}}$, is the position vector of the i-th cell, $N_{\text{tot}} \in \mathbb{N}$ is the total number of cells, $\mathbf{X} := (\mathbf{X}_1, \dots, \mathbf{X}_{N_{\text{tot}}})$, and $\dot{\mathbf{X}} := (\dot{\mathbf{X}}_1, \dots, \dot{\mathbf{X}}_{N_{\text{tot}}})$. The function $\mathbf{F}$ includes several effects: from the detection of chemical signals u (chemotaxis, lateral inhibition) to mutual interactions between cells (alignment, adhesion, repulsion). The damping term $-\mu \dot{\mathbf{X}}_i$, with μ constant, represents the cell adhesion to the substrate. All these effects take into account a non local sensing radius.

On the molecular scale, chemical signals $u(\mathbf{x}, t) : \Omega \times [0, T] \to \mathbb{R}$ are described by a diffusion equation

$$\partial_t u = D \Delta u + S(t, \mathbf{X}, u),$$

with possible source or degradation terms given in S, that can depend on time, on cell spatial distribution of the cells, and on chemical factor u.

Finally the leader-follower cell state, involved in the mesenchymal-epithelial differentiation, is performed by a switch variable, whose evolution in time is given by a suitable threshold function.

Now, let $\mathbf{X}_i(t)$ be the position of the i-th cell, $\varphi_i(t)$ the state variable assuming the values 0-1 respectively for a follower-leader cell, $f(\mathbf{x}, t)$ the concentration of the FGF3-FGF10 (equivalent) signals and $s(\mathbf{x}, t)$ the concentration of the chemokine SDF-1a, our model reads:

$$\left\{ \begin{aligned}
\ddot{\mathbf{X}}_i \; &= \frac{\alpha}{W} \int_{\mathbf{B}(\mathbf{X}_i, \bar{R})} \nabla s(\mathbf{x}, t) w_i(\mathbf{x})\, d\mathbf{x} + \frac{\gamma(1 - \varphi_i)}{W} \int_{\mathbf{B}(\mathbf{X}_i, \bar{R})} \nabla f(\mathbf{x}, t) w_i(\mathbf{x})\, d\mathbf{x} \\
&\quad + \frac{1}{\bar{N}_i} \sum_{j : \mathbf{X}_j \in \mathbf{B}(\mathbf{X}_i, R_1) \setminus \{\mathbf{X}_i\}} \mathbf{H}(\dot{\mathbf{X}}_j - \dot{\mathbf{X}}_i) + \sum_{j : \mathbf{X}_j \in \mathbf{B}(\mathbf{X}_i, R_5) \setminus \{\mathbf{X}_i\}} \mathbf{K}(\mathbf{X}_j - \mathbf{X}_i) \\
&\quad - \left[\mu_{\mathrm{F}} + (\mu_{\mathrm{L}} - \mu_{\mathrm{F}})\varphi_i\right] \dot{\mathbf{X}}_i, \\
\varphi_i \; &= \left\{ \begin{array}{ll}
0, & \text{if } \dfrac{\delta}{W} \displaystyle\int_{\mathbf{B}(\mathbf{X}_i, \bar{R})} s(\mathbf{x}, t) w_i(\mathbf{x})\, d\mathbf{x} \\
& \quad - \dfrac{k_{\mathrm{F}} + (k_{\mathrm{L}} - k_{\mathrm{F}})\varphi_i}{W} \displaystyle\int_{\mathbf{B}(\mathbf{X}_i, \bar{R})} \dfrac{f(\mathbf{x}, t)}{f_{\max} + f(\mathbf{x}, t)} w_i(\mathbf{x})\, d\mathbf{x} + \lambda \Gamma(n_i) \leq 0, \\
1, & \text{otherwise,}
\end{array} \right. \\
\partial_t f \; &= D \Delta f + \xi \sum_{j=1}^{N_{\text{tot}}} \varphi_j \chi_{\mathbf{B}(\mathbf{X}_j, R_3)} - \eta f, \\
\partial_t s \; &= -\sigma s \sum_{j=1}^{N_{\text{tot}}} \chi_{\mathbf{B}(\mathbf{X}_j, R_3)},
\end{aligned} \right. \tag{0.1}$$

where α, γ, μ_{L}, μ_{F}, δ, k_{L}, k_{F}, λ, D, ξ, η, σ are given positive constants, and $\bar{R}$, R_i, $i = 1, \ldots, 5$, are suitable sensing radii (some of them included in the functions $\mathbf{K}(\mathbf{X}_j - \mathbf{X}_i)$ and $\Gamma(n_i)$). More details about the notations and the choice of parameters will be given in Section 3.2. Here we remark that we will assume some groups of parameters to have different values depending on the leader ("L") or follower ("F") cell state. They are marked by the respective letter in subscript position. This will be justified in Sections 3.2 and 3.7.

In particular, the integral terms in $(0.1)_{1,2}$, related to the detection of a chemical signal by the i-th cell in its neighbourhood, represent a weighted average, through a truncated Gaussian weight $w_i(\mathbf{x})$, over a ball centred in $\mathbf{X}_i$ with sensing radius $\bar{R}$.

First term in equation $(0.1)_1$ translates the haptotactic attraction exerted on the cells by the SDF-1a signal (Murray, 2003; Perthame, 2007), similarly the second term is the chemotactic effect of the FGF factor, that acts only on a follower cell ($\varphi_i = 0$) due to the activation of the FGFR receptor, while leader cells ($\varphi_i = 1$), producing FGF signal, do not activate their receptors (mutual exclusion previously described). In the third and fourth term we will include cell-cell interaction via mechanical forces, due to filopodia. $\mathbf{H}(\dot{\mathbf{X}}_j - \dot{\mathbf{X}}_i)$ is an alignment term inspired by the Cucker-Smale mechanism (Cucker and Smale, 2007a), though in our case it is coupled with other effects. This term is taken proportional to a weighted average of the differences in the cell velocities, $\bar{N}_i$ being the number of neighbours of the i-th cell. Namely, we choose

$$\mathbf{H}(\dot{\mathbf{X}}_j - \dot{\mathbf{X}}_i) := [\beta_{\mathrm{F}} + (\beta_{\mathrm{L}} - \beta_{\mathrm{F}})\varphi_i\varphi_j] \frac{R_1^2}{R_1^2 + ||\mathbf{X}_j - \mathbf{X}_i||^2} (\dot{\mathbf{X}}_j - \dot{\mathbf{X}}_i),$$

where β_{F} and β_{L} are positive constants, respectively for a follower or a leader cell. A similar term, applied in a biological context, can be found in Szabò et al (2006), Arboleda-Estudillo et al (2010), and Sepúlveda et al (2013), since the seminal work of Vicsek et al (1995) (see Sections 2.5–2.7). In our case this alignment effect will be justified in Section 3.7.

The function $\mathbf{K}(\mathbf{X}_j - \mathbf{X}_i)$ will include adhesion-repulsion effects on suitable sensing regions. In this regard we assume

$$\mathbf{K}(\mathbf{X}_j - \mathbf{X}_i) := \begin{cases} -\omega_{\mathrm{rep}} \left(\dfrac{1}{||\mathbf{X}_j - \mathbf{X}_i||} - \dfrac{1}{R_4} \right) \dfrac{\mathbf{X}_j - \mathbf{X}_i}{||\mathbf{X}_j - \mathbf{X}_i||}, & \text{if} \quad ||\mathbf{X}_j - \mathbf{X}_i|| \le R_4; \\ \\ \bar{\omega}_{\mathrm{adh}} \left(||\mathbf{X}_j - \mathbf{X}_i|| - R_4 \right) \dfrac{\mathbf{X}_j - \mathbf{X}_i}{||\mathbf{X}_j - \mathbf{X}_i||}, & \text{if} \quad R_4 < ||\mathbf{X}_j - \mathbf{X}_i|| \le R_5; \end{cases}$$

where $R_5 > R_4$ and $\bar{\omega}_{\mathrm{adh}} := \omega_{\mathrm{adh,F}} + (\omega_{\mathrm{adh,L}} - \omega_{\mathrm{adh,F}})\varphi_i\varphi_j$, with ω_{rep}, $\omega_{\mathrm{adh,L}}$, $\omega_{\mathrm{adh,F}}$ differentiated constants for a leader or a follower cell. In practice, we consider a repulsion in the form $1/r$, r being the distance between two cells, and a linear elastic attraction. Similar terms can be found, for instance, in D'Orsogna et al (2006), Cristiani et al (2011a), Joie et al (2014), Albi and Pareschi (2013).

The last term in $(0.1)_1$ is due to the cell adhesion to the substrate, possibly with a different damping coefficient according to Rubinstein et al (2009), Fournier et al (2010), Bayly et al (2012).

In equation $(0.1)_2$ the switch variable φ_i represents the follower-leader state of the i-th cell, corresponding respectively to the values 0-1. Its definition takes into account the three conditions for the leader-to-follower transition that we have briefly discussed above, i.e. the low level of SDF-1a concentration (first term), the high level of FGF factor (second term) and the lateral inhibition effect in $\Gamma(n_i)$. This last function will depend on the number n_i of neighbours surrounding the i-th cell in a fixed interaction range. The coefficients $k_{\mathrm{L}} < k_{\mathrm{F}}$ make then a possibly delayed inverse follower-to-leader transition (see Section 3.2).

Equations $(0.1)_{3,4}$ describe the concentration of the main chemical signals involved in the biological process, respectively the FGF growth factor and the chemokine SDF-1a. In the first equation next to the diffusion term, we consider the sources of FGF defined substantially by the shape of a cell. So we can take characteristic functions of a ball centred on each leader cell, with a radius equal to the cell ray. On the other hand, follower cells do not produce the growth factors. An (exponential) molecular degradation term is then taken into account with constant rate η. In equation $(0.1)_4$ the SDF-1a concentration degrades when its molecules bind with the receptor CXCR-4b. Similarly to the FGF equation, we will consider characteristic functions centred on each cell of the primordium (see Section 3.2).

Initial and boundary conditions for system (0.1) are represented by the initial position and cell velocity,

$$\mathbf{X}_i(0) = \mathbf{X}_{i0}, \quad \text{and} \quad \dot{\mathbf{X}}_i(0) = \mathbf{0}, \quad i = 1, \ldots, N_{\mathrm{tot}},$$

together with the initial cell state of leader,

$$\varphi_i(0) = 1, \quad i = 1, \ldots, N_{\mathrm{tot}}.$$

For the FGF signal we will assume zero initial concentration and, since no chemoattractant is supposed to leave the spatial domain Ω, a classical homogeneous Neumann condition is imposed on the boundary:

$$f(\mathbf{x}, 0) = 0; \quad \frac{\partial f}{\partial \mathbf{n}} = 0, \quad \text{on } \partial\Omega.$$

Finally, since initially SDF-1a is only located in a given region, we will assume

$$s(\mathbf{x}, 0) = s_0(\mathbf{x}),$$

distributed on a stripe according to the experimental observation in Ghysen and Chaudière (2004), see also Section 3.2.

Main results

Starting from system (0.1), we will prove the existence of stationary solutions biologically relevant and consistent with the formation of the neuromast structures. Namely, we will define and investigate particular configurations, that we will name *N-rosettes*, formed by a leader cell in the centre, surrounded by N follower cells, whose centres are located on the vertices of a regular polygon of N sides, centred in the leader cell (Figure 0.3).

Assuming some physically reasonable hypotheses on the distances between the cells and on the interaction radii, from geometrical considerations some properties

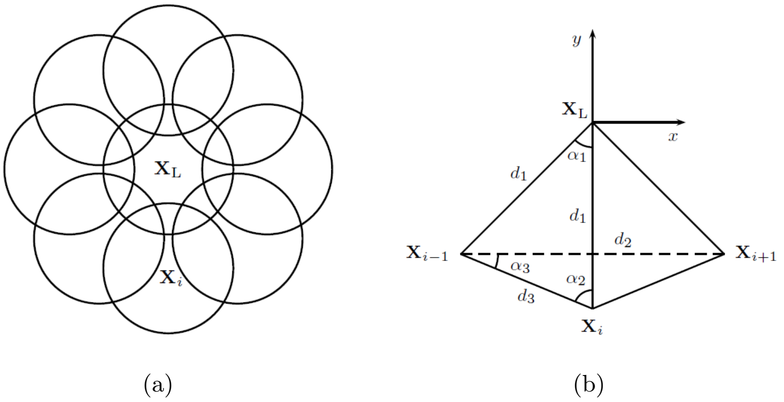

Figure 0.3. (a) Example of 8-rosette with a leader centred in $\mathbf{X}_\mathrm{L}$ and 8 followers centred in $\mathbf{X}_i$, $i = 1, \dots, 8$. (b) Geometrical configuration of a N-rosette with a leader cell centred in $\mathbf{X}_\mathrm{L}$ and some followers centred in $\mathbf{X}_{i-1}$, $\mathbf{X}_i$, $\mathbf{X}_{i+1}$ (see also Section 3.4).

will be deduced for our steady solutions. Among these, for instance, we will prove the existence of an upper bound for N and of a range of possible distances, depending on N, that will be admissible in a N-rosette. Such values are in a good agreement with the experimental observations shown in Lecaudey et al (2008). Moreover, the stationary model will impose important restrictions on some parameters of the system, which will be used in the numerical tests of the dynamical case. About the stability of the steady configurations we will give then a numerical assessment. In the temporal range of the real phenomenon we will observe the N-rosettes be stable. For more details we refer to Section 3.4.

Finally, from a dynamical point of view some numerical simulations will be performed to show the behaviour of the model and its qualitative and quantitative accuracy to describe the evolution of the cell aggregate. In this regard we will develop a numerical approximation scheme based on finite differences. The parameters of the system, fixed in part by the steady model, will be estimated from the biological-modelling literature or by a suitable numerical data fitting (see Section 3.7). Our numerical tests will show a nice agreement with biological evidences, both on the spatio-temporal scale and on the chemical concentration scale of the physical process (see previous Figure 0.2 (b)). Furthermore, we will see that our model can reproduce the self-generation of chemical gradient by the migrating cells of the primordium, a mechanism hypothesized for the cell migration in embryos (Dambly-Chaudiére et al, 2007; Scherber et al, 2012) and recently proved *in vivo* on the zebrafish by Donà et al (2013) (see Section 3.6–3.7).

Part II - A mathematical model of collective motion under alignment and chemotaxis

In the second part of the thesis (comprising the fourth chapter) we will propose a hybrid mathematical model of collective motion based on an alignment and chemotactic effect in a system of interacting particles. This model, which can be considered an extension of Cucker-Smale model (Cucker and Smale, 2007a), will be studied both from the analytical and the numerical point of view. The coupling between alignment effect, performed by a Cucker and Smale-like term, and chemotaxis is already considered, as we have seen, in the first part of the thesis in relation to the mathematical model for the zebrafish lateral line (see Chapter 3).

Collective motion models, of which the Cucker-Smale model is an example, describe the collective behaviour of individuals through simple interaction rule (alignment, attraction, repulsion) or their combinations. The main feature in collective dynamics is that the individual action is strongly influenced by the interaction with other units, with respect to the case in which the single was alone. Collective motions were observed in many living and non-living systems: fluids, nano swimmers, flocks of birds, schools of fish, swarms, herds of mammals, cell aggregates, crowds of humans (Vicsek and Zafeiris, 2012). The research in this area is of great interest for the applications in many fields of the real life, from biomedical field, in relation to the collective motion of cells, to socio-economic field, to the problems of human engineering (see Section 2.5, and also Naldi et al, 2010; Méhes and Vicsek, 2014).

The Cucker-Smale model describes the collective behaviour of N interacting particles under an alignment effect. The original model (Cucker and Smale, 2007a) was proposed for flocks of birds, but it can be applied in a more general context, looking at the alignment as a consensus attainment in a group (Couzin et al, 2005). Previous works, from which Cucker and Smale were inspired, can be found since the paper of Vicsek et al (1995), and similar studies are discussed in Tsitsiklis (1984), Jadbabaie et al (2003). However, the Cucker-Smale's paper is known to have shown an analytical result on the asymptotic behaviour in a group of autonomous agents under an alignment effect.

The hypothesis assumed by the model is that the force acting on a single particle is a weighted average of the differences of its velocity with those of the other particles. Let us consider $N \in \mathbb{N}$ agents with position and velocity given by $\mathbf{X}_i, \mathbf{V}_i \in \mathbb{R}^n$, for $i = 1, \ldots, N$, in continuous time the model reads:

$$\begin{cases} \dot{\mathbf{V}}_i = \dfrac{\beta}{N} \displaystyle\sum_{j=1}^{N} \dfrac{\alpha_1}{\left(\alpha_2 + \|\mathbf{X}_i - \mathbf{X}_j\|^2\right)^{\sigma}} (\mathbf{V}_j - \mathbf{V}_i), \\ \\ \dot{\mathbf{X}}_i = \mathbf{V}_i, \end{cases} \tag{0.2}$$

where β, α_1, α_2, σ are positive constants and $\|\cdot\|$ is the Euclidean norm in $\mathbb{R}^n$.

In Cucker and Smale (2007a) it is shown, by an analytical point of view, that under suitable initial data and parameters of the model the system of particles evolves to a so called *flocking state*, in which all agents have the same velocity. This result has been then improved by Ha and Liu (2009) through an explicit Lyapunov functional approach. A key parameter of the system is the exponent σ in (0.2), that translates the rate of decay when the alignment effect spatially propagates in the group. In particular it is proved that, if $\sigma \in [0, 1/2]$, then the flocking behaviour is always ensured, regardless of initial data (*unconditional flocking*), while, if $\sigma \in (1/2, +\infty)$, the flocking state is guaranteed only under suitable parameters and initial configurations of the system (*conditional flocking*), but in general the group may be scattered.

Cucker and Smale-like models have been widely employed in collective dynamics (see Sections 2.6–2.7) and several applications have found confirmation from the biological field to the collective motion of different interacting groups (Szabò et al, 2006; Belmonte et al, 2008; Arboleda-Estudillo et al, 2010; Sepúlveda et al, 2013; Albi and Pareschi, 2013).

Recently, many extensions have been proposed, providing some analytical results about them. Among these, we find alignment models with noise (Cucker and Mordecki, 2008), phototaxis (Ha and Levy, 2009), repulsion Cucker and Dong (2010), individual with a preferred heading velocity (Cucker and Huepe, 2008), see also Section 4.1.

In Chapter 4, starting from equations (0.2), we will propose a Cucker and Smale-like model with chemotaxis effect for a system of N interacting particles. We will consider a hybrid description: discrete for the particle scale and continuous at the chemical level. In particular, we will assume that the force acting on a single particle will be given by an alignment term, proportional to the differences of velocity with the other particles, and by a chemotactic term, typically proportional to the gradient of concentration of a chemical signal $f(\mathbf{x}, t)$, supposed produced by the particles themselves (Murray, 2003; Perthame, 2007). Then, for the signal $f(\mathbf{x}, t)$ we will assume a dissipative diffusion equation with source, as discussed in Section 3.2. If the cells are supposed to be circles of radius R, whose centres are located in $\mathbf{X}_i$ with velocity $\mathbf{V}_i$, the model reads:

$$\begin{cases} \dot{\mathbf{V}}_i = \dfrac{\beta}{N} \displaystyle\sum_{j=1}^{N} \dfrac{1}{\left(1 + \frac{\|\mathbf{X}_i - \mathbf{X}_j\|^2}{R^2}\right)^{\sigma}} (\mathbf{V}_j - \mathbf{V}_i) + \gamma \nabla f(\mathbf{X}_i, t), \\ \\ \dot{\mathbf{X}}_i = \mathbf{V}_i, \\ \\ \partial_t f = D \Delta f + \xi \displaystyle\sum_{j=1}^{N} \chi_{\mathbf{B}(\mathbf{X}_j, R)} - \eta f, \end{cases} \tag{0.3}$$

where $\beta, \sigma, \gamma, D, \xi, \eta$ are positive constants, and $\chi_{\mathbf{B}(\mathbf{X}_j, R)}$ is the characteristic function of the ball centred in $\mathbf{X}_j$ with radius R.

Initial data will be given by initial position and velocity of the cells and by the zero concentration of the chemoattractant f.

Main results

Starting from system (0.3) we will consider, for analytical and numerical simplicity, the two-dimensional case. By a fixed–point argumentation we will prove local existence and uniqueness of the solution (see Section 4.3). Then, providing a suitable principle of continuation of solutions, we will extend the local existence and uniqueness for all $t \in [0, +\infty)$ (see Section 4.4).

In relation to the asymptotic behaviour of the proposed model, we will consider particular equilibrium configurations corresponding to a state in which all particles of the system have the same position with zero velocity. From an analytical point of view, we will prove their asymptotic stability on a linearized version of the system

(0.3) around these equilibrium points. In particular, through a suitable Lyapunov functional, we will show the asymptotic convergence of the position and velocity of the particles toward those of their centre of mass. Then the centre of mass of the system is proved to go to zero asymptotically in time (see Section 4.5). The behaviour of the full nonlinear system will then be tested, from a numerical point of view, performing several meaningful dynamical simulations (Figure 0.4). For them a numerical approximation scheme based on finite differences will be employed. Our results will show a complete concordance with the behaviour of the linearized system (see Section 4.6). Moreover, they suggest that an analytical convergence result on the nonlinear system could possibly be obtained.

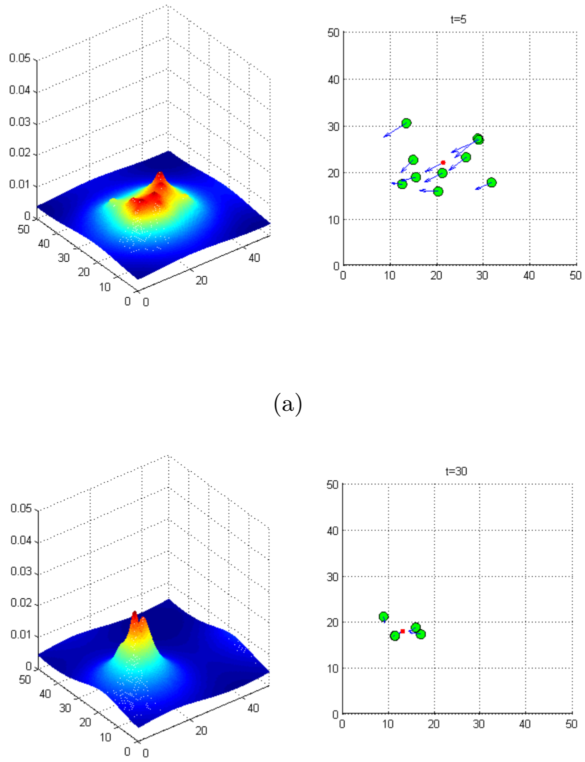

(a)

(b)

Figure 0.4. An example of dynamical simulation of the model (0.3) proposed in Chapter 4.

Hence, we remark that while the original Cucker-Smale model displays two possible behaviour, conditional and unconditional flocking, here, also when the dispersion of the group could occur solely with an alignment interaction, the chemotaxis effect ensures in any case the flocking state, moreover with the stronger condition that all particles converge in a same position with zero velocity. Among the various numerical simulations, inspired from our model on the lateral line in Chapter 3, we will consider also the case of two kinds of cells, named leaders and followers: both subjected to the alignment effect and chemotaxis, but only the first expressing the chemical signal. In this case we will observe the convergence of the group toward the sources of the chemoattractant. Finally, we will consider the collective motion under chemotaxis, neglecting the alignment effect. Our numerical tests, in this regard, seem to show the absence of convergence, and an oscillating motion of the particles around their centre of mass presents. This suggests that, in our model, the only chemotactic effect is unable to reproduce biological phenomena involving stationary aggregates.

Plan of the thesis

The present thesis is organized in four chapters.

In Chapter 1 we will introduce biological elements about the morphogenetic process occurring in the development of the lateral line in a zebrafish. After a first discussion on the lateral line system and on its fundamental relevance in the current scientific research we will focus on the main mechanisms of chemical signaling and collective cell migration, that will be taken into account later in our mathematical formulation of the phenomenon.

In Chapter 2 we will provide a mathematical-modelling background that, starting from the morphogenesis on the chemical scale, will gradually lead us to discuss the existing mathematical models, proposed in the last years to describe collective motion in living system and in particular in the biological field. Example of numerical simulations, and their comparison with experimental evidences will be briefly shown, taken from the recent modelling literature.

In Chapter 3 we will introduce our hybrid mathematical model describing the self-organizing cell migration in the zebrafish lateral line primordium. We will discuss the derivation of the model, justifying our modelling choices and comparing them with the existing literature. Particular steady states, corresponding to the emerging neuromasts, will then be investigated and their stability will be numerically assessed. Moreover, after a description of the designed numerical approximation scheme, some dynamical simulations will be proposed to show the powerful and the limit of our approach. Finally, we will discuss the estimate of the parameters of the model, derived in part by the biological and the modelling literature, in part by the stationary model or by a numerical data fitting.

In Chapter 4 we will propose a Cucker and Smale-like mathematical model of collective motion. Our hybrid model will describe a system of interacting particles under an alignment and chemotaxis effect. From an analytical point of view, local and global existence and uniqueness of the solution will be proved. Furthermore, the asymptotic behaviour of the model will be investigated on a linearized form of the system. From a numerical point of view, through an approximation scheme based on finite differences, the full nonlinear system will be simulated and some significant dynamical tests will be shown. Numerical results will be compared with those analytical, and new perspectives will be proposed.

Future perspectives

In relation to the first part of the present thesis, we remark that, as every model, the proposed mathematical model for the zebrafish lateral line has some limits in its applicability. For instance, in this model all cells are equally supposed to be circular and deformations in cell shape are not taken into account, but they are described only indirectly, introducing suitable interacting radii. Then, the mathematical description is limited only at the processes occurring from the beginning of the cell migration to the deposition of neuromasts. Biological phenomena arising in the next few hours post-fertilization, or in the time after the neuromast formation, are neglected. A possible extension of the model could investigate subsequent or concomitant processes with respect to the lateral line development. Moreover, as we could observed, in our modelling choice, next to the biological immediately evident mechanisms described in the existing literature, such as chemotaxis effects, chemical signal diffusion, cell adhesion-repulsion, damping term, it was necessary to introduce other effects, as our lateral inhibition model, cell alignment, differentiated parameters for the leader-follower cell state, to obtain consistent results with the experimental observations. This could represent a starting point to perform further biological experiments in such a context to validate our assumptions, to provide a better calibration of our model, or to propose new insights. Recently, we have launched a collaboration with some clinicians to apply our basic model to describe cell aggregates in analogous systems, for instance in relation to cardiac stem cells for which a hybrid mathematical description, with interactions similar to these discussed in this thesis, seems to be appropriate. Particular spherical structures (cardiospheres), characterizing such type of cells under certain conditions, suggest also an extension of the model to the three-dimensional case.

For the second part of the thesis, in a more theoretical framework, the analytical convergence result obtained on the linearized model of collective motion with alignment and chemotaxis could be extended to the nonlinear case. Furthermore, the “toy model” may be expanded introducing other interactions, such as adhesion-repulsion, damping or lateral inhibition effect, or considering more cell populations and different chemical signals. It would be meaningful, for instance, to study the general model proposed on the zebrafish lateral line and to establish analytical results about the neuromast formation and their detachment.

Chapter 1

Morphogenesis of the zebrafish lateral line

1.1 Introduction

In this chapter we will describe the biological processes that regulate the growth and the development of the lateral line in zebrafishes. After a discussion on the lateral line system, we will focus on the primary mechanisms that concur to this morphogenetic phenomenon. Particular emphasis will be given on the biological aspects that will be take into account to design, in next chapters, a mathematical model consistent with the experimental observations presented here.

Morphogenesis is the process that leads to the development of patterns and forms during the embryonic stage of an individual. The part of biology which studies the formation and the development of the embryo, from the fertilization to the birth, is then called embryology, and the set of the involved processes embryogenesis. Embryogenesis consists in a series of phenomena of growth, differentiation and organogenesis. In general, we can distinguish three main stages. The first stage is the cleavage, a rapid cell division occurring after fertilization, with no significant growth, producing a cluster of cells (morula) of the same size as the original zygote. At the end of this process the embryo is called blastula and is formed by a spherical single layer of cells (the blastoderms) surrounding a fluid-filled cavity. The second stage consists in the gastrulation, a process of migration and self-organization in which three cell layers, called germ layers, originate (ectoderm, mesoderm and endoderm). During this phase the embryo is called gastrula. The third stage is the organogenesis, the development of the internal organs of the individual. Each germ layer gives rise to specific tissues and organs. In general the ectoderm, the outermost layer, gives rise to epidermis and other tissues that will later form the nervous system (see also Section 1.2). The mesoderm, located between the ectoderm and the endoderm, gives rise to the various internal organs, such as hart, kidney, connective tissue and blood vessels. The endoderm, the innermost layer, leads to the formation of the epithelium of the digestive and respiratory system and of the organs such as liver and pancreas (Reece et al, 2013).

During the embryonic stage, morphogenetic processes can involve molecular and cellular scale. On chemical scale many substances, called morphogens, govern the pattern of tissue development. Local concentration gradients act on the cells providing a spatial information and controlling their organization and differentiation. In general, we can distinguish three types of signals: intracellular signals, which act when a molecule activates a receptor located on the cell surface, and give rise to signaling cascades inside the cell; long range diffusive signals, that direct the spatial cell organization in surrounding tissue (e.g. chemotaxis, Section 2.2); cell interaction, for instance through cell adhesion molecules such as integrins and cadherins (see Sections 1.3–1.4). On the cell scale morphogenesis concerns the change in the cellular structure or how cells interact in tissues, implying tissue elongation, thinning, folding or separation of one tissue into distinct layers (Gilbert, 2000). For example, the cellular differentiation such as the mesenchymal-epithelial transition, induce a change from a motile cell state, characterized by large migratory properties, to a polarized state, in which cells tend to remain closely connected through cell-cell junctions. Conversely the reverse process epithelial-mesenchymal transition (see Sections 1.4).

In the next sections we introduce, from a biological point of view, the morphogenesis process arising during the early development of the lateral line system in a zebrafish embryo.

1.2 The zebrafish lateral line

The *lateral line* is a sensory system, which is present in fish and amphibians, that is used to detect movement and vibration in the surrounding water within few centimeters, and is involved in a large variety of behaviours, from prey detection to predator avoidance, school swimming and sexual courtship. It extends from the head to the tail along each flank of the fish, and it is formed by a set of sensory organs, the *neuromasts*, arranged on the body surface in specific patterns. The neuromasts, located between the ear and the eye, form the so-called anterior lateral line system (ALL), while neuromasts on the body and tail form the *posterior lateral line* system (PLL) (Ghysen and Chaudière, 2004; Coombs and Netten, 2005), see Figure 1.1. Each neuromast consists by sensory hair cells at its centre. While the neuromast is embedded in the epidermis, each hair cell extends a ciliary bundle into the water, covered with a gelatinous cupula, in this way water movement is shared with the movement of the bundle. The hair cells are then innervated by sensory neurons and are surrounded by other support cells, which provide support during growth and regeneration of the sensory hair cells following injury (Chitnis et al, 2012), see Figure 1.2.

The function of the lateral line has attracted the attention of biologists for over a hundred and fifty years, and currently remains a subject of active study by sensory ecologists and physiologists (Dijkgraaf, 1989). The lateral line primordium has contributed to a deeper understanding in many fundamental issues, such as: how interactions between multiple signaling pathways direct the coordination of cell fate and morphogenesis during development, how collective migration is controlled, and how an organ responds to injury and replaces damaged components (Chitnis et al, 2012). In relation to the disorders of the nervous system, lateral line have been used to understand how the genetic defects cause functional abnormalities in the human brain, spinal cord and sensory organs.

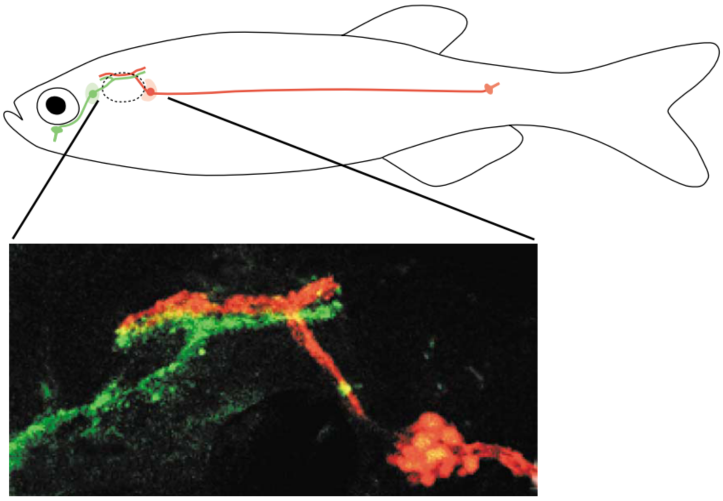

Figure 1.1. Scheme of an adult fish, illustrating the innervation of ALL and PLL. The photograph below shows the organization of ALL (green) and PLL (red) in a young larvae (source Ghysen and Chaudière, 2004). Neuromasts are not shown, but they can be imaged located along the green and the red line, in a pattern similar to that in Figure 1.3 showing a zebrafish embryo.

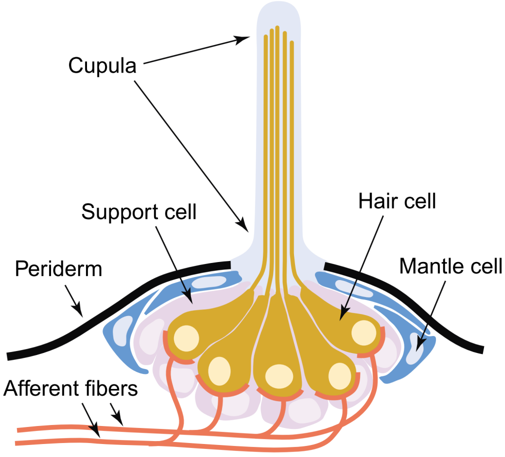

Figure 1.2. A scheme of a neuromast, comprising a core of mechanosensory hair cells, surrounded by support cells, and innervated by sensory neurons (source Ghysen and Chaudière, 2004).

Recent studies (Haas and Gilmour, 2006; Nechiporuk and Raible, 2008; Lecaudey et al, 2008, see also Haddon et al, 1998; Itoh and Chitnis, 2001; Draper et al, 2001; Ghysen and Chaudière, 2004; Li et al, 2004; Matsuda and Chitnis, 2010; Sarrazin et al, 2010; Mizoguchi et al, 2011; Sweet et al, 2011) have investigated migration and self-organization in the zebrafish (*Danio rerio*) lateral line system, where a complex system of receptor activation drives embryonic cells, rather than a guidance determined by birth. However, the complete mechanism for cells arranging and organization is still relatively poorly understood (Lecaudey et al, 2008).

The zebrafish represents an important vertebrate model organism in scientific research. It is particularly efficient for its regenerative abilities. Precursors to all major organs are visible within 36 hours of fertilization, and hatching takes place from 12 to 36 hours later. Moreover, its genome has been fully sequenced. The major advantages for scientists are due to its embryonic development, that is easily observable and testable, in fact zebrafishes embryos are robust, transparent, and able to develop outside their mother (Dahm, 2006). In particular lateral line is located on the surface, under the skin, and it is easy to monitor and to selectively label. Research with zebrafishes has brought improvements in the fields of developmental biology, oncology (Xiang et al, 2009), toxicology, reproductive studies, genetics, neurobiology, stem cell research and regenerative medicine (Major and Poss, 2007). Several transgenic models of cancer could be made using zebrafishes, such as melanoma, leukemia and pancreatic cancer (Liu and Leach, 2011). The great ability to regenerate skin, heart and (in larval stages) brain, makes the zebrafish a model for tissue repair (Major and Poss, 2007). In cardiovascular research, the zebrafish has been employed to model blood clotting, blood vessel development, kidney development and disease (Drummond, 2005). Finally, in relation to the immune system, many human infectious diseases have be modelled in zebrafish (Meeker and Trede, 2008).

Loosely speaking, lateral line formation in the zebrafish consists in a group of mesenchymal cells, in the range 80–100 cells (Haas and Gilmour, 2006; Sarrazin et al, 2010), that migrate driven by a haptotactic signal. In a second phase, a process of differentiation in the rear of the migrating group induces a mesenchymal-epithelial transition that is at the origin of the detachment of rosette-shaped structures (about four-five along the body, Nechiporuk and Raible, 2008). This corresponds to the growth and location of neuromasts along the two flanks of the embryo (Figure 1.3 (a)). In general we can state two primary mechanisms that concur to this morphogenesis process: a collective migration, and a neuromast assembly.

1.3 The collective cell migration. The role of the SDF-1a signal

About zebrafish PLL, recent studies and experimental observations (Haas and Gilmour, 2006; Lecaudey et al, 2008; Nechiporuk and Raible, 2008) show an initial elongated single group of mesenchymal cells (called *primordium*) in the otic vesicle, in which we can distinguish a *trailing region* near the head and a *leading region* oriented towards the future tail of the embryo. It can be morphologically visible just at about 18 hours post-fertilization (Mizoguchi et al, 2011; Nechiporuk and Raible, 2008). Mesenchymal cells, as we will see below, among early embryonic cells are characterized of large migratory properties, due to long finger-like protrusions called filopodia or lamellapodia that adhere on the adhesive sites and pull the cell along them (Walbot and Holder, 1987; Alberts et al, 1994). Different is the case of epithelial cells, as will be remarked in Section 1.4.

In the following few hours, a total cell migration begins posteriorly, from head to tail, with a constant velocity of about 69 $\mu\mathrm{m}\,\mathrm{h}^{-1}$ (Lecaudey et al, 2008). Then the cells in the trailing region assemble into rosette structures (proto-neuromasts), that

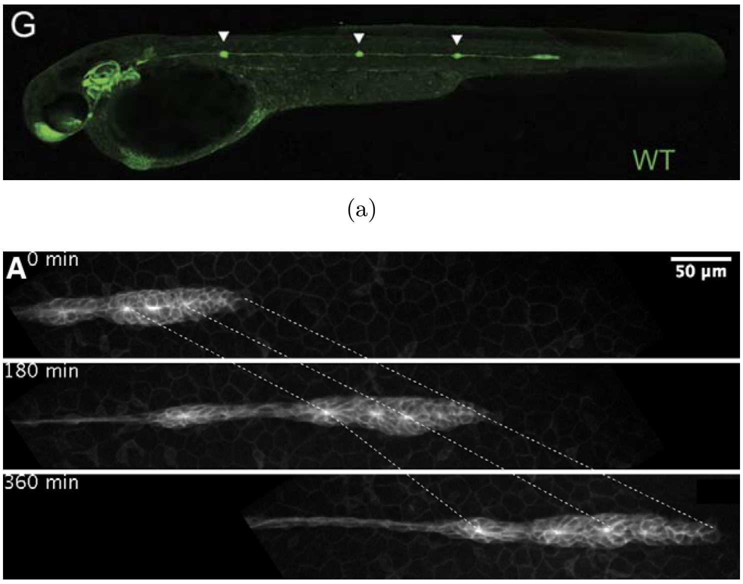

(a)

(b)

Figure 1.3. (a) A zebrafish embryo during the posterior lateral line formation. Green dots are the deposited neuromasts during the cell migration (source Haas and Gilmour, 2006). (b) Time-lapse movie of the cell migration in the zebrafish lateral line. We distinguish a leading region on the right on the tip of the migrating group of cell, and a trailing region on the left toward the head of the embryo. The detachment of rosette-shaped groups of cells in the trailing region corresponds to the neuromast deposition (source Lecaudey et al, 2008).

are progressively deposited during the migration to form neuromasts (Nechiporuk and Raible, 2008), see Figures 1.3 (b)–1.4 (a).

About cell migration a very important role is played by chemokines as the *stromal cell-derived factor-1a* (*SDF-1a*) and its *CXCR4b* receptor (Ghysen and Chaudière, 2004; Haas and Gilmour, 2006). The former is expressed by the horizontal myoseptum, that separates the dorsal and ventral axial muscles, and acts as a haptotactic stripe for the migrating cells; the latter is expressed by the primordium itself (Li et al, 2004). Experimental observation show that SDF-1a is synthesized by a narrow stripe, approximately three cells wide (Ghysen and Chaudière, 2004). We speak about haptotaxis when cells are attracted towards concentration gradients of a chemical substance expressed or bound on a surface (e.g. in this case the horizontal myoseptum). In general, if such signal diffuses in a fluid or in a tissue we refer to chemotaxis (see Section 2.2).

SDF-1 is a chemokine protein strongly haptotactic, produced in two forms: SDF-1a and SDF-1b. SDF-1/CXCR4 interaction is involved in many long-distance migration events, such as homing lymphocytes (in which this genes were originally discovered), the migration of metastases and the germ cells in both fish and mice (Doitsidou et al, 2002; Knaut et al, 2003). In particular, in tumour metastasis cancer cells that express the receptor CXCR4 are attracted to metastasis target tissues that release the ligand SDF-1 (Muller et al, 2001). During embryogenesis it directs the migration of cells from foetal liver to bone marrow and the formation of large blood

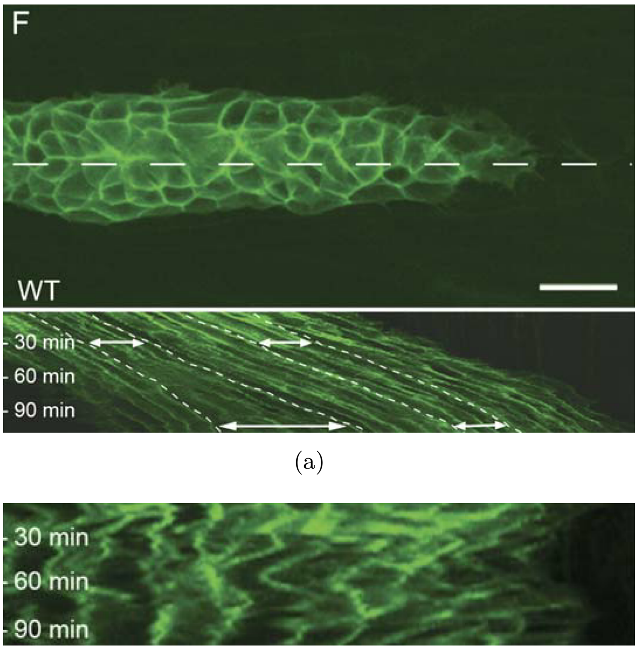

(a)

(b)

Figure 1.4. (a) Kymograph analysis of cell movement. Dotted line on the top represents the region used for the kymograph. In the bottom panel the vertical axis represents the time. The lines are shown predominantly parallel, meaning that cells migrate at a constant speed and maintain a relative position (dotted lines). The deceleration of cells at the back of the primordium, in view of the deposition of neuromasts, can be seen in the increased distance between the two dotted lines on the left (source Haas and Gilmour, 2006). (b) Cell movement is strongly uncoordinated in absence of CXCR4b function, with a "zig-zag" pattern in the kymograph analysis (source Haas and Gilmour, 2006).

vessels. In adulthood, SDF-1 plays an important role in angiogenesis by recruiting endothelial progenitor cells from the bone marrow through a CXCR4 dependent mechanism (Zheng et al, 2007).

Chemokine signaling is necessary to drive migration. In fact, it has been proved that, in absence of CXCR4b, cell movements are strongly uncoordinated, with a "zig-zag" pattern, as can be seen performing kymograph analysis, where a marked region of the primordium is observed and represented in a figure in which the vertical axis indicates the time (see Figure 1.4 (b)). Moreover, next to the chemoattractant chemokine, migration within the primordium is guaranteed by a *cell-cell interaction*, exerted by an adhesion force via filopodia. This is confirmed by two observations in Haas and Gilmour (2006): firstly, cells lacking CXCR4b receptor, transplanted into wild-type primordium, preserve their migration through the contact with neighboring cells; secondly, even a small number of wild-type cells, transplanted in a mutant primordium (lacking the SDF-1a receptor), after moving themselves toward the leading edge can restore the collective migration. These mechanisms were first demonstrated in models of epithelial wound healing, where the movement of cells in epithelial sheets toward each other, to fill a gap created by the wound, also involves collective migration (Chitnis et al, 2012). Additional studies have been performed in other model systems for collective migration, such as endothelial cells in tissue culture, border cells in the Drosophila system, and metastatic cancer cells (Haas and Gilmour, 2006; Friedl and Gilmour, 2009). In Figure 1.5 (a) a wild-type cells, marked in green, have been transplanted in a wild-type ("normal") primordium, marked in red. On the right panel cells display filopodia in the direction of migration. In Figure 1.5 (b) cells lacking of the chemokine receptor CXCR4b, marked in green, are placed in a wild-type primordium, marked in red. On the right panel cells have a similar dynamic behaviour as in Figure 1.5 (a), suggesting a strong interaction within the primordium via mechanical force with neighbouring cells, rather than a direct response to the extrinsic SDF-1a cue. Mutant cells rather than being passive hitchhikers, make an active contribution to lateral line migration. In Figure 1.6 a small number (about 5 %) of wild-type cells (in red) have been transplanted into a CXCR4b-deficient primordium (in green). The kymograph analysis below shows, in the top half, "zig-zag" lines, whereas, in the bottom half, the lines become parallel, implying that a small number of wild-type cells can rescue the lateral line migration defect in CXCR4b through cell-cell mechanical contacts.

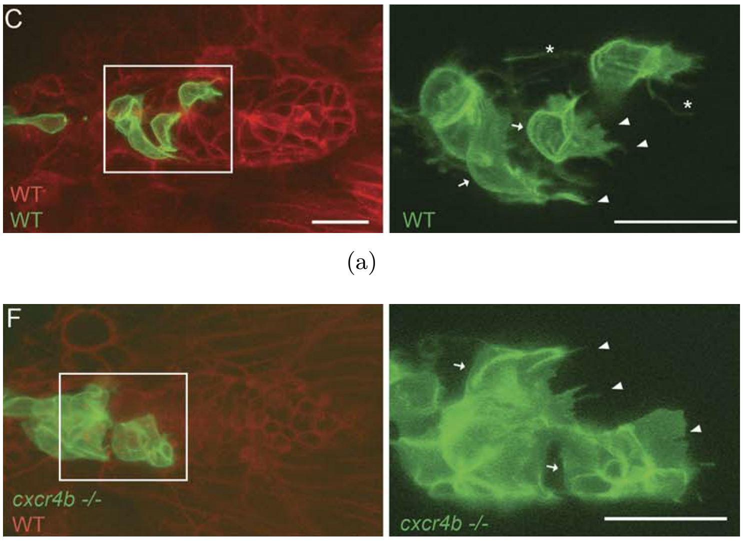

(a)

(b)

Figure 1.5. (a) Wild-type cells, marked in green (●), have been transplanted in a wild-type primordium, marked in red (●). On the right panel cells display filopodia in the direction of migration. (b) Cells lacking of the chemokine receptor CXCR4b, marked in green, are placed in a wild-type primordium, marked in red. On the right panel cells display filopodia with a similar dynamic behaviour as in (a), suggesting the existence, within the primordium, of cell-cell interaction via mechanical forces (source Haas and Gilmour, 2006).

In this context other studies (Liu et al, 2003a; Kerstetter et al, 2004; Papusheva and Heisenberg, 2010; Liu et al, 2011; Mertz et al, 2013) have shown that *intercellular adhesion*, typically through molecules as the *cadherins*, and *cell-substratum adhesion*, through *integrins*, have a crucial role in the spatial organization of tissues and in embryonic development, including the growth of the zebrafish lateral line. Integrins

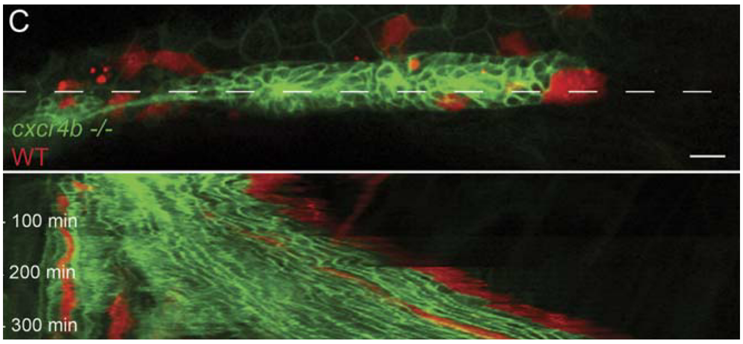

Figure 1.6. A small number (about 5 %) of wild-type cells (in red ●) transplanted into a CXCR4b-deficient primordium (in green ●) can rescue the lateral line migration. The kymograph analysis below shows, in the top half, “zig-zag” lines, whereas, in the bottom half, the lines become parallel, implying a normal lateral line migration. This suggests that wild-type cell can interact, through contact forces, with neighbouring cells (source Haas and Gilmour, 2006).

are transmembrane receptors that mediate the attachment between a cell and its surroundings. They have two main functions: attachment of the cell to the extracellular matrix, and signal transduction from the extracellular matrix to the cell. So, in addition to transmitting mechanical forces, in cell migration and in the immune system, they are involved in cell signaling and the regulation of cell cycle, shape, and motility. Integrins work alongside other transmembrane proteins such as cadherins. Cadherins have been shown to modify local traction forces and monolayer contractility, and cadherin-based cell–cell adhesions are important in mechanical activity of epithelial cells and have implications in the mechanical regulation of epithelial tissues during development and disease. Usually, epithelial cells express E-cadherin, which binds preferentially to other E-cadherin molecules, while in mesenchymal cells are found other cadherin types such as N-cadherin (Mertz et al, 2013). Integrin- and cadherin-mediated adhesion allows cells and tissues to respond to mechanical stimuli from their environment and to change shape without loosing integrity (Papusheva and Heisenberg, 2010, and references therein).

1.4 The neuromast assembly. The role of the FGF signal

To understand the mechanism which drives the rosette organization and neuromast deposition (a mechanism however not yet completely described, Lecaudey et al, 2008), we have to make some considerations.

As we have anticipated, a second development phase in the zebrafish lateral line consists in a mesenchymal-epithelial transition (MET). In Section 1.3 we have seen that mesenchymal cells have large migratory and invasive properties, here epithelial cells, on the contrary, tend to be stationary and they are packed together closely connected to each other by cell-cell junctions. For this, MET induces a passage from a motile to a polarized cell state (Alberts et al, 1994). This transition occurs in many processes during embryogenesis and early development, but it is involved also in wound healing, cancer metastasis, somitogenesis, cardiogenesis (Nakaya et al, 2004; Nakajima et al, 2000; Li et al, 2011). MET is also reversible as epithelial-mesenchymal transition (EMT), and both MET and EMT can arise in a same process. In wound healing, keratinocytes (the predominant cell type in the epidermis) at the border of the wound initially undergo EMT, to allow the cells to migrate, then undergo re-epithelialization or MET when the wound is closed. A similar mechanism occurs in cancer progression from the initiation to the completion of the invasion-metastasis (Chaffer and Weinberg, 2011).

Several signaling pathways induce MET process, such as growth factors, integrins, cell adhesion molecules. About the zebrafish lateral line, epithelialization and the consequent neuromast formation are strongly influenced by the concentration of *fibroblast growth factors* (*FGFs*) and their receptors *FGFRs* (Nechiporuk and Raible, 2008; Lecaudey et al, 2008). As we will see below the mutually exclusive expression of FGF and FGFR characterizes respectively the mesenchymal or epithelial cell state.

FGFs are a large family of polypeptide growth factors found in a variety of multicellular organisms, including invertebrates. Their several functions include cell growth, chemotaxis, cell migration, differentiation, cell survival, and apoptosis. FGFs play an important role in embryonic development in invertebrates and vertebrates. The intracellular transmission of FGF signal takes place through the receptors FGFRs, that bind FGF molecules and activate a complex signaling cascade schematized in Figure 1.7 (Böttcher and Niehrs, 2005).

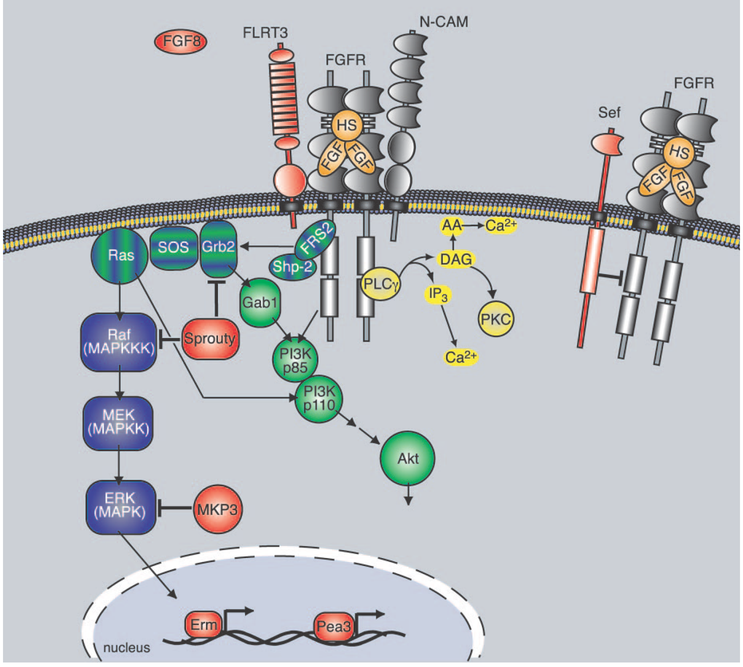

Figure 1.7. Scheme for the complex intracellular signaling cascades activated by receptors FGFRs (located in the cell surface on the top) when bind FGF molecules. The nucleus is marked in the bottom (see also Böttcher and Niehrs, 2005).

In zebrafishes embryo, FGF signaling plays a chemotactic action in morphogenetic movements, driving cells to assemble rosettes and gives rise to the subdivision of the lateral line. Among the 22 members of the FGF family, only FGF3 and FGF10 are expressed by the primordium (Böttcher and Niehrs, 2005). Moreover, it was shown that they are substantially equivalent, in fact, inactivation of FGF3 or FGF10 alone does not alter significantly the development of the primordium, demonstrating a robustness of the system (Lecaudey et al, 2008). On the other hand, using a FGFR inhibitor SU5402 strongly affects the primordium: cells became disorganized and neuromast deposition stops. In this case also the collective migration is compromised, probably due to an alteration also in CXCR4b receptors (Nechiporuk and Raible, 2008), see Figure 1.8 (a). This can be confirmed comparing the kymograph analysis of the SU5402-treated primordium in Figure 1.8 (b) with that in Figure 1.4 (b), where the receptor CXCR4b have been inhibited.

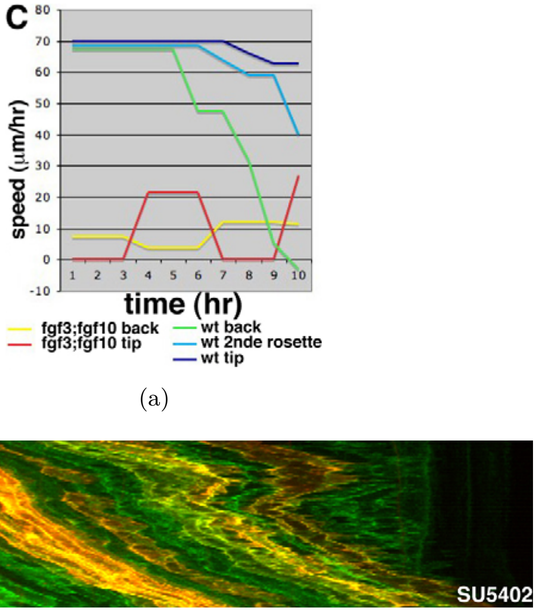

(a)

(b)

Figure 1.8. (a) Velocity of migration of the tip of the primordium (dark blue line), the second rosette (blue line) and the back of the wild-type primordium (green line). Decreasing velocity in blue line occurs in correspondence of the detachment of a neuromast. Red and yellow lines are the tip and the back velocity of a mutant primordium with absence of FGF activity. In this case cell movements become strongly uncoordinated. (b) Kymograph of a primordium treated with SU5402. A back and forth movement of the primordium can be seen before it stops (source Lecaudey et al, 2008).

Therefore, the rosette formation depends mainly on the total level of FGF and, as we will see below, on its location. We observe also that FGF and FGFR expressions are mutually exclusive, as confirmed by the location of their molecules: the former, broadly expressed in the leading region, and focused in one or two cells at the centre of the rosettes (the future neuromasts) in the trailing region; the latter, at the same time, expressed in the trailing region except the FGF foci (Nechiporuk and Raible, 2008; Lecaudey et al, 2008), see Figure 1.9.

This observation, in the aim of designing a mathematical model in Chapter 3,

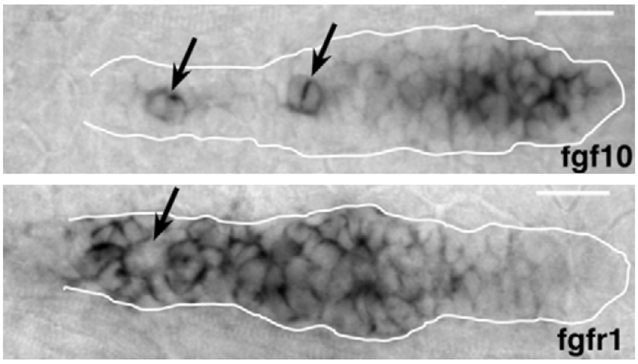

Figure 1.9. FGF and FGFR are mutually exclusive. FGF is expressed in the leading region, and focused in one or two cells at the centre of the rosettes in the trailing region (arrows), while FGFR expressed in the trailing region except the FGF foci (arrow). The image is taken at 36 hours after-fertilization, scale bars are 20 μm (adapted from Lecaudey et al, 2008).

suggests to divide the cell population into two groups: the *leader* mesenchymal cells (expressing FGF), and the *follower* epithelial cells (expressing FGFR). At the beginning, all the cells belong to the leading group. Afterwards, under certain conditions (see Section 1.5), some leaders in the trailing zone start to become followers, except one or two leader cells located in the centre, that maintain their mesenchymal state. Now, the follower cells are driven towards the chemotactic FGF source and form a rosette-shaped structure. The confirmation that follower cells adopt a epithelial behaviour is given by their change in the cell shape. In Figure 1.10 (a), left panel (A), we can observe the centre of a rosette with a leader cell surrounding by other follower cells, which clearly display constricted apical surfaces. In the higher magnification in the left panel (B) are evident the three kinds of cell-cell junctions typical of epithelial cells: tight junctions, adherens junctions, desmosomes. On the right panel is shown a time-lapse analysis of a transverse-view orientation of the primordium. In the rear of the leading region we can show that rosettes are formed through the surface constriction of neighbouring cells. The change in cell shape in the mesenchymal-epithelial transition can be read also in Figure 1.10 (b), where the height/width ratio is measured. In wild-type embryo, with a normal FGF activity, cells in the rosettes have a columnar shape (on the left), while cells deprived of FGF signaling maintain a more spherical shape (on the right). In fact loss of FGF activity, implies that no leader-follower transition can occurs (Lecaudey et al, 2008).

In Figure 1.11 (a) is shown a scheme for the rosette formation in a wild-type primordium, and the absence of rosettes in the case of FGF loss-of-function. In the transverse view, in Figure 1.11 (b), the cell-cell junctions in a rosette are displayed. Finally, as a proto-neuromast becomes fully mature, it is detached from the trailing edge, and a new rosette is formed again in a cyclic mechanism.

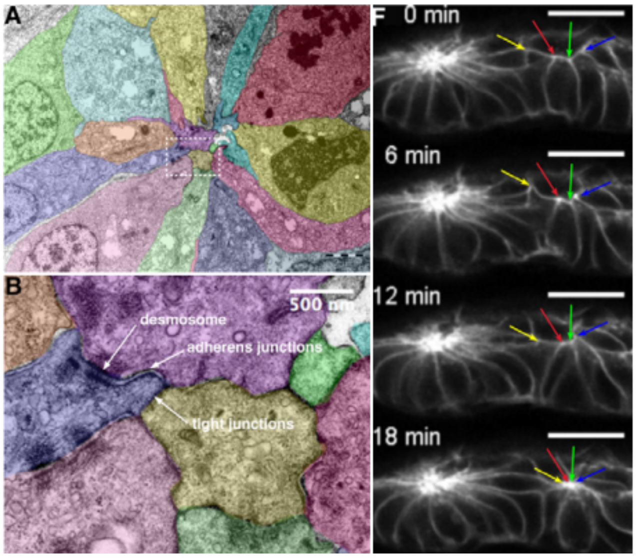

(a)

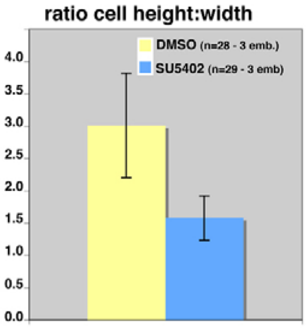

(b)

Figure 1.10. (a) Upper left panel: a rosette structure showing constricted apical surfaces of the follower cells that surround the central leader. Lower left panel: a magnification of the dotted region marked in the upper panel. Three epithelial cell-cell junctions are displayed: tight junctions, adherens junctions, desmosomes. Right panel: time-lapse analysis of a wild-type rosette formation reveals the constriction of the apical surfaces of several cells. (b) Quantification of the cellular height/width ratio measured for 28 wild-type cells (yellow ●) and 29 mutant cells treated with SU5402 (blue ●). Under normal FGF activity, cells in the rosettes present a columnar shape (on the left), while cells deprived of FGF signaling (on the right) maintain a more spherical shape (adapted from Lecaudey et al, 2008).

1.5 Leaders to followers transition

Let us now summarize some rules that model the transition from a leader cell into a follower, corresponding to the activation of the FGFR receptor. We can state that the transition occurs under the following three concomitant conditions:

1) a low level of SDF-1a (Ghysen and Chaudière, 2004);

2) a high level of FGF (Lecaudey et al, 2008);

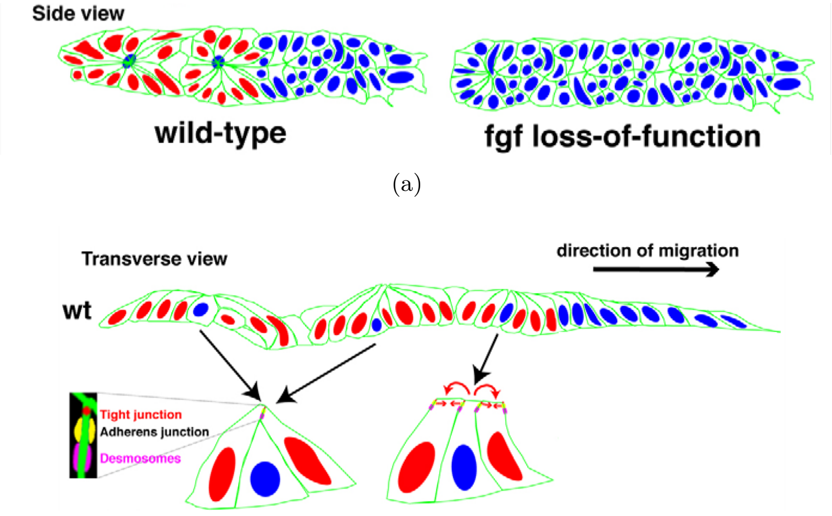

(a)

(b)

Figure 1.11. Scheme for the rosette formation. (a) Side view. On the left, blue cells (●) are the mesenchymal-like leaders, that express FGF ligand; red cells (●) are the epithelial-like follower that express FGFR. On the right, in absence of FGF activity all cells remains equally leader. (b) Transverse view. Followers in the rosette show the three cell-cell junctions typical of the epithelial state (adapted from Lecaudey et al, 2008).

3) influence of *lateral inhibition* (Haddon et al, 1998; Itoh and Chitnis, 2001; Hart et al, 2003; Matsuda and Chitnis, 2010; Mizoguchi et al, 2011; Sweet et al, 2011).

The first condition implies that rosette formation begins in the trailing region, where SDF-1a signal is already degraded by cells in the leading edge.

The lateral inhibition in the third condition is a common phenomenon in embryology: a cell that adopts a particular feature inhibits its immediate neighbours from doing likewise (Chitnis et al, 2012). In this way, groups of cells influence one another to make different structures, favoring the differentiation. In the zebrafish lateral line the lateral inhibition is supposed to be an essential mechanism to explain how FGF signal is progressively restricted in one or two leader cells in the neuromast (Matsuda and Chitnis, 2010). However, still remain some unresolved issues, for example how these one or two favored leaders result selected in the centre of a rosette (Chitnis et al, 2012). As in other embryological processes, here the lateral inhibition is mediated by the proteins Delta and Notch. The Notch protein spans the cell membrane, with small extracellular and intracellular regions. When a ligand proteins, such as Delta, binds the extracellular domain, the notch signal is transmitted to the cell nucleus (notch cascade) to modify gene expression and to promote cell specialization (Lai, 2004).

In view of our mathematical model in Chapter 3, we propose to translate above condition 3) considering leader-to-follower transition favored by a low number of cells in the neighbourhood. In this manner condition 3), together with condition 2), implies that followers, activating FGFR receptor, inhibit the same activation in a central leader, that represents the cell “more surrounded” by other cells, so that it will express a significantly higher level of FGF signal, due to the exclusion of the FGF production in the followers (Lecaudey et al, 2008). On the other hand, a cell at the edge of the primordium would receive no inhibition from neighbours and would be more likely to become follower. Although other models can be imagined in relation with the lateral inhibition mechanism, this seems to be the most appropriate, and probably the simplest one, in order to obtain the observed structure of neuromasts (see Chapter 3). Finally, we remark that the leader-follower transition can be reversible, possibly with a time delay. In fact, blocking FGF activity makes all cells equally leader and causes the consequent melting of formed rosettes (Lecaudey et al, 2008).

Lateral inhibition mechanisms, via Notch signaling pathway, are widespread and control other multiple cell differentiation processes during embryonic and adult life. Among these, Notch signaling has a role in neuronal function and development (Gaiano and Fishell, 2002; Aguirre et al, 2010), angiogenesis (Liu et al, 2003b), ventricular development and differentiation (Grego-Bessa et al, 2007), cancers (Bolós et al, 2007). Similar inhibitory mechanisms can be found also in sensory systems. For instance, in visual response lateral inhibition increases the contrast and sharpness. When in dark a small light stimulates photoreceptors on retina, those in the centre of stimulus will transduce the “light” signal to the brain, whereas neighbouring photoreceptors are inhibited to do this, sending a “dark” signal to the brain. This contrast between light and dark produces sharper images. Similarly in tact, when an area of the skin is touched, the central region is excited and the peripheral region is inhibited. This avoids the overlapping of different receptive fields, and allows a greater sensory precision (Kevin, 2008).

We conclude this chapter observing that our mathematical model on the zebrafish lateral line, proposed later in this thesis, will be consistent with the biological observations, here discussed, if we consider chemical effects concomitant with other cell mechanisms, as alignment, damping and adhesion-repulsion effects (see Chapter 3).

Chapter 2

Modelling background: chemical signals, cell movements, and collective motion

In this chapter we give an overview about some mathematical models that provide a modelling backgrounds for our model proposed in Chapter 3, concerning the development and the morphogenesis of the zebrafish lateral line primordium. The discussion presented here follows a path that, starting from the mechanisms lying on the chemical scale, leads gradually to introduce, on the cellular scale, typical interactions emerging in the collective dynamics of cells. Different scales for both chemical and cellular points of view are necessary for an accurate description of the biological process analyzed in Chapter 1, and will be take into account later in the our mathematical formulation.

2.1 Reaction diffusion equation

As we have seen in Chapter 1, a morphogenesis process, although controlled at the genetic scale, can be the result of a series of biological mechanisms occurring during the early development. A pattern or a form, that mathematically can be given for example by spatially heterogeneous steady states, in general are not anticipated solely by genetic information. The basic theory of morphogenesis, at chemical scale, was put forward in a seminal paper by Turing (1952), using the *reaction diffusion equation*, that we now derive following the approach given in Murray (2003).

Let V be an arbitrarily fixed volume with boundary ∂V. The principle of mass conservation states that the rate of the amount of material $u(\mathbf{x}, t)$, for instance the concentration of chemical signal, in V is equal to the rate of flow $\mathbf{J}$ of material across ∂V into V, plus the material created in V:

$$\frac{\partial}{\partial t}\int_V u(\mathbf{x}, t)\, dv = -\int_{\partial V} \mathbf{J}\cdot\mathbf{n}\, ds + \int_V g\, dv, \tag{2.1}$$

where $\mathbf{n}$ is the outward unit normal to V and g represents the source of material, depending possibly on u, $\mathbf{x}$ and t. Now, assuming $u(\mathbf{x}, t)$ continuous, the divergence theorem implies

$$\int_{\partial V} \mathbf{J} \cdot \mathbf{n}\, ds = \int_V \nabla \cdot \mathbf{J}\, dv. \tag{2.2}$$

Substituting (2.2) in equation (2.1), we obtain

$$\int_V \left(\frac{\partial u}{\partial t} + \nabla \cdot \mathbf{J} - g(u, \mathbf{x}, t) \right) dv = 0. \tag{2.3}$$

Since V is arbitrary the integrand must be zero, giving the continuity equation

$$\frac{\partial u}{\partial t} + \nabla \cdot \mathbf{J} = g(u, \mathbf{x}, t). \tag{2.4}$$

For $\mathbf{J}$ we can consider the classic *Fick's law*, for which the flux goes from regions of high concentration to regions of low concentration, with a magnitude that is proportional to the concentration gradient. With this assumption we write

$$\mathbf{J} = -D\nabla u, \tag{2.5}$$

where in general D can be a function of $\mathbf{x}$ and u. From equation (2.5), equation (2.4) becomes

$$\frac{\partial u}{\partial t} = \nabla \cdot (D\nabla u) + g(u, \mathbf{x}, t). \tag{2.6}$$

If D is a constant, the reaction diffusion equation reads

$$\frac{\partial u}{\partial t} = D\Delta u + g(u, \mathbf{x}, t). \tag{2.7}$$

Starting from this equation Turing (1952) considered two chemical species $u(\mathbf{x}, t)$ and $w(\mathbf{x}, t)$, satisfying a system of coupled equation of the form (2.7). Despite the diffusion can be considered a stabilising process, Turing showed that if the diffusion coefficients of the two substances are different, inhomogeneous patterns can evolve by diffusion driven instability (Turing instability). In practice, under certain conditions, chemical substances can react and diffuse to produce spatial patterns, depending both on the chemicals and on the geometry of the domain.

Let us consider the system

$$\begin{cases} \dfrac{\partial u}{\partial t} = D_u \Delta u + \Gamma(u, w), \\[2ex] \dfrac{\partial w}{\partial t} = D_w \Delta w + \Sigma(u, w), \end{cases} \tag{2.8}$$

where $u(\mathbf{x}, t)$ and $w(\mathbf{x}, t)$ are two chemical materials, and $\Gamma(u, w)$ and $\Sigma(u, w)$ are the reaction terms. The conditions for Turing instability can be found linearizing system (2.8) in the presence and in the absence of diffusion. Suppose (u_0, w_0) is a homogeneous steady state. The linearized of (2.8) about $\mathbf{z} = (u - u_0, w - w_0)$, with $D_u = D_w = 0$, is

$$\partial_t \mathbf{z} = \mathbf{A}\mathbf{z}, \tag{2.9}$$

where

$$\mathbf{A} = \begin{pmatrix} \Gamma_u(u_0, w_0) & \Gamma_w(u_0, w_0) \\ \Sigma_u(u_0, w_0) & \Sigma_w(u_0, w_0) \end{pmatrix} \tag{2.10}$$

is the Jacobian matrix of the vector field (Γ, Σ). The solution (u_0, w_0) is linearly stable if the eigenvalues $\mathbf{A}$ have negative real parts, that is

$$\begin{cases} \operatorname{tr} \mathbf{A} < 0, \\ \det \mathbf{A} > 0. \end{cases} \tag{2.11}$$

Now, we consider the full system (2.8) linearized about $\mathbf{z} = (u - u_0, w - w_0)$ in the form

$$\partial_t \mathbf{z} = \mathbf{A}\mathbf{z} + \mathbf{D}\Delta\mathbf{z}, \tag{2.12}$$

where

$$\Delta\mathbf{z} = \begin{pmatrix} \Delta u \\ \Delta w \end{pmatrix}, \quad \mathbf{D} = \begin{pmatrix} D_u & 0 \\ 0 & D_w \end{pmatrix}. \tag{2.13}$$

We can solve equation (2.12) looking for solutions of the form

$$\mathbf{z}(\mathbf{x}, t) = \sum_k c_k e^{\lambda t} \mathbf{z}_k(\mathbf{x}), \tag{2.14}$$

where c_k are determined by a Fourier expansion of the initial condition and $\mathbf{z}_k$ solves the eigenvalue problem

$$\begin{cases} \Delta\mathbf{z} = -k^2 \mathbf{z}, \\ \text{boundary conditions}, \end{cases} \tag{2.15}$$

k being the eigenvalue. Inserting (2.14) in (2.12) we have

$$\lambda \mathbf{z}_k(\mathbf{x}) = \mathbf{A}\mathbf{z}_k + \mathbf{D}\Delta\mathbf{z}_k, \tag{2.16}$$

and from $(2.15)_1$ we derive

$$\left(\lambda \mathbf{I} - \mathbf{A} + \mathbf{D}k^2\right) \mathbf{w}_k = \mathbf{0}. \tag{2.17}$$

Equation (2.17) has non-trivial solutions if

$$\det \left(\lambda \mathbf{I} - \mathbf{A} + \mathbf{D}k^2\right) = 0, \tag{2.18}$$

that is

$$\begin{cases} \lambda^2 + \lambda \left[k^2 \operatorname{tr} \mathbf{D} - \operatorname{tr} \mathbf{A}\right] + h(k^2) = 0, \\ h(k^2) = D_w D_u k^4 - \left(\Gamma_u D_w + D_u \Sigma_w\right) k^2 + \det \mathbf{A}. \end{cases} \tag{2.19}$$

Now, the solution (2.14) will be unstable if $\operatorname{Re}\lambda > 0$ for some $k \neq 0$. That is, from (2.19),

$$k^2 \operatorname{tr}\mathbf{D} < \operatorname{tr}\mathbf{A}, \quad \text{or} \quad h(k^2) < 0, \tag{2.20}$$

for some k. Since $\operatorname{tr}\mathbf{D} > 0$, the condition $(2.11)_1$ assumed for (u_0, w_0) excludes $(2.20)_1$, and the only possibility to have $\operatorname{Re}\lambda > 0$ is $h(k^2) < 0$. From $(2.11)_2$, taking into account $\det\mathbf{A} > 0$, a necessary but not sufficient condition for $h(k^2) < 0$ is

$$(\Gamma_u D_w + D_u \Sigma_w) > 0$$

in $(2.19)_2$. Moreover, the function h, depending on k^2, is a concave upward parabola with $h(0) = \det\mathbf{A}$, so that a sufficient condition is given requiring the minimum of the parabola to be negative. Differentiating $h(k^2)$ with respect to k^2, we find

$$\begin{aligned} k^2_{\min} &:= \frac{(\Gamma_u D_w + D_u \Sigma_w)}{2 D_w D_u}, \\ h_{\min} &:= h\left(k^2_{\min}\right) = \det\mathbf{A} - \frac{(\Gamma_u D_w + D_u \Sigma_w)^2}{4 D_w D_u}, \end{aligned}$$

and we require

$$\det\mathbf{A} < \frac{(\Gamma_u D_w + D_u \Sigma_w)^2}{4 D_w D_u}.$$

Hence, transition between stability and instability occurs when

$$h_{\min} = 0 \Leftrightarrow \det\mathbf{A} = \frac{(\Gamma_u D_w + D_u \Sigma_w)^2}{4 D_w D_u}.$$

So, if the parameters of the system (diffusion coefficients, reaction kinetics, etc.) assume appropriate values, we can have instability for the state (u_0, w_0) in presence of diffusion.

The reaction diffusion models, starting from Turing's considerations, have been widely adopted as a possible mechanism for generating biological pattern in morphogenesis (see the books edited by Chaplain et al, 1999 and by Maini and Othmer, 2000). For example they have applied to explain the pattern formation in the animal coat, such as on the zebra, leopard, but also in the butterfly wings and during the regeneration of some marine algae (Murray, 2003). Other applications include the segmentation of the embryo of Drosophila (fruit fly) (Kauffman et al, 1978) and the early insect development (Hunding, 1999; Meinhardt, 2000).

Despite of the large applicability reaction diffusion models have also an intrinsic limit: they take into account only the chemical scale, neglecting the spatial organization of the cells in response to particular stimulus. The reaction of an organism (cell) to an external stimulus is generally called *taxis*. Based on the type of stimulus, and on the organism's response, the word taxis is often preceded by a prefix. Many types of taxis have been identified, for example the aerotaxis, the response of an organism to variation in oxygen concentration, the phototaxis, the response to variation in light intensity and direction, the galvanotaxis, the response to electrical current, and so on (Martin, 1983; Menzel, 1979). In the following sections we will consider the *chemotaxis*, i.e. the influence of chemical substances present in the environment on the movement of motile organisms (cells).

2.2 Chemotaxis

In ecology it is well known that a large number of insects and animals rely on an acute sense of smell for transmitting information between members of their species. Pheromone release is an important mean for communication, predation and attraction mating partners: it influences the direction of the population movements (Murray, 2002, 2003). The movement towards a higher concentration of the chemical substance is termed positive chemotaxis, and the chemical substance that lead to positive chemotaxis is a chemoattractant. Movement towards lower concentrations is the negative chemotaxis and the chemical substance is said a repellent. When the chemical signal is expressed or bound on a surface (e.g. extracellular matrix, polymer substrate) generally we speak about haptotaxis.

In biological processes the formation of cells aggregations (amoebae, bacteria, etc.) is regulated by the response of the species populations to the change of the chemical concentrations in the environment. In multicellular organisms, chemotaxis of cell populations plays a crucial role throughout the life cycle. During embryonic development it plays a role in organizing cell positioning, for example during gastrulation (Dormann and Weijer, 2006), and patterning of the nervous system. In Chapter 1, for instance, we have observed the role of chemotaxis in the migration and self-organization of embryonic cells in the zebrafish lateral line. In the adult life, it directs immune cell migration to sites of inflammation (Di Russo et al, 2010) and fibroblasts to heal a wounded region. Same mechanisms allow tumour cells to invade the surrounding environment (Condeelis et al, 2005) or stimulate new blood vessel growth (Larrivee and Karsan, 2000).

A seminal model on the chemotaxis has been proposed by Keller and Segel (Keller and Segel, 1970, 1971) in relation to the morphogenesis of the Dictyostelium discodeum (slime mold), and it is based on a system of reaction diffusion equations, by adding a chemotactic term.

Let us now derive the chemotaxis equation following the approach in Murray (2002). Many further approaches, like stochastic and discrete methods, have been developed to derive this class of models, as it is reviewed by Horstmann (2004).

We consider a cell population $c(\mathbf{x}, t)$ and a chemoattractant $u(\mathbf{x}, t)$ which give rise to a movement of cells up the gradient. In the continuity equation (2.4), for $c(\mathbf{x}, t)$ we can write

$$\frac{\partial c}{\partial t} + \nabla \cdot \mathbf{J} = f(c), \tag{2.21}$$

where $f(c)$ represents the growth term for the cells and the flux $\mathbf{J}$ is given by the contributions of the diffusion and of the chemotaxis:

$$\mathbf{J} = \mathbf{J}_{\text{diffusion}} + \mathbf{J}_{\text{chemotaxis}}. \tag{2.22}$$

While $\mathbf{J}_{\text{diffusion}}$ can be chosen according to the Fick's low (2.5), the chemotaxis contribution is reasonably in form

$$\mathbf{J}_{\text{chemotaxis}} = c\,h(u)\nabla u, \tag{2.23}$$

where $h(u)$ is a function of the attractant concentration and the flux is considered increasing with the number of cells $c(\mathbf{x},t)$. With this assumptions the basic *reaction-diffusion-chemotaxis equation* is

$$\frac{\partial c}{\partial t} = \nabla \cdot (D_c \nabla c) - \nabla \cdot (c\, h(u) \nabla u) + f(c), \tag{2.24}$$

where D_c is diffusion coefficient of the cells.

In relation to the chemical $u(\mathbf{x},t)$ we can consider the reaction diffusion equation in the form (2.6):

$$\frac{\partial u}{\partial t} = \nabla \cdot (D_u \nabla u) + g(c,u), \tag{2.25}$$

where D_u is the diffusion coefficient of u and $g(c,u)$ is a kinetics/source term, depending on u and c.

The function $g(c,u)$ can assume various forms, for example in the model of Keller and Segel (1971) it is $g(c,u) = k_1 c - k_2 u$, where k_1 and k_2 are positive constants. This suggests in $k_1 c$ a spontaneous production of chemoattractant proportional to the number of cells, while $-k_2 u$ represents a molecular (exponential) degradation if the chomotactic signal is not produced by the cells. If we neglect the cell production rate, $f(c) = 0$, with h a constant function and with constant diffusion coefficients we obtain the system

$$\begin{cases} \dfrac{\partial c}{\partial t} = D_c \Delta c - h \nabla \cdot (c \nabla u)\,, \\[2ex] \dfrac{\partial u}{\partial t} = D_u \Delta u + k_1 c - k_2 u. \end{cases} \tag{2.26}$$

Starting from Keller-Segel model a lot of variations have been proposed, which differ in the choice of the chemotactic sensitivity function and the reaction terms in the species equation or in the chemical ones. Models based on the Keller-Segel equations have been employed in embryonic pattern formation processes, such as the formation of primitive streak, pigmentation patterning and cell colonisation (Murray and Myerscough, 1991; Painter et al, 2000; Landman et al, 2003). In relation to the tumour growth, mathematical models have extensively included chemotactic terms, for example in the migration of invasive cancer cells (Perumpanani et al, 1996), in the tumour-induced angiogenesis (Chaplain, 2000; Mantzaris et al, 2004), in the macrophage invasion into tumours (Owen and Sherratt, 1997).

2.3 Mechanochemical models for morphogenesis

The prevalent aspect of the Keller and Segel-like models is the chemical control in the movement of cells. Next to this, above all in highly structured multicellular organisms, the migration of a single cell can be strongly influenced by the change of many essential features during the motion, such as shape, adhesion and, more generally, force generation (Rorth, 2007). In this case becomes relevant to consider the role that mechanical forces play in the morphogenetic process concomitantly with chemical effects. In fact, in the chemical models (reaction-diffusion and chemotaxis models) the morphogenesis process takes place sequentially to the chemical pattern formation, and the mechanical shaping of form during embryogenesis is not taken into account. Once the chemical prepattern has been laid down, the cells execute their mechanical response according to the chemical instructions. On the other hand, in the mechanochemical approach mechanical state of a cell or tissue can influence its chemical state, so that pattern formation and morphogenesis are considered as simultaneous processes, with a constant interaction between the movements in the patterns and in the shape of the cells with the tissue.

The basic mechanochemical models have been proposed by Oster and Murray in relation to the morphogenesis of internal tissues (dermis and mesenchyme) or external tissue (epithelium) (Murray, 1983; Oster et al, 1983; Murray and Oster, 1984a,b; Maini, 1999). Similar approaches have found then application in continuum models for vasculogenesis and wound healing (see also Murray, 2003; Fusi, 2009). In general, in these mechanochemical models three features are taken into account: cells migrate within a tissue substratum of fibrous extracellular matrix (ECM) and other cells; cells can generate large traction forces on the elastic ECM and on the surface of other cells; the dynamics of both cells and ECM is mediated by some chemical growth factors, which regulate both cell proliferation and ECM reorganization. These continuum models, typically, consist of four equations governing the conservation equation of the cell population density and of the chemical signals, the mechanical balance of forces between the cells and the ECM, the conservation equation for the ECM.

Let $c(\mathbf{x},t)$ the cell density, $u(\mathbf{x},t)$ a chemical factor (in general summarizing the behaviour of a class of chemicals that take part in the system), $\rho(\mathbf{x},t)$ the ECM density, and $\boldsymbol{\sigma}(\mathbf{x},t)$ the stress tensor for the mechanical cell-ECM interaction. For $c(\mathbf{x},t)$ we can consider the conservation equation (2.21)

$$\frac{\partial c}{\partial t} + \nabla \cdot \mathbf{J}^c = f(c,u),$$

where $f(c,u)$ can represent a kinetic term (mitosis, apoptosis, etc.) and the flux $\mathbf{J}^c$ is given by the contributions of

$$\mathbf{J}^c = \mathbf{J}^c_{\text{diffusion}} + \mathbf{J}^c_{\text{chemotaxis}} + \mathbf{J}^c_{\text{haptotaxis}} + \mathbf{J}^c_{\text{convection}}. \tag{2.27}$$

The first two terms in (2.27) can be given as in equations (2.21)–(2.24), according respectively to the Fick's low, and to the chemotaxis contribution:

$$\mathbf{J}^c_{\text{diffusion}} = -D_c \nabla c, \tag{2.28}$$

and

$$\mathbf{J}^c_{\text{chemotaxis}} = \chi(c,u)\nabla u, \tag{2.29}$$

where $\chi(c,u)$ is the chemotactic sensitivity factor. For the haptotactic term we consider that the traction exerted by the cells generates gradients in the ECM density $\rho(\mathbf{x},t)$. Then cells tend to move up the adhesive gradient, so the simplest assumption is a flux proportional to $c\nabla\rho$:

$$\mathbf{J}^c_{\text{haptotaxis}} = a\, c \nabla \rho,$$

a being a constant. In the last term of (2.27) if $\mathbf{r}$ is the displacement vector of the ECM and $\partial \mathbf{r}/\partial t$ is the velocity of deformation of the ECM, the amount of transported cells is c times this velocity:

$$\mathbf{J}^c_{\text{convection}} = c\frac{\partial \mathbf{r}}{\partial t}.$$

Similarly, for $u(\mathbf{x}, t)$ we can write the continuity equation (2.4):

$$\frac{\partial u}{\partial t} + \nabla \cdot \mathbf{J}^u = g(c, u),$$

where $\mathbf{J}^u = \mathbf{J}^u_{\text{diffusion}} + \mathbf{J}^u_{\text{convection}}$ is given as in (2.28)–(2.29), that is

$$\mathbf{J}^u_{\text{diffusion}} = -D_u \nabla u,$$

and

$$\mathbf{J}^u_{\text{convection}} = u\frac{\partial \mathbf{r}}{\partial t},$$

then $g(c, u)$ accounts for production and consumption of chemical by cells and for natural chemical decay.

The conservation equation for the ECM density $\rho(\mathbf{x}, t)$ can be written as

$$\frac{\partial \rho}{\partial t} + \nabla \cdot \mathbf{J}^\rho = s(c, u, \rho),$$

where $s(c, u, \rho)$ is the rate of secretion and degradation of matrix by the cells. The flux $\mathbf{J}^\rho$ is assumed to be due only to convection since in the ECM the linked mesh-like structure implies that the effects of diffusion is negligible:

$$\mathbf{J}^\rho = \rho\frac{\partial \mathbf{r}}{\partial t}.$$

Moreover, since the mechanical deformations are small, it is reasonable to model the material of cells and ECM as a linear, isotropic viscoelastic continuum with stress tensor $\boldsymbol{\sigma}(\mathbf{x}, t)$. The linear momentum balance equation assumes the form

$$\nabla \cdot \boldsymbol{\sigma} = \rho \mathbf{F}(\mathbf{r}),$$

where $\mathbf{F}(\mathbf{r})$ represents the external forces acting on the tissue, and the inertia effects are neglected due to the high viscosity of the tissue itself.

Finally, starting from the previous consideration, a typical formulation from which most of the mechanochemical models of morphogenesis are derived can be summarized by the following system:

$$\begin{cases} \dfrac{\partial c}{\partial t} = \nabla \cdot \left(D_c \nabla c - \chi(c, u) \nabla u - a\, c \nabla \rho - c\dfrac{\partial \mathbf{r}}{\partial t} \right) + f(c, u), \\[2ex] \dfrac{\partial u}{\partial t} = \nabla \cdot \left(D_u \nabla u - u\dfrac{\partial \mathbf{r}}{\partial t} \right) + g(c, u), \\[2ex] \dfrac{\partial \rho}{\partial t} = \nabla \cdot \left(-\rho\dfrac{\partial \mathbf{r}}{\partial t} \right) + s(c, u, \rho), \\[2ex] \nabla \cdot \boldsymbol{\sigma} = \rho \mathbf{F}(\mathbf{r}). \end{cases}$$

2.4 Discrete, continuous, and hybrid approaches

As we have seen in Chapter 1 a morphogenesis process can involve only a restricted number of living entities and the migration of a single cell is strongly influenced by the motion of the other units. For this, it may be needed to investigate the cell behaviour in more detail. In general, the necessity to take into account phenomena occurring at different spatial and/or temporal scales leads to consider different mathematical tools, such as *continuous*, *discrete* or *hybrid* models, though the distinction among them is not so well defined (see the reviews by Turner et al, 2004; Preziosi and Tosin, 2009 and the papers by Schaller and Meyer-Hermann, 2006; Drasdo, 2005; Stolarska et al, 2009).

Continuous model, where all variables are considered to be defined at every point in space and time changes continuously, are useful when the length scale over which we wish to investigate the phenomenon is much greater than the diameter of the individual elements (e.g. the diameter of one cell). These models frequently involve the development of a reaction-diffusion equation (or other PDEs) and have been found to be appropriate, for example, in the study of pattern formation in nature, vasculogenesis and wound healing through chemical and mechanochemical models (see Sections 2.1–2.3).

On the other hand, when we are interested in the behaviour of individual cells, and in their interactions with other cells and the surrounding medium, we can consider discrete models, such as Individual-Cells-Based Models (IBMs) (Anderson et al, 2007) or cellular automata (von Neumann and Burks edit., 1966). In these latter models cells are treated as points moving in the space on a lattice or several lattice nodes according to certain rules designed from existing biological observations (Turner and Sherratt, 2002; Dormann and Deutsch, 2002). Discrete models have widely applied in many biological fields, form ecology (Berec, 2002), to pattern formation (Wootton, 2001), from tumour growth (Ferreira et al, 1998; Kansal et al, 2000; Patel et al, 2001), to angiogenesis (Markus et al, 1999). A class of discrete models does admit continuous cellular positions (Honda et al, 2000; Palsson and Othmer, 2000; Drasdo, 2003; Drasdo et al, 2004; Dallon and Othmer, 2004; Galle et al, 2005), for this they allow to include directly the information about microscopic physical interactions.

We remark that there is not a single way to approach the same biological phenomenon and, in some cases, the same biological problem admits different models. Clearly, each of these models admit advantages and disadvantages. For instance, continuous PDE models are computationally cheaper and more appropriate to describe the behaviour of tissues from the macroscopic point of view, but, they do not take into account sub-cellular mechanisms such as signal transduction, expression or internalisation of receptors, and so on. Conversely, IBMs models show more accuracy in describing the cellular level, but they might become computationally expensive when they involve a large number of cells, and inefficient in providing a general outlook on the system as a whole. Moreover, the lattice descriptions in the cellular automata have the disadvantage of violating the isotropy of space (though the lattice artefacts can be avoided by introducing stochastic interaction rules) and it is still quite difficult to relate the parameters of cellular automata to physically relevant quantities (Schaller and Meyer-Hermann, 2006).

A mixture of discrete and continuous models are the so called hybrid models. In general there are two types of this approach. The most common one, and historically the first, treats various biological constituents using different scale of description. Typically, cells are described by a discrete approach using spatially discrete variables (e.g. IBMs, cellular automata, etc.), while molecules and extracellular matrix are described with continuous variables (e.g. diffusion equations, more general partial differential equation, etc.) (see for instance (Anderson and Chaplain, 1998; Anderson et al, 2007; Schaller and Meyer-Hermann, 2005; Joie et al, 2014; Colin et al, 2013)). These hybrid models are called also *hybrid discrete in continuous models*. Other hybrid models are the so called *interfacing hybrid models* (Preziosi and Tosin, 2009), in which the spatial domain is partitioned in few time-dependent domains, and the constituents (usually the cells) are described by discrete variable in a portion of the spatial domain or by continuous variables in the rest of domain (see for instance Ramis-Conde et al, 2009, or Ramis-Conde et al, 2008 about the cancer cell invasion).

Clearly, the use of different scales of description, e.g. continuous and discrete framework, of a same biological process requires that the models give rise to similar solutions at length scales where their ranges of applicability overlap. This leads to investigate the link between macroscopic and microscopic scales (Turner et al, 2004; Schaller and Meyer-Hermann, 2006), and various mathematical techniques can be employed to get more formal and consistent results, such as homogenisation methods or fluid-dynamic and diffusion limits (Shipley et al, 2009; Chauviere et al, 2007; Bellomo et al, 2007; Chalub et al, 2004; Drasdo, 2005).

As we have seen, in hybrid models we can applied, for a same process, different scales chosen suitably for the description of various constituents, or a same constituent is treated under different points of view, depending on the portion of the spatial domain of interest. Recently, new multiscale models have been developed based on a measure-theoretic approach (Piccoli and Tosin, 2009; Cristiani et al, 2010; Piccoli and Tosin, 2011), where a same constituent can be described, in the whole domain, in a unique framework in which microscopic and macroscopic points of view coexist (see Cristiani et al, 2011b, and the recent book Cristiani et al, 2014). These models, applied first to crowd dynamics, allow a balance between micro- and macro-contribution through a combination of singular and absolutely continuous measures with respect to the Lebesgue measure of the space. In this way, one can suitably focalize the granularity of individuals (interaction with a single) and the macroscopic description of crowd flow (interaction with the mass). A first attempt to apply this framework in a biological context, about the cell behaviour, can be found in Colombi et al (2014).

In Chapter 3, starting from the experimental observations described in Chapter 1, we will formulate a mathematical model for the formation of the lateral line in a zebrafish embryo. As we have seen, this biological process involve 80-100 migrating cells, driven by chemical signals and, subsequently, self-organized in specific pattern. In order to formulate a consistent mathematical model, we will adopt a hybrid discrete in continuous description as mentioned above. On the chemical scale molecules will be represented by continuous concentrations, while cells will be considered as discrete entities, moving in a continuous space. The cell scale, at which migration and self-organization processes belong, will include some typical interactions emerging in the so called *collective motions*. In the next sections, we will give an overview about this general topic, that concerns not only biological systems, but also many other living systems, and even non-living systems.

2.5 Collective motion

A collective motion is a form of collective behaviour in which individual units interact in simple (alignment, attraction, repulsion) or complex way (combination of simple interactions). The main feature of collective behaviour is that the individual unit's action is strongly dominated by the influence of other units, so that its motion results very different from how it would be if it was alone. The pattern of behaviour is determined by the collective effects due to the other agents of the system (Vicsek and Zafeiris, 2012). Examples of collective motion are exhibited by many systems, from non-living systems, such as certain fluids, nano swimmers, simple robots, to living systems, such as flocks of birds, schools of fish, swarms of insects, herds of mammals, cell aggregates, crowds of humans.

Many reasons of aggregations in a given system have been proposed. Coordinated motion of cells results in making a biological process more efficient (e.g. in embryogenesis, wound healing, immune response, etc.), while in the case of tumour cell invasion it appears to speed up the progression of the decease (Méhes and Vicsek, 2014). For the animals entities it is observed that a group can more efficiently explore surrounding environments, to enhance foraging capability and detection of predators (Pitcher et al, 1982); being in a group offers protection against attacks by predators (Ioannou et al, 2008) and increases the locomotion efficiency (Fish, 1995).

The study in the field of collective motion, besides showing spectacular manifestations of certain systems, plays an essential role in a number of real-life situations. The research in the collective motion of cells brings important advantages understanding growth, development and disease of many organs and tissues. Some species, especially those that can be easily treated experimentally, represent a paradigm for understanding more complex organisms, including humans, as we have seen, for instance, in Chapter 1 in relation to the zebrafish. Also the collective behaviour of animals groups can be useful in some problems of human engineering and in socio-economic field (Naldi et al, 2010). Understanding crowd dynamics gives advantages to better forecast the behaviour of pedestrian flows (Helbing et al, 1997; Faria et al, 2010; Piccoli and Tosin, 2009; Bruno et al, 2011; Cristiani et al, 2010; Moussaïd et al, 2011), or suggests the best placement of entrances, exits and emergency gates in a given environment (combining, for example, a differential model with one of optimal control, Cristiani et al, 2015).

Collective motion has been extensively studied in recent year in a great variety of systems: non-living systems, macromolecules, bacteria colonies, amoeba, insects, fish, birds, mammals, humans. Many references can be found in the review by Vicsek and Zafeiris (2012). As regard to the cell systems we can cite, from a biological point of view, Haas and Gilmour (2006), Lecaudey et al (2008), Friedl and Gilmour (2009), Donà et al (2013), and from a modelling point of view Szabò et al (2006), Belmonte et al (2008), Arboleda-Estudillo et al (2010), Streichan et al (2011), Sepúlveda et al (2013), Joie et al (2014), Colin et al (2013).

2.6 Basic models in collective motion

Basic mathematical models about collective motion are substantially based on three steering behaviours of the units: a) *alignment*, in order to move in the same direction of average heading direction of neighbouring units; b) *separation*, in order to avoid crowding; c) *cohesion*, to remain close to the average position of neighbours.

2.6.1 Alignment models

Perhaps the simplest model in collective motion is represented by the Cuker-Smale model (Cucker and Smale, 2007a,b). In this model only an alignment effect is considered for a system of N interacting particles. The original model was proposed for a flock of birds, but its applicability is to general phenomena where autonomous agents reach a consensus, e.g. animal herding, emergence of common languages in primitive societies, etc. (Couzin et al, 2005).

The hypothesis of this model is that the force acting on every particle (bird) is a weighted average of the differences of its velocity with those of the other particles (birds). In particular, for $N \in \mathbb{N}$ particles, the proposed model, in continuous time $t \in \mathbb{R}_{\geq 0}$, can be written in the form

$$\begin{cases} \dot{\mathbf{V}}_i = \dfrac{\beta}{N} \displaystyle\sum_{j=1}^{N} \dfrac{\alpha_1}{\Big(\alpha_2 + \|\mathbf{X}_i - \mathbf{X}_j\|^2\Big)^{\sigma}} (\mathbf{V}_j - \mathbf{V}_i), \\ \dot{\mathbf{X}}_i = \mathbf{V}_i, \end{cases} \tag{2.30}$$

where $\mathbf{X}_i, \mathbf{V}_i \in \mathbb{R}^n$, for $i = 1, \dots, N$, are the position and the velocity of the i-th particle, β, α_1, α_2, σ are positive constants and $\|\cdot\|$ is the Euclidean norm in $\mathbb{R}^n$. In particular σ captures the rate of decay of the influence between agents in the flock as they separate in space, and it is a fundamental parameter in the time-asymptotic behaviour of system (2.30) (see below).

Cuker-Smale model is not the first to be proposed in this context. In fact, the first flocking simulator was published by Reynolds (1987) and it was based on differential equations describing the trajectories of the moving objects, taking into account three interactions: alignment, attraction and repulsion. The starting point of the Cuker-Smale model is represented by the seminal paper of Vicsek et al (1995). Previous analytic studies can be found also in Tsitsiklis (1984), Jadbabaie et al (2003). The Vicsek model (Vicsek et al, 1995), in discrete time, can be written as

$$\begin{cases} \mathbf{V}_i(t+1) = V_0 \frac{\langle \mathbf{V}_i(t) \rangle_R}{\|\langle \mathbf{V}_i(t) \rangle_R\|} + \text{perturbation}, \\ \mathbf{X}_i(t+1) = \mathbf{X}_i(t) + \mathbf{V}_i(t+1), \end{cases} \tag{2.31}$$

where V_0 is a fixed absolute velocity, and $\langle \dots \rangle_R$ denotes averaging of the velocities within a circle of radius R surrounding particle i. The expression $\frac{\langle \mathbf{V}_i(t) \rangle_R}{|\langle \mathbf{V}_i(t) \rangle_R|}$ provides a unit vector pointing in the average direction of motion within this circle.

The main differences with the Cucker-Smale model are the interactions, which here have the same intensity, but they are restricted to a circle around a given particle, and the existence of noise.

Nevertheless, Cucker-Smale's paper is widely known to have established an analytical exact result on the convergence to consensus of the autonomous agents: under suitable initial data their model implies that the state of the group converges to one in which all particles move with the same velocity, said *flocking state*. The main convergence result in Cucker and Smale (2007a) has been improved by Ha and Liu (2009), proving that for $\sigma \in [0, 1/2]$ there is global *unconditional flocking* of system (2.30) regardless of initial configurations, while for $\sigma \in (1/2, +\infty)$ there is *conditional flocking*, that is only certain classes of initial data and parameters of the system reduce to a flocking state, but in general the dispersion of the flock may occur, see Figures 2.1–2.2.

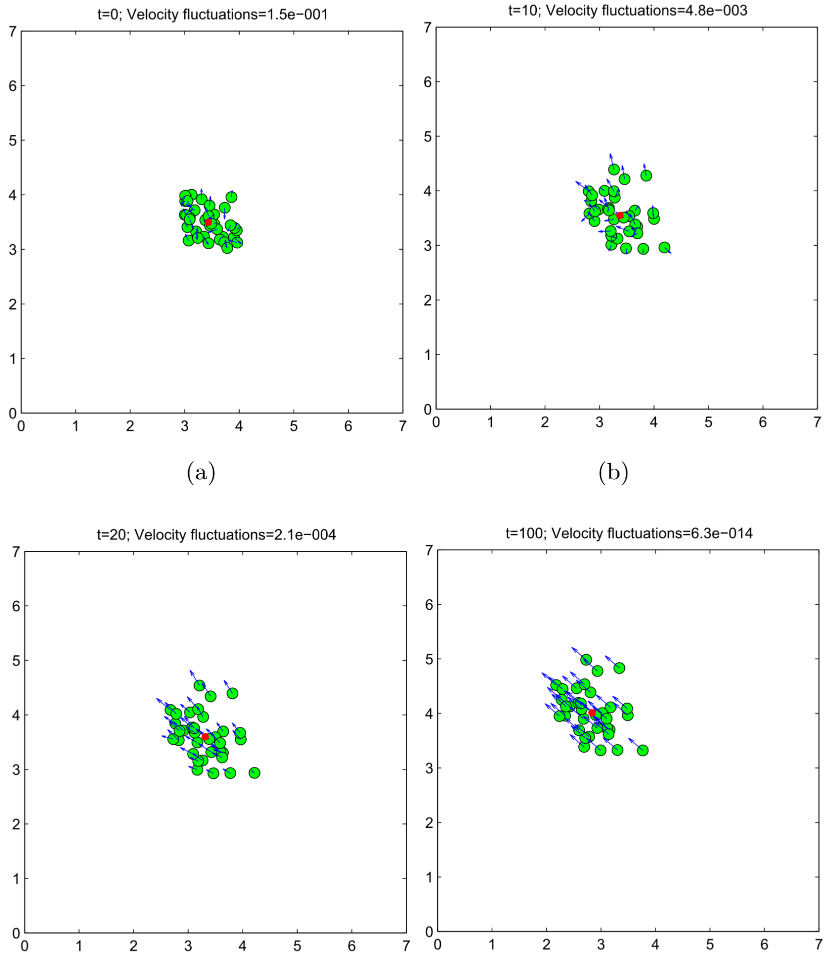

(a) (b) (c) (d)

Figure 2.1. A numerical simulation of the Cucker-Smale model with parameter $\sigma = 0.5$. With this condition the flocking behaviour is ensured, as shown by the velocity fluctuations in the titles of the panels (see also Chapter 4 for more details).

Cucker and Smale-like models have been recently widely applied in many contexts, for example in the biological field by Szabò et al (2006), Belmonte et al (2008), Arboleda-Estudillo et al (2010), Sepúlveda et al (2013), and vary extensions have

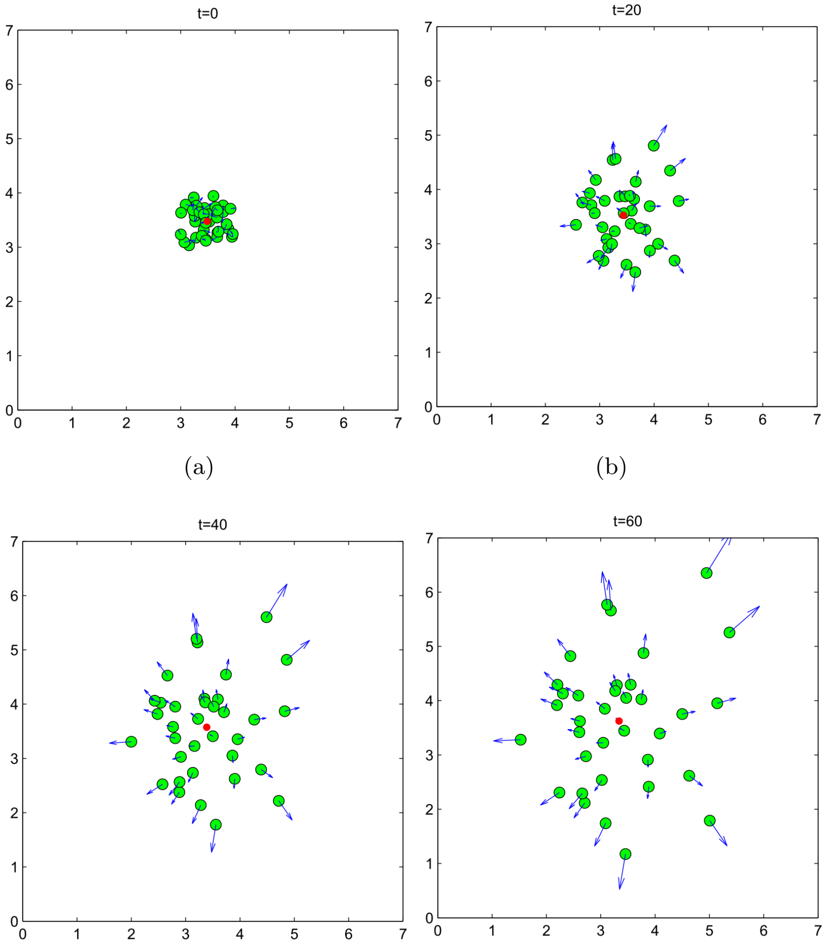

(a) (b)

(c) (d)

Figure 2.2. A numerical simulation of the Cucker-Smale model with parameter $\sigma = 2$. In this case the flocking behaviour is not ensured and the dispersion of the initial group can occur.

been proposed. For example, Cucker and Dong (2010, 2011) added a repelling force between particles in equation $(2.30)_1$, proving an analogous convergence theorem ensuring, on certain conditions, flocking behaviour, in addition without collision between particles. Ha and Levy (2009) applied system (2.30) to describe the motion of phototactic bacteria (i.e., bacteria that move towards light), adding a force that move excited bacteria towards the light source in equation $(2.30)_1$, and an additional equation for the excitation level of each particle. Also in this case, under particular conditions, it is proved that the asymptotic velocity of the particles tends to an identical terminal velocity. Other models have introduced noise (Cucker and Mordecki, 2008), stochastic equations (Ha et al, 2009), leader individuals with a preferred heading direction (Cucker and Huepe, 2008), see also Chapter 4 for further details.

In Chapter 4, starting from the model introduced in Chapter 3 describing the zebrafish lateral line formation, we will propose an extension of the Cucker-Smale model including a chemotactic effect acting on the particles of the system.

2.6.2 Attraction-repulsion models

Next alignment models, other models have shown that the motion of particles may become ordered even if no explicit alignment rule is applied, but alignment is introduced into the collision in an indirect way. For example Derzsi et al (2009) simulated a model in which the particles tend to maintain a given absolute velocity V_0 and the only interaction between them is a repulsive linear force acting in a suitable range. The system can be written as:

$$\begin{cases} \dot{\mathbf{V}}_i = \mathbf{V}_i \left(\frac{V_0}{\|\mathbf{V}_i\|} - 1 \right) + \mathbf{F}_i + \boldsymbol{\xi}_i, \\ \dot{\mathbf{X}}_i = \mathbf{V}_i, \end{cases} \tag{2.32}$$

where $\boldsymbol{\xi}_i$ is noise,

$$\mathbf{F}_i := \sum_{j \neq i} \mathbf{F}_{ij} + \mathbf{F}_i \text{ (wall)} \tag{2.33}$$

$$\mathbf{r}_{ij} := \mathbf{X}_i - \mathbf{X}_j \tag{2.34}$$

$$\mathbf{F}_{ij} := \begin{cases} K\mathbf{r}_{ij} \left(\frac{r_0}{\|\mathbf{r}_{ij}\|} - 1 \right), & \text{if} \quad \|\mathbf{r}_{ij}\| \leq r_0; \\ 0, & \text{otherwise.} \end{cases} \tag{2.35}$$

Strömbom (2011), instead, considered a similar model in which only the attraction is taken into account, in suitable ranges of action. His simulations give rise to a great variety of pattern, such as swarms (particles with low and varying alignment), undirected mills (particles move in a circular path around a common centre) and moving aligned groups (particles move in a highly aligned manner), see Figure 2.3.

A model that considers both attraction and repulsion effects is given in D'Orsogna et al (2006), and it is useful to describe schools of fish. The equations are

$$\begin{cases} \dot{\mathbf{V}}_i = (\alpha - \beta ||\mathbf{V}_i||^2)\mathbf{V}_i - \dfrac{1}{N} \displaystyle\sum_{1 \leq j \leq N} \nabla_{\mathbf{X}_i} H(||\mathbf{X}_i - \mathbf{X}_j||), \\ \dot{\mathbf{X}}_i = \mathbf{V}_i, \end{cases} \tag{2.36}$$

where H can be, for example,

$$H(r) = \frac{r^a}{a} - \frac{r^b}{b}, \quad 0 < b < a, \tag{2.37}$$

that is, we have a attraction term (of strength depending on a) and a repulsion term (of strength depending on b). The term $(\alpha - \beta ||\mathbf{V}_i||^2)\mathbf{V}_i$ gives a self-propulsion effect, since particles reach a given velocity $||\mathbf{V}_i|| = \sqrt{\alpha/\beta}$ (Figure 2.4).

Attraction-repulsion models are employed also to describe pedestrian flows in crowd dynamics. Repulsion effects represent the behaviour of a pedestrian to steer clear of the crow, with a preference for uncrowded areas, while attraction or cohesion

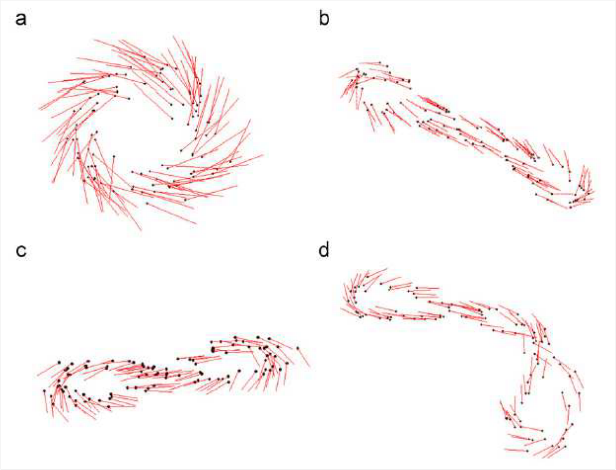

Figure 2.3. A simulation of the model proposed by Strömbom. Particular structures appear introducing a blind angle: (a) a fully oriented mill; (b)–(d) rotating chains with respectively zero, one and two self-intersections (source Strömbom, 2011).

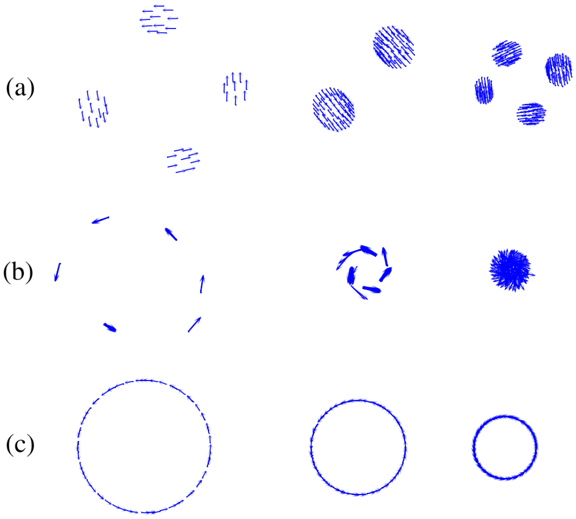

Figure 2.4. A simulation of the D'Orsogna et al. model. (a) Catastrophic geometry: the clump shrink as the number of particles increases. (b) Ring clumping. (c) Ring structure (source D'Orsogna et al, 2006).

translate the tendency to not remain isolated. This can intervene occasionally in those groups whose individuals share specific relationship, as group of tourist in a guided tours. Such models consider, unlike animals and other living system, that pedestrians experience strong interactions with the environment, due to the high complexity of the space in which they typically move, endowed of many obstacles. In order to take this aspect into account, the velocity of a pedestrian can split in the sum (possibly weighted) of two contribution $\mathbf{V} = \mathbf{V}_\mathrm{d} + \mathbf{V}_\mathrm{i}$, where $\mathbf{V}_\mathrm{d}$ is a desired velocity, that is the velocity (trajectory) of an individual depending only by the geometry of the space, in the absence of other pedestrians; $\mathbf{V}_\mathrm{i}$ is the interaction velocity, that is determined by the behaviour of the other individuals, through repulsion or cohesion effects incoming in accordance with various possible modeling choices (for further details we refer, for instance, to Piccoli and Tosin, 2009; Cristiani et al, 2010; Bruno et al, 2011; Bellomo et al, 2012)

2.6.3 Three zone models

Combining together alignment, attraction and repulsion effects, we can obtain the so called *three zone models* (Aoki, 1982). These models are based on three basic rules: an individual tends to maintain a certain distance from their mates, to avoid collisions; if the individual is sufficiently distant from their mates, it aligns its direction to their neighbours; if the individual is too far from the others, it is attracted towards their mates, this to avoid being isolated or in the periphery. From this observations the perception zone is divided into three non-overlapping regions: a *repulsion zone*, an *aligment zone*, and an *attraction zone*.

Clearly, the shape of these zones will necessarily take into account the sensory capabilities of the individual. For example, the visual field of a bird does not extend behind its body, fishes can accompany visual signals with those coming from their lateral line, while cells can feel stimuli around them via filopodia (see also Chapter 1). This leads to introduce the concept of the *cone of vision*, see Figure 2.5 (Huth and Wissel, 1992; Couzin et al, 2002; Hemelrijk and Hildenbrandt, 2008). In general the cone of interaction is not only animal-dependent, but it can also vary depending on the type of motion, environmental conditions, presence of predators, and aim of the displacement (Cristiani et al, 2011a).

Couzin et al (2002) proposed a model based on the three interaction zones. Varying the width of the perception zones and some parameters of the model the simulations exhibit various basic type of collective motion: swarm, with little or no parallel orientation; milling, with individuals that rotate around an empty core; parallel group and highly parallel group (Figure 2.6).

A similar model that include alignment and attraction-repulsion effect on suitable interaction zones, with noise, has been proposed by Grégoire et al (2003) and Grégoire and Chaté (2004), as a an extension of the Vicsek's model (2.31).

In all models seen here the interaction occurs in the so called “metric” way, that is, each unit interacts only with those particles which are closer than a predefined distance, that is a fixed “range of interaction”. Recent studies of starling flocks, on the other hand, have shown that each bird modifies its position relative to the mates directly surrounding it (typically six or seven individuals), no matter how close or how far away those animals are. In this type of behaviour, referred as

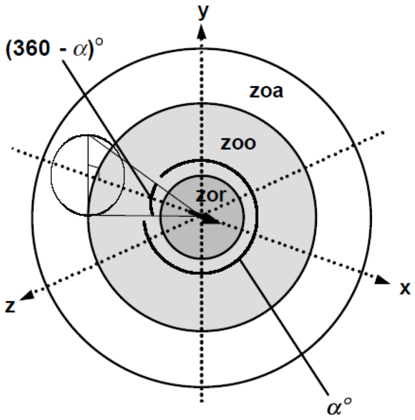

Figure 2.5. Perception zones centred around an individual. If some mates enter in *repulsion zone* (named “zor”) the individual moves away from them into the opposite direction to avoid collision. If no mates are in the repulsion zone, the individual aligns itself with neighbours within the *orientation zone* (named “zoo”). Finally, the individual is attracted toward its mates in the *attraction zone* (named “zoa”). The angle α represents the *visual cone*, and $360° - \alpha$ is the blind area (source Couzin et al, 2002).

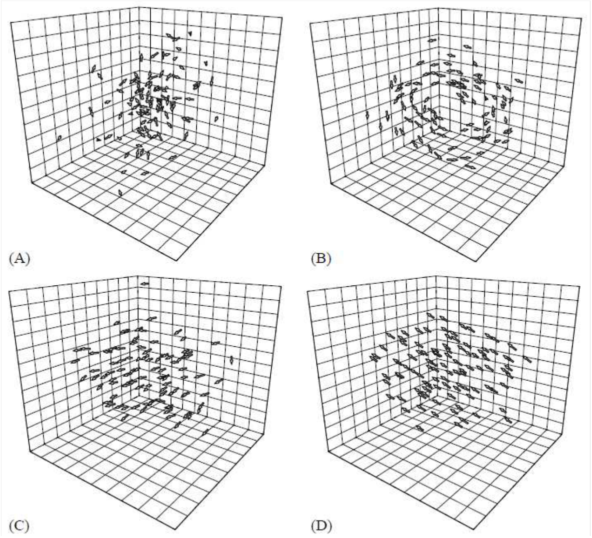

Figure 2.6. The collective behaviour exhibited by the Couzin et al. model: (A) swarm, with little orientation; (B) torus, in which individuals rotate around an empty core; (C) dynamic parallel group; (D) highly parallel group (source Couzin et al, 2002).

“topological” interaction (Ballerini et al, 2008), the radius of perception is adjusted by each individual, in such way that the neighbourhood of interaction encompasses a predefined mass of other individuals felt comfortable to interact with it (see Cristiani et al, 2010, 2011a and references therein).

In particular Cristiani et al (2011a), showed that, choosing a suitably restricted angle of vision, together with a topological interaction, it is possible to reproduce the main structure of animal group (e.g. clusters, lines and V-like structures) with a agent-based zone model including only the superposition of attraction and repulsion effect, so that the alignment effect is not taken into account (Figure 2.7). In their first order system (that models the velocity of the individuals) the linear attraction and the repulsion term as $1/r$, r being the distance between the individuals, are similar to those described in Section 2.6.2.

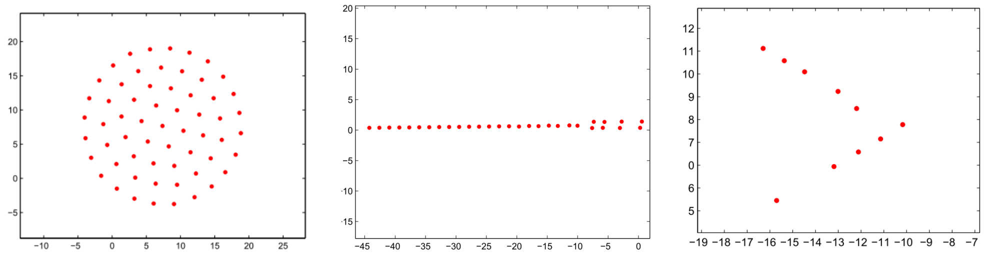

(a) (b) (c)

Figure 2.7. The main structure of animal group obtained with the model proposed by Cristiani et al. (a) A round cluster; (b) a line formation; (c) a V-like pattern. The group is moving horizontally from left to right (source Cristiani et al, 2011a).

A development of the three zone model, as proposed by Albi and Pareschi (2013), can describe the dynamics of a large group of agents influenced by a small number of external agent. This can find application in nature when the presence of external agents such as predators or leaders modify the internal dynamics of a group (flock of birds, school of fishes, herd of sheeps), see Figure 2.8. The proposed model, endowed of both metric and topological interaction, considers different level of descriptions, from a microscopic description, to a kinetic model obtained through a mean-field limit, and finally to a macroscopic system through a hydrodynamic limit.

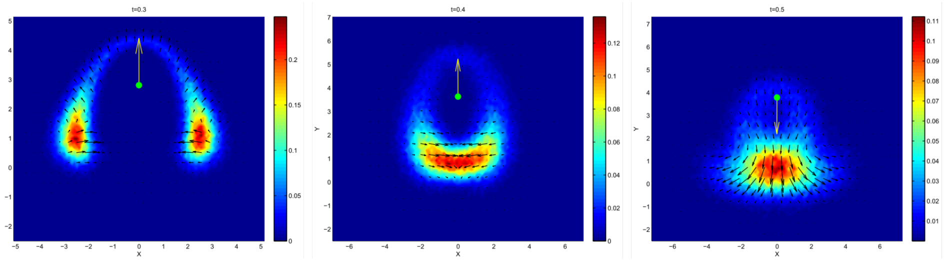

Figure 2.8. A numerical simulation of the model proposed by Albi et al. showing a swarm attacked by a predator (marked with a green dot ●) (source Albi and Pareschi, 2013).

2.7 Collective motion of cells

In multicellular organisms cell migration plays a fundamental role in both embryonic development (gastrulation, neural crest migration, etc.) and in the normal physiological responses of adults (wound healing, immune response, cancer metastasis, etc.). Precision, coordination and robustness in cell movement are likely to render more efficient a biological processes. From this, for example, may depend the difficulty of fighting metastasis in a invasive movement of tumour cells.

According to Rorth (2007), in living organisms there are different strategies for cell movement. We can distinguish three typical behaviour (Figure 2.9).

1) Groups can be associated loosely with occasional contact and much of the apparent cohesion might come from essentially solitary cells following the same tracks and cues. These are germ cells in many organisms, neural crest cells in the embryos of mammals, sperm cells.

2) Groups can be more tightly associated and the cells normally never dissociate. These groups have the feature that the moving structure has an inherent polarity, a free “front” and an attached “back”. An example of these groups was given in Chapter 1 in relation to the cell migration in the lateral line primordium. Other examples can be found in the vascular system and in wound healing.

3) Cluster of cells can be strongly associated, but the cluster is free, without an definite “front” or “back”. Example of this cells are shown in the Drosophila and in the zebrafish.

A particular feature of the second group of cells described above can be the presence of “leader cells” situated at the front edge of the group, that guide the motion of all cells and also provide the necessary traction forces for them. This has been suggested by many studies, for example on the model zebrafish (Haas and Gilmour, 2006; Lecaudey et al, 2008; Nechiporuk and Raible, 2008; Donà et al, 2013). In Section 1.3 we have seen in the zebrafish lateral line primordium few cells on the tip of a migrating group of cells to follow the concentration gradient on a strip of chemokine signal (SDF1-a), and the total migration is ensured by cell-cell adhesion via transmembrane proteins, said cadherins. In a second stage of development some leader cells become the centre of particular rosette-shaped structures, the neuromasts, and attract other follower cells via a mechanism based on the chemoattractant fibroblast growth factor (FGF), and on its receptor FGFR (see Section 1.4).

Many mathematical models have investigated collective motions of cells in both, two-dimensional framework, such as sheet migration of cells, wound healing, streaming behaviour of endothelial cells, and three-dimensional framework, such as vascular network formation and gastrulation (see for instance the reviews by Méhes and Vicsek, 2014 and Hatzikirou and Deutsch, 2007). In order to provide a modelling background for the next chapter, we will cite some of them.

Szabò et al (2006) using an attraction-repulsion discrete flocking model similar to which in Section 2.6.2 studied the collective migration of keratocytes, tissue cells obtained from the scales of goldfish (Figure 2.10).

In the same framework, Sepúlveda et al (2013) have proposed a minimal model for the collective motion of cells in an actively moving epithelium. Their zone model, written as

$$\frac{d\mathbf{V}_i}{dt} = \sum_{j\,\text{n.n.}\,i} \left[\frac{\alpha}{N_i} (\mathbf{V}_j - \mathbf{V}_i) + \mathbf{f}_{ij} \right] - \beta \mathbf{V}_i + \sigma \boldsymbol{\xi}_i, \tag{2.38}$$

uses a Cucker-Smale term, performed on the N_i cells j that are the nearest neighbours of cell i, joined with a force $\mathbf{f}_{ij}$ between neighbours cells i and j, which is repulsive with a hard-core at short distances and attractive at longer distances. Moreover, a damping term in the form $-\beta\mathbf{V}_i$ and a noise $\sigma\boldsymbol{\xi}_i$ are considered. The model has then

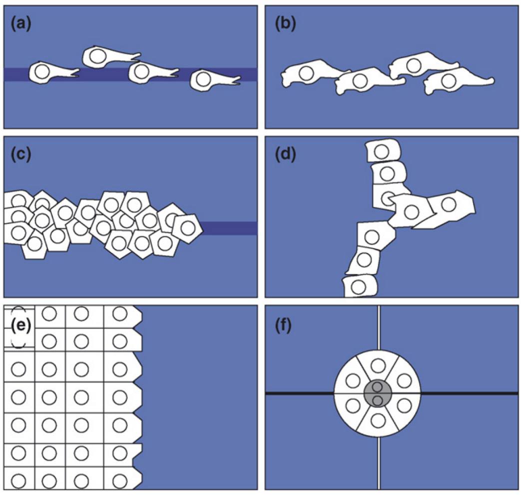

Figure 2.9. Different types of collective cell migration. The moving cells are in white, with gray circles indicating nuclei. The substrate is blue and purple lines can be a chemoattractant. Movement is from left to right. (a) and (b) show a loosely associated groups of cells, that make contact rarely (a) or frequently (b). For example germ cells, neural-crest cells, sperm cells. The degree of freedom of these cells is sometimes restricted by tracks. (c) Migrating cells in a fish lateral line. We distinguish a fixed “front” and a “back”. (d) A vascular-type branch: the cell remain associated through the central bud grow out from the existing epithelium and the cells. (e) An epithelial sheet moving to close a wounded region; cells have a small degree of freedom. (f) A cluster of moving cells (source Rorth, 2007).

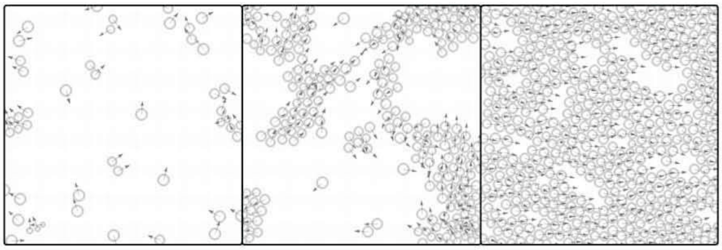

Figure 2.10. Numerical simulation of the Szabò et al. model for three different values of keratocytes number. According to the experimental observations, as cell density increases cell motility undergoes collective ordering (source Szabò et al, 2006).

been tested experimentally on the motion of Madin-Darby Canine Kidney cells, that are commonly used as a general model for epithelial cells, finding a nice agreement (Figure 2.11).

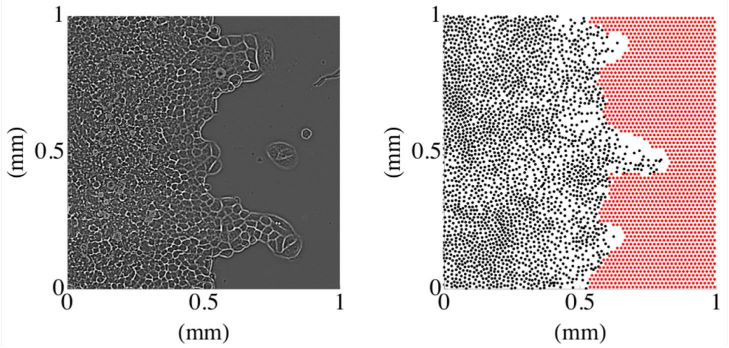

Figure 2.11. A numerical simulation of the Sepulveda et al. model compared with experimental observations. The plot describes a border progression: the motion of cells in a confluent epithelium is triggered by the unmasking of free surface. On the left there is an image from an experiment and on the right a numerical simulation. In the right panel the positions of the particles are shown as black dots on the left (●), while red dots on the right (●) mark the free surface (source Sepúlveda et al, 2013).

A hybrid model, agent-based at cellular scale and continuous at molecular level, has been proposed by Joie et al (2014) to describe the migration and the orientation of endothelial cells (cells covering the interior surface of blood vessels, lymphatic vessels and heart) seeded on bioactive micropatterned polymers (e.g. adhesion peptides or growth factor peptides that make the cells adhere). The behaviour of cells on bioactive substrates is a key component in tissue engineering, for instance in the creation of tissue *in vitro* for subsequent implantation. The model, starting from biological experiments, considers ellipsoidal cells (rounded cells become a particular case) in a bidimensional framework, since cells do not overlap. If $\mathbf{X}_i$ is the position of the centre of the i-th cell the acting force is the contribution of

$$\ddot{\mathbf{X}}_i = \mathbf{F}_\mathrm{c} + \mathbf{F}_\mathrm{r} + \mathbf{F}_\mathrm{f} + \mathbf{F}_\mathrm{a}, \tag{2.39}$$

where $\mathbf{F}_\mathrm{c}$ represents the attraction toward a chemoattractant φ,

$$\mathbf{F}_\mathrm{c}(t, \mathbf{x}) = \nabla\varphi(t, \mathbf{x}), \tag{2.40}$$

produced by the cells themselves and satisfying a suitable Poisson equation (since diffusion occurs on smaller timescale). $\mathbf{F}_\mathrm{r}$ is a repulsive force in the form $1/r^2$ (r being the distance between two cells), considering also the orientation $\mathbf{L}_i$ of the ellipses, from which different distances between the cell boundaries may depend:

$$\mathbf{F}_\mathrm{r}(\mathbf{L}_i, \mathbf{X}_i) = \alpha_\mathrm{r} f_\mathrm{r}(\mathbf{L}_i) \sum_{j=1}^{N} \frac{\mathbf{X}_i - \mathbf{X}_j}{\|\mathbf{X}_j - \mathbf{X}_i\|^3}. \tag{2.41}$$

$\mathbf{F}_\mathrm{f}$ is a friction force proportional to the velocity, that takes into account the bioactive substrate:

$$\mathbf{F}_\mathrm{f}(\mathbf{X}_i) = -\alpha_\mathrm{f} f_\mathrm{f}(\mathbf{X}_i)\dot{\mathbf{X}}_i. \tag{2.42}$$

Finally $\mathbf{F}_{\mathrm{a}}(\mathbf{X}_i, \mathbf{L}_i)$ translates the attractive force of the adhesive areas that acts when a part of the cell is located on the nutrient path, while vanishes if a cell is completely on the polymer region, or outside this region. A numerical simulation of this model is shown in Figure 2.12.

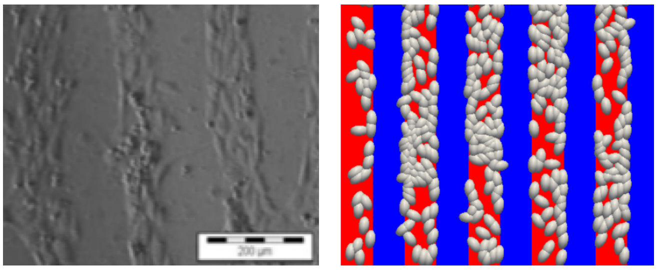

(a) (b)

Figure 2.12. Position and orientation of endothelial cells on 100 μm bioactive strips using the model proposed by Joie et al. (a) An image from an experiment; (b) a numerical simulation (adapted from Joie et al, 2014).

In a previous paper Colin et al (2013) derived also a continuous version of the preview model, in good agreement with the experimental data. Nevertheless the cell orientation, taken into account by the hybrid model, is an experimental datum and plays a crucial role in such biological structures (Joie et al, 2014).

In a three-dimensional framework Arboleda-Estudillo et al (2010) investigated the zebrafish gastrulation, the formation of the main germ layers of the embryo, from which tissues and organs eventually originate. In their model four different forces are considered: an attraction-repulsion force, a chemotactic force that provide a polarized migration, an alignment force like in (2.31), a noise force modelling random migration (Figure 2.13).

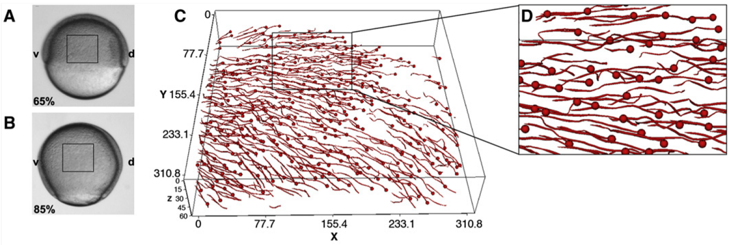

Figure 2.13. (A) Image of the zebrafish embryo at the beginning of gastrulation (6.5 hours post-fertilization (hpf)); (B) the embryo at midgastrulation (8.5 hpf). Animal pole is to the top and dorsal to the right. (C) Trajectories of mesendodermal cells during midgastrulation taken in the region marked with a rectangle in (A)-(B). Spheres indicate the endpoint of each track. (D) A magnification of the box shown in (C) (source Arboleda-Estudillo et al, 2010).

In Chapter 3 we will design a mathematical model describing the cell migration and the self-organization in the zebrafish lateral line primordium. It will be a hybrid model: continuous on the chemical scale and discrete at cellular level. For the chemicals, classic chemotaxis equations will be considered while, for the moving cells, we will include suitable interaction terms, which will take into account the collective dynamics of the migrating group. Finally, the model will include an equation for the mesenchymal-epithelial transition process in the cell state, that produce a change in the cell behaviour (see Chapter 1).

Chapter 3

A hybrid mathematical model for self-organizing cells in the early development of the zebrafish lateral line

3.1 Introduction

In Chapter 1 we have described the morphogenetic processes that arise in the zebrafish posterior lateral line, during growth and development stage.

Two main phases have been investigated: the total migration of mesenchymal cells driven by the haptotactic chemokine SDF-1a through its receptor CXCR4b, and the process of differentiation in the rear of the migrating group, inducing a mesenchymal epithelial transition. In this second phase the growth factor FGF, mutually exclusive with its receptor FGFR allowed us, also in order to formulate a suitable mathematical model, to distinguish cell population in two types: leader cells, that produce FGF signal but do not activate the receptor FGFR and follower cells, that expressing FGFR do not produce any growth factor. Then we have identified concomitant mechanisms based on the total level of FGF, SDF-1a and on a lateral inhibition effect, that lead to a formation of rosette-shaped structure in the trailing region of the migrating primordium. This configurations, characterizing the so called proto-neuromasts, present one or two leader cells in their centre, surrounded by some other followers. When this aggregates become fully mature, they are deposited during the migration. This corresponds to the growth and location of neuromasts along the two flanks of the embryo.

Our aim, in this chapter, is to obtain a minimal mathematical model which is able to:

a) describe the collective cell migration, the formation and the detachment of the neuromasts, in the spatial and temporal scale of the experimental observations;

b) ensure the existence and stability of the rosette structures characterizing the emerging neuromasts, as stationary solutions of the system.

Request a) will lead us to introduce in our model various effects, some of them experimentally evident (as chemotaxis, cell adhesion-repulsion, damping effects, chemical signals diffusion), others (as cell alignment, lateral inhibition mechanism, change of parameters in the mesenchymal-epithelial transition), biologically reasonable, introduced in order to reproduce observed results in literature. Request b), among other, allows us to obtain some important restrictions on the range of the parameter values of the model, which will be used in the numerical simulations of the dynamical case, other parameters being obtained from biological literature or by a numerical data fitting. This aspect will be recovered in Sections 3.7–3.8. Finally, performing suitable numerical tests, we will find for our model a nice agreement with biological evidences both in the stationary and in the dynamical setting.

This chapter is organized as follows: In Section 3.2 the mathematical model is introduced and its main features are discussed. In Section 3.3 a nondimensional form of the model is derived, fixing suitable characteristic quantities. Section 3.4 deals with the study of the stationary configuration of the rosettes, and their stability. In Sections 3.5 we describe the numerical approximation scheme for the equations involved in the model, and in Section 3.6 some 2D numerical tests are presented, with the aim of illustrating the power and the limits of our approach. Section 3.7 concerns with the estimate of the parameters used in the dynamical simulations and a list of the main dimensional and nondimensional coefficients is provided. Finally, Section 3.8 is devoted to the conclusions.

3.2 The basic mathematical model

Starting from the biological observations in Chapter 1, here we design a *discrete in continuous* hybrid mathematical model which takes into account the difference between the cellular and the chemical scale (see Section 2.4). At the cellular level the model is discrete and includes the equation of motion and the equation of the leader-follower state for each single cell, while at the molecular level the model is continuous and it is based on the equations for the various chemical signals. This is a reasonable choice if we think that the total number of cells involved in the morphogenesis process is in the range 80–100 (see Chapter 1). For analytical and computational simplicity in our analysis we will consider only the 2D case, although we do not expect great changes passing to 3D, since experimental observations suggest that these phenomena involve only a thin cell layer.

For cell motion we use a second order dynamic equation, which takes into account the forces acting on the cells. These forces are given by chemical signals, such as chemotaxis, and mechanical interaction between cells, as alignment, adhesion, repulsion (see Mertz et al (2013) for experimental results in this direction). About alignment effects, we base our description on the seminal paper by Cucker and Smale (2007a), while for the attraction-repulsion effects we refer to the mechanism introduced by D'Orsogna et al (2006) (see Section 2.6). All these effects take into account a non local sensing radius. Moreover a damping term, proportional to the velocities and due to cell adhesion to the substrate, is considered (Rubinstein et al, 2009; Fournier et al, 2010; Bayly et al, 2012).

For the chemical growth factors, because of the equivalence between FGF3 and

FGF10, we consider a single concentration and a single receptor, that we will name respectively FGF and FGFR (see Chapter 1). The SDF-1a effect is described by a haptotactic term produced by the gradient of the concentration of this chemokine, see Eisenbach and Lengeler (2004) for some biological backgrounds, while mathematical references can be found in Murray (2003) and Perthame (2007). In the same way, the action of FGFR on a follower cell is described by a chemotactic effect due to the gradient of the FGF produced by a leader cell. The concentration of chemical signals FGF and SDF-1a are then described using diffusion equations with possible source or degradation terms (see Sections 2.1–2.2).

Finally, the follower-leader differentiation is represented mathematically by a switch state variable, which change its value according to the level of some related functions, which take into account the concentrations of SDF-1a and of FGF, and also the number of cells in a given neighbourhood of the given cell, according to the conditions exhibited in Section 1.5.

A simplify attempt in the modelling of collective migration guided by chemical signals, tested on the lateral line formation in the zebrafish primordium, can be found in Streichan et al (2011). Although this model is proposed in full 2D framework, solutions are obtained only in 1D, and a limited number of effects occurs in the model. In particular, only one type of cells is considered, i.e.: there is no differentiation in the cell state, and neuromast structure is neglected.

Starting from the above considerations, we work in the following framework:

$$
\boxed{
\begin{array}{rl}
\begin{array}{l}\text{acceleration of} \\ i\text{-th cell}\end{array} & = \text{haptotactic effect of SDF-1a} \\
& + \text{chemotactic effect of FGF source on the followers} \\
& + \text{cells alignment} + \text{cell adhesion and repulsion} \\
& + \text{damping effect} \\
i\text{-th cell kind} & = \begin{cases} \text{follower,} & \text{if} \quad \text{low level of SDF-1a} + \text{high level of FGF} \\ & \qquad +\text{absence of lateral inhibition} \\ \text{leader,} & \qquad \text{otherwise} \end{cases} \\
\begin{array}{l}\text{rate of change of} \\ \text{FGF signal}\end{array} & = \text{diffusion} + \text{production} + \text{molecular degradation} \\
\begin{array}{l}\text{rate of change of} \\ \text{SDF-1a signal}\end{array} & = \text{degradation}
\end{array}
}
$$

Let $\mathbf{X}_i(t)$ be the position of a single i-th cell, $s(\mathbf{x}, t)$ the SDF-1a concentration, $f(\mathbf{x}, t)$ the total FGF concentration (including both FGF3 and FGF10), $\varphi_i(t)$ a variable that distinguishes a i-th cell to be, at time t, a leader ($\varphi_i(t) = 1$) or a follower ($\varphi_i(t) = 0$). We introduce the following equations:

$$\begin{cases} \ddot{\mathbf{X}}_i &= \alpha \mathbf{F}_1(\nabla s) + \gamma(1-\varphi_i)\mathbf{F}_1(\nabla f) + \mathbf{F}_2(\dot{\mathbf{X}}) + \mathbf{F}_3(\mathbf{X}) \\ & \quad - [\mu_\mathrm{F} + (\mu_\mathrm{L} - \mu_\mathrm{F})\varphi_i]\,\dot{\mathbf{X}}_i, \\ \varphi_i &= \begin{cases} 0, & \text{if} \quad \delta F_1(s) - [k_\mathrm{F} + (k_\mathrm{L} - k_\mathrm{F})\varphi_i]\, F_1(h(f)) + \lambda\Gamma(n_i) \le 0, \\ 1, & \quad\ \text{otherwise}, \end{cases} \\ \partial_t f &= D\Delta f + \xi F_4(\mathbf{X}) - \eta f, \\ \partial_t s &= -\sigma s F_5(\mathbf{X}), \end{cases} \tag{3.1}$$

where α, γ, μ_L, μ_F, δ, k_L, k_F, λ, D, ξ, η, σ are given positive constants, and $F_n(\cdot)$, $n = 1, \dots, 5$, are suitable functions.

The term F_1, which is related to the detection of a chemical signal by i-th cell in its neighbourhood, is taken to be a weighted average over a ball of radius $\bar{R}$ and centred in $\mathbf{X}_i$:

$$F_1(g(\mathbf{x}, t)) := \frac{1}{W} \int_{\mathbf{B}(\mathbf{X}_i, \bar{R})} g(\mathbf{x}, t) w_i(\mathbf{x})\, d\mathbf{x}, \tag{3.2}$$

where

$$\mathbf{B}(\mathbf{X}_i, \bar{R}) := \left\{ \mathbf{x} : ||\mathbf{x} - \mathbf{X}_i|| \le \bar{R} \right\}, \tag{3.3}$$

$||\cdot||$ being the Euclidean norm,

$$w_i(\mathbf{x}) := \begin{cases} 2\exp\left(-||\mathbf{x} - \mathbf{X}_i||^2 \dfrac{\log 2}{\bar{R}^2}\right) - 1, & \text{if} \quad ||\mathbf{x} - \mathbf{X}_i|| \le \bar{R}; \\ 0, & \quad\ \text{otherwise}; \end{cases} \tag{3.4}$$

is a truncated Gaussian weight function, and

$$W := \int_{\mathbf{B}(\mathbf{X}_i, \bar{R})} w_i(\mathbf{x})\, d\mathbf{x}, \tag{3.5}$$

independently of i. A similar definition holds for the vector quantity $\mathbf{F}_1$. Reasonably we will choose $\bar{R}$ larger than the cell radius R (see Section 3.7), so (3.2) describes a chemical signal that is sensed more in the centre of the cell and less at the edge of the cell extensions. The second term in $(3.1)_1$ refers to the attraction of a follower cell toward a source of FGF ligand. The switch variable φ_i makes this term zero for a leader cell that, expressing FGF, does not activate FGFR receptors (see Chapter 1).

The effect included in the third term of $(3.1)_1$ represents a possible cell alignment. For it we assume a Cucker and Smale-like *flocking term*:

$$\mathbf{F}_2(\dot{\mathbf{X}}) := \frac{1}{\bar{N}_i} \sum_{j : \mathbf{X}_j \in \mathbf{B}(\mathbf{X}_i, R_1) \setminus \{\mathbf{X}_i\}} \mathbf{H}(\dot{\mathbf{X}}_j - \dot{\mathbf{X}}_i). \tag{3.6}$$

Here R_1 is a suitable radius of influence,

$$\bar{N}_i := \text{card}\,\{j : \mathbf{X}_j \in \mathbf{B}(\mathbf{X}_i, R_1)\}\,, \tag{3.7}$$

and the function $\mathbf{H}$ depends on the relative velocities $\dot{\mathbf{X}}_j - \dot{\mathbf{X}}_i$, i.e.:

$$\mathbf{H}(\dot{\mathbf{X}}_j - \dot{\mathbf{X}}_i) := [\beta_{\mathrm{F}} + (\beta_{\mathrm{L}} - \beta_{\mathrm{F}})\varphi_i\varphi_j]\,\frac{R_1^2}{R_1^2 + ||\mathbf{X}_j - \mathbf{X}_i||^2}(\dot{\mathbf{X}}_j - \dot{\mathbf{X}}_i), \tag{3.8}$$

β_{F}, β_{L} being constants. In particular we can have different coefficients of alignment for a leader or follower cell: the product $\varphi_i\varphi_j$ makes the coefficient equal to β_{F} if at least one of the two cell is follower ($\varphi_i\varphi_j = 0$) and equal to β_{L} in the case of two leaders ($\varphi_i\varphi_j = 1$). We remark that the flocking term given by (3.8) (Cucker and Smale, 2007a; Ha and Liu, 2009), in our model is coupled with other effects, as chemotaxis and attraction-repulsion effects (see below), and it is also computed on a truncated domain. Similar mechanisms, as given in (3.8), have been applied in biological contexts by Szabò et al (2006), Arboleda-Estudillo et al (2010), and Sepúlveda et al (2013), since the seminal paper of Vicsek et al (1995) (see Sections 2.5–2.7). In the following we will assume $R_1 = \bar{R}$ (see Section 3.7), but in principle they can be different. In Section 3.7 we will give a justification for the introduction of an alignment term.

The function $\mathbf{F}_3$ includes adhesion-repulsion effects. In particular repulsion occurs at a distance between the centres of two cells less than R_4 and takes into account the effects of a possible cell deformation. Conversely, adhesion occurs at a distance greater than R_4 and less than $R_5 > R_4$, and it is due to a mechanical interaction between cells via filopodia. We assume

$$\mathbf{F}_3(\mathbf{X}) := \sum_{j:\mathbf{X}_j \in \mathbf{B}(\mathbf{X}_i, R_5)\setminus\{\mathbf{X}_i\}} \mathbf{K}(\mathbf{X}_j - \mathbf{X}_i), \tag{3.9}$$

where the function $\mathbf{K}$ depends on the relative positions $\mathbf{X}_j - \mathbf{X}_i$, i.e.:

$$\mathbf{K}(\mathbf{X}_j - \mathbf{X}_i) := \begin{cases} -\omega_{\mathrm{rep}}\left(\dfrac{1}{||\mathbf{X}_j - \mathbf{X}_i||} - \dfrac{1}{R_4}\right)\dfrac{\mathbf{X}_j - \mathbf{X}_i}{||\mathbf{X}_j - \mathbf{X}_i||}, & \text{if} \quad ||\mathbf{X}_j - \mathbf{X}_i|| \le R_4; \\[2ex] \bar{\omega}_{\mathrm{adh}}\,(||\mathbf{X}_j - \mathbf{X}_i|| - R_4)\,\dfrac{\mathbf{X}_j - \mathbf{X}_i}{||\mathbf{X}_j - \mathbf{X}_i||}, & \text{if} \quad R_4 < ||\mathbf{X}_j - \mathbf{X}_i|| \le R_5; \end{cases} \tag{3.10}$$

with

$$\bar{\omega}_{\mathrm{adh}} := \omega_{\mathrm{adh,F}} + (\omega_{\mathrm{adh,L}} - \omega_{\mathrm{adh,F}})\varphi_i\varphi_j,$$

ω_{rep}, $\omega_{\mathrm{adh,L}}$, $\omega_{\mathrm{adh,F}}$ being constants. In practice we will choose $R_4 = 2R$ (see Section 3.7), so that repulsion occurs when two cells start to be effectively overlapped. We note that function $(3.10)_1$ gives a repulsion which goes as $1/r$, r being the distance between the centres of two cells, as we can find in Cristiani et al (2011a,b); Colombi et al (2014). The function $(3.10)_2$ represents Hooke's law of elasticity, with different elastic coefficients for a leader cell and for a follower. In particular we have $\omega_{\mathrm{adh,F}}$ if at least one of the two cells is a follower ($\varphi_i\varphi_j = 0$) and $\omega_{\mathrm{adh,L}} > \omega_{\mathrm{adh,F}}$ if two cells are both leaders ($\varphi_i\varphi_j = 1$). The introduction of two different elastic coefficients is reasonable taking into account the different cell adhesion molecules (E-cadherins and N-cadherins) expressed in the mesenchymal or epithelial state (see Section 1.4 and Armstrong et al, 2009). Similar terms can be found in Albi and Pareschi (2013), Joie et al (2014) and references therein. We remark that adhesion $(3.10)_2$ and alignment (3.8) produce different effects, though they both refer to a cell-cell interaction: the former a radial effect, the latter a tangential effect. In some models of collective motion alignment, adhesion and repulsion act on non-overlapping regions (see Section 2.6.3). Here, taking into account a possible effect of the cell extensions, we suppose that the alignment occurs inside a interacting area, overlapped in part to the repulsion region.

The last term in the first equation is due to the cell adhesion to the substrate (see, for instance, Rubinstein et al, 2009; Fournier et al, 2010; Bayly et al, 2012), possibly with a different damping coefficient for a leader (μ_{L}, given by $\varphi_i = 1$) or a follower cell (μ_{F}, given by $\varphi_i = 0$).

The second equation in (3.1) defines the switch variable φ_i for the i-th cell. The leader-to-follower transition is performed requiring that the threshold function at the right hand side of $(3.1)_2$ is less than zero, according to the three conditions described in Chapter 1. For the FGF detection in $F_1(h(f))$ we choose the following form for the function $h(f)$:

$$h(f) := \frac{f}{f_{\max} + f}, \tag{3.11}$$

where $f_{\max}$ is constant. The function (3.11) includes a possible saturation effect when FGF molecules tend to occupy all receptors of a cell. The coefficients k_{L} and k_{F}, related respectively to a leader and a follower cell, provides a delay in the inverse follower-to-leader transition setting suitably $k_{\mathrm{L}} < k_{\mathrm{F}}$, this in accordance to observations in Section 1.5. About the lateral inhibition mechanism, as proposed in Section 1.5, we introduce a function $\Gamma(n_i)$ that counts the number n_i of cells in a suitable neighbourhood of the i-th cell, with radius of influence R_2, namely

$$\Gamma(n_i) := \frac{e^{n_i}}{e^{n_i} + \Gamma_0} - \frac{1}{1 + \Gamma_0}, \tag{3.12}$$

where

$$n_i := \operatorname{card}\left\{ j : \mathbf{X}_j \in \mathring{\mathbf{B}}(\mathbf{X}_i, R_2) \setminus \{\mathbf{X}_i\} \right\}, \tag{3.13}$$

Γ_0 is a constant, and $\mathring{\mathbf{B}}(\mathbf{X}_i, R_2)$ is the interior of $\mathbf{B}(\mathbf{X}_i, R_2)$. The function (3.12) is justified if we think of a neuromast as made by a single central leader and some followers around. In this context (3.12) takes very different values when it is evaluated on a central cell or on a cell on the boundary of the primordium. Moreover, it provides a fast saturation effect when n increases, so that a central leader perceives about the same inhibition effect from a certain value of n. This is useful to describe the possibility to obtain neuromasts with a variable number of cells, according to experimental observations (generally 8-12 cells) (Lecaudey et al, 2008). A suitable value for the constant Γ_0 is given in Section 3.7, then we will choose the radius $R_2 = 2R$ in order to consider lateral inhibition as a pressure effect that occurs when two cells start to be overlapped.

In the diffusion equation $(3.1)_3$, only leader cells are responsible of the production of FGF, so that

$$F_4(\mathbf{X}) := \sum_{j=1}^{N_{\text{tot}}} \varphi_j \chi_{\mathbf{B}(\mathbf{X}_j, R_3)}, \tag{3.14}$$

where N_{tot} is the total number of cells, and

$$\chi_{\mathbf{B}(\mathbf{X}_j, R_3)} := \begin{cases} 1, & \text{if} \quad \mathbf{x} \in \mathbf{B}(\mathbf{X}_j, R_3); \\ 0, & \quad\;\;\; \text{otherwise.} \end{cases} \tag{3.15}$$

Similarly, in equation $(3.1)_4$ we take

$$F_5(\mathbf{X}) := \sum_{j=1}^{N_{\text{tot}}} \chi_{\mathbf{B}(\mathbf{X}_j, R_3)},$$

in which the variable φ_i does not appear now, because both leaders and followers are involved in the haptotactic process. Typically, we will choose $R_3 = R$ considering that the source of FGF and the degradation of SDF-1a signal is substantially defined by the dimension of a single cell (see Section 3.7).

The above observations are then summarized in the following model:

$$\begin{cases}
\ddot{\mathbf{X}}_i & = \dfrac{\alpha}{W} \displaystyle\int_{\mathbf{B}(\mathbf{X}_i, \bar{R})} \nabla s(\mathbf{x}, t) w_i(\mathbf{x}) \, d\mathbf{x} + \dfrac{\gamma(1-\varphi_i)}{W} \displaystyle\int_{\mathbf{B}(\mathbf{X}_i, \bar{R})} \nabla f(\mathbf{x}, t) w_i(\mathbf{x}) \, d\mathbf{x} \\
& \quad + \dfrac{1}{\bar{N}_i} \displaystyle\sum_{j : \mathbf{X}_j \in \mathbf{B}(\mathbf{X}_i, R_1) \setminus \{\mathbf{X}_i\}} \mathbf{H}(\dot{\mathbf{X}}_j - \dot{\mathbf{X}}_i) + \displaystyle\sum_{j : \mathbf{X}_j \in \mathbf{B}(\mathbf{X}_i, R_5) \setminus \{\mathbf{X}_i\}} \mathbf{K}(\mathbf{X}_j - \mathbf{X}_i) \\
& \quad - [\mu_{\text{F}} + (\mu_{\text{L}} - \mu_{\text{F}}) \varphi_i] \, \dot{\mathbf{X}}_i, \\
\varphi_i & = \begin{cases} 0, & \text{if} \quad \dfrac{\delta}{W} \displaystyle\int_{\mathbf{B}(\mathbf{X}_i, \bar{R})} s(\mathbf{x}, t) w_i(\mathbf{x}) \, d\mathbf{x} \\ & \quad - \dfrac{k_{\text{F}} + (k_{\text{L}} - k_{\text{F}})\varphi_i}{W} \displaystyle\int_{\mathbf{B}(\mathbf{X}_i, \bar{R})} \dfrac{f(\mathbf{x}, t)}{f_{\max} + f(\mathbf{x}, t)} w_i(\mathbf{x}) \, d\mathbf{x} + \lambda \Gamma(n_i) \leq 0, \\ 1, & \quad \text{otherwise,} \end{cases} \\
\partial_t f & = D \Delta f + \xi \displaystyle\sum_{j=1}^{N_{\text{tot}}} \varphi_j \chi_{\mathbf{B}(\mathbf{X}_j, R_3)} - \eta f, \\
\partial_t s & = -\sigma s \displaystyle\sum_{j=1}^{N_{\text{tot}}} \chi_{\mathbf{B}(\mathbf{X}_j, R_3)},
\end{cases} \tag{3.16}$$

where the functions $\mathbf{H}(\dot{\mathbf{X}}_j - \dot{\mathbf{X}}_i)$ and $\mathbf{K}(\mathbf{X}_j - \mathbf{X}_i)$ are given by (3.8) and (3.10). Initial and boundary conditions have to be specified. For the i-th cell we set

$$\mathbf{X}_i(0) = \mathbf{X}_{i0}; \quad \text{and} \quad \dot{\mathbf{X}}_i(0) = \mathbf{0}, \quad i = 1, \ldots, N_{\text{tot}}, \tag{3.17}$$

together with the fact that all the cells are initially in the leader state:

$$\varphi_i(0) = 1, \quad i = 1, \dots, N_{\text{tot}}. \tag{3.18}$$

Now, let $\Omega = [a, b] \times [c, d]$ be our domain, for FGF signal we require zero initial concentration and homogeneous Neumann boundary condition:

$$f(\mathbf{x}, 0) = 0; \quad \frac{\partial f}{\partial \mathbf{n}} = 0, \quad \text{on } \partial\Omega. \tag{3.19}$$

No-flow boundary condition $(3.19)_2$ is justified if we think of an experiment in which our domain is isolated from the surrounding environment. Then, since initially SDF-1a is only located in a given region

$$s(\mathbf{x}, 0) = s_0(\mathbf{x}), \tag{3.20}$$

where $s_0(\mathbf{x})$ has compact support in Ω. In particular we consider a rectangular stripe of width $2l$, $[\bar{a}, \bar{b}] \times [m - l, m + l]$, with $[\bar{a}, \bar{b}] \subset [a, b]$, $m = (c + d)/2$, and

$$s_0(x, y) := \Phi(x)\Psi(y), \tag{3.21}$$

where, for instance, we choose

$$\Phi(x) := \frac{s_{\max}}{2} \left[\tanh\left(\frac{x - c_1}{c_2} \right) + 1 \right] \chi_{[\bar{a}, \bar{b}]}, \tag{3.22}$$

$s_{\max}$ is the initial maximum SDF-1a concentration, c_1, c_2 are constants. The function (3.22) yields a non uniform haptotactic gradient, that is stronger at the beginning and then tends to saturate when cells acquire enough velocity. Values for c_1, c_2 will be given in Section 3.6. Then we set

$$\Psi(y) := u_\varepsilon(y) * \chi_{[m-l,m+l]}(y) = \int_c^d u_\varepsilon(y - \tau)\chi_{[m-l,m+l]}(y)\, d\tau, \tag{3.23}$$

the convolution of $\chi_{[m-l,m+l]}(y)$ with a positive and symmetric mollifier

$$u_\varepsilon(y) := \begin{cases} \dfrac{1}{J}\dfrac{1}{\varepsilon}\, e^{-\dfrac{1}{1 - (y/\varepsilon)^2}}, & \text{if} \quad -\varepsilon < y < \varepsilon; \\ 0, & \text{otherwise}; \end{cases} \tag{3.24}$$

where

$$J := \int_{-\varepsilon}^{\varepsilon} \frac{1}{\varepsilon}\, e^{-\dfrac{1}{1 - (y/\varepsilon)^2}}\, dy, \tag{3.25}$$

is the normalization factor. The mollifier (3.24) is introduced to have sufficient smoothness for $s_0(\mathbf{x})$. A suitable value for the positive constant ε will be given in Section 3.6.

Although we have introduced an initial gradient for SDF-1a, we have tested in our simulations that the cells of the primordium can self-generate their own gradient, so the collective migration can be ensured, with a reduced velocity, even fixing a constant initial data, along the x-axis, for the SDF1-1a signal. Biological studies in this regard have been performed recently by Donà et al (2013). Anyway we find that an initial gradient for the SDF-1a signal is necessary to reach a cell velocity consistent with the experimental data (see also Sections 3.6–3.7).

3.3 The nondimensional model

Though we tend to use dimensional times and distances in the plots for easier comparison with experiments, the qualitative behaviour of the model (3.16) is more clearly described using a nondimensional form based on the following dimensionless quantities:

$$
\begin{gathered}
t^* := \frac{t}{T}, \quad \mathbf{x}^* := \frac{\mathbf{x}}{R}, \quad \mathbf{X}^* := \frac{\mathbf{X}}{R}, \quad f^* := \frac{f}{f_{\max}}, \quad s^* := \frac{s}{s_{\max}},\\
W^* := \frac{W}{R^2}, \quad R_i^* := \frac{R_i}{R} \quad i = 1, \dots, 5, \quad \bar{R}^* := \frac{\bar{R}}{R},\\
\alpha^* := \frac{\alpha s_{\max} T^2}{R^2}, \quad \beta_{\mathrm{L}}^* := \beta_{\mathrm{L}} T, \quad \beta_{\mathrm{F}}^* := \beta_{\mathrm{F}} T, \quad \gamma^* := \frac{\gamma f_{\max} T^2}{R^2}, \quad \omega_{\mathrm{rep}}^* := \frac{\omega_{\mathrm{rep}} T^2}{R^2},\\
\omega_{\mathrm{adh,L}}^* := \omega_{\mathrm{adh,L}} T^2, \quad \omega_{\mathrm{adh},F}^* := \omega_{\mathrm{adh,F}} T^2, \quad \mu_{\mathrm{L}}^* := \mu_{\mathrm{L}} T, \quad \mu_{\mathrm{F}}^* := \mu_{\mathrm{F}} T, \quad \delta^* := \frac{\delta s_{\max}}{\lambda},\\
k_{\mathrm{L}}^* := \frac{k_{\mathrm{L}}}{\lambda}, \quad k_{\mathrm{F}}^* := \frac{k_{\mathrm{F}}}{\lambda}, \quad D^* := \frac{DT}{R^2}, \quad \xi^* := \frac{\xi T}{f_{\max}}, \quad \eta^* := \eta T,\\
\sigma^* := \sigma T, \quad c_1^* := \frac{c_1}{R}, \quad c_2^* := \frac{c_2}{R}, \quad \varepsilon^* := \frac{\varepsilon}{R},
\end{gathered}
$$

where T a characteristic time (see Section 3.7). With these definitions, and maintaining for simplicity the asterisks only for the nondimensional constants, we have

$$
\left\{
\begin{array}{ll}
\ddot{\mathbf{X}}_i & = \dfrac{\alpha^*}{W} \displaystyle\int_{\mathbf{B}(\mathbf{X}_i, \bar{R}^*)} \nabla s(\mathbf{x}, t) w_i(\mathbf{x})\, d\mathbf{x} + \dfrac{\gamma^*(1-\varphi_i)}{W} \displaystyle\int_{\mathbf{B}(\mathbf{X}_i, \bar{R}^*)} \nabla f(\mathbf{x}, t) w_i(\mathbf{x})\, d\mathbf{x}\\[2ex]
 & \quad + \dfrac{1}{\bar{N}_i} \displaystyle\sum_{j: \mathbf{X}_j \in \mathbf{B}(\mathbf{X}_i, R_1^*) \setminus \{\mathbf{X}_i\}} \mathbf{H}(\dot{\mathbf{X}}_j - \dot{\mathbf{X}}_i) + \displaystyle\sum_{j: \mathbf{X}_j \in \mathbf{B}(\mathbf{X}_i, R_5^*) \setminus \{\mathbf{X}_i\}} \mathbf{K}(\mathbf{X}_j - \mathbf{X}_i)\\[2ex]
 & \quad - \left[\mu_{\mathrm{F}}^* + (\mu_{\mathrm{L}}^* - \mu_{\mathrm{F}}^*)\varphi_i\right] \dot{\mathbf{X}}_i,\\[2ex]
\varphi_i & = \begin{cases} 0 \quad \text{if} \quad \dfrac{\delta^*}{W} \displaystyle\int_{\mathbf{B}(\mathbf{X}_i, \bar{R}^*)} s(\mathbf{x}, t) w_i(\mathbf{x})\, d\mathbf{x} \\[2ex] \qquad - \dfrac{k_{\mathrm{F}}^* + (k_{\mathrm{L}}^* - k_{\mathrm{F}}^*)\varphi_i}{W} \displaystyle\int_{\mathbf{B}(\mathbf{X}_i, \bar{R}^*)} \dfrac{f(\mathbf{x}, t)}{1 + f(\mathbf{x}, t)} w_i(\mathbf{x})\, d\mathbf{x} + \Gamma(n_i) \le 0,\\[2ex] 1 \quad \text{otherwise}, \end{cases}\\[2ex]
\partial_t f & = D^* \Delta f + \xi^* \displaystyle\sum_{j=1}^{N_{\mathrm{tot}}} \varphi_j \chi_{\mathbf{B}(\mathbf{X}_j, R_3^*)} - \eta^* f,\\[2ex]
\partial_t s & = -\sigma^* s \displaystyle\sum_{j=1}^{N_{\mathrm{tot}}} \chi_{\mathbf{B}(\mathbf{X}_j, R_3^*)},
\end{array}
\right.
\tag{3.26}
$$

where $w_i(\mathbf{x})$ and W are given by (3.4)–(3.5) replacing $\bar{R}$ with $\bar{R}^*$, then

$$
\Gamma(n_i) := \frac{e^{n_i}}{e^{n_i} + \Gamma_0} - \frac{1}{1 + \Gamma_0}, \tag{3.27}
$$

$$
n_i := \operatorname{card}\left\{j : \mathbf{X}_j \in \mathring{\mathbf{B}}(\mathbf{X}_i, R_2^*) \setminus \{\mathbf{X}_i\}\right\}, \tag{3.28}
$$

$$
\bar{N}_i := \operatorname{card}\left\{j : \mathbf{X}_j \in \mathbf{B}(\mathbf{X}_i, R_1^*)\right\}, \tag{3.29}
$$

$$\mathbf{H}(\dot{\mathbf{X}}_j - \dot{\mathbf{X}}_i) := [\beta^*_{\mathrm{F}} + (\beta^*_{\mathrm{L}} - \beta^*_{\mathrm{F}})\varphi_i\varphi_j]\,\frac{R_1^{*2}}{R_1^{*2} + ||\mathbf{X}_j - \mathbf{X}_i||^2}(\dot{\mathbf{X}}_j - \dot{\mathbf{X}}_i), \tag{3.30}$$

and

$$\mathbf{K}(\mathbf{X}_j - \mathbf{X}_i) := \begin{cases} -\omega^*_{\mathrm{rep}}\left(\dfrac{1}{||\mathbf{X}_j - \mathbf{X}_i||} - \dfrac{1}{R^*_4}\right)\dfrac{\mathbf{X}_j - \mathbf{X}_i}{||\mathbf{X}_j - \mathbf{X}_i||}, & \text{if} \quad ||\mathbf{X}_j - \mathbf{X}_i|| \le R^*_4; \\ \bar{\omega}^*_{\mathrm{adh}}\left(||\mathbf{X}_j - \mathbf{X}_i|| - R^*_4\right)\dfrac{\mathbf{X}_j - \mathbf{X}_i}{||\mathbf{X}_j - \mathbf{X}_i||}, & \text{if} \quad R^*_4 < ||\mathbf{X}_j - \mathbf{X}_i|| \le R^*_5; \end{cases} \tag{3.31}$$

with

$$\bar{\omega}^*_{\mathrm{adh}} := \omega^*_{\mathrm{adh,F}} + (\omega^*_{\mathrm{adh,L}} - \omega^*_{\mathrm{adh,F}})\varphi_i\varphi_j.$$

Initial and boundary conditions are still given by (3.17)–(3.23). In particular in (3.22), (3.24), and (3.25) we have to replace $s_{\max}$, c_1, c_2 and ε, with $s^*_{\max} = 1$, c^*_1, c^*_2 and ε^*.

3.4 Steady states and stability

Now we will investigate particular steady states for our model. They are biologically relevant, because they correspond to the neuromast basic structure (see Chapter 1). This will be useful also to provide us a range of variability for some parameters or to specify some of their ratios. First we consider the stationary form of system (3.26)

$$\begin{cases} \dfrac{\gamma^*(1-\varphi_i)}{W}\displaystyle\int_{\mathbf{B}(\mathbf{X}_i,\bar{R}^*)} \nabla f(\mathbf{x}) w_i(\mathbf{x})\,d\mathbf{x} + \sum_{j:\mathbf{X}_j \in \mathbf{B}(\mathbf{X}_i,R^*_5)\setminus\{\mathbf{X}_i\}} \mathbf{K}(\mathbf{X}_j - \mathbf{X}_i) = \mathbf{0}, \\ \varphi_i = \begin{cases} 0, & \text{if} \quad -\dfrac{k^*_{\mathrm{F}} + (k^*_{\mathrm{L}} - k^*_{\mathrm{F}})\varphi_i}{W}\displaystyle\int_{\mathbf{B}(\mathbf{X}_i,\bar{R}^*)} \frac{f(\mathbf{x})}{1+f(\mathbf{x})} w_i(\mathbf{x})\,d\mathbf{x} + \Gamma(n_i) \le 0, \\ 1, & \quad \text{otherwise}, \end{cases} \\ D^*\Delta f = \eta^* f - \xi^* \displaystyle\sum_{j=1}^{N_{\mathrm{tot}}} \varphi_j \chi_{\mathbf{B}(\mathbf{X}_j,R^*_3)}, \\ s = 0, \end{cases} \tag{3.32}$$

with

$$\frac{\partial f}{\partial \mathbf{n}} = 0, \quad \text{on } \partial\Omega.$$

Then we give the following

Definition 1 *We will call N-*rosette *($N \ge 2$) a configuration formed by a leader cell surrounded by N follower cells with their centres located on the vertices of a regular polygon of N sides (or a segment if $N = 2$) centred in the leader cell (Figure 3.1 (a)).*

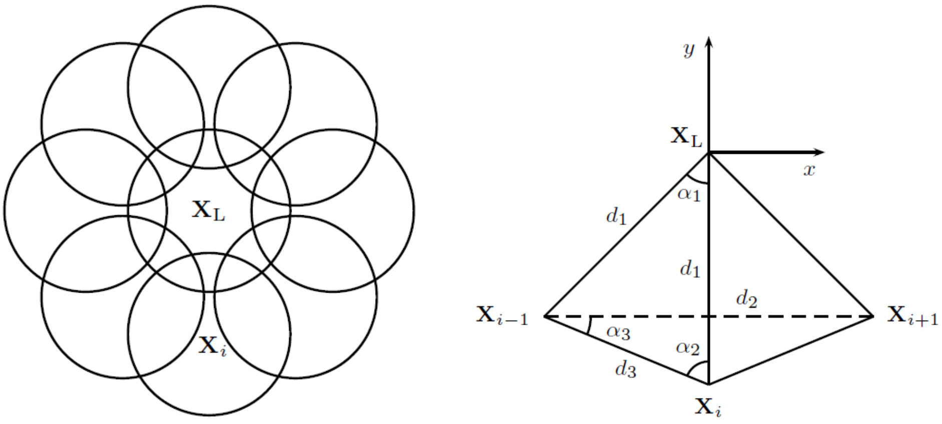

(a) (b)

Figure 3.1. (a) Example of 8-rosette with a leader centred in $\mathbf{X}_\mathrm{L}$ and 8 followers centred in $\mathbf{X}_i$, $i = 1, \ldots, 8$. (b) Geometrical configuration of a N-rosette with a leader cell centred in $\mathbf{X}_\mathrm{L}$ and some followers centred in $\mathbf{X}_{i-1}$, $\mathbf{X}_i$, $\mathbf{X}_{i+1}$.

With reference to Figure 3.1 (b), we call $\mathbf{X}_\mathrm{L}$ the centre of the leader cell, $\mathbf{X}_i$ the centre of a follower, d_1 the distance between the followers and the leader, d_2 the distance between two followers in alternating position (e.g. $\mathbf{X}_{i-1}$ and $\mathbf{X}_{i+1}$), d_3 the distance between two adjoining followers (e.g. $\mathbf{X}_i$ and $\mathbf{X}_{i+1}$), and α_1, α_2, α_3 the angles in the figure.

By symmetry considerations we set:

$$\alpha_1 = \frac{2\pi}{N}, \quad \alpha_2 = \frac{\pi - \alpha_1}{2}, \quad \alpha_3 = \frac{\pi}{2} - \alpha_2 = \frac{\pi}{N}, \tag{3.33}$$

$$d_2 = 2d_1 \sin\frac{2\pi}{N}, \tag{3.34}$$

$$d_3 = 2d_1 \sin\frac{\pi}{N}. \tag{3.35}$$

Now we assume the following physically reasonable hypotheses for a N-rosette:

1) the range of lateral inhibition is equal to the range of repulsion between cells:

$$R_2 = R_4; \tag{3.36}$$

2) the followers are located in the range of the lateral inhibition of the leader:

$$d_1 \leq R_2; \tag{3.37}$$

3) there is no repulsion between adjoining followers if $N = 2, 3$:

$$d_3 \geq R_4; \tag{3.38}$$

there is no repulsion between followers in alternating position if $N \geq 4$:

$$d_2 \geq R_4. \tag{3.39}$$

We point out that Hypothesis 1) is justified if we think of repulsion and lateral inhibition both due to the pressure between cell membranes. Hypothesis 2) is a direct consequence of the definition of a N-rosette. Finally, Hypothesis 3) ensures that repulsion, seen as a pressure effect, can be exerted only by adjacent cells, and not bypassing a single cell or considering cells completely overlapped. In particular in Hypothesis 3), for $N = 2, 3$, followers in alternating position coincide respectively with the same cell and with adjoining followers, this justifies (3.38).

Taking system (3.32) and Hypotheses (3.36)–(3.39) into account, we can state the following results.

Proposition 1 *There exist N-rosettes if and only if $N \leq 12$. Moreover the distance d_1, depending on N, can vary in the following ranges:*

$$\frac{1}{2\sin\frac{\pi}{N}} \leq \frac{d_1}{R_4} \leq 1, \quad \textit{if} \quad N = 2, 3, \tag{3.40}$$

$$\frac{1}{2\sin\frac{2\pi}{N}} \leq \frac{d_1}{R_4} \leq 1, \quad \textit{if} \quad 4 \leq N \leq 12. \tag{3.41}$$

Proof. Condition (3.40) is a consequence of (3.37), (3.36), (3.38), and (3.35). While (3.41) is a consequence of (3.37), (3.36), (3.39), and (3.34). In particular (3.41) is not empty if and only if $N \leq 12$.

The maximum number of cells, which is provided by the previous proposition, is consistent with the experimental observations as shown in Lecaudey et al (2008).

Proposition 2 *In a N-rosette there are repulsion and lateral inhibition effects between adjoining followers if and only if $N \geq 4$. In particular if $N \geq 6$ these effects do not depend on d_1, and if $N = 4, 5$ this holds if and only if*

$$\frac{1}{2\sin\frac{2\pi}{N}} \leq \frac{d_1}{R_4} < \frac{1}{2\sin\frac{\pi}{N}}, \quad N = 4, 5. \tag{3.42}$$

Proof. Hypothesis 1) ensures that this proof holds both for repulsion and lateral inhibition effects. If $N = 2, 3$ the statement is true thanks to Hypothesis 3).
If $N \geq 6$ from (3.35), (3.36), and (3.37) we have

$$d_3 \leq d_1 \leq R_2 = R_4,$$

independently from d_1.
If $N = 4, 5$, using (3.35) we have repulsion if and only if

$$d_3 = 2d_1 \sin\frac{\pi}{N} < R_4. \tag{3.43}$$

From (3.43) and (3.41) equation (3.42) follows.

Now, in order to fix the range of variability for some parameters we solve the nondimensional system (3.32) for a N-rosette with a leader in $\mathbf{X}_\mathrm{L}$, setting a frame centred $\mathbf{X}_\mathrm{L}$ with axes passing through the centre of a follower (Figure 3.1 (b)). For simplicity we introduce the following symbols:

$$\overline{\nabla f(\mathbf{X}_i)} := \frac{1}{W} \int_{\mathbf{B}(\bar{R}^*, \mathbf{X}_i)} \nabla f(\mathbf{x}) w_i(\mathbf{x}) \, d\mathbf{x},$$

$$\overline{\overline{f(\mathbf{X}_i)}} := \frac{1}{W} \int_{\mathbf{B}(\bar{R}^*, \mathbf{X}_i)} \frac{f(\mathbf{x})}{1 + f(\mathbf{x})} w_i(\mathbf{x}) \, d\mathbf{x},$$

to denote the weighted average of the functions ∇f and $\frac{f}{1+f}$.

Firstly, equation $(3.32)_2$ for each follower and for the leader becomes respectively:

$$\varphi_i = 0 \Leftrightarrow -k^*_\mathrm{F} \overline{\overline{f(\mathbf{X}_i)}} + \Gamma(n) \leq 0, \quad i = 1, \ldots, N, \tag{3.44}$$

$$\varphi_0 = 1 \Leftrightarrow -k^*_\mathrm{L} \overline{\overline{f(\mathbf{X}_\mathrm{L})}} + \Gamma(N) > 0, \tag{3.45}$$

where the function Γ is given by (3.27). Here the number n, which is related to the lateral inhibition, is given by (3.28) and, by symmetry considerations, it does not depend on i. Moreover, according to Hypothesis 2) and Proposition 2, it takes only the values 1 or 3: if $N \geq 6$, or $N = 4, 5$ and holds condition (3.42), we have to take $n = 3$, otherwise $n = 1$. The case $n = 3$ means that on the i-th cell we have the lateral inhibition of the leader cell and of the two adjoining followers, while in the case $n = 1$ we have only the lateral inhibition of the leader cell. The other cases for n are not possible due to conditions (3.36)–(3.39) assumed on the distances.

Now, the function $f(\mathbf{x})$, which is needed in (3.44) and (3.45), is the solution in the domain Ω of equation $(3.32)_3$, with Neumann boundary condition, that in this case takes the form

$$D^* \Delta f = \eta^* f - \xi^* \chi_{\mathbf{B}(\mathbf{X}_\mathrm{L}, R^*_3)}, \tag{3.46}$$

$$\frac{\partial f}{\partial \mathbf{n}} = 0, \quad \text{on } \partial\Omega, \tag{3.47}$$

$\mathbf{X}_\mathrm{L}$ being the centre of the leader cell, the only one that produces FGF signal. If Ω is a circular domain centred in the leader cell, radial symmetry of the solution of (3.46) and (3.47) implies the quantities $\overline{\overline{f(\mathbf{X}_i)}}$ to be the same for all i, so that (3.44) and (3.45) become

$$k^*_\mathrm{F} \geq \bar{k}^*_\mathrm{F} := \Gamma(n) / \overline{\overline{f(\mathbf{X}_i)}}, \tag{3.48}$$

$$k^*_\mathrm{L} < \bar{k}^*_\mathrm{L} := \Gamma(N) / \overline{\overline{f(\mathbf{X}_\mathrm{L})}}. \tag{3.49}$$

Now we try to obtain a numerical estimate for the bound functions $\bar{k}^*_\mathrm{F}$ and $\bar{k}^*_\mathrm{L}$, as N changes. We set a domain $\Omega = [0, 200] \times [0, 200]$ (μm^2) with a single leader cell located in $\mathbf{X}_\mathrm{L} = (100, 100)$ (μm). We choose the square domain size sufficiently large, so that its influence on the solution can be neglected in the time period of interest. Then equations (3.46) and (3.47) are numerically solved in such a domain, as described in Section 3.5 to follow, using a spatial discretization corresponding to $\Delta x = \Delta y = 0.2$ μm. Parameters D^*, η^*, ξ^*, R^*_2, R^*_3, R^*_4, $\bar{R}^*$ used here are listed in Table 3.3, Section 3.7.

Figure 3.2 shows a numerical estimate for the lower bound $\bar{k}^*_\mathrm{F}$ in (3.48). For each fixed value of N, $N = 2, \ldots, 12$, the curve indicates the value of $\bar{k}^*_\mathrm{F}$ as a functions

Table 3.1. Numerical values of the upper bound $\bar{k}_{\mathrm{L}}^{*}$ in (3.49) for $N = 2, \ldots, 12$. In practice fixing N we have the upper bound of k_{L}^{*} for the existence of a steady N-rosette.

N	$\bar{k}_{\mathrm{L}}^{*}$ (nondim.)	N	$\bar{k}_{\mathrm{L}}^{*}$ (nondim.)
2	0.6707	8	1.8187
3	1.1580	9	1.8230
4	1.5146	10	1.8245
5	1.6987	11	1.8251
6	1.7769	12	1.8253
7	1.8073		

of d_1, which is the distance between leader and follower. In practice, taking into account a N-rosette configuration as in Figure 3.1 (b), the numerical value of $f(\mathbf{x})$ is used to compute $\overline{\overline{f(\mathbf{X}_i)}}$ as the distance d_1 from $\mathbf{X}_i$ to $\mathbf{X}_{\mathrm{L}}$, suitably discretized, changes. Depending on the number of cells that make lateral inhibition on $\mathbf{X}_i$, also the numerator $\Gamma(n)$, can vary, for a fixed N, with respect to d_1 as established by Proposition 2. Since the scale of the curves is essentially different as N changes, we present our results in two different pictures in Figure 3.2. Notice that the range of the distance d_1 to be considered depends on N according to (3.40) and (3.41) in Proposition 1: the starting point on the curve is marked by a “$\bullet$”, while the ending point is represented by $d_1 = R_4$ for all N. We have already observed that $\Gamma(n)$ can only obtain the values $\Gamma(1)$ or $\Gamma(3)$ according to Proposition 2. So, clearly, the curves for $N = 2, 3$ are overlapped (Figure 3.2 (a)), the same for $N = 6, \ldots, 12$ (Figure 3.2 (b)). For $N = 4, 5$ the curves start in Figure 3.2 (b), when $\Gamma(n) = \Gamma(3)$, until $d_1 \approx 14$ μm for $N = 4$, and $d_1 \approx 17$ μm for $N = 5$ (markers “$\times$”), then $\Gamma(n)$ becomes $\Gamma(1)$ and, for larger values of d_1, the curves continue in Figure 3.2 (a). For $N = 12$ the right hand side of (3.48) assumes a single value in $d_1 = R_4$ in Figure 3.2 (b).

On the other hand, using again the numerical solution of $f(\mathbf{x})$, the right hand side of (3.49) can be tabulated as N changes. Its values are given in Table 3.1.

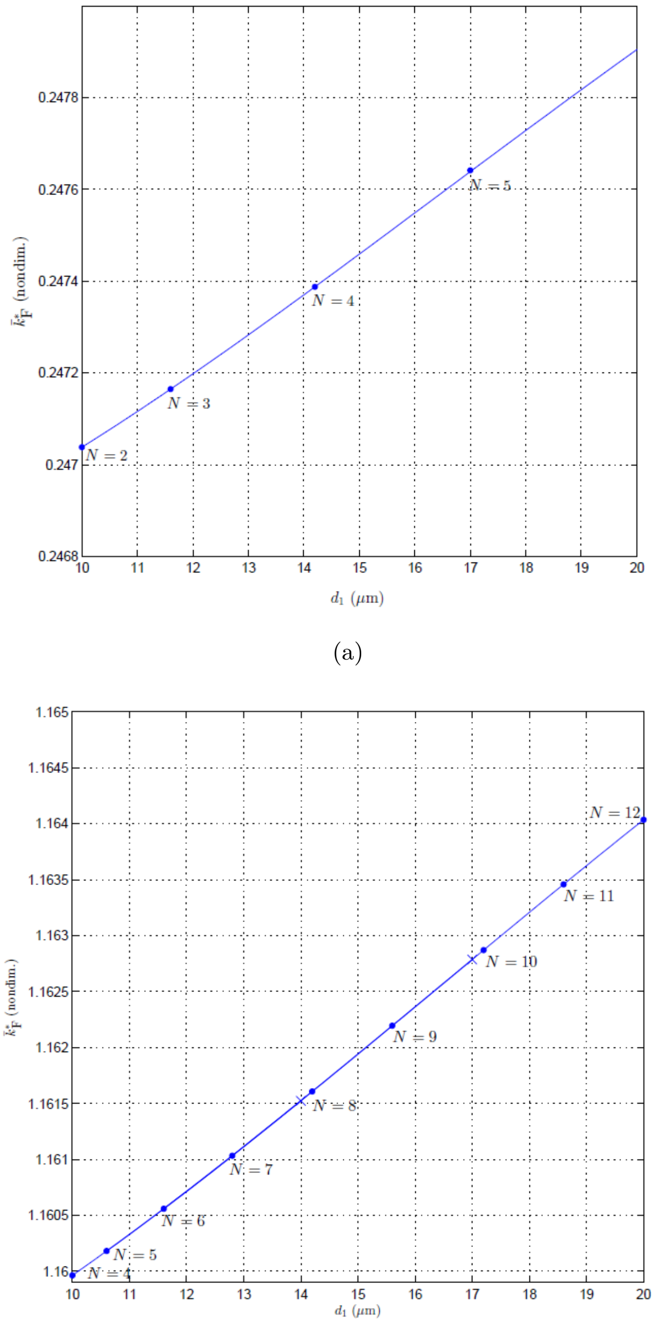

(a)

(b)

Figure 3.2. Numerical plot of the lower bound $\bar{k}_F^*$ in (3.48) as a function of d_1. The curve gives the lower bound for k_F^* for a fixed N and d_1. Since the scale of the curves is essentially different, we present in (a) the case $N = 2, 3$, in which the curves are overlapped, and similarly in (b) the case $N = 6, \ldots, 12$. The starting point on the curves is marked by "●", while the ending point is represented by $d_1 = R_4$ for all N. For $N = 4, 5$ the curves start in (b) until $d_1 \approx 14$ μm and $d_1 \approx 17$ μm respectively (markers "×"), then for larger values of d_1 they continue in (a). For $N = 12$ the curve is reduced to a single value in $d_1 = R_4$ in (b).

Now, equation $(3.32)_1$ becomes

$$\sum_{j:\mathbf{X}_j \in \mathbf{B}(\mathbf{X}_\mathrm{L}, R_5^*) \setminus \{\mathbf{X}_\mathrm{L}\}} \mathbf{K}(\mathbf{X}_j - \mathbf{X}_\mathrm{L}) = \mathbf{0}, \tag{3.50}$$

$$\gamma^* \overline{\nabla f(\mathbf{X}_i)} + \sum_{j:\mathbf{X}_j \in \mathbf{B}(\mathbf{X}_i, R_4^*) \setminus \{\mathbf{X}_i\}} \mathbf{K}(\mathbf{X}_j - \mathbf{X}_i) = \mathbf{0}, \quad i = 1, \dots, N, \tag{3.51}$$

respectively for the leader and for each follower. Here $\mathbf{K}$ contains only repulsion term:

$$\mathbf{K}(\mathbf{X}_j - \mathbf{X}_i) := -\omega_\mathrm{rep}^* \left(\frac{1}{||\mathbf{X}_j - \mathbf{X}_i||} - \frac{1}{R_4^*} \right) \frac{\mathbf{X}_j - \mathbf{X}_i}{||\mathbf{X}_j - \mathbf{X}_i||}.$$

For symmetry (3.50) is identically satisfied. Then in (3.51) $f(\mathbf{x}, t)$ is given by (3.46) and (3.47), so in a circular domain Ω we can write the same relation for all i. For example, in relation to Figure 3.1 (b), we have

$$\gamma^* \overline{\partial_y f(\mathbf{X}_i)} - \omega_\mathrm{rep}^* h_1(d_1^*) - \omega_\mathrm{rep}^* h_2(N, d_1^*) = 0, \tag{3.52}$$

in which $\omega_\mathrm{rep}^* h_1(d_1^*)$ represents the repulsion of the leader:

$$h_1(d_1^*) := \frac{1}{d_1^*} - \frac{1}{R_4^*},$$

$d_1^* = d_1/R$ is the nondimensional value of d_1, and $\omega_\mathrm{rep}^* h_2(N, d_1^*)$ is the possible repulsion of two adjoining followers according to (3.35) and Propositions 1–2, namely:

$$h_2(N, d_1^*) := \begin{cases} 0, & \text{if } \ N = 2, 3; \\ 2\left(\dfrac{1}{2 d_1^* \sin \frac{\pi}{N}} - \dfrac{1}{R_4^*} \right) \sin \dfrac{\pi}{N}, & \text{if } \ N = 4, 5 \wedge \frac{d_1^*}{R_4^*} < \frac{1}{2 \sin \frac{\pi}{N}}; \\ 0, & \text{if } \ N = 4, 5 \wedge \frac{1}{2 \sin \frac{\pi}{N}} \leq \frac{d_1^*}{R_4^*} \leq 1; \\ 2\left(\dfrac{1}{2 d_1^* \sin \frac{\pi}{N}} - \dfrac{1}{R_4^*} \right) \sin \dfrac{\pi}{N}, & \text{if } \ 6 \leq N \leq 12. \end{cases} \tag{3.53}$$

We remark that equation (3.52) is useful for two reasons. First, if we know an experimental value for the distance d_1^* we can obtain, fixing N, the ratio $\omega_\mathrm{rep}^*/\gamma^*$ as a function of d_1^*:

$$\frac{\omega_\mathrm{rep}^*}{\gamma^*} = \Theta_N(d_1^*) := \frac{\overline{\partial_y f(\mathbf{X}_i)}}{h_1(d_1^*) + h_2(N, d_1^*)}. \tag{3.54}$$

On the other hand, if Θ_N is invertible, we can express d_1^* as a function of ω_rep^* and γ^* that is the equilibrium distance for a N-rosette fixed the physical parameters.

Figure 3.3 represents a dimensional numerical plot of Θ_N for $N = 2, \dots, 12$. It shows that Θ_N is monotone with respect to d_1 for all N, so that relation (3.54) is invertible. To obtain this plot the value of $f(\mathbf{x})$ has been obtained numerically from (3.46) and (3.47) as previously described, fixing the same domain and the same parameters. Then the right hand side of (3.54), for a fixed N, is computed on a discretized distance d_1^*, as done to obtain Figure 3.2. The domain of the curves, again as in Figure 3.2, is given by (3.40) and (3.41); now it represents the admissible distances d_1 for a N-rosette, as N changes. Symbol “•” marks the origin of the curves. For $N = 2, 3$ the curves are overlapped (first line in the top) because for them $h_2 = 0$ (see (3.54) and (3.53)). For $N = 4, 5$ the curves coincide with the curve $N = 2, 3$ when h_2 becomes zero. This happens about for $d_1 > 14\ \mu$m for $N = 4$, and about for $d_1 > 17\ \mu$m for $N = 5$, as we can see in $(3.53)_{2,3}$. The curves corresponding to $N = 2, \ldots, 6$ have a vertical asymptote in $d_1 = R_4$ where the functions h_1 and h_2 in (3.54) become zero. Conversely, for $N = 7, \ldots, 12$, Θ_N is defined in $d_1 = R_4$. In particular for $N = 12$, due to (3.41), the curve is reduced to a single value in $d_1 = R_4$ given by $\Theta_{12}(R_4)$ (marker “•” on the right).

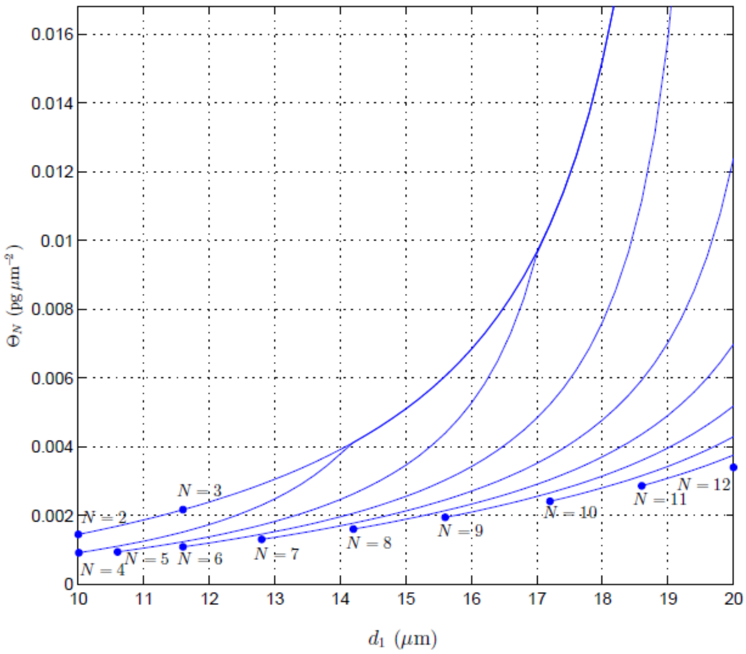

Figure 3.3. Dimensional numerical plot of Θ_N for $N = 2, \ldots, 12$, that demonstrates that this function is monotone with respect to d_1 and then invertible. The first two curves, for $N = 2, 3$, coincide (first line in the top). Then, from the top to the bottom, we have the curves related to $N = 5, \ldots, 11$. For $N = 4, 5$ the curves go to coincide with the first curve on the top about from $d_1 > 14\ \mu$m, and $d_1 > 17\ \mu$m respectively. For $N = 12$ the curve is reduced to a single value in $d_1 = R_4$. In practice fixing N and d_1 we have the value of Θ_N that provides in (3.54) the ratio of the parameters ω_{rep}^* and γ^*.

Typical values for N and d_1 (or d_1^*) to be used in (3.48), (3.49), and (3.54) will be given in Section 3.7.

Now, in order to test numerically a steady N-rosette, we perform a dynamical simulation of the model (3.26), as described in Section 3.5, with initial data given by a solution of the stationary system (3.32). With this type of simulations we verify that our numerical approximation scheme, discussed later in Section 3.5, is adequate to keep in time the stationary solutions of our interest.

In particular, we consider the spatial domain $\Omega = [0, 200] \times [0, 200]$ (μm^2) and the time interval $[0, 50]$ (h), that is a typical time range used in the experimental observations (Nechiporuk and Raible, 2008). Spatial and temporal discretizations are respectively $\Delta x = \Delta y = 0.2\,\mu$m and $\Delta t = 0.01$ h. Initial data are set as follows:

$$\mathbf{X}_i(0) = \mathbf{X}_{i0}, \tag{3.55}$$

$\mathbf{X}_{i0}$ being a 8-rosette centred in $\mathbf{X}_{\mathrm{L}}(0) = (100, 100)$ (μm), with follower-leader distance fixed at $d_1 = \frac{3}{2}R$ (see Section 3.7 and Figure 3.4 (a)),

$$\dot{\mathbf{X}}_i(0) = \mathbf{0}, \tag{3.56}$$

$$f(\mathbf{x}, 0) = f_0(\mathbf{x}), \tag{3.57}$$

with $f_0(\mathbf{x})$ solution of equation $(3.32)_3$ with homogeneous Neumann boundary condition in the same domain,

$$s(\mathbf{x}, 0) = 0, \tag{3.58}$$

according to $(3.32)_4$. The parameters used here are listed in Section 3.7 (see Tables 3.2–3.3).

We see that our numerical results demonstrate that, with good approximation, the initial configuration stays constant in time. Figure 3.4 shows evolution in space of the dimensional solution at four different time steps: $t = 0, 16, 32, 50$ h. Green colour marks the leader cell ($\varphi_i = 1$), and red colour marks a follower cell ($\varphi_i = 0$). Contour plot in the background is related to the FGF signal concentration, while the variable $s(\mathbf{x}, t)$ is not shown. Figure 3.5 shows the evolution in time of the maximum relative error on the position,

$$E_{\max,\mathrm{rel}}(t) := \frac{\max_{1 \le i \le N_{\mathrm{tot}}} \|\mathbf{X}_i(t) - \mathbf{X}_{i0}\|}{R}, \tag{3.59}$$

and the maximum velocity

$$V_{\max}(t) := \max_{1 \le i \le N_{\mathrm{tot}}} \left\| \dot{\mathbf{X}}_i(t) \right\|. \tag{3.60}$$

$E_{\max,\mathrm{rel}}$ suggests a deviation from the initial position in the order of 10^{-3} times cell radius, while $V_{\max}$ is in the order of 10^{-4} μm h^{-1}, which is very small with respect to the cell velocity during migration that is around 69 μm/h (Lecaudey et al, 2008). Plots in Figure 3.4 are obtained computing, in our numerical simulation, quantities (3.59) and (3.60) at each time step.

Now the stability of a N-rosette will be numerically investigated. Starting from the previous numerical test we perform a dynamical simulation perturbing the initial equilibrium configuration of the 8-rosette. Namely, each centre of a follower cell is translated of a ray vector whose magnitude and direction are random number in the interval $[0, 5]$ (μm) and $[0, 2\pi]$. Spatial domain and parameters are the same as in the previous simulation, while the time range is set to $[0, 60]$ (h).

Figure 3.6 shows the evolution in space of the dimensional solution at four time steps: $t = 0, 20, 40, 60$ h. Colour convention is the same as Figure 3.4. Figure 3.7

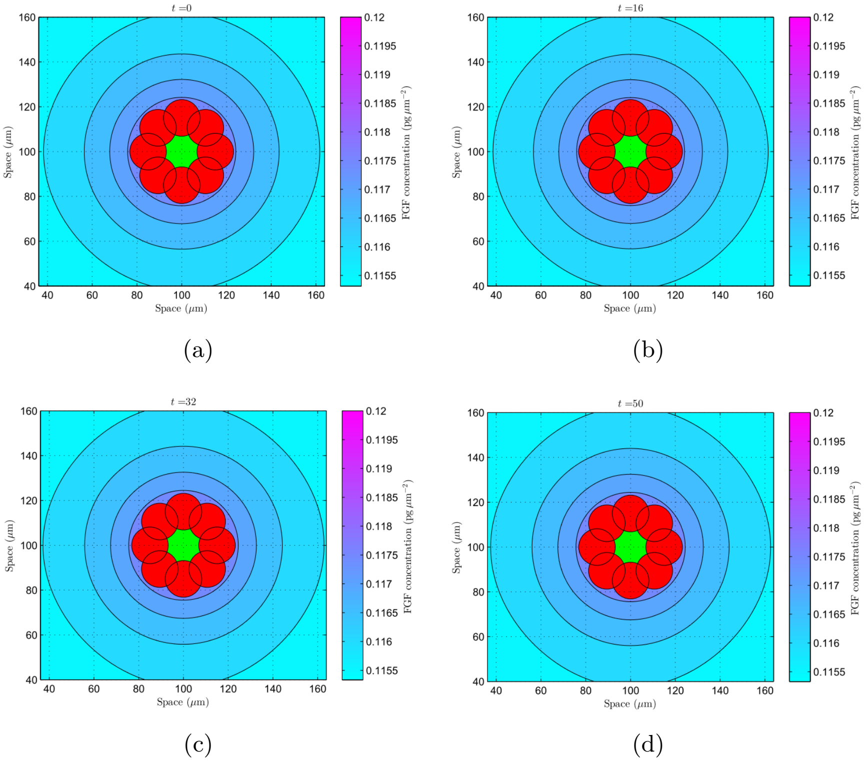

(a) (b)

(c) (d)

Figure 3.4. Numerical simulation of a steady solution given by a 8-rosette. (a)-(d) are related respectively to the dimensional plot at four different time steps: $t = 0, 16, 32, 50$ h. System (3.26) is solved as described in Section 3.5 in $\Omega = [0, 200] \times [0, 200]$ (μm^2) (plot refers only to a part of the domain) and in $[0, 50]$ (h). Spatial and temporal discretization is set to $\Delta x = \Delta y = 0.2$ μm and $\Delta t = 0.01$ h. Initial data are given by (3.55)–(3.58). The parameters used here are listed in Section 3.7. Green colour (●) marks the leader cell, red colour (●) a follower cell, contour plot in the background is the FGF signal concentration. Variable $s(\mathbf{x}, t)$ is not shown.

shows the evolution in time of the maximum relative error on the position $E_{\max,\mathrm{rel}}(t)$ and the maximum velocity $V_{\max}(t)$. $E_{\max,\mathrm{rel}}$ indicates a deviation from the initial position in the order of 10^{-1} times cell radius, and also $V_{\max}$ is small, being in the order of 10^{-2} μm h^{-1}. Our data demonstrate as the equilibrium configuration of our 8-rosette is stable. Furthermore, numerical simulations show that similar results can hold also if $N \neq 8$, for instance for $N = 5$ or 10 (data not shown). We note that in a physically reasonable time range we do not observe the asymptotic stability of the rosette structures, which is actually not expected, but just the simple stability.

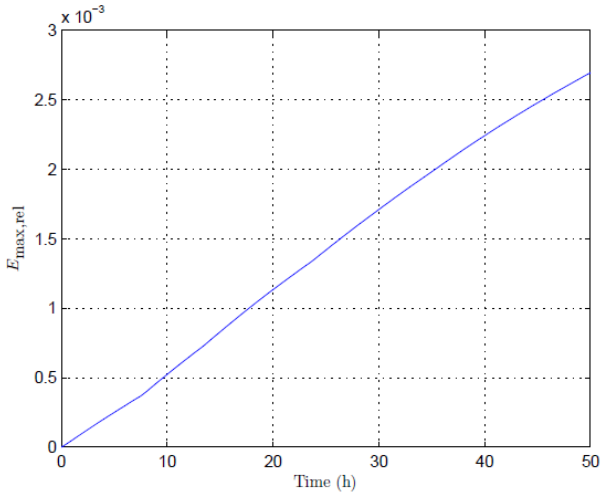

(a)

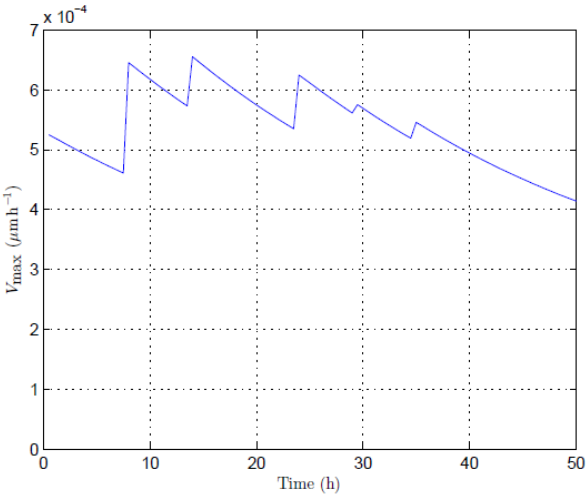

(b)

Figure 3.5. Numerical assessment of a steady 8-rosette. (a) Plot in time of the maximum relative error $E_{\mathrm{max,rel}}(t)$. (b) Plot of the maximum velocity $V_{\mathrm{max}}(t)$.

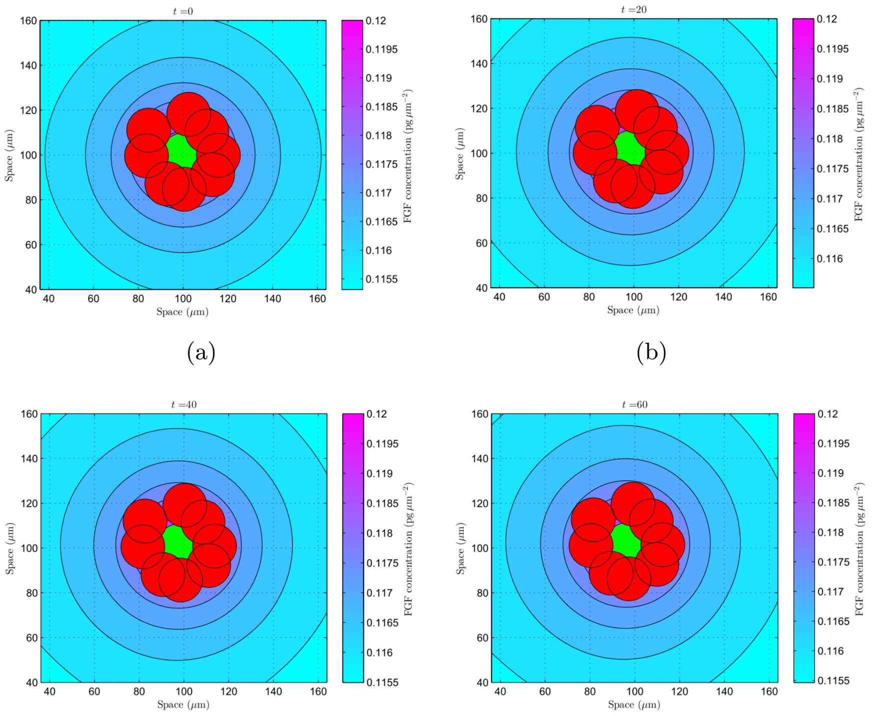

(a) (b)

(c) (d)

Figure 3.6. Numerical assessment of stability of a 8-rosette. (a)-(d) are related respectively to the dimensional plot at $t = 0, 20, 40, 60$ h. System (3.26) is solved as described in Section 3.5 in $\Omega = [0, 200] \times [0, 200]$ (μm^2) (plot refers only to a part of the domain) and in $[0, 50]$ (h). Spatial and temporal discretization is the same as in Figure (3.4). Initial data are given by a perturbation of positions (3.55), and by (3.56)–(3.58). The parameters used here are listed in Section 3.7. Green colour (●) marks the leader cell, red colour (●) a follower cell, contour plot in the background is the FGF signal concentration. Variable $s(\mathbf{x}, t)$ is not shown.

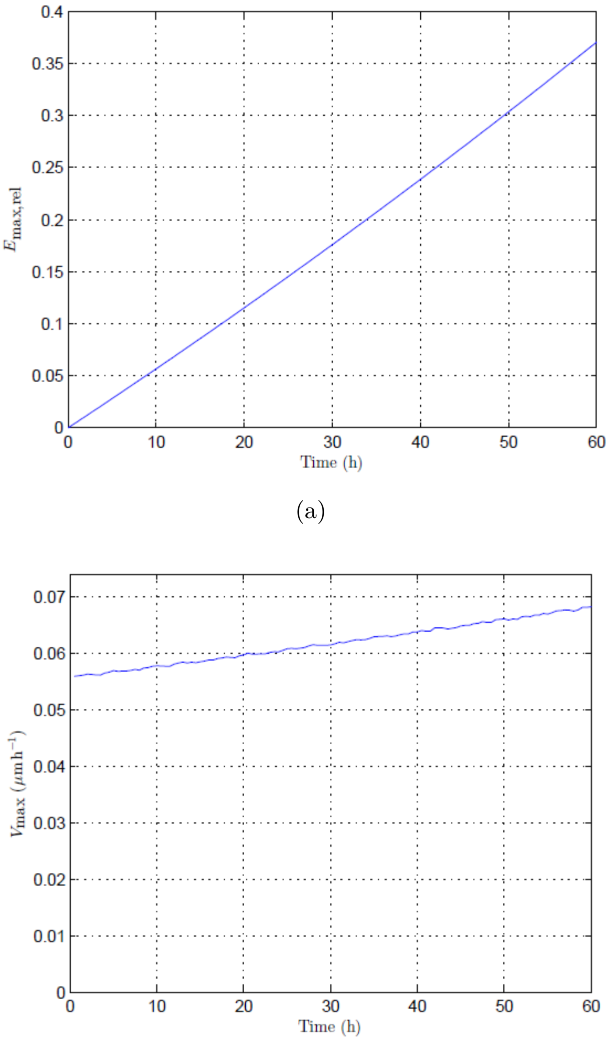

(a)

(b)

Figure 3.7. Numerical assessment of stability of a 8-rosette. (a) Plot in time of the maximum relative error $E_{\mathrm{max,rel}}(t)$. (b) Plot of the maximum velocity $V_{\mathrm{max}}(t)$.

3.5 Numerical approximation

In this section we discuss the numerical approximation scheme of system (3.26), that for convenience we rewrite below, reducing the equation for $\ddot{\mathbf{X}}$ to a first order system:

$$\left\{\begin{array}{ll}
\dot{\mathbf{Y}}_i & = \dfrac{\alpha^*}{W}\displaystyle\int_{\mathbf{B}(\mathbf{X}_i,\bar{R}^*)} \nabla s(\mathbf{x},t) w_i(\mathbf{x})\, d\mathbf{x} + \dfrac{\gamma^*(1-\varphi_i)}{W}\displaystyle\int_{\mathbf{B}(\mathbf{X}_i,\bar{R}^*)} \nabla f(\mathbf{x},t) w_i(\mathbf{x})\, d\mathbf{x} \\
 & +\dfrac{1}{\bar{N}_i}\displaystyle\sum_{j:\mathbf{X}_j\in\mathbf{B}(\mathbf{X}_i,R_1^*)\setminus\{\mathbf{X}_i\}} \mathbf{H}(\mathbf{Y}_j-\mathbf{Y}_i) + \displaystyle\sum_{j:\mathbf{X}_j\in\mathbf{B}(\mathbf{X}_i,R_5^*)\setminus\{\mathbf{X}_i\}} \mathbf{K}(\mathbf{X}_j-\mathbf{X}_i) \\
 & -\left[\mu_{\mathrm{F}}^* + (\mu_{\mathrm{L}}^*-\mu_{\mathrm{F}}^*)\varphi_i\right]\mathbf{Y}_i, \\
\dot{\mathbf{X}}_i & = \mathbf{Y}_i, \\
\varphi_i & = \left\{\begin{array}{ll}
0, \quad \text{if} & \dfrac{\delta^*}{W}\displaystyle\int_{\mathbf{B}(\mathbf{X}_i,\bar{R}^*)} s(\mathbf{x},t) w_i(\mathbf{x})\, d\mathbf{x} \\
 & -\dfrac{k_{\mathrm{F}}^* + (k_{\mathrm{L}}^*-k_{\mathrm{F}}^*)\varphi_i}{W}\displaystyle\int_{\mathbf{B}(\mathbf{X}_i,\bar{R}^*)} \dfrac{f(\mathbf{x},t)}{1+f(\mathbf{x},t)} w_i(\mathbf{x})\, d\mathbf{x} + \Gamma(n_i) \le 0, \\
1, & \text{otherwise},
\end{array}\right. \\
\partial_t f & = D^*\Delta f + \xi^* \displaystyle\sum_{j=1}^{N_{\mathrm{tot}}} \varphi_j \chi_{\mathbf{B}(\mathbf{X}_j,R_3^*)} - \eta^* f, \\
\partial_t s & = -\sigma^* s \displaystyle\sum_{j=1}^{N_{\mathrm{tot}}} \chi_{\mathbf{B}(\mathbf{X}_j,R_3^*)},
\end{array}\right. \tag{3.61}$$

where

$$w_i(\mathbf{x}) := \left\{\begin{array}{ll} 2\exp\left(-||\mathbf{x}-\mathbf{X}_i||^2\dfrac{\log 2}{\bar{R}^{*2}}\right) - 1, \quad \text{if} & ||\mathbf{x}-\mathbf{X}_i|| \le \bar{R}^*; \\ 0, & \text{otherwise}; \end{array}\right. \tag{3.62}$$

$$W := \int_{\mathbf{B}(\mathbf{X}_i,\bar{R}^*)} w_i(\mathbf{x})\, d\mathbf{x}, \tag{3.63}$$

$$\Gamma(n_i) := \frac{e^{n_i}}{e^{n_i}+\Gamma_0} - \frac{1}{1+\Gamma_0}, \tag{3.64}$$

$$n_i := \text{card}\left\{j : \mathbf{X}_j \in \mathring{\mathbf{B}}(\mathbf{X}_i,R_2^*)\setminus\{\mathbf{X}_i\}\right\}, \tag{3.65}$$

$$\bar{N}_i := \text{card}\left\{j : \mathbf{X}_j \in \mathbf{B}(\mathbf{X}_i,R_1^*)\right\}, \tag{3.66}$$

$$\mathbf{H}\left(\mathbf{Y}_j-\mathbf{Y}_i\right) := \left[\beta_{\mathrm{F}}^* + (\beta_{\mathrm{L}}^*-\beta_{\mathrm{F}}^*)\varphi_i\varphi_j\right] \frac{R_1^{*2}}{R_1^{*2}+||\mathbf{X}_j-\mathbf{X}_i||^2}(\mathbf{Y}_j-\mathbf{Y}_i), \tag{3.67}$$

and

$$\mathbf{K}(\mathbf{X}_j-\mathbf{X}_i) := \begin{cases} -\omega^*_{\text{rep}}\left(\dfrac{1}{||\mathbf{X}_j-\mathbf{X}_i||}-\dfrac{1}{R^*_4}\right)\dfrac{\mathbf{X}_j-\mathbf{X}_i}{||\mathbf{X}_j-\mathbf{X}_i||}, & \text{if} \quad ||\mathbf{X}_j-\mathbf{X}_i|| \le R^*_4; \\ \bar{\omega}^*_{\text{adh}}\left(||\mathbf{X}_j-\mathbf{X}_i||-R^*_4\right)\dfrac{\mathbf{X}_j-\mathbf{X}_i}{||\mathbf{X}_j-\mathbf{X}_i||}, & \text{if} \quad R^*_4 < ||\mathbf{X}_j-\mathbf{X}_i|| \le R^*_5; \end{cases} \tag{3.68}$$

with

$$\bar{\omega}^*_{\text{adh}} := \omega^*_{\text{adh,F}} + (\omega^*_{\text{adh,L}} - \omega^*_{\text{adh,F}})\varphi_i\varphi_j.$$

Initial and boundary conditions are

$$\mathbf{X}_i(0) = \mathbf{X}_{i0}; \quad \text{and} \quad \dot{\mathbf{X}}_i(0) = \mathbf{0}, \quad i = 1, \dots, N_{\text{tot}}, \tag{3.69}$$

$$\varphi_i(0) = 1, \quad i = 1, \dots, N_{\text{tot}}, \tag{3.70}$$

$$f(\mathbf{x}, 0) = 0; \quad \frac{\partial f}{\partial \mathbf{n}} = 0, \quad \text{on } \partial\Omega, \tag{3.71}$$

where Ω is the spatial domain, and finally

$$s(\mathbf{x}, 0) = s_0(\mathbf{x}), \tag{3.72}$$

as in (3.21)–(3.25).

The methods used in the numerical simulations employ a 2D finite difference scheme. We consider the spatial domain $\Omega = [a, b] \times [c, d]$ and the spatial steps Δx, Δy, such that $[a, b]$ is divided in $M = \frac{b-a}{\Delta x}$ intervals, and $[c, d]$ in $N = \frac{d-c}{\Delta y}$ intervals, with M, N integers. Then we introduce a Cartesian grid consisting of grid points (x_m, y_n), where $x_m = m\Delta x$ and $y_n = n\Delta y$. The same can be done for the time interval $[0, T]$, in this case if Δt is the time step, t_k will be the n-th temporal step, i.e. $t_k = k\Delta t$. With the notation $u^k_{m,n}$ we denote the approximation of a function $u(x, y, t)$ at the grid point (x_m, y_n, t_k).

We remind the basic tool in the finite difference schemes, i.e. the following possible approximations:

$$\frac{\partial u}{\partial x}(x_m, y_n, t_k) \approx \begin{cases} D^+_x u^k := \dfrac{u^k_{m+1,n} - u^k_{m,n}}{\Delta x}, \\ D^-_x u^k := \dfrac{u^k_{m,n} - u^k_{m-1,n}}{\Delta x}, \\ D^0_x u^k := \dfrac{u^k_{m+1,n} - u^k_{m-1,n}}{2\Delta x}. \end{cases} \tag{3.73}$$

Similarly can be done for the derivatives with respect to the other variables. Combining, for example, $(3.73)_{1,2}$ in the form $D^+_x D^-_x u^k$ or $D^-_x D^+_x u^k$ (and analogously for the variable y) we obtain the standard centred approximation for the second derivatives:

$$\begin{aligned} \frac{\partial^2 u}{\partial x^2}(x_m, y_n, t_k) &\approx D^2_x u^k := \frac{u^k_{m-1,n} - 2u^k_{m,n} + u^k_{m+1,n}}{\Delta x^2}, \\ \frac{\partial^2 u}{\partial y^2}(x_m, y_n, t_k) &\approx D^2_y u^k := \frac{u^k_{m,n-1} - 2u^k_{m,n} + u^k_{m,n+1}}{\Delta y^2}. \end{aligned} \tag{3.74}$$

While $(3.73)_{1,2}$ are a first order accurate approximation, $(3.73)_3$ and (3.74) are second order accurate.

We start to describe the approximation of the parabolic equation $(3.61)_4$. The right hand side is composed of the diffusion term, the source term, and the stiff degradation term $-\eta^* f$. In order to eliminate this last quantity we perform the classical exponential transformation

$$f(\mathbf{x}, t) = e^{-\eta^* t} u(\mathbf{x}, t), \tag{3.75}$$

which leads to the diffusion equation with source for $u(\mathbf{x}, t)$:

$$\partial_t u = D^* \Delta u + e^{\eta^* t} \xi^* \sum_{j=1}^{N_{\text{tot}}} \varphi_j \chi_{\mathbf{B}(\mathbf{X}_j, R_3^*)}, \tag{3.76}$$

with initial and boundary conditions

$$u(\mathbf{x}, 0) = 0; \quad \frac{\partial u}{\partial \mathbf{n}} = 0, \quad \text{on } \partial\Omega. \tag{3.77}$$

Now, for this equation we apply a central difference scheme in space, i.e. the 5-point stencil for the Laplacian, and the parabolic Crank-Nicolson scheme in time (Morton and Mayers, 2005; LeVeque, 2007). The source term in taken in explicit, in the form

$$\xi^* \sum_{j=1}^{N_{\text{tot}}} \varphi_j^k \chi_{\mathbf{B}(\mathbf{X}_j^k, R_3^*)},$$

where the discretized characteristic function is

$$\chi_{\mathbf{B}(\mathbf{X}_j^k, R_3^*)} = \begin{cases} 1, & \text{if} \quad (x_m, y_n) \in \mathbf{B}(\mathbf{X}_j^k, R_3^*); \\ 0, & \qquad \text{otherwise.} \end{cases} \tag{3.78}$$

The numerical scheme can be written as

$$\begin{aligned} \frac{u_{m,n}^{k+1} - u_{m,n}^k}{\Delta t} &= \frac{D^*}{2} \left(D_x^2 u^{k+1} + D_y^2 u^{k+1} \right) + \frac{D^*}{2} \left(D_x^2 u^k + D_y^2 u^k \right) \\ &+ \frac{1}{2} e^{\eta^* (k+1) \Delta t} \xi^* \sum_{j=1}^{N_{\text{tot}}} \varphi_j^k \chi_{\mathbf{B}(\mathbf{X}_j^k, R_3^*)} \\ &+ \frac{1}{2} e^{\eta^* k \Delta t} \xi^* \sum_{j=1}^{N_{\text{tot}}} \varphi_j^k \chi_{\mathbf{B}(\mathbf{X}_j^k, R_3^*)}, \end{aligned}$$

where the second finite differences $D_x^2 u$ and $D_y^2 u$ are given by (3.74). For Neumann boundary condition (3.77) we use a second order accurate onesided approximation, namely:

$$\begin{aligned}
&\frac{\partial u^k}{\partial x}(x_0,y_n)\approx\frac{1}{2\Delta x}\left(-3u^k_{0,n}+4u^k_{1,n}-u^k_{2,n}\right)=0, && n=1,\dots,N-1,\\
&\frac{\partial u^k}{\partial x}(x_M,y_n)\approx\frac{1}{2\Delta x}\left(3u^k_{M,n}-4u^k_{M-1,n}+u^k_{M-2,n}\right)=0, && n=1,\dots,N-1,\\
&\frac{\partial u^k}{\partial y}(x_m,y_0)\approx\frac{1}{2\Delta y}\left(-3u^k_{m,0}+4u^k_{m,1}-u^k_{m,2}\right)=0, && m=1,\dots,M-1,\\
&\frac{\partial u^k}{\partial x}(x_m,y_N)\approx\frac{1}{2\Delta y}\left(3u^k_{m,N}-4u^k_{m,N-1}+u^k_{m,N-2}\right)=0, && m=1,\dots,M-1.
\end{aligned} \tag{3.79}$$

In practice, in the numerical simulations we will choose the domain size sufficiently large that over the time period of interest have a negligible impact on the solution.

In relation to the stationary form of $(3.61)_4$

$$D^*\Delta f=\eta^* f-\xi^*\chi_{\mathbf{B}(\mathbf{X}_\mathrm{L},R^*_3)}, \tag{3.80}$$

$$\frac{\partial f}{\partial \mathbf{n}}=0,\quad \text{on } \partial\Omega, \tag{3.81}$$

used in Section 3.4 (eqs. (3.46)–(3.47)) to discuss the steady states of the model, we adopt the central scheme:

$$D^*\left(D^2_x f+D^2_y f\right)=\eta^* f_{m,n}-\xi^*\chi_{\mathbf{B}(\mathbf{X}_\mathrm{L},R^*_3)}, \tag{3.82}$$

in which $D^2_x u$ and $D^2_y u$ are defined by (3.74) and $\chi_{\mathbf{B}(\mathbf{X}_\mathrm{L},R^*_3)}$ is given by (3.78), where here $\mathbf{X}_\mathrm{L}$ is the fixed centre of the leader cell, the only one that produces FGF signal. Then boundary condition (3.81) is treated using (3.79) for $f_{m,n}$.

For equation $(3.61)_5$ we put the right hand side explicitly in time, and we write the numerical scheme

$$\frac{s^{k+1}_{m,n}-s^k_{m,n}}{\Delta t}=-\sigma^* s^k_{m,n}\sum_{j=1}^{N_\mathrm{tot}}\chi_{\mathbf{B}(\mathbf{X}^k_j,R^*_3)}, \tag{3.83}$$

where the characteristic function is computed as in (3.78).

Now we consider equation $(3.61)_1$. For it we apply a one step IMEX method, putting totally implicit in time the term containing $\mathbf{H}\left(\mathbf{Y}_j-\mathbf{Y}_i\right)$ and the term $-\left[\mu^*_\mathrm{F}+(\mu^*_\mathrm{L}-\mu^*_\mathrm{F})\varphi_i\right]\mathbf{Y}_i$ at the right hand side, while totally explicit the other terms (Hundsdorfer and Verwer, 2003). The two-dimensional weighted integrals in $(3.61)_1$ can be computed by a 2D quadrature formula, which due to the truncated Gaussian weight function $w_i(\mathbf{x})$ given in (3.62), is reduced to a sum of the discretized integrand function on the grid points belonging to the ball $\mathbf{B}(\mathbf{X}_i,\bar{R}^*)$. For a integrand function $g(\mathbf{x},t)$ holds

$$\frac{1}{W}\int_{\mathbf{B}(\mathbf{X}_i,\bar{R}^*)} g(\mathbf{x},t)w_i(\mathbf{x})\,d\mathbf{x}\approx\frac{1}{\mathcal{W}}\sum_{m,n\text{ s.t. }(x_m,y_n)\in\mathbf{B}(\mathbf{X}^k_i,\bar{R}^*)} g^k_{m,n}(w_i)^{(k)}_{m,n}, \tag{3.84}$$

where $(w_i)^{(k)}$ is the weight function centred in $\mathbf{X}^k$ at time step t_k, and $\mathcal{W}$ is defined by

$$\mathcal{W} := \sum_{m,n \text{ s.t. } (x_m,y_n)\in\mathbf{B}(\mathbf{X}_i^k,\bar{R}^*)} (w_i)^{(k)}_{m,n}. \tag{3.85}$$

The gradients in equation $(3.61)_1$ are approximated with the second order difference:

$$\nabla g(x_m, y_n, t_k) \approx \nabla_{m,n} g^k, \tag{3.86}$$

where, from $(3.73)_1$,

$$\nabla_{m,n} g^k := \left(\frac{g^k_{m+1,n} - g^k_{m,n-1}}{2\Delta x}, \frac{g^k_{m,n+1} - g^k_{m,n-1}}{2\Delta y} \right). \tag{3.87}$$

Equation $(3.61)_2$ is then solved with the forward Euler method. The scheme for equations $(3.61)_{1,2}$ can be summarized as

$$\begin{cases} \dfrac{\mathbf{Y}_i^{k+1} - \mathbf{Y}_i^k}{\Delta t} & = \dfrac{\alpha^*}{\mathcal{W}} \displaystyle\sum_{m,n \text{ s.t. } (x_m,y_n)\in\mathbf{B}(\mathbf{X}_i^k,\bar{R}^*)} \left(\nabla_{m,n} s^k\right) (w_i)^{(k)}_{m,n} \\ & + \dfrac{\gamma^*(1-\varphi_i^k)}{\mathcal{W}} \displaystyle\sum_{m,n \text{ s.t. } (x_m,y_n)\in\mathbf{B}(\mathbf{X}_i^k,\bar{R}^*)} \left(\nabla_{m,n} f^k\right) (w_i)^{(k)}_{m,n} \\ & + \dfrac{1}{\bar{N}_i} \displaystyle\sum_{j:\mathbf{X}_j^k\in\mathbf{B}(\mathbf{X}_i^k,R_1^*)\setminus\left\{\mathbf{X}_i^k\right\}} \mathbf{H}(\mathbf{Y}_j^{k+1} - \mathbf{Y}_i^{k+1}) \\ & + \displaystyle\sum_{j:\mathbf{X}_j^k\in\mathbf{B}(\mathbf{X}_i^k,R_5^*)\setminus\left\{\mathbf{X}_i^k\right\}} \mathbf{K}(\mathbf{X}_j^k - \mathbf{X}_i^k) - \left[\mu_{\mathrm{F}}^* + (\mu_{\mathrm{L}}^* - \mu_{\mathrm{F}}^*)\varphi_i\right] \mathbf{Y}_i^{k+1}, \\ \dfrac{\mathbf{X}_i^{k+1} - \mathbf{X}_i^k}{\Delta t} & = \mathbf{Y}_i^k, \end{cases} \tag{3.88}$$

in which

$$\bar{N}_i := \mathrm{card}\left\{ j : \mathbf{X}_j^k \in \mathbf{B}(\mathbf{X}_i^k, R_1^*) \right\}, \tag{3.89}$$

$$\mathbf{H}\left(\mathbf{Y}_j^k - \mathbf{Y}_i^k\right) := \left[\beta_{\mathrm{F}}^* + (\beta_{\mathrm{L}}^* - \beta_{\mathrm{F}}^*)\varphi_i^k\varphi_j^k\right] \frac{R_1^{*2}}{R_1^{*2} + ||\mathbf{X}_j^k - \mathbf{X}_i^k||^2} (\mathbf{Y}_j^k - \mathbf{Y}_i^k), \tag{3.90}$$

and

$$\mathbf{K}(\mathbf{X}_j^k - \mathbf{X}_i^k) := \begin{cases} -\omega_{\mathrm{rep}}^* \left(\dfrac{1}{||\mathbf{X}_j^k - \mathbf{X}_i^k||} - \dfrac{1}{R_4^*} \right) \dfrac{\mathbf{X}_j^k - \mathbf{X}_i^k}{||\mathbf{X}_j^k - \mathbf{X}_i^k||}, & \text{if } ||\mathbf{X}_j^k - \mathbf{X}_i^k|| \leq R_4^*; \\ \bar{\omega}_{\mathrm{adh}}^* \left(||\mathbf{X}_j^k - \mathbf{X}_i^k|| - R_4^* \right) \dfrac{\mathbf{X}_j^k - \mathbf{X}_i^k}{||\mathbf{X}_j^k - \mathbf{X}_i^k||}, & \text{if } R_4^* < ||\mathbf{X}_j^k - \mathbf{X}_i^k|| \leq R_5^*; \end{cases} \tag{3.91}$$

with

$$\bar{\omega}^*_{\mathrm{adh}} := \omega^*_{\mathrm{adh,F}} + (\omega^*_{\mathrm{adh,L}} - \omega^*_{\mathrm{adh,F}})\varphi_i^k \varphi_j^k.$$

Finally, the variable $\varphi_i(t)$ is computed putting in explicit the right hand side of $(3.61)_3$ and using the above discretizations:

$$\varphi_i^{k+1} = \begin{cases} 0, \quad \text{if} \ \dfrac{\delta^*}{\mathcal{W}} \displaystyle\sum_{m,n \text{ s.t. } (x_m,y_n)\in \mathbf{B}(\mathbf{X}_i^k,\bar{R}^*)} s^k_{m,n}(w_i)^{(k)}_{m,n} \\[2ex] \qquad -\dfrac{k^*_{\mathrm{F}} + (k^*_{\mathrm{L}} - k^*_{\mathrm{F}})\varphi_i^k}{\mathcal{W}} \displaystyle\sum_{m,n \text{ s.t. } (x_m,y_n)\in \mathbf{B}(\mathbf{X}_i^k,\bar{R}^*)} \dfrac{f^k_{m,n}}{1+f^k_{m,n}}(w_i)^{(k)}_{m,n} \\[2ex] \qquad +\Gamma(n_i^{(k)}) \leq 0, \\[2ex] 1, \qquad \text{otherwise}, \end{cases} \tag{3.92}$$

where $n_i^{(k)}$ is given by (3.65) at k-th time step, that is

$$n_i^{(k)} := \mathrm{card}\left\{ j : \mathbf{X}_j^k \in \mathring{\mathbf{B}}(\mathbf{X}_i^k, R_2^*) \setminus \left\{\mathbf{X}_i^k\right\}\right\}. \tag{3.93}$$

About the spatial and temporal step, in the numerical simulations we chose $\Delta x = \Delta y$ and, since for short time the value of variable $u(\mathbf{x},t)$ in (3.76) is near to zero and the forcing term is discontinuous, we need to stabilize the numerical scheme for few time steps using the standard parabolic CFL condition $\Delta t \sim \frac{\Delta x^2}{D^*}$ (Morton and Mayers, 2005). In practice, after the first time steps, we were able to change the CFL condition and to adopt the more favorable restriction $\Delta t \sim \Delta x$.

Let us summarize, in the following system, the foregoing considerations concerning the time discretization, putting in blue (●) the time explicit terms, in red (●) those taken in implicit, and in green (●) the terms for which we have used the Cranck-

Nicolson scheme in time:

$$\left\{\begin{aligned}
\dot{\mathbf{Y}}_i &= \frac{\alpha^*}{W}\int_{\mathbf{B}(\mathbf{X}_i,\bar{R}^*)} \nabla s(\mathbf{x},t)w_i(\mathbf{x})\,d\mathbf{x} + \frac{\gamma^*(1-\varphi_i)}{W}\int_{\mathbf{B}(\mathbf{X}_i,\bar{R}^*)} \nabla f(\mathbf{x},t)w_i(\mathbf{x})\,d\mathbf{x}\\
&\quad +\frac{1}{\bar{N}_i}\sum_{j:\mathbf{X}_j\in\mathbf{B}(\mathbf{X}_i,R_1^*)\setminus\{\mathbf{X}_i\}} \mathbf{H}(\mathbf{Y}_j-\mathbf{Y}_i)+\sum_{j:\mathbf{X}_j\in\mathbf{B}(\mathbf{X}_i,R_5^*)\setminus\{\mathbf{X}_i\}} \mathbf{K}(\mathbf{X}_j-\mathbf{X}_i)\\
&\quad -[\mu_{\mathrm{F}}^*+(\mu_{\mathrm{L}}^*-\mu_{\mathrm{F}}^*)\varphi_i]\,\mathbf{Y}_i,\\
\dot{\mathbf{X}}_i &= \mathbf{Y}_i,\\
\varphi_i &= \begin{cases} 0, & \text{if } \dfrac{\delta^*}{W}\displaystyle\int_{\mathbf{B}(\mathbf{X}_i,\bar{R}^*)} s(\mathbf{x},t)w_i(\mathbf{x})\,d\mathbf{x} \\ & \quad -\dfrac{k_{\mathrm{F}}^*+(k_{\mathrm{L}}^*-k_{\mathrm{F}}^*)\varphi_i}{W}\displaystyle\int_{\mathbf{B}(\mathbf{X}_i,\bar{R}^*)} \frac{f(\mathbf{x},t)}{1+f(\mathbf{x},t)}w_i(\mathbf{x})\,d\mathbf{x}+\Gamma(n_i)\le 0,\\ 1, & \text{otherwise,}\end{cases}\\
f &= e^{-\eta^* t}u, \quad \text{where} \quad \partial_t u = D^*\Delta u + e^{\eta^* t}\xi^*\sum_{j=1}^{N_{\mathrm{tot}}}\varphi_j\chi_{\mathbf{B}(\mathbf{X}_j,R_3^*)},\\
\partial_t s &= -\sigma^* s\sum_{j=1}^{N_{\mathrm{tot}}}\chi_{\mathbf{B}(\mathbf{X}_j,R_3^*)},
\end{aligned}\right. \tag{3.94}$$

3.6 Numerical tests

Simulation 1

Now we simulate the zebrafish lateral line growth in a two-dimensional space, during a dimensional time range of 20 h. Using the numerical method proposed in Section 3.5 we solve system (3.26) in a domain $\Omega = [0, 5000] \times [0, 1240]$ ($\mu\mathrm{m}^2$), with a spatial and temporal discretization given respectively by $\Delta x = \Delta y = 5\,\mu\mathrm{m}$ and $\Delta t = 0.001$ h. Parameters values used here are listed in Section 3.7 (Tables 3.2–3.3). Initial and boundary conditions are given by (3.17)–(3.23). In particular, as initial datum $\mathbf{X}(0)$, we set 90 cells equally distributed in the stripe $[600, 1180] \times [600, 640]$ ($\mu\mathrm{m}^2$) at a distance between their centres of 17 μm, and then randomized around their position with radius in the range $[0, 3]$ (μm) and angles in $[0, 2\pi]$ (Figure 3.8 (a)). As initial condition $s(\mathbf{x}, 0)$ in equation (3.22) we fix $c_1 = 838$ μm (the inflection point of the hyperbolic tangent is about at the middle of the primordium), $c_2 = 200$ μm, and $[\bar{a}, \bar{b}] = [600, 5000]$ (μm). Then in (3.23) and (3.25) we choose $l = 20$ μm and $\varepsilon = 10$ μm. The initial datum for SDF-1a is consistent with observations in Ghysen and Chaudière (2004), which describe a narrow stripe, approximately three cells wide.

Figures 3.8, 3.9, 3.10 show the numerical simulations of the lateral line evolution as described above at different time steps. As usual, green colour marks leader cells ($\varphi_i = 1$), and red colour the followers ($\varphi_i = 0$). Contour plot in the background is related to the FGF signal concentration, while 1D-plots in the upper panels refer to a longitudinal section in the graph of $s(\mathbf{x}, t)$, through the middle of the initial strip of chemoattractant.

In our simulation we can observe, in the first few hours after migration starts, the leader-to-follower transition of some cells in the trailing region of the primordium, up to about $t = 6.5$ h when a first rosette starts detaching (Figure 3.8 (b)). This is consistent with the experimental results presented in the supplementary material in Nechiporuk and Raible (2008) and Lecaudey et al (2008), that show a time of about 3–6 h for the first rosette separation. Figure 3.9 (a) shows the formation of a second rosette in the new trailing region, meanwhile in the first rosette the lateral inhibition process is completed leaving two leader cells. Then in the next time steps, until about $t = 19$ h, we observe the detachment of the other two rosettes (Figures 3.9 (b) 3.10). We note that the somewhat rectangular shape of the rosettes is due to the initial position and to the large cell friction, and it should assume a more circular look on a larger time interval, because of the radial symmetry of the FGF sources. More circular shapes have been obtained in Simulation 2 below (Figures 3.12–3.14).

In Figure 3.11 we have plotted migration velocity of the tip of the primordium versus time for 6 hours. Taking into account the velocity of 69 μm/h given in Lecaudey et al (2008), we observe a good agreement with our results. Moreover we observe a decrease in velocity in correspondence to the formation of the first rosette. This is substantially comparable with the velocity plot shown by Figure 1.8 in Chapter 1.

Another interesting behaviour of the migrating group of cells, that come out from our simulations, can be inferred considering the evolution in time of the SDF-1a stripe shown in the upper panels of Figures 3.8–3.10. Although we have considered a nonuniform initial distribution of chemoattractant like in (3.22), it appears somewhat constant, except an initial gradient along the primordium. During the motion, due to the contact degradation of the SDF-1a, the gradient of the chemoattractant becomes about zero along the trailing region of the primordium, while a new gradient is generated by the tip cells from the almost constant chemokine stripe. This feature, known as *self-generation* of chemokine gradient, has been hypothesized for the cell migration in embryos from the requirement of long-range gradients (Dambly-Chaudiére et al, 2007; Scherber et al, 2012). The first *in vivo* proof for this hypothesis has been recently shown in Donà et al (2013), exactly in relation to the zebrafish posterior lateral line. In the parameters discussion in Section 3.7 we will show that the total cell migration can be ensured even with an initial constant chemokine distribution along the x-axis.

Finally, from the numerical simulations, we observe a flocking behaviour in cell migration, according to the results shown in Cucker and Smale (2007a) and Ha and Liu (2009) for term (3.6), although in our model other effects are involved, as chemotaxis and adhesion-repulsion terms. We recall that in Ha and Liu (2009) flocking behaviour occurs unconditionally when the power of the denominator in (3.8) is less or equal to 1/2, and conditionally if this power is greater than 1/2. Taking into account our power in equation (3.8) and our initial data in (3.17) we would be in the case of conditional flocking if we used the original Cucker-Smale model, and although we consider a truncated sensing domain and we have many additional effects, we observe consistent results.

Simulation 2

In this test we simulate 120 cells of the zebrafish lateral line in the domain $\Omega = [0, 5000] \times [0, 1240]$ (μm^2). At $t = 0$ the cells are randomly assigned along the stripe $[600, 1680] \times [600, 640]$ (μm^2) with a distance between their centre randomly chosen in the range [17,20] μm (Figure 3.12 (a)). Numerical methods, spatial and temporal discretization are as in Simulation 1. Parameters values are chosen according to Tables 3.2–3.3, as described in Section 3.7. Initial and boundary conditions for $\dot{\mathbf{X}}(t)$, $\varphi(t)$, $f(\mathbf{x}, t)$ and $s(\mathbf{x}, t)$ and are give by $(3.17)_2$–(3.23). The parameters in equations (3.22), (3.23) and (3.25), relative to $s(\mathbf{x}, 0)$, are chosen as in Simulation 1.

Figures 3.12–3.14 show the numerical simulations on a total time of observation of 9.5 h. As usual, leader cells are in green, follower cells in red. Contour plot in the bottom panel is related to the FGF signal concentration, while 1D-plots in the upper panel refer to a longitudinal section in the graph of $s(\mathbf{x}, t)$, through the middle of the strip of chemoattractant.

The proposed plots display, in the first hours after the migration starts, the degradation of the chemotactic signal due to the migrating primordium. At the same time the leader-to-follower transition occurring in the trailing region. At about $t = 2$ h a rosette begins to take shape in the tail of the primordium (Figure 3.12 (b)), and it is deposited at about $t = 5.5$ h (Figure 3.13 (a)). At $t = 7.5$ h a second proto-neuromast is visible in the trailing region (Figure 3.13 (b)), and finally at $t = 9.5$ h two rosette have been deposited during the migration of the primordium (Figure 3.14). As in Simulation 1, from the upper panels related to SDF-1a stripe, we observe the self-generation of chemokine gradient by the primordium during the collective migration.

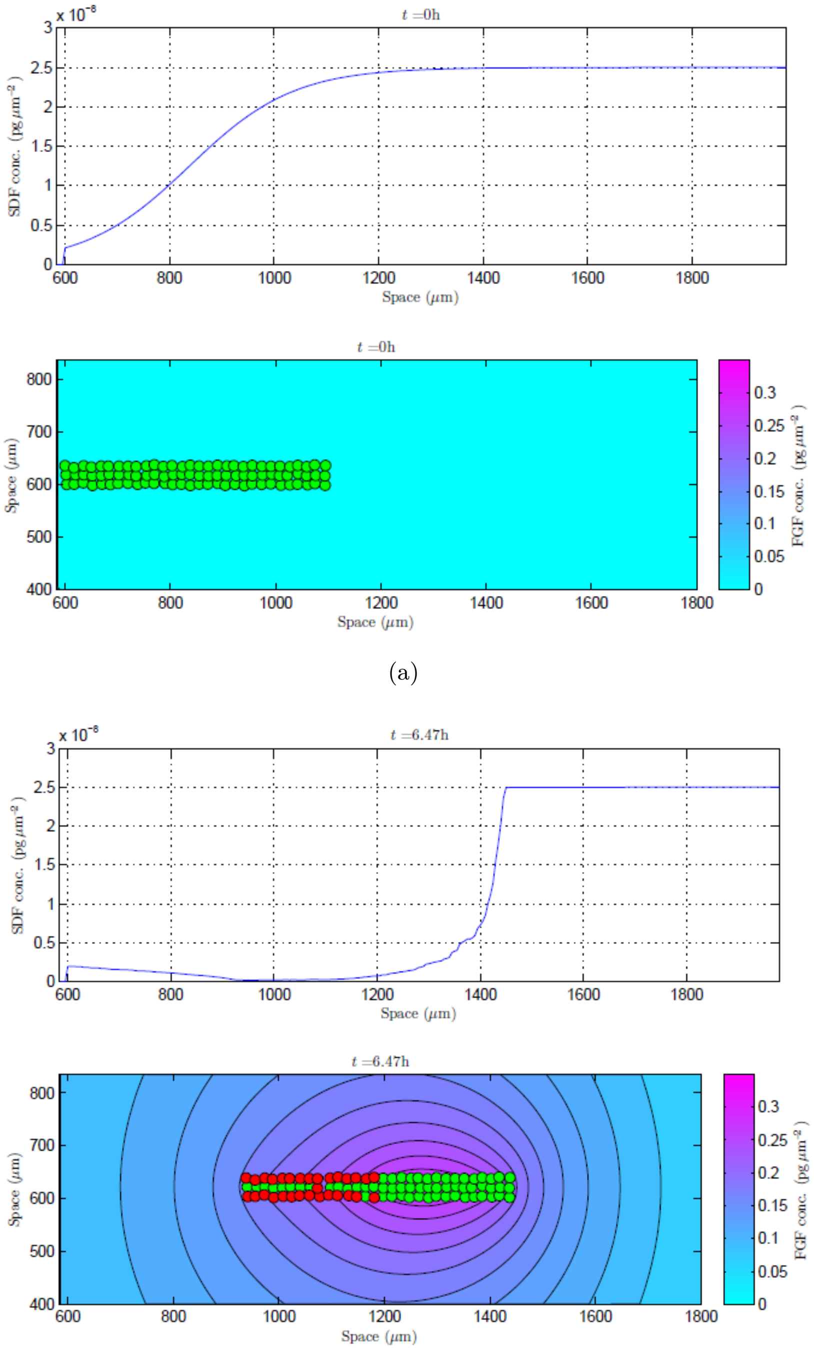

(a)

(b)

Figure 3.8. **Simulation 1**. Numerical simulation of the lateral line growth at five different time steps: $t = 0, 6.47$ h, next three time steps $t = 10.15, 15.64, 19$ h are plotted in Figures 3.9–3.10. System (3.26) is solved in the domain $\Omega = [0, 5000] \times [0, 1240]$ (μm^2) (plot shows only a part of the domain), with a spatial and temporal discretization given respectively by $\Delta x = \Delta y = 5\,\mu$m and $\Delta t = 0.001$ h. Parameters values used here are listed in Section 3.7. Initial and boundary conditions are given by (3.17), (3.18), (3.19), and (3.21). In particular, about the initial condition $s(\mathbf{x}, 0)$, in equation (3.22) we have fixed $c_1 = 838$ μm, $c_2 = 200$ μm, and $[\bar{a}, \bar{b}] = [600, 5000]$ (μm). Then in (3.23) and (3.25) we have chosen $l = 20$ μm and $\varepsilon = 10$ μm. Green colour (●) is for leader cells, red colour (●) for the followers. The variable $s(\mathbf{x}, t)$ is shown in a 1D-plot, only along a longitudinal section through the middle of the initial strip of chemoattractant. Contour plot in the background indicates the FGF concentration.

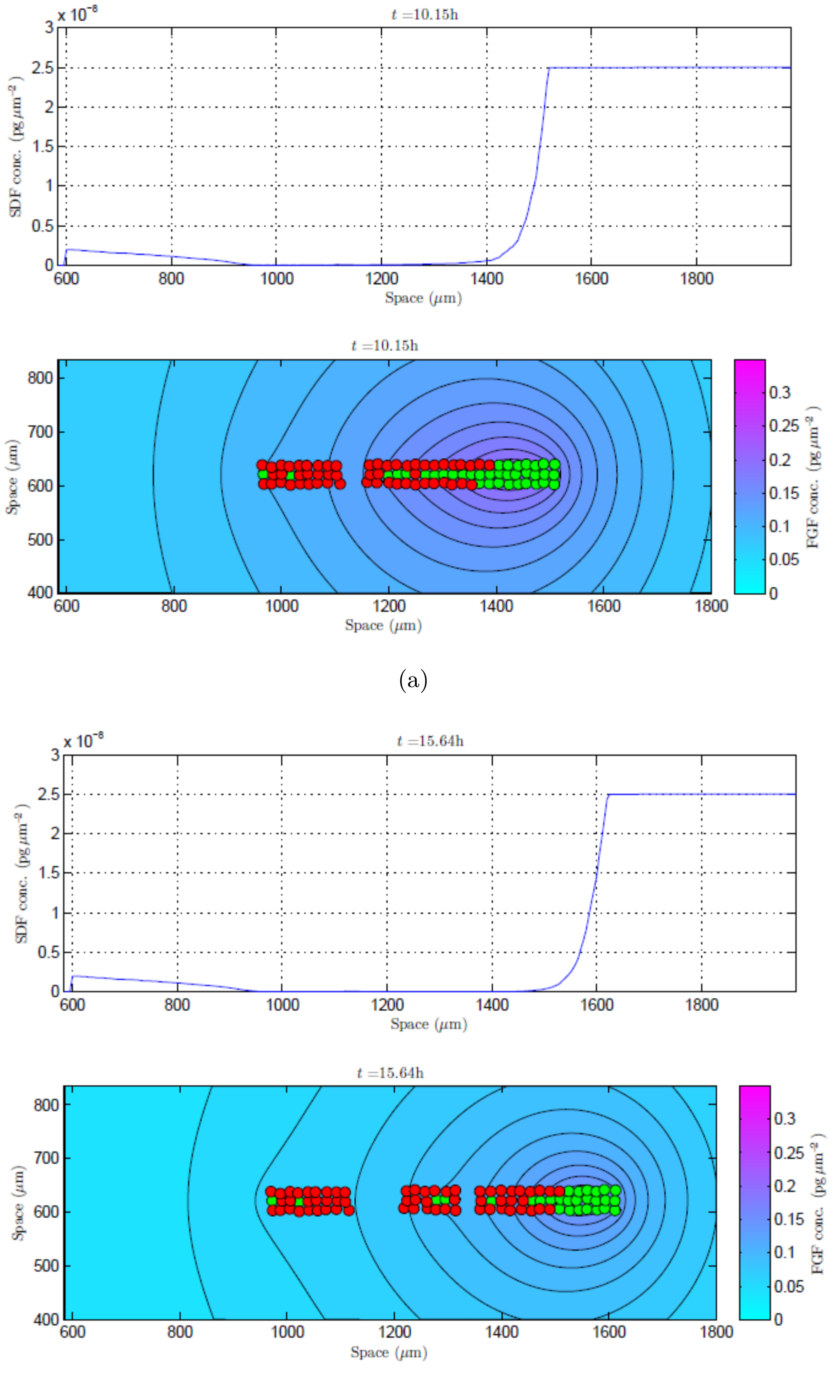

(a)

(b)

Figure 3.9. Continuation of Figure 3.8. Numerical simulation of the lateral line growth at time steps: $t = 10.15, 15.64$ h.

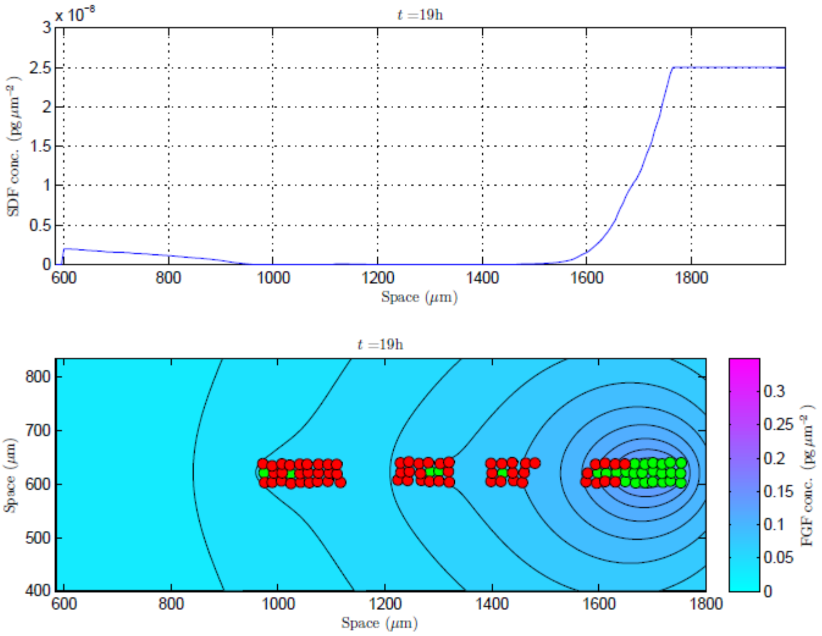

Figure 3.10. Continuation of Figure 3.9. Numerical simulation of the lateral line growth at time step: $t = 19$ h.

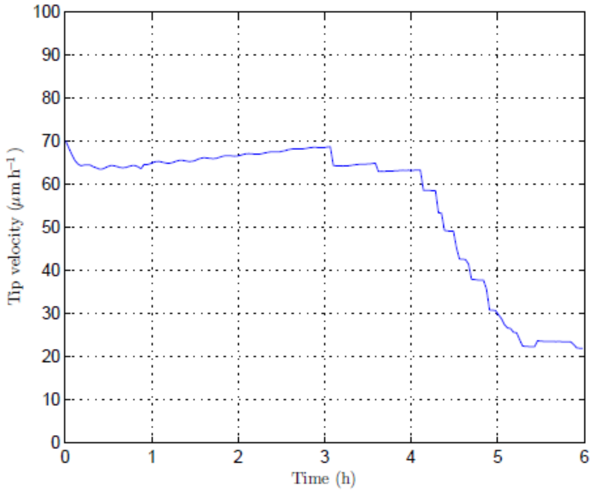

Figure 3.11. Numerical dimensional plot of the velocity of tip of the primordium during migration versus time.

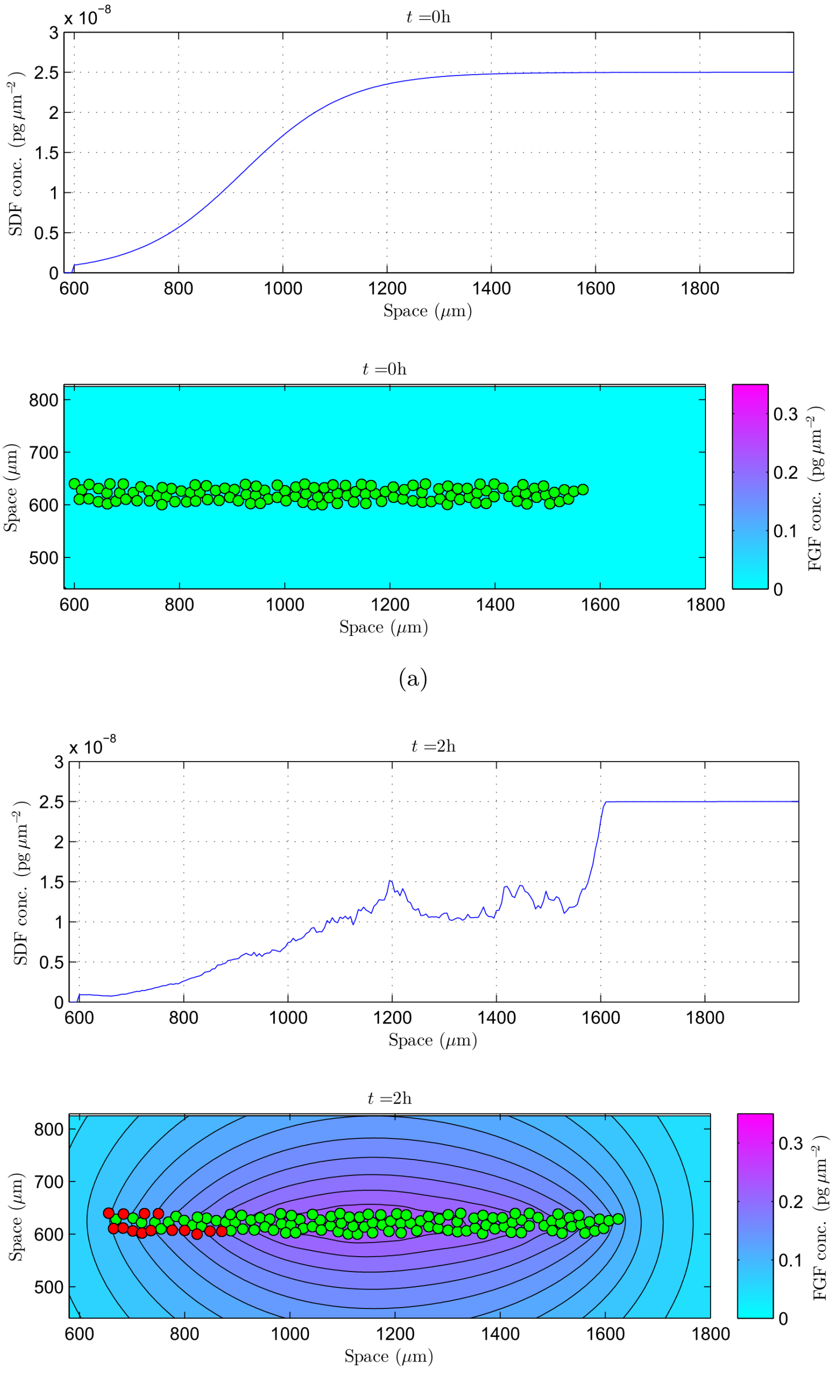

(a)

(b)

Figure 3.12. **Simulation 2**. Numerical simulation of the lateral line growth at five different time steps: $t = 0, 2$ h, next three time steps $t = 5.5, 7.5, 9.5$ h are plotted in Figures 3.13–3.14. System (3.26) is solved in the domain $\Omega = [0, 5000] \times [0, 1240]$ (μm^2) (plot shows only a part of the domain), with a spatial and temporal discretization given respectively by $\Delta x = \Delta y = 5\,\mu$m and $\Delta t = 0.001$ h. Parameters values used here are listed in Section 3.7. Initial and boundary conditions are given by (3.17)–(3.19), and (3.21). The initial condition $s(\mathbf{x}, 0)$, in equation (3.22) we have fixed $c_1 = 838$ μm, $c_2 = 200$ μm, and $[\bar{a}, \bar{b}] = [600, 5000]$ (μm). Then in (3.23) and (3.25) we have chosen $l = 20$ μm and $\varepsilon = 10$ μm. Green colour (●) is for leader cells, red colour (●) for the followers. The variable $s(\mathbf{x}, t)$ is shown in the upper panel in a 1D-plot, only along a longitudinal section through the middle of the strip of SDF-1a. Contour plot in the bottom panel indicates the FGF concentration.

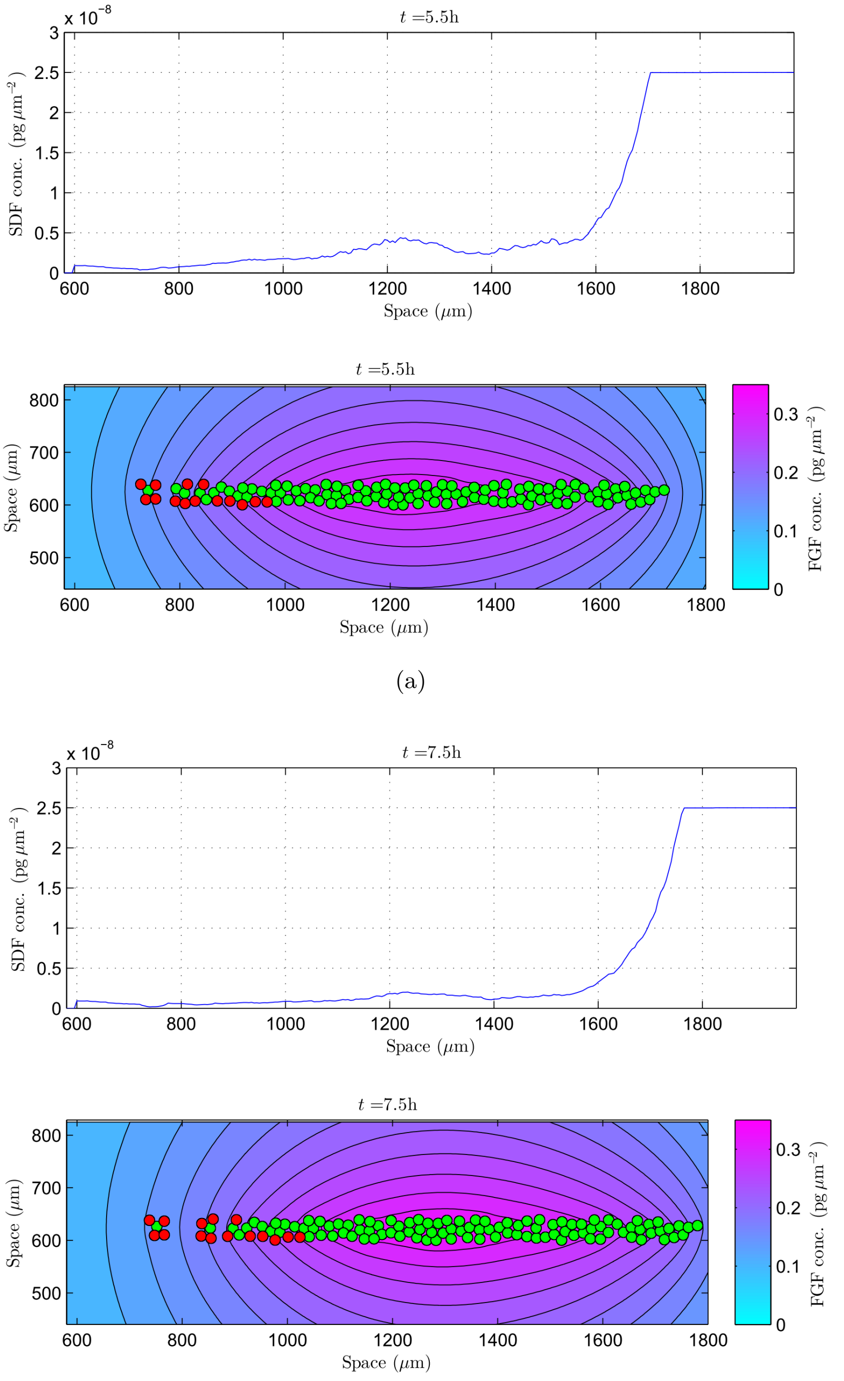

(a)

(b)

Figure 3.13. Continuation of Figure 3.12. Numerical simulation of the lateral line growth at time steps: $t = 5.5, 7.5$ h.

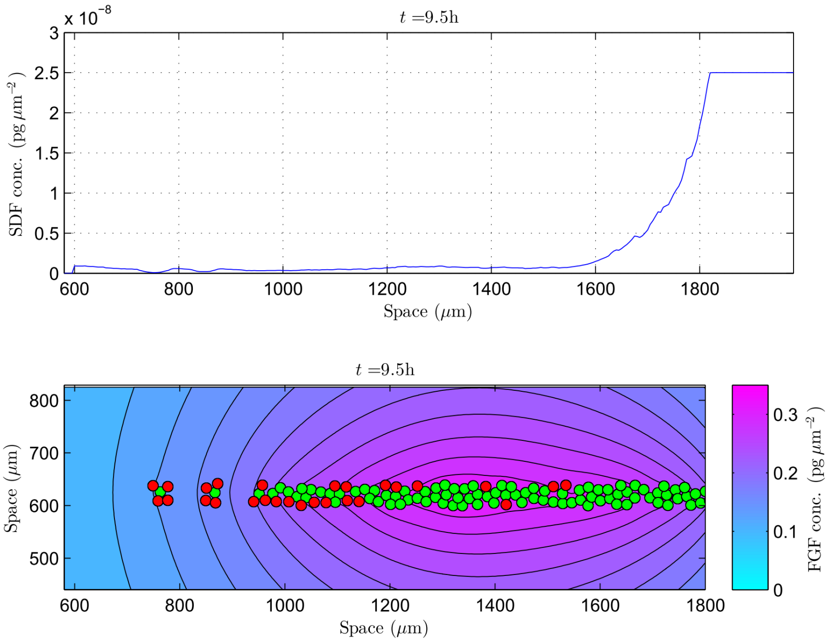

Figure 3.14. Continuation of Figure 3.9. Numerical simulation of the lateral line growth at time step: $t = 9.5$ h.

3.7 Parameter estimates

About the choice of the parameters of the model, we point out that while some values can be found or estimated from the biological or modelling literature, the others have been obtained by numerical data fitting or using some relations provided by the stationary model.

Tables 3.2–3.3 summarize respectively the values of the dimensional and nondimensional parameters. In the case of a range of variability for a parameter, the selected value, used in the simulations, is put in brackets. Finally, the last column in Table 3.2 specifies the references for the provided data.

Now we will make some comments in this regard. Firstly, cell radius R is fixed to 10 μm starting from the experimental data in Lecaudey et al (2008). Radii $\bar{R}$, R_1, are chosen to be equal to 20 μm, taking into account a possible effect of cell extensions (see Stolarska et al, 2009 and references therein). Radius R_2 is chosen to be equal to 20 μm considering the lateral inhibition activated when two cells start to be in touch. Radius R_3, concerning with the range of production or degradation of a chemical signaling, is set to be equal to R, because we think to a source or a drain defined by the dimension of a single cell. For R_4 and R_5 we fix respectively the values 20 μm and 25 μm. First value provides a repulsion force when two cells start to be overlapped (see equation $(3.10)_1$), second values implies an adhesion force in the spatial radial range 20–25 μm.

The values of Γ_0, α, β_{L}, β_{F}, γ, $\omega_{\mathrm{adh,F}}$, μ_{F}, δ/λ, and σ, are obtained by a numerical data fitting on the respective dimensionless values, in order to obtain in the simulations a cell migration velocity and a neuromast formation consistent with the experimental results. This values are marked as "data fitting" in Table 3.2. In particular, Γ_0 controls the slope of the function (3.12), and its value has been chosen to mark a sharp difference in (3.12) between a cell in the centre of the primordium and one on the boundary. However, we have found that changes in the value of Γ_0 do not influence significantly the behaviour of the system.

Then, by numerical tests we have seen that α, the coefficient related to the SDF-1a haptotactic effect, influences almost linearly the velocity of the cell migration in the first few hours before the transition leader-to-follower occurs (see Figure 3.15 (a), shown with dimensional values, as for the other figures of this section). This is expected from equation $(3.16)_1$ if we consider a regime of uniform velocity. The value for α is then fixed to have a cell velocity of ≈ 69 μm/h according to Lecaudey et al (2008).

The values of β_{L} and β_{F} influence cell alignment. Without the alignment effect we have tested that the repulsion alone is not sufficient to ensure a distance between the cells consistent with the experimental observations. Values too small of β_{L} (about $< 5 \times 10^{17}$ h^{-1}) imply a large transverse compression of the primordium (with distances between the centres of the cells less than 40% of the cell diameter), causing even a crossing over of the cells (see Figure 3.15 (b)). In Figure 3.16 there is a schematic configuration of the migrating primordium, displaying the effects resulting from "too small" values of β_{L}.

The range of variability of β_{F}, $\omega_{\mathrm{adh,F}}$, μ_{F}, and γ, suggested in Table 3.2, have been taken in order to have the neuromast detachment. Outside these ranges we can not reproduce a complete neuromast formation. Precisely we find that, β_{F}, which is related to the alignment effect for follower cells is to be fixed, remaining in the range of β_{L}, at least two orders of magnitude smaller than β_{L} (see Figure 3.17 (a), and Table 3.2).

Similarly, $\omega_{\mathrm{adh,F}}$, which represents the coefficient of the elastic adhesion for the followers, is to be chosen, in the range of $\omega_{\mathrm{adh,L}}$, about two orders of magnitude smaller than $\omega_{\mathrm{adh,L}}$ (see Figure 3.17 (b)). The parameter μ_{F}, that is the damping coefficient for a follower cell can be fixed about one order of magnitude larger than μ_{L} (see Figure 3.18 (a)).

For γ, the coefficient related to the FGF chemotactic effect, we find the range indicated in Table 3.2 (numerical data are given in Figure 3.18 (b)).

The parameter δ/λ influences the switch variable $\varphi_i(t)$, and its increasing values produce, at the same time t, a number of leader-to-follower transition gradually decreasing. The range proposed in Table 3.2 ensures, after about 10; h after the migration begins, a remaining number of leaders from 25% to about 55% over the total cell number in the primordium (see Figure 3.19 (a)). These percentages are reasonable in view of the results presented in Lecaudey et al (2008), although it would be interesting to quantify, experimentally, the number of leader and follower cells.

Finally, the parameter σ, related to the degradation of the SDF1-1a signal, affects the gradient of the chemoattractant and then the cell velocity during migration. Its value in Table 3.2 has been fixed to have, in the first few hours before leader-to-follower transition, a velocity consistent with the data in Lecaudey et al (2008) (numerical data in Figure 3.20 (a)). As we have seen, an interesting aspect, that has come out from our tests, is that the cells of the primordium can self-generate their own gradient. Evidence for this has recently be obtained by Donà et al (2013). Even fixing a constant initial datum along the x-axis for the SDF1-1a, with non zero values for σ we are able to reproduce the collective motion, though with a reduced velocity for the same values of σ. Comparing the case with initial gradient of SDF-1a and the case of zero initial gradient along the x-axis, we find, for the value of σ used in Table 3.2, a decreased velocity of about 20% (Figures 3.20 (a)–(b)). Anyway an initial gradient for the SDF-1a signal seems to be necessary, since for too large values of σ we observe a detachment of the head of the primordium. In Figure 3.21 we report a dynamical simulation where we have considered a constant SDF1-1a initial concentration and the value of σ fixed in Table 3.2.

About the information on the parameters arising from the stationary model, we refer to formulas (3.48), (3.49), (3.54), Table 3.1, and Figures 3.2, 3.3. The first two relations give us a limitation for $k_{\mathrm{F}}^* := k_{\mathrm{F}}/\lambda$ and $k_{\mathrm{L}}^* := k_{\mathrm{L}}/\lambda$, the ratios of the coefficient of sensitivity to FGF signal and the coefficient of lateral inhibition for a leader and for a follower cell, while the third one provides a value of ω_{rep}, related to the repulsion coefficient, when we have fixed γ by a numerical data fitting, as mentioned before. Namely, the right hand side of these equations depend on N and d_1^* once the other parameters are chosen. So, to obtain the values in Tables 3.2–3.3 we have fixed for an example $N = 8$ and $d_1^* = 3/2R^*$. They represent reasonable values under the experimental observations in Nechiporuk and Raible (2008) and Lecaudey et al (2008).

Then a value for ξ, the parameter of FGF production, is obtained from the respective nondimensional value ξ^* in order to have the maximum nondimensional value of FGF $f^*_{\max} = 1$ in our domain (see numerical data in Figure 3.19 (b)). Finally, other constants are estimable from data available in literature: $s_{\max}$, the maximum concentration of SDF-1a, from Kirkpatrick et al (2010); $f_{\max}$, the maximum concentration of FGF from Walshe and Mason (2003); $\omega_{\mathrm{adh,L}}$, the elastic adhesion for a leader cell, from Bell et al (1984); μ_{L}, the damping coefficient for a leader cell, from Rubinstein et al (2009); D, the diffusion coefficient of FGF, from Yeh et al (2003), Filion and Popel (2005) and a phenomenological formula in He and Niemeyer (2003); η, the degradation constant of FGF, from Beenken and Mohammadi (2009), Lee and Blaber (2010), using the FGF half-life estimates.

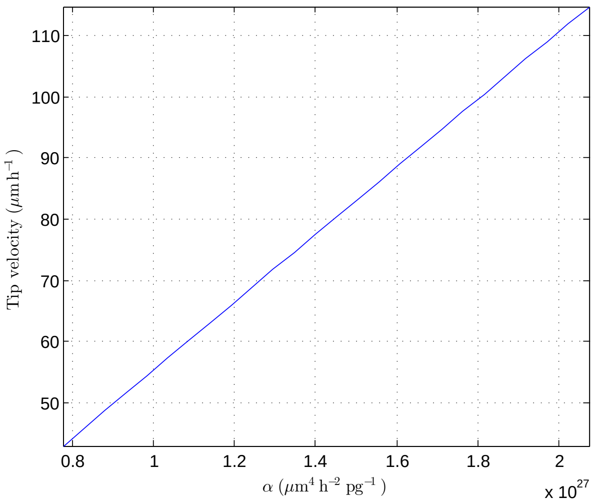

(a)

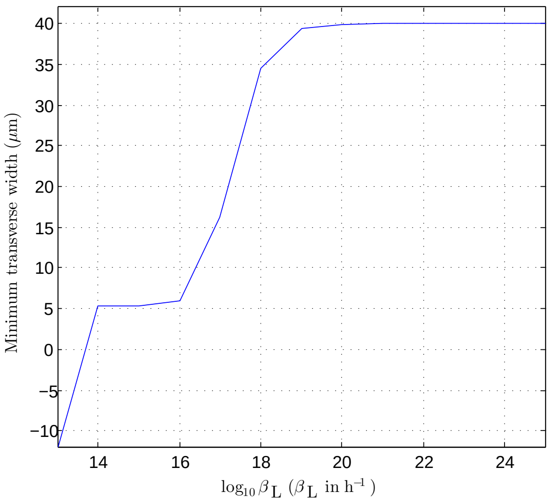

(b)

Figure 3.15. Dimensional plot related to the influence of the coefficients α and β_L on the cell migration, fixing the other parameters as in Table 3.2. The time interval of observation is about 0.5 h after the migration starts. (a) Influence of the coefficient α on the tip velocity of the primordium. Explored range for α: 7.78×10^{26}–$2.07 \times 10^{26} \mu\mathrm{m}^4\,\mathrm{h}^{-2}\,\mathrm{pg}^{-1}$. (b) Influence of coefficient β_L on the minimum width of the primordium (minimum distance between the centres of the cells on the flanks of the primordium). x-axis is in logarithmic scale. Explored range for β_L is 1×10^{13}–1×10^{25} h^{-1}. Values on y-axis close to zero, in correspondence of small values of β_L, imply a large transverse compression of the primordium. Negative values mean even a crossing over of the cells.

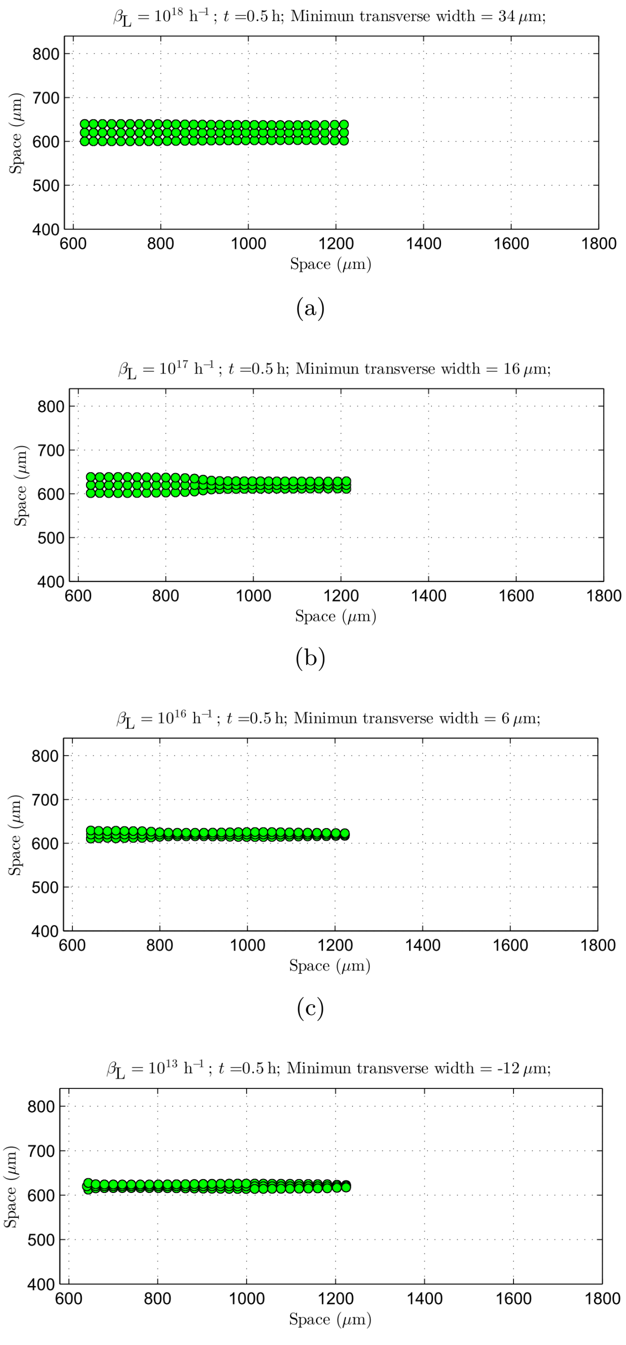
$\beta_{\rm L} = 10^{18}$ h^{-1} ; t =0.5 h; Minimun transverse width = 34 μm;

(a)

$\beta_{\rm L} = 10^{17}$ h^{-1} ; t =0.5 h; Minimun transverse width = 16 μm;

(b)

$\beta_{\rm L} = 10^{16}$ h^{-1} ; t =0.5 h; Minimun transverse width = 6 μm;

(c)

$\beta_{\rm L} = 10^{13}$ h^{-1} ; t =0.5 h; Minimun transverse width = -12 μm;

(d)

Figure 3.16. Schematic configuration of the migrating primordium displaying a large transverse compression for "small" values of the coefficient $\beta_{\rm L}$. In the domain $\Omega = [0, 5000] \times [0, 1240]$ (μm^2) 90 cells have been located, at $t = 0$, uniformly on the stripe $[600, 1180] \times [600, 640]$ (μm^2). The time of observation is $t = 0.5$ h. Chemical signals are not plotted and only a part of the domain is shown. In plots (a)-(d) we have used the parameters fixed in Tables 3.2–3.3, while for $\beta_{\rm L}$ we choose respectively the values $\beta_{\rm L} = 10^{18}, 10^{17}, 10^{16}, 10^{13}$ h^{-1}. In each panel is indicated, in the title, the minimum distance between the centres of the cells on the two flanks of the primordium. For $\beta_{\rm L} = 10^{18}$ in (d) we have a negative value, meaning that cells have crossed over each other.

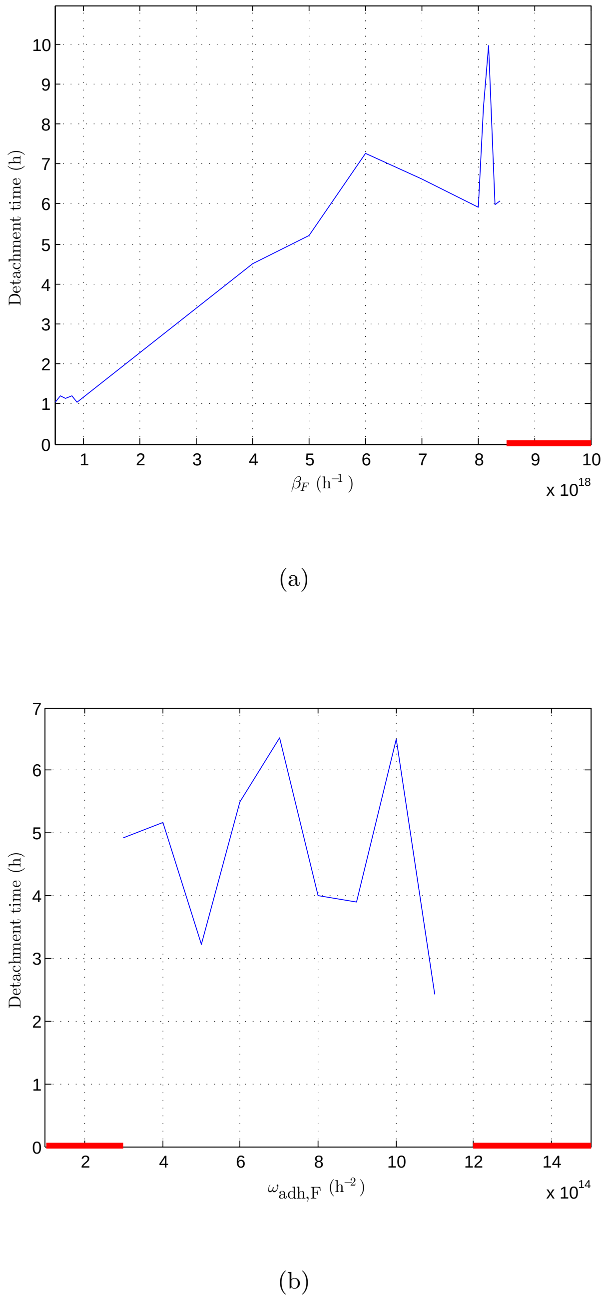

Figure 3.17. Influence of the coefficients β_{F} and ω_{F} on the detachment time of a neuromast, fixing the other parameters as in Table 3.2. The time interval of observation is about 10 hours after the migration starts. The red lines on the x-axis mean that for those values of the coefficients we have no complete detachment of neuromasts. (a) Influence of the coefficient β_{F}. Explored range for β_{F}: 5×10^{17}–1×10^{19} h^{-1}. Notice that the lower bound of this range coincides with the acceptable lower bound for β_{L} given in Table 3.2. (b) Influence of the coefficient ω_{F}. Explored range for ω_{F}: 1×10^{14}–1.5×10^{15} h^{-2}.

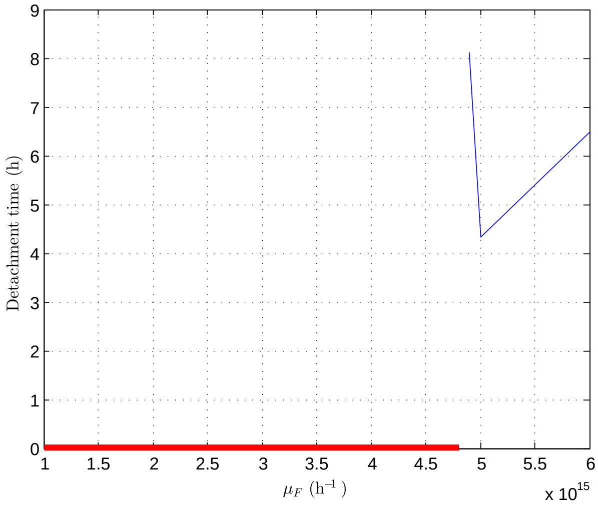

(a)

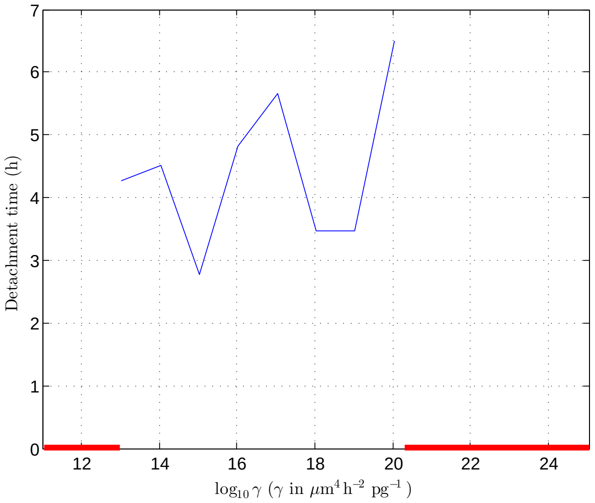

(b)

Figure 3.18. Influence of the coefficients μ_F and γ on the detachment time of a neuromast, fixing the other parameters as in Table 3.2. The time interval of observation is about 10 hours after the migration begins. The red lines on the x-axis mean that for those values of the coefficients we have no complete detachment of neuromasts. (a) Influence of the coefficient μ_F. Explored range for μ_F: 1×10^{15}–5.82×10^{15} h^{-1}. Notice that the upper bound of this range coincides with the upper bound for μ_L given in Table 3.2. (b) Influence of the coefficient γ. x-axis is in logarithmic scale. Explored range for γ: 1.08×10^{11}–1.08×10^{25} μm^4 h^{-2} pg^{-1}.

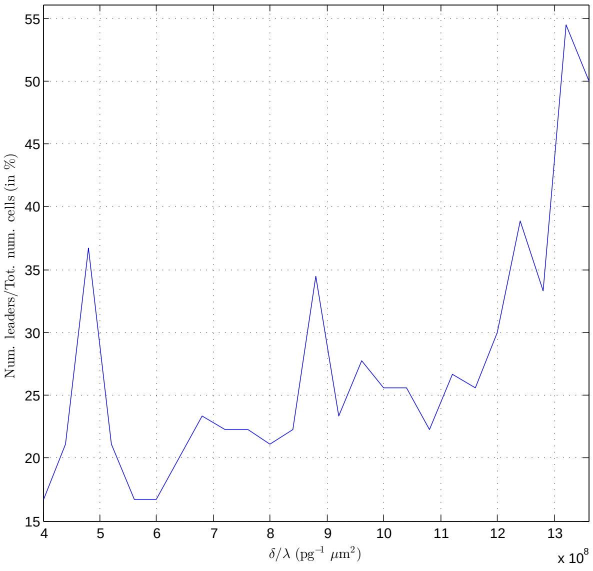

(a)

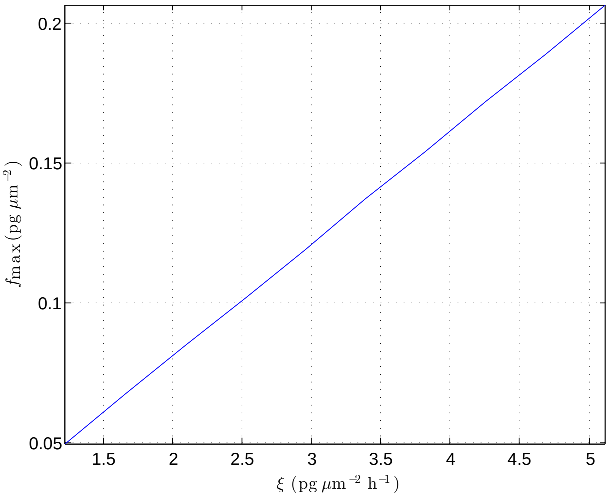

(b)

Figure 3.19. (a) Influence of the coefficient δ/λ on the number of leader-follower transition, fixing the other parameters as in Table 3.2. The time interval considered is 10 hours after the migration begins. Explored range for δ/λ: 4×10^8–1.36×10^9 $\mathrm{pg}^{-1}\,\mu\mathrm{m}^2$. (b) Influence of the coefficient ξ on the maximum concentration $f_{\max}$ of FGF. Explored range for ξ: 1.2312–5.1192 $\mathrm{pg}\,\mu\mathrm{m}^{-2}\,\mathrm{h}^{-1}$.

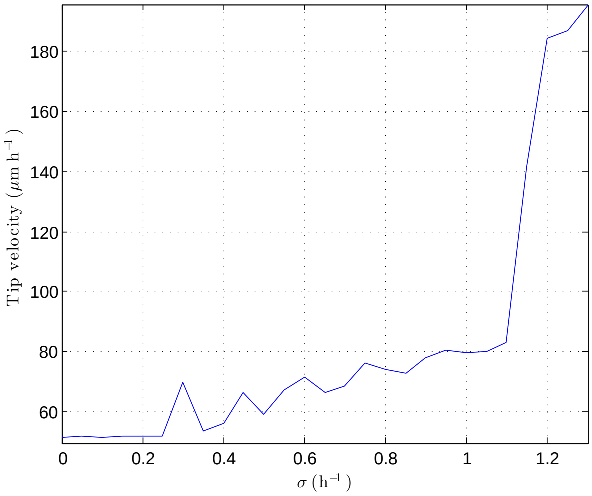

(a)

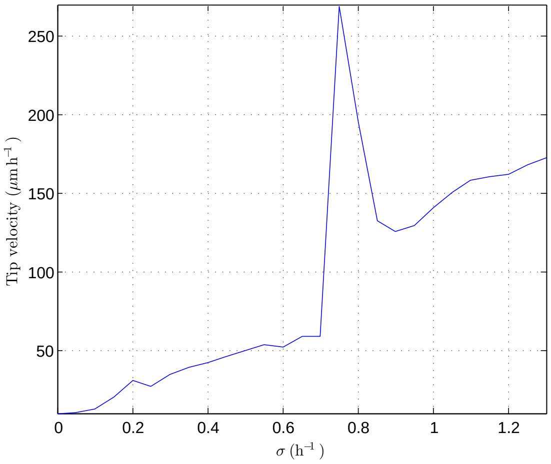

(b)

Figure 3.20. Influence of the coefficient σ on the tip velocity of the primordium, fixing the other parameters as in Table 3.2. The tip velocity is computed after 1 hour of migration, and before the leader-follower transition occurs. The explored range for σ is 0–1.3 h^{-1}. (a) The case of initial gradient of SDF-1a given by (3.21)–(3.23). The pick in correspondence of $\sigma \approx 1.2$ h^{-1} indicates that higher values of the parameter causes the detachment of the head of the migrating group of cells and its motion to a greater velocity. (b) The case of zero initial gradient of SDF-1a (constant initial concentration of SDF-1a). With non zero values for σ we are able to reproduce the collective motion, though with a reduced velocity with respect to the case of initial gradient of haptoattractant. The pick in $\sigma \approx 0.75$ h^{-1} means, as above, the detachment of the head of the primordium.

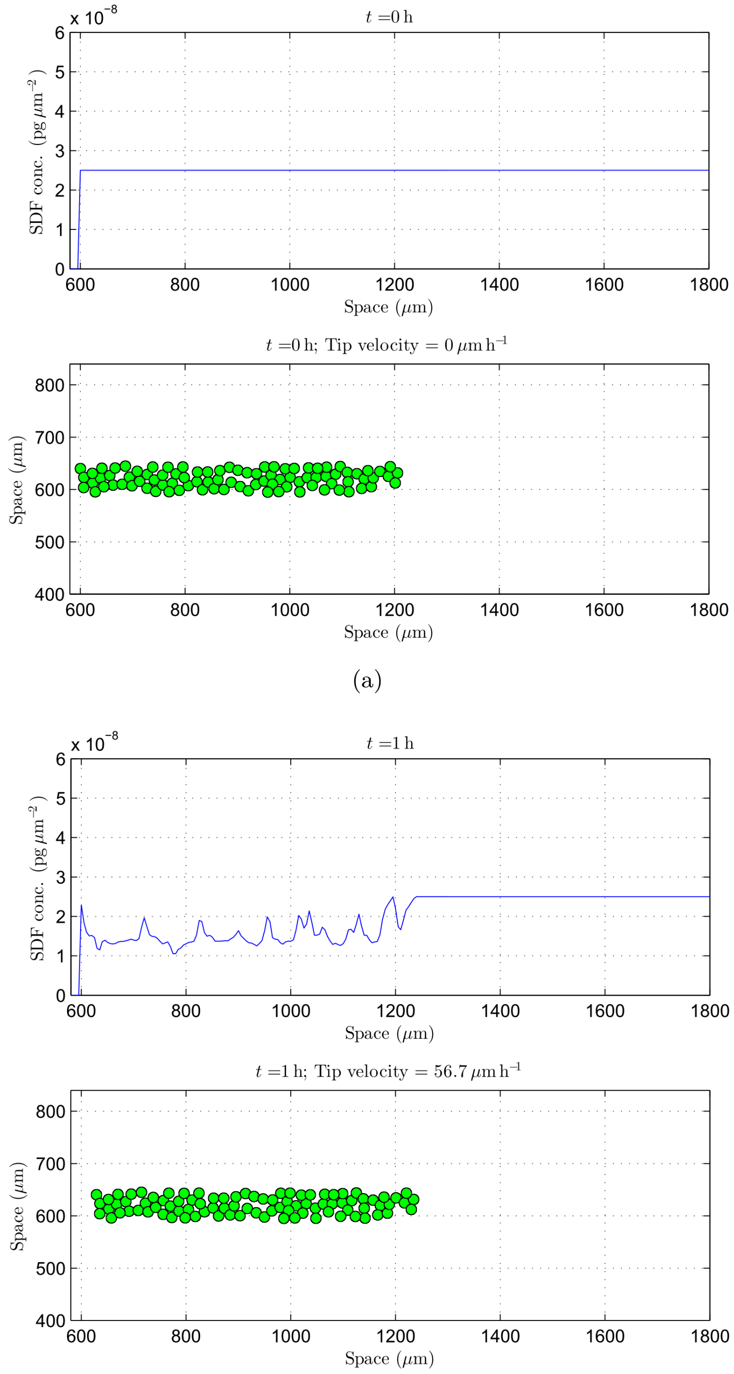

(a)

(b)

Figure 3.21. A dynamical simulation of the migrating primordium with a constant initial datum for the SDF-1a signal along the x-axis. The initial position of the cells is taken randomly on the stripe $[600, 1480] \times [600, 640]$ (μm^2) with a distance between their centre chosen randomly in the range [17,20] μm. Parameters values are fixed as in Table 3.2. In particular, the SDF-1a at $t = 0$ is fixed constant to its biological maximum value given in the table. In the upper panel the chemokine concentration is plotted in a transverse section along the middle of the primordium. Tip velocity is displayed in the title of the lower panel, while the FGF signal is not shown. Despite the initial zero gradient of the haptotactic signal along the x-axis, the migrating cells can self-generate their own gradient and ensure the collective motion. In (b) at $t = 1$ h we can observe a velocity of about 56.7 $\mu m\,$h^{-1}.

Table 3.2. Estimates of physical parameter values.

Parameter	Definition	Value or range (used value)	Source
R	cell radius	$10\ \mu\mathrm{m}$	Lecaudey et al (2008)
$\bar{R}$	detection radius of chemicals	$20\ \mu\mathrm{m}$	biological assumption
R_1	detection radius of cellular alignment	$20\ \mu\mathrm{m}$	biological assumption
R_2	detection radius of lateral inhibition	$20\ \mu\mathrm{m}$	biological assumption
R_3	radius of production/degradation of chemicals	$10\ \mu\mathrm{m}$	biological assumption
R_4	radius of action of repulsion between cells	$20\ \mu\mathrm{m}$	biological assumption
R_5	radius of action of adhesion between cells	$25\ \mu\mathrm{m}$	biological assumption
T	characteristic time	$1/3600\ \mathrm{h}$	Rubinstein et al (2009)
s_{max}	maximum concentration of SDF-1a	3.6×10^{-8}–6.5×10^{-8} $(2.5 \times 10^{-8})\ \mathrm{pg}\,\mu\mathrm{m}^{-2}$	Kirkpatrick et al (2010)
f_{max}	maximum concentration of FGF	1×10^{-1}–(1.2×10^{-1}) $\mathrm{pg}\,\mu\mathrm{m}^{-2}$	Walshe and Mason (2003)
Γ_0	constant in function (3.12)	10 nondim.	data fitting
α	coefficient of SDF-1a haptotactic effect per unit mass	1.31×10^{27} $\mu\mathrm{m}^4\,\mathrm{h}^{-2}\,\mathrm{pg}^{-1}$	data fitting on Lecaudey et al (2008)
β_{L}	coefficient of cell flocking per unit mass for a leader cell	$> 5 \times 10^{17}\ (5 \times 10^{20})\ \mathrm{h}^{-1}$	data fitting
β_{F}	coefficient of cell flocking per unit mass for a follower cell	$5 \times 10^{17}\ \mathrm{h}^{-1}$–$1.68 \times 10^{-2}\beta_{\mathrm{L}}$ $(5 \times 10^{18}\ \mathrm{h}^{-1})$	data fitting
γ	coefficient of FGF chemotactic effect per unit mass	1.08×10^{13}–(1.08×10^{20}) $\mu\mathrm{m}^4\,\mathrm{h}^{-2}\,\mathrm{pg}^{-1}$	data fitting
ω_{rep}	coefficient of repulsion per unit mass	$2.03 \times 10^{17}\ \mu\mathrm{m}^2\,\mathrm{h}^{-2}$	from steady model, formula (3.54)
$\omega_{\mathrm{adh,L}}$	elastic constant per unit mass for a leader cell	1.296×10^{14}–1.296×10^{19} $(5.5 \times 10^{16})\ \mathrm{h}^{-2}$	Bell et al (1984)
$\omega_{\mathrm{adh,F}}$	elastic constant per unit mass for a follower cell	$0.55 \times 10^{-2}\omega_{\mathrm{adh,L}}$–$2 \times 10^{-2}\omega_{\mathrm{adh,L}}$ $(5.5 \times 10^{14}\ \mathrm{h}^{-2})$	data fitting
μ_{L}	damping coefficient for a leader cell per unit mass	(5.82×10^{14})–5.82×10^{15} h^{-1}	Rubinstein et al (2009)
μ_{F}	damping coefficient for a follower cell per unit mass	$8.42\,\mu_{\mathrm{L}}$–$(5.82 \times 10^{15}\ \mathrm{h}^{-1})$	data fitting

δ/λ	ratio of coefficient of sensitivity to SDF-1a and coefficient of lateral inhibition	8.8×10^8–1.36×10^9 (1.12×10^9) $\mathrm{pg}^{-1}\,\mu\mathrm{m}^2$	data fitting
k_{L}/λ	ratio of coefficient of sensitivity to FGF signal for a leader cell and coefficient of lateral inhibition	< 1.8187 (1.7) nondim.	from steady model, formula (3.49)
k_{F}/λ	ratio of coefficient of sensitivity to FGF signal for a follower cell and coefficient of lateral inhibition	≥ 1.1619 (17) nondim.	from steady model, formula (3.48)
D	diffusion coefficient	69985–84184 (78950) $\mu\mathrm{m}^2\,\mathrm{h}^{-1}$	He and Niemeyer (2003); Filion and Popel (2005); Yeh et al (2003)
ξ	coefficient of production of FGF	2.9592 $\mathrm{pg}\,\mu\mathrm{m}^{-2}\,\mathrm{h}^{-1}$	data fitting on Walshe and Mason (2003)
η	degradation constant of FGF	0.09–0.69(0.2) h^{-1}	Beenken and Mohammadi (2009); Lee and Blaber (2010)
σ	degradation constant of SDF-1a	0.55–0.7 (0.6) h^{-1}	data fitting on Lecaudey et al (2008)

Table 3.3. Estimates of dimensionless parameter values.

Parameter	Definition	Value or range (used value)
$\bar{R}^*$	$\bar{R}/R$	2
R_1^*	R_1/R	2
R_2^*	R_2/R	2
R_3^*	R_3/R	1
R_4^*	R_4/R	2
R_5^*	R_5/R	2,5
Γ_0	Γ_0	10
α^*	$\alpha s_{\max} T^2/R^2$	2.53×10^{10}
β_{L}^*	$\beta_{\mathrm{L}} T$	$> 1.39 \times 10^{14}$ (1.39×10^{17})
β_{F}^*	$\beta_{\mathrm{F}} T$	1.39×10^{14}–$1.68 \times 10^{-2} \beta_{\mathrm{L}}^*$ (1.39×10^{15})
γ^*	$\gamma f_{\max} T^2/R^2$	10^3–(10^{10})
ω_{rep}^*	$\omega_{\mathrm{rep}} T^2/R^2$	1.57×10^8
$\omega_{\mathrm{adh,L}}^*$	$\omega_{\mathrm{adh,L}} T^2$	10^7–10^{12} (4.24×10^9)
$\omega_{\mathrm{adh,F}}^*$	$\omega_{\mathrm{adh,F}} T^2$	$0.55 \times 10^{-2} \omega_{\mathrm{adh,L}}^*$ $-2 \times 10^{-2} \omega_{\mathrm{adh,L}}^*$ (4.24×10^7)
μ_{L}^*	$\mu_{\mathrm{L}} T$	(1.62×10^{11})–1.62×10^{12}
μ_{F}^*	$\mu_{\mathrm{F}} T$	$8.42 \mu_{\mathrm{L}}^*$–(1.62×10^{12})
δ^*	$\delta s_{\max}/\lambda$	22–34 (28)
k_{L}^*	k_{L}/λ	< 1.8187 (1.7)
k_{F}^*	k_{F}/λ	≥ 1.1619 (17)
D^*	DT/R^2	0.1944–0.2338 (0.2193)
ξ^*	$\xi T/f_{\max}$	0.0069
η^*	ηT	2.5×10^{-5}–1.92×10^{-4} (5.56×10^{-5})
σ^*	σT	1.531×10^{-4}–1.948×10^{-4} (1.67×10^{-4})

3.8 Conclusions

We have proposed in this chapter a *discrete in continuous* mathematical model describing the formation of the lateral line in the zebrafish primordium. Under suitable hypotheses, we have shown that our model admits particular biologically relevant steady solutions. They corresponds to the formation of neuromasts along the two flanks of the embryo. Then their stability has been assessed numerically. Finally, the dynamical model has been tested by 2D numerical simulations and the results have been compared with some experimental observations. In particular we have observed that the moving cells can also self-generate their own chemokine gradient during the migration, a mechanism recently proved *in vivo* on the zebrafish by Donà et al (2013).

Clearly we remark that the model proposed here presents some limits. Firstly, cells are supposed to be all equally circular, so that deformation effects are neglected. On the other hand they can be partially recovered introducing influence radii. Secondly, only a limited number of biological interactions have been modeled, and this in a time range starting with the beginning of the migration of the primordium. For example, biological phenomena occurring in the next few hours post-fertilization, or in the time after the rosette deposition have not been taken into account. However we have followed the framework of the studies Nechiporuk and Raible (2008) and Lecaudey et al (2008), and a good concordance with the experimental data can be inferred.

Finally, we remark that with respect to these studies, some mechanism are biologically evident, as chemotaxis effects, cell adhesion-repulsion, damping effects, chemical signals diffusion, others, as our lateral inhibition term, cell alignment, differentiated parameters in the leader-follower transition, have been introduced to obtain a nice agreement with biological evidences. It would be interesting to have experimental evidence in this regard.

Chapter 4

A hybrid mathematical model of collective motion under alignment and chemotaxis

4.1 Introduction

In Section 2.6 we have introduced the Cucker-Smale model (Cucker and Smale, 2007a,b) as a model of alignment for a system of interacting particles that, for convenience we write again below.

Let $\mathbf{X}_i, \mathbf{V}_i \in \mathbb{R}^n$, for $i \in \{1, \dots, N\} \subset \mathbb{N}$, respectively the position and the velocity of the i-th particle, and let $t \in \mathbb{R}_{\geq 0}$, the model can be written as

$$\begin{cases} \dot{\mathbf{V}}_i = \dfrac{\beta}{N} \displaystyle\sum_{j=1}^{N} \dfrac{\alpha_1}{\left(\alpha_2 + \|\mathbf{X}_i - \mathbf{X}_j\|^2\right)^{\sigma}} (\mathbf{V}_j - \mathbf{V}_i), \\ \\ \dot{\mathbf{X}}_i = \mathbf{V}_i, \end{cases} \tag{4.1}$$

where β, α_1, α_2, σ are positive constants, and $\|\cdot\|$ is the Euclidean norm in $\mathbb{R}^n$.

Cucker and Smale showed that, under suitable parameters and initial data, their model implies that the state of the flock converges to one in which all particles move with the same velocity. This depends mainly on the exponent σ in $(4.1)_1$, that translates the rate of decay of the influence between agents in the flock as a function of their distance in space. The main convergence result proved in Cucker and Smale (2007a) has been improved by Ha and Liu (2009), using an explicit Lyapunov functional approach. First, as in this last reference, we can give the definition of *time-asymptotic flocking* as follows:

Definition 2 *Given system* (4.1)*, let* $\mathbf{X}_{CM} = \frac{1}{N}\sum_{i=1}^{N}\mathbf{X}_i$ *and* $\mathbf{V}_{CM} = \frac{1}{N}\sum_{i=1}^{N}\mathbf{V}_i$ *position and velocity of the centre of mass. System* (4.1) *has a time-asymptotic flocking if and only if* $(\mathbf{X}_i, \mathbf{V}_i)$*,* $i = 1, \dots, N$*, satisfy the two conditions:*

1) the velocity fluctuations go to zero time-asymptotically (velocity alignment):

$$\lim_{t\to+\infty} \sum_{i=1}^{N} \|\mathbf{V}_i(t) - \mathbf{V}_{CM}(t)\|^2 = 0; \tag{4.2}$$

2) the position fluctuations are uniformly bounded in time t (forming a group):

$$\sup_{0\leq t\leq +\infty} \sum_{i=1}^{N} \|\mathbf{X}_i(t) - \mathbf{X}_{CM}(t)\|^2 < +\infty. \tag{4.3}$$

Notice that the square root of the quantities under the limit operation in (4.2)–(4.3) is proportional to the standard deviations of $\mathbf{X}_i(t)$ and $\mathbf{V}_i(t)$ around the centre of mass system. Cucker and Smale (2007a) and Ha and Liu (2009) proved that for $\sigma \in [0, 1/2]$ occurs a global *unconditional flocking* of system (4.1), as stated in Definition 2, regardless of initial configurations, while for $\sigma \in (1/2, +\infty)$ there is *conditional flocking*, that is only some parameters and initial data lead to a flocking state, but in general the dispersion of the flock may occur.

As we have seen in Section 2.6, Cucker-Smale model gave rise to many extensions and it is an ingredient of the three zone models. Cucker and Smale-like models have been recently widely applied in many contexts, from the biological field to the collective dynamics of different interacting groups of individuals (Szabò et al, 2006; Belmonte et al, 2008; Arboleda-Estudillo et al, 2010; Sepúlveda et al, 2013; Albi and Pareschi, 2013).

There are also some extensions of the Cucker-Smale model for which exact analytical results have been proved. Among these we cite Cucker and Dong (2010, 2011), that added a repulsion force between particles in equation $(4.1)_1$. Their model can be written as

$$\begin{cases} \dot{\mathbf{V}}_i & = \dfrac{\beta}{N} \displaystyle\sum_{j=1}^{N} \dfrac{\alpha_1}{\left(\alpha_2 + \|\mathbf{X}_i - \mathbf{X}_j\|^2\right)^{\sigma}} (\mathbf{V}_j - \mathbf{V}_i) \\ & \quad + \Lambda(||\mathbf{V}_i - \mathbf{V}_j||) \displaystyle\sum_{j=1}^{N} g(||\mathbf{X}_i - \mathbf{X}_j||)(\mathbf{X}_i - \mathbf{X}_j), \\ \dot{\mathbf{X}}_i & = \mathbf{V}_i, \end{cases} \tag{4.4}$$

where

$$\Lambda(||\mathbf{V}_i - \mathbf{V}_j||) := \left(\frac{1}{N} \sum_{i\geq j} ||\mathbf{V}_i - \mathbf{V}_j||^2 \right)^{1/2},$$

and a possible functional form for g can be

$$g(||\mathbf{X}_i - \mathbf{X}_j||) := \frac{1}{(||\mathbf{X}_i - \mathbf{X}_j||^2 - d_0)^{\theta}}, \tag{4.5}$$

where $\theta > 1$ and $d_0 > 0$ a constant.

For system (4.4) it is possible to prove results similar to those valid for the Cucker-Smale model. Let the initial position satisfying the condition $\|\mathbf{X}_i(0) - \mathbf{X}_j(0)\|^2 > d_0$, for all $i \neq j$. If $\sigma \leq 1/2$ we have unconditional flocking (convergence to a common velocity), in addition avoiding collisions, that is exist two constant B_0 and $d > d_0$ such that, for all $t \geq 0$, $\Lambda(\|\mathbf{X}_i(t) - \mathbf{X}_j(t)\|) \leq B_0$ and $\|\mathbf{X}_i(t) - \mathbf{X}_j(t)\| > d$, for all $i \neq j$. The case $\sigma > 1/2$ implies a conditional flocking without collision, occurring only under certain parameters and initial data.

Another extension of the Cucker-Smale model has been proposed by Ha and Levy (2009) to describe the motion of phototactic bacteria, bacteria that move towards light. They assume that there exists some form of communication between bacteria, that is an excitation level associated with each cell. When the excitation level pass over a critical threshold the bacteria initiate a motion towards the light source. This speed term is added in equation $(4.1)_1$ as an external force, and system (4.1) is then coupled with an equation for the excitation level. As for the velocities, the excitation level depends on the excitation of the surrounding bacteria, and for each bacterium it is assumed a weighted average of the differences of its excitation with those of the other bacteria. For $i = 1, \dots, N$, the following system is proposed:

$$\begin{cases} \dot{\mathbf{V}}_i = \dfrac{\lambda_1}{N} \displaystyle\sum_{j=1}^{N} g_1\left(\mathbf{X}_j, \mathbf{X}_i\right)\left(\mathbf{V}_j - \mathbf{V}_i\right) + I_0(u_\infty \hat{e}_s - \mathbf{V}_i)\left(1 - \varphi(\varsigma_i; \varsigma_{cr})\right), \\ \\ \dot{\mathbf{X}}_i = \mathbf{V}_i, \\ \\ \dot{\varsigma}_i = \dfrac{\lambda_2}{N} \displaystyle\sum_{j=1}^{N} g_2(\varsigma_j - \varsigma_i) + I_0 \varphi(\varsigma_i; \varsigma_{cp}), \end{cases} \tag{4.6}$$

where λ_1, λ_2 are constants, $g_1(\cdot)$ and $g_2(\cdot)$ are suitable symmetric weight functions, I_0 is the constant intensity of the light source, u_∞ is the terminal speed of particles, $\hat{e}_s$ is the unit vector of the light source, ς_{cr} and ς_{cp} are critical excitation values, and φ is a suitable 0-1 threshold function. For system (4.6) Ha and Levy (2009) proved that when all particles are fully excited after a finite time (excitation over the critical threshold, that implies $\varphi(\varsigma_i; \varsigma_{cr}) = 0$), their asymptotic velocity tends to an identical terminal velocity.

Among other models, Cucker and Mordecki (2008) introduced an alignment effect with noise and Ha et al (2009) studied flocking behaviour with a stochastic Cucker-Smale model. Finally Cucker and Huepe (2008) introduced in the model a group of individuals with a preferred heading direction. The convergence to a collective group swarming state with constant velocity is analytically proved for a range of parameters and initial conditions. This demonstrates in part, with simple equations, the results shown by the model by Couzin et al (2005) in relation to the mechanisms of leadership and decision-making in biological systems.

In this chapter, starting from our model proposed in Chapter 3, in which we have coupled the Cucker-Smale model with many other effects, we study, both from an analytical and a numerical point of view, the coupling between an alignment and chemotaxis mechanism for a system of interacting particles. From the analytic point of view we prove existence and uniqueness of solution of our model. Then, on a linearized form of the system, a time-asymptotic convergence result is obtained. In particular, through a suitable Lyapunov functional, we show that position and velocity of all the particles, for $t \to +\infty$, go to those of their centre of mass. Moreover, the velocity of the centre of mass tends time-asymptotically to zero. From a numerical point of view we test this result on the full nonlinear system, finding a complete concordance with the behaviour shown by the linearized system.

Hence, we observe that while in the Cucker-Smale model two conditions may occur, conditional and unconditional flocking, in our model the flocking behaviour, as given in Definition 2, is always ensured, also when the only alignment effect produce the dispersion of the group. Moreover, we have the stronger conditions that all the particles converge in a single position, i.e. their centre of mass, and that the velocity of the centre of mass go to zero.

Among the numerical simulations, we propose, inspired from Chapter 3, the case of two cell populations: leader cells corresponding to the sources of the chemotactic signal, and follower cells that do not produce any chemical signal, both subject to the alignment and chemotaxis force. In this case, we observe the convergence of cells towards the foci of chemoattractant. Then, we try to simulate the system under the only chemotactic effect, neglecting the alignment term. Our numerical results display here the absence of convergence in the particle group, with oscillating fluctuations around their centre of mass.

It has also to be noticed that the analytical results about existence and uniqueness, and about the asymptotic behaviour of the solution are obtained on the whole space, whereas numerical simulations are performed on a bounded domain, with periodic boundary conditions.

Clearly, it is of interest to extend our analytical convergence result on the nonlinear system, at least for “small” initial data. The numerical simulations suggest that such result could possibly be obtained.

The chapter continues with five sections. In Section 4.2 we design our hybrid mathematical model of collective motion. Section 4.3 deals with the analytical study of the local existence and uniqueness of the solution. Then in Section 4.4 this result is extended and the global existence and uniqueness is proved. Section 4.5 is devoted to investigate the asymptotic behaviour of the model on a linearized form of the system around the equilibrium configurations. In Section 4.6 we show and discuss some meaningful dynamical simulations of the nonlinear model. Finally, Section 4.7 includes the conclusions.

4.2 The basic mathematical model

Starting from model (4.1), we suppose that the force acting on each particle is given by an alignment term, proportional to the differences of velocity with the other particles and weighed on the distances, and by a chemotactic attraction towards higher concentration of a chemical signal $f(\mathbf{x}, t)$, supposed produced by the particles themselves. Typically this last force is proportional to the gradient of the concentration ∇f (Murray, 2003; Eisenbach and Lengeler, 2004; Perthame, 2007). In our hybrid description, while particles are considered discrete entities the signal f is supposed continuous and its rate of change in time is equal to a diffusion term, a source term, and a molecular degradation, as discussed in Section 3.2. If each particles is endowed of a radius R, describing its circular shape, the source of signal can be given by a characteristic function on a ball of radius R centred on each particle.

In our hypotheses we can write the following system:

$$\begin{cases} \dot{\mathbf{V}}_i = \dfrac{\beta}{N}\displaystyle\sum_{j=1}^{N} \dfrac{1}{\left(1+\frac{\|\mathbf{X}_i-\mathbf{X}_j\|^2}{R^2}\right)^{\sigma}}(\mathbf{V}_j-\mathbf{V}_i)+\gamma\nabla f(\mathbf{X}_i), \\ \\ \dot{\mathbf{X}}_i = \mathbf{V}_i, \\ \\ \partial_t f = D\Delta f + \xi\displaystyle\sum_{j=1}^{N}\chi_{\mathbf{B}(\mathbf{X}_j,R)} - \eta f, \end{cases} \tag{4.7}$$

where $\beta, \sigma, \gamma, D, \xi, \eta, R$ are positive constants, and

$$\chi_{\mathbf{B}(\mathbf{X}_j,R)} := \begin{cases} 1, & \text{if} \quad \mathbf{x}\in\mathbf{B}(\mathbf{X}_j,R); \\ 0, & \quad\text{otherwise;} \end{cases}$$

with

$$\mathbf{B}(\mathbf{X}_j,R) := \{\mathbf{x} : ||\mathbf{x}-\mathbf{X}_j|| \le R\}\,.$$

Initial data are given by initial position and velocity for each particle:

$$\mathbf{X}(0) = \mathbf{X}_0,$$
$$\mathbf{V}(0) = \mathbf{V}_0,$$

with $\mathbf{X} = (\mathbf{X}_1,\dots,\mathbf{X}_N)$, $\mathbf{V} = (\mathbf{V}_1,\dots,\mathbf{V}_N)$, and by the initial concentration of signal, that we assume

$$f(\mathbf{x},0) := f_0 = 0. \tag{4.8}$$

We note that equation $(4.7)_3$ can be analytically solved making the classical exponential transformation:

$$f = e^{-\eta t}u,$$

with $u(\mathbf{x},t)$ solution of

$$\partial_t u = D\Delta u + \xi e^{\eta t}\sum_{j=1}^{N}\chi_{\mathbf{B}(\mathbf{X}_j,R)}.$$

Now, if

$$\Gamma(\mathbf{x},t) := \frac{1}{(4\pi D t)^{n/2}}e^{-\frac{||\mathbf{x}||^2}{4Dt}}$$

is the fundamental solution of the heat equation on $\mathbb{R}^n$, using the Duhamel's principle we have

$$\begin{aligned} f(\mathbf{x},t) &= (\Gamma(\mathbf{x},t)*f_0)e^{-\eta t} + e^{-\eta t}\int_0^t \Gamma(\mathbf{x},t-\tau)*\left(\xi e^{\eta\tau}\sum_{j=1}^{N}\chi_{\mathbf{B}(\mathbf{X}_j(\tau),R)}\right)d\tau \\ &= \xi\sum_{j=1}^{N}\int_0^t e^{-\eta(t-\tau)}\int_{\mathbb{R}^n}\Gamma(\mathbf{x}-\bar{\mathbf{x}},t-\tau)\chi_{\mathbf{B}(\mathbf{X}_j(\tau),R)}\,d\bar{\mathbf{x}}d\tau \end{aligned} \tag{4.9}$$

where $*$ is the convolution operation in the variable $\mathbf{x}$, and $f_0 = 0$ by the initial condition (4.8) $f_0 = 0$.

In the following, for analytical and numerical simplicity, we will discuss the case of N particles in $\mathbb{R}^2$. First, if $\mathbf{x} = (x_1, x_2)$ and $\bar{\mathbf{x}} = (\bar{x}_1, \bar{x}_2)$, from (4.9) we can write

$$f(x_1, x_2, t) = \xi \sum_{j=1}^{N} \int_0^t \iint_{\mathbf{B}(\mathbf{X}_j(\tau), R)} \frac{e^{-\eta(t-\tau)} e^{-\frac{(x_1-\bar{x}_1)^2 + (x_2-\bar{x}_2)^2}{4(t-\tau)D}}}{4\pi(t-\tau)D} \, d\bar{x}_1 \, d\bar{x}_2 \, d\tau. \tag{4.10}$$

With a simple change of variables it is easy to see that the integrand in (4.10) is L^1 with respect to τ in $(0, t)$. In fact, if we define

$$\tilde{x}_1 = \frac{x_1 - \bar{x}_1}{\sqrt{4(t-\tau)D}}, \tag{4.11}$$

$$\tilde{x}_2 = \frac{x_2 - \bar{x}_2}{\sqrt{4(t-\tau)D}}, \tag{4.12}$$

and

$$\mathbf{\Phi}(\tilde{x}_1, \tilde{x}_2) := \left(-\tilde{x}_1 \sqrt{4(t-\tau)D} + x_1, -\tilde{x}_2 \sqrt{4(t-\tau)D} + x_2 \right),$$

we have the Jacobian

$$\det \left[\partial \mathbf{\Phi} / \partial \tilde{\mathbf{x}} \right] = \begin{vmatrix} -\sqrt{4(t-\tau)D} & 0 \\ 0 & -\sqrt{4(t-\tau)D} \end{vmatrix} = 4(t-\tau)D.$$

In the new variables (4.10) becomes

$$\begin{aligned} f(x_1, x_2, t) &= \xi \sum_{j=1}^{N} \int_0^t \iint_{\tilde{\mathbf{B}}} \frac{e^{-\eta(t-\tau)} e^{-\frac{\tilde{x}_1^2 + \tilde{x}_2^2}{4(t-\tau)D} 4(t-\tau)D}}{4\pi(t-\tau)D} 4(t-\tau)D \, d\tilde{x}_1 \, d\tilde{x}_2 \, d\tau \\ &= \frac{\xi}{\pi} \sum_{j=1}^{N} \int_0^t e^{-\eta(t-\tau)} \iint_{\tilde{\mathbf{B}}} e^{-(\tilde{x}_1^2 + \tilde{x}_2^2)} \, d\tilde{x}_1 \, d\tilde{x}_2 \, d\tau, \end{aligned} \tag{4.13}$$

where $\tilde{\mathbf{B}}$ is obtained from $\mathbf{B}$ under transformations (4.11)–(4.12). In (4.13) the integrand is L^1 in $(0, t)$, with respect to τ.

Now, if $\nabla f = (\partial_{x_1} f, \partial_{x_2} f)$ is the chemotactic gradient, and $\mathbf{X}_i = (X_{i1}, X_{i2})$, $\mathbf{V}_i = (V_{i1}, V_{i2})$ are respectively the position and the velocity of the i-th cell, we obtain

$$\partial_{x_1} f(x_1, x_2, t) = \xi \sum_{j=1}^{N} \int_0^t \iint_{\mathbf{B}(\mathbf{X}_j(\tau),R)} \frac{e^{-\eta(t-\tau)} e^{-\frac{(x_1-\bar{x}_1)^2+(x_2-\bar{x}_2)^2}{4(t-\tau)D}}}{4\pi(t-\tau)D}$$

$$\times \left(-\frac{2(x_1-\bar{x}_1)}{4(t-\tau)D}\right) d\bar{x}_1\, d\bar{x}_2\, d\tau$$

$$= -\xi \sum_{j=1}^{N} \int_0^t \frac{e^{-\eta(t-\tau)}}{4\pi(t-\tau)D} \int_{X_{j2}(\tau)-R}^{X_{j2}(\tau)+R} e^{-\frac{(x_2-\bar{x}_2)^2}{4(t-\tau)D}}$$

$$\times \int_{X_{j1}(\tau)-\sqrt{R^2-(\bar{x}_2-X_{j2}(\tau))^2}}^{X_{j1}(\tau)+\sqrt{R^2-(\bar{x}_2-X_{j2}(\tau))^2}} e^{-\frac{(x_1-\bar{x}_1)^2}{4D(t-\tau)}} \frac{2(x_1-\bar{x}_1)}{4(t-\tau)D} d\bar{x}_1\, d\bar{x}_2\, d\tau$$

$$= -\xi \sum_{j=1}^{N} \int_0^t \frac{e^{-\eta(t-\tau)}}{4\pi(t-\tau)D} \int_{X_{j2}(\tau)-R}^{X_{j2}(\tau)+R} e^{-\frac{(x_2-\bar{x}_2)^2}{4(t-\tau)D}}$$

$$\times \left(e^{-\frac{\left(x_1-X_{j1}(\tau)-\sqrt{R^2-\left[\bar{x}_2-X_{j2}(\tau)\right]^2}\right)^2}{4(t-\tau)D}} - e^{-\frac{\left(x_1-X_{j1}(\tau)+\sqrt{R^2-\left[\bar{x}_2-X_{j2}(\tau)\right]^2}\right)^2}{4(t-\tau)D}} \right) d\bar{x}_2\, d\tau$$

$$= -\xi \sum_{j=1}^{N} \int_0^t \frac{e^{-\eta(t-\tau)}}{4\pi(t-\tau)D} \int_{-R}^{+R} e^{-\frac{(x_2-X_{j2}(\tau)-\tilde{x}_2)^2}{4(t-\tau)D}} \left(e^{-\frac{\left(x_1-X_{j1}(\tau)-\sqrt{R^2-\tilde{x}_2^2}\right)^2}{4(t-\tau)D}} \right.$$

$$\left. -e^{-\frac{\left(x_1-X_{j1}(\tau)+\sqrt{R^2-\tilde{x}_2^2}\right)^2}{4(t-\tau)D}} \right) d\tilde{x}_2\, d\tau, \tag{4.14}$$

where in the last step we have used the change of variables

$$\tilde{x}_2 = \bar{x}_2 - X_{j2}(\tau).$$

Similarly we can proceed for $\partial_{x_2} f(x_1, x_2, t)$.

Finally substituting (4.14) into $(4.7)_1$ we can summarize, for $i = 1, \dots, N$, the following system:

$$
\begin{cases}
\dot{V}_{i1} & = \dfrac{\beta}{N}\displaystyle\sum_{j=1}^{N} \dfrac{1}{\left(1+\frac{||\mathbf{X}_i-\mathbf{X}_j||^2}{R^2}\right)^{\sigma}}(V_{j1}-V_{i1}) \\[2ex]
& -\gamma\xi \displaystyle\int_0^t \dfrac{e^{-\eta(t-\tau)}}{4\pi(t-\tau)D} \sum_{j=1}^{N} \int_{-R}^{+R} e^{-\frac{(X_{i2}(t)-X_{j2}(\tau)-\tilde{x}_2)^2}{4(t-\tau)D}} \left(e^{-\frac{\left(X_{i1}(t)-X_{j1}(\tau)-\sqrt{R^2-\tilde{x}_2^2}\right)^2}{4(t-\tau)D}} \right. \\[2ex]
& \left. -e^{-\frac{\left(X_{i1}(t)-X_{j1}(\tau)+\sqrt{R^2-\tilde{x}_2^2}\right)^2}{4(t-\tau)D}} \right) d\tilde{x}_2\, d\tau, \\[2ex]
\dot{V}_{i2} & = \dfrac{\beta}{N}\displaystyle\sum_{j=1}^{N} \dfrac{1}{\left(1+\frac{||\mathbf{X}_i-\mathbf{X}_j||^2}{R^2}\right)^{\sigma}}(V_{j2}-V_{i2}) \\[2ex]
& -\gamma\xi \displaystyle\int_0^t \dfrac{e^{-\eta(t-\tau)}}{4\pi(t-\tau)D} \sum_{j=1}^{N} \int_{-R}^{+R} e^{-\frac{(X_{i1}(t)-X_{j1}(\tau)-\tilde{x}_1)^2}{4(t-\tau)D}} \left(e^{-\frac{\left(X_{i2}(t)-X_{j2}(\tau)-\sqrt{R^2-\tilde{x}_1^2}\right)^2}{4(t-\tau)D}} \right. \\[2ex]
& \left. -e^{-\frac{\left(X_{i2}(t)-X_{j2}(\tau)+\sqrt{R^2-\tilde{x}_1^2}\right)^2}{4(t-\tau)D}} \right) d\tilde{x}_1\, d\tau \\[2ex]
\dot{X}_{i1} & = V_{i1}, \\[1ex]
\dot{X}_{i2} & = V_{i2}.
\end{cases}
\tag{4.15}
$$

4.3 Local existence and uniqueness of the solution

In this section, using a fixed point argumentation, we prove for (4.15) local existence and uniqueness of the solution. In the next section, then, this result will be extended proving global existence and uniqueness. In the following discussion classic results will be adapted for our equations.

First, let $\mathbf{y} = (\mathbf{V}_1, \ldots, \mathbf{V}_N, \mathbf{X}_1, \ldots, \mathbf{X}_N)$ the solution vector, and let

$$\mathbf{q} := (\mathbf{q}_1, \mathbf{q}_2),$$

with

$$\begin{aligned}
q_{1,i1} &:= \frac{\beta}{N}\sum_{j=1}^{N} \frac{1}{\left(1+\frac{\|\mathbf{X}_j-\mathbf{X}_i\|^2}{R^2}\right)^{\sigma}}(V_{j1}-V_{i1}), && (4.16)\\
q_{1,i2} &:= \frac{\beta}{N}\sum_{j=1}^{N} \frac{1}{\left(1+\frac{\|\mathbf{X}_j-\mathbf{X}_i\|^2}{R^2}\right)^{\sigma}}(V_{j2}-V_{i2}), && (4.17)\\
q_{2,i1} &:= V_{i1}, && (4.18)\\
q_{2,i2} &:= V_{i2}. && (4.19)
\end{aligned}$$

and then

$$\mathbf{p} := (\mathbf{p}_1, \mathbf{p}_2),$$

with

$$\begin{aligned}
p_{1,i1} &:= \sum_{j=1}^{N}\int_{-R}^{+R} e^{-\frac{(X_{i2}(t)-X_{j2}(\tau)-\tilde{x}_2)^2}{4(t-\tau)D}} \left(e^{-\frac{\left(X_{i1}(t)-X_{j1}(\tau)-\sqrt{R^2-\tilde{x}_2^2}\right)^2}{4(t-\tau)D}} \right.\\
&\quad \left. -e^{-\frac{\left(X_{i1}(t)-X_{j1}(\tau)+\sqrt{R^2-\tilde{x}_2^2}\right)^2}{4(t-\tau)D}} \right) d\tilde{x}_2, && (4.20)\\
p_{1,i2} &:= \sum_{j=1}^{N}\int_{-R}^{+R} e^{-\frac{(X_{i1}(t)-X_{j1}(\tau)-\tilde{x}_1)^2}{4(t-\tau)D}} \left(e^{-\frac{\left(X_{i2}(t)-X_{j2}(\tau)-\sqrt{R^2-\tilde{x}_1^2}\right)^2}{4(t-\tau)D}} \right.\\
&\quad \left. -e^{-\frac{\left(X_{i2}(t)-X_{j2}(\tau)+\sqrt{R^2-\tilde{x}_1^2}\right)^2}{4(t-\tau)D}} \right) d\tilde{x}_1, && (4.21)\\
p_{2,i1} &= p_{2,i2} = 0.
\end{aligned}$$

Finally, if

$$C(t-\tau) := \frac{\gamma\xi e^{-\eta(t-\tau)}}{4\pi(t-\tau)D},$$

system (4.15) can be written as

$$\dot{\mathbf{y}} = \mathbf{q}(\mathbf{y}) + \int_0^t C(t-\tau)\mathbf{p}(t-\tau, \mathbf{y}(t), \mathbf{y}(\tau))\, d\tau.$$

Integrating from 0 to t we have

$$\mathbf{y} = \mathbf{y}_0 + \int_0^t \mathbf{q}(\mathbf{y}(\tau))\, d\tau + \int_0^t\int_0^s C(s-\tau)\mathbf{p}(s-\tau, \mathbf{y}(s), \mathbf{y}(\tau))\, d\tau\, ds,$$

with $\mathbf{y}_0 = \mathbf{y}(0)$. Then, interchanging the order of integration in the second integral we have

$$\mathbf{y} = \mathbf{y}_0 + \int_0^t \left[\mathbf{q}(\mathbf{y}(\tau)) + \int_\tau^t C(s-\tau)\mathbf{p}(s-\tau, \mathbf{y}(s), \mathbf{y}(\tau))\, ds\right] d\tau, \tag{4.22}$$

or

$$\mathbf{y} = \mathbf{y}_0 + \int_0^t \left[\mathbf{q}(\mathbf{y}(\tau)) + \mathbf{h}(t, \tau, \mathbf{y}(\tau))\right] d\tau, \tag{4.23}$$

with

$$\mathbf{h}(t, \tau, \mathbf{y}(\tau)) := \int_\tau^t C(s-\tau)\mathbf{p}(s-\tau, \mathbf{y}(s), \mathbf{y}(\tau))\, ds,$$

Now, let $a, b > 0$, we consider the set

$$S = \left\{(t, \tau, s, \mathbf{y}) : 0 \le \tau \le s \le t \le a,\ \|\mathbf{y}(t) - \mathbf{y}_0\| \le b\right\}.$$

Since $\mathbf{q}(\mathbf{y})$ is continuous on S, we can define

$$M_1 = \max_S \|\mathbf{q}(\mathbf{y})\|. \tag{4.24}$$

Then, to prove that $\mathbf{h}(t, \tau, \mathbf{y}(\tau))$ is continuous in S, firstly we prove that $C(s-\tau)\mathbf{p}(s-\tau, \mathbf{y}(s), \mathbf{y}(\tau))$ in $L^1(\tau, t)$ with respect to variable s. It is sufficient to demonstrate the integrability around $s = \tau$. Starting from (4.20), we consider $p_{1,i1}(s-\tau, \mathbf{y}(s), \mathbf{y}(\tau))$, and the change of variables

$$\frac{X_{i2} - X_{j2} - \tilde{x}_2}{\sqrt{4(s-\tau)D}} = z. \tag{4.25}$$

Since the quantity in brackets is bounded by 1, we have

$$\begin{aligned}
|p_{1,i1}(s-\tau, \mathbf{y}(s), \mathbf{y}(\tau))| &\le \sum_{j=1}^N \int_{-R}^{+R} e^{-\frac{(X_{i2}(s) - X_{j2}(\tau) - \tilde{x}_2)^2}{4(s-\tau)D}}\, d\tilde{x}_2 \\
&= \sqrt{4(s-\tau)D} \sum_{j=1}^N \int_{\frac{X_{i2} - X_{j2} - R}{\sqrt{4(s-\tau)D}}}^{\frac{X_{i2} - X_{j2} + R}{\sqrt{4(s-\tau)D}}} e^{-z^2}\, dz \\
&\le \sqrt{4(s-\tau)D} \sum_{j=1}^N \int_{-\infty}^{+\infty} e^{-z^2}\, dz \\
&= \bar{M}\sqrt{4(s-\tau)D},
\end{aligned}$$

with

$$\bar{M} := N \int_{-\infty}^{+\infty} e^{-z^2}\, dz. \tag{4.26}$$

The same holds for $p_{1,i2}$ in (4.21), so we can write

$$\|\mathbf{p}(s-\tau, \mathbf{y}(s), \mathbf{y}(\tau))\| \le \bar{M}\sqrt{2N}\sqrt{4(s-\tau)D}, \tag{4.27}$$

and

$$|C(s-\tau)|\, \|\mathbf{p}(s-\tau, \mathbf{y}(s), \mathbf{y}(\tau))\| \le \frac{\gamma\xi\bar{M}\sqrt{2N}e^{-\eta(s-\tau)}}{2\pi\sqrt{(s-\tau)D}}. \tag{4.28}$$

Now $C(s-\tau)\mathbf{p}(s-\tau,\mathbf{y}(s),\mathbf{y}(\tau))$ is continuous in $\mathbf{y}$ and, from (4.28), it is $L^1(\tau,t)$ with respect to variable s, so $\mathbf{h}(t,\tau,\mathbf{y}(\tau))$ is continuous in S, and we can define

$$M_2 = \max_S \|\mathbf{h}(t,\tau,\mathbf{y}(\tau))\| . \tag{4.29}$$

To prove local existence and uniqueness we want to obtain a Lipschitz condition in S for the functions $\mathbf{q}$ and $\mathbf{p}$ with respect to the variable $\mathbf{y}$. First, because of $\mathbf{q}$ is C^1 on S, the Jacobian matrix $[\partial\mathbf{q}/\partial\mathbf{y}]$ is bounded on S uniformly in τ, so $\mathbf{q}$ satisfies the Lipschitz condition

$$\|\mathbf{q}(\mathbf{y}_1)-\mathbf{q}(\mathbf{y}_2)\| \le L_1 \|\mathbf{y}_1-\mathbf{y}_2\| , \tag{4.30}$$

with L_1 positive constant and $(t,\tau,s,\mathbf{y}_1)$, $(t,\tau,s,\mathbf{y}_2) \in S$.

Then, from (4.20) we define

$$\bar{p}_{1,i1,j1}(s-\tau,\mathbf{y}(s),\mathbf{y}(\tau),\tilde{x}_2) := e^{-\frac{\left(X_{i1}(s)-X_{j1}(\tau)-\sqrt{R^2-\tilde{x}_2^2}\right)^2}{4(s-\tau)D}} - e^{-\frac{\left(X_{i1}(s)-X_{j1}(\tau)+\sqrt{R^2-\tilde{x}_2^2}\right)^2}{4(s-\tau)D}} . \tag{4.31}$$

For the Jacobian matrix of (4.31), hold the following equalities

$$\frac{\partial\bar{p}_{1,i1,j1}}{\partial V_{k1}} = \frac{\partial\bar{p}_{1,i1,j1}}{\partial V_{k2}} = 0$$

$$\frac{\partial\bar{p}_{1,i1,j1}}{\partial X_{k1}} = \begin{cases} -\left[e^{-\frac{\left(X_{i1}(s)-X_{j1}(\tau)-\sqrt{R^2-\tilde{x}_2^2}\right)^2}{4(s-\tau)D}} \frac{X_{i1}(s)-X_{j1}(\tau)-\sqrt{R^2-\tilde{x}_2^2}}{2(s-\tau)D} \right. \\ \left. -e^{-\frac{\left(X_{i1}(s)-X_{j1}(\tau)+\sqrt{R^2-\tilde{x}_2^2}\right)^2}{4(s-\tau)D}} \frac{X_{i1}(s)-X_{j1}(\tau)+\sqrt{R^2-\tilde{x}_2^2}}{2(s-\tau)D}\right], & k=i; \\ \delta_{jk}\left[e^{-\frac{\left(X_{i1}(s)-X_{j1}(\tau)-\sqrt{R^2-\tilde{x}_2^2}\right)^2}{4(s-\tau)D}} \frac{X_{i1}(s)-X_{j1}(\tau)-\sqrt{R^2-\tilde{x}_2^2}}{2(s-\tau)D} \right. \\ \left. -e^{-\frac{\left(X_{i1}(s)-X_{j1}(\tau)+\sqrt{R^2-\tilde{x}_2^2}\right)^2}{4(s-\tau)D}} \frac{X_{i1}(s)-X_{j1}(\tau)+\sqrt{R^2-\tilde{x}_2^2}}{2(s-\tau)D}\right], & k\neq i; \end{cases}$$

$$\frac{\partial\bar{p}_{1,i1,j1}}{\partial X_{k2}} = 0.$$

Since these quantities are bounded in S uniformly in $\tilde{x}_2$, τ, s, we can write

$$|\bar{p}_{1,i1,j1}(s-\tau,\mathbf{y}_1(s),\mathbf{y}_1(\tau),\tilde{x}_2) - \bar{p}_{1,i1,j1}(s-\tau,\mathbf{y}_2(s),\mathbf{y}_2(\tau),\tilde{x}_2)| \le$$

$$l_2\left(\|\mathbf{y}_1(s)-\mathbf{y}_2(s)\| + \|\mathbf{y}_1(\tau)-\mathbf{y}_2(\tau)\|\right), \tag{4.32}$$

where l_2 is a positive constant, and $(\tau, s, \mathbf{y}_1)$, $(\tau, s, \mathbf{y}_2) \in S$. From this we deduce

$$
\begin{aligned}
& |p_{1,i1}(s-\tau, \mathbf{y}_1(s), \mathbf{y}_1(\tau)) - p_{1,i1}(s-\tau, \mathbf{y}_2(s), \mathbf{y}_2(\tau))| \leq \\
& \sum_{j=1}^{N} \int_{-R}^{+R} \left| e^{-\frac{(X_{i2}^{(1)}(s)-X_{j2}^{(1)}(\tau)-\tilde{x}_2)^2}{4D(s-\tau)}} - e^{-\frac{(X_{i2}^{(2)}(s)-X_{j2}^{(2)}(\tau)-\tilde{x}_2)^2}{4D(s-\tau)}} \right| \\
& \times |\bar{p}_{1,i1,j1}(s-\tau, \mathbf{y}_1(s), \mathbf{y}_1(\tau), \tilde{x}_2) - \bar{p}_{1,i1,j1}(s-\tau, \mathbf{y}_2(s), \mathbf{y}_2(\tau), \tilde{x}_2)| \, d\tilde{x}_2 \\
& =_{(4.32),(4.25)} \sqrt{4D(s-\tau)} l_2 \left(\|\mathbf{y}_1(s) - \mathbf{y}_2(s)\| + \|\mathbf{y}_1(\tau) - \mathbf{y}_2(\tau)\| \right) \\
& \times \sum_{j=1}^{N} \left(\int_{\frac{X_{i2}^{(1)}(s)-X_{j2}^{(1)}(\tau)-R}{\sqrt{4(s-\tau)D}}}^{\frac{X_{i2}^{(1)}(s)-X_{j2}^{(1)}(\tau)+R}{\sqrt{4(s-\tau)D}}} e^{-z^2}\, dz + \int_{\frac{X_{i2}^{(2)}(s)-X_{j2}^{(2)}(\tau)-R}{\sqrt{4(s-\tau)D}}}^{\frac{X_{i2}^{(2)}(s)-X_{j2}^{(2)}(\tau)+R}{\sqrt{4(s-\tau)D}}} e^{-z^2}\, dz \right) \\
& \leq \sqrt{4D(s-\tau)} l_2 \left(\|\mathbf{y}_1(s) - \mathbf{y}_2(s)\| + \|\mathbf{y}_1(\tau) - \mathbf{y}_2(\tau)\| \right) 2 \sum_{j=1}^{N} \int_{-\infty}^{+\infty} e^{-z^2}\, dz \\
& =_{(4.26)} \sqrt{4D(s-\tau)} 2\bar{M} l_2 \left(\|\mathbf{y}_1(s) - \mathbf{y}_2(s)\| + \|\mathbf{y}_1(\tau) - \mathbf{y}_2(\tau)\| \right),
\end{aligned}
$$

where we have used the change of variables (4.25). Moreover, $X^{(1)}$, $X^{(2)}$ are the variables belonging respectively to the vectors $\mathbf{y}_1$, $\mathbf{y}_2$, and $(t, \tau, s, \mathbf{y}_1)$, $(t, \tau, s, \mathbf{y}_2) \in S$.

The same can be done for $p_{1,i2}$, so $\mathbf{p}$ satisfy the following condition in $\mathbf{y}$ on S:

$$
\begin{aligned}
\|\mathbf{p}(s-\tau, \mathbf{y}_1(s), \mathbf{y}_1(\tau)) - \mathbf{p}(s-\tau, \mathbf{y}_2(s), \mathbf{y}_2(\tau))\| \leq \sqrt{4D(s-\tau)} L_2 \left(\|\mathbf{y}_1(s) - \mathbf{y}_2(s)\| \right. \\
\left. + \|\mathbf{y}_1(\tau) - \mathbf{y}_2(\tau)\| \right), \qquad (4.33)
\end{aligned}
$$

with L_2 a suitable positive constant that incorporates previous constants, and $(\tau, s, \mathbf{y}_1)$, $(\tau, s, \mathbf{y}_2) \in S$.

Now, we fix

$$
T = \min \left\{ a, \frac{b}{M_1 + M_2}, \frac{1}{L_1 + 2L_2 M} \right\}, \tag{4.34}
$$

with M_1, M_2 given by (4.24)–(4.29), and

$$
M := \int_0^{+\infty} |C(z)| \sqrt{4Dz}\, dz. \tag{4.35}
$$

To prove local existence and uniqueness for the solution of (4.23) we first recall some classic results (see, for instance, Burton, 2005):

Definition 3 *Let $(\mathcal{B}, \rho)$ be a metric space and $\mathbf{A} : \mathcal{B} \to \mathcal{B}$. The operator $\mathbf{A}$ is a contraction operator if there is an $\alpha \in (0,1)$ such that $x, y \in \mathcal{B}$ imply*

$$
\rho\left[\mathbf{A}(x), \mathbf{A}(y)\right] \leq \alpha \rho(x, y).
$$

Theorem 1 (Banach–Caccioppoli Fixed–Point Theorem) *Let $(\mathcal{B}, \rho)$ be a complete metric space and $\mathbf{A} : \mathcal{B} \to \mathcal{B}$ a contraction operator. Then there is a unique $\phi \in \mathcal{B}$ with $\mathbf{A}(\phi) = \phi$. Furthermore, if $\psi \in \mathcal{B}$ and if $\{\psi_n\}$ is defined inductively by $\psi_1 = \mathbf{A}(\psi)$ and $\psi_{n+1} = \mathbf{A}(\psi_n)$, then $\psi_n \to \phi$, the unique fixed point. That is, the equation $\mathbf{A}(\phi) = \phi$ has one and only one solution.*

Then we prove the following

Theorem 2 *Equation* (4.23) *has a unique solution on* $[0, T]$, *where* T *is defined in* (4.34).

Proof. We consider the functional space

$$\mathcal{B} = \left\{ \mathbf{y} \in C^0 \left([0, T] \right) : ||\mathbf{y} - \mathbf{y}_0||_{C^0} \leq b \right\},$$

where

$$||\mathbf{y} - \mathbf{z}||_{C^0} := \sup_{0 \leq t \leq T} \|\mathbf{y}(t) - \mathbf{z}(t)\|,$$

and we define the functional $\mathbf{A} : \mathcal{B} \to \mathcal{B}$ as

$$\mathbf{A}(\mathbf{y})(t) := \mathbf{y}_0 + \int_0^t \left[\mathbf{q}(\mathbf{y}(\tau)) + \mathbf{h}(t, \tau, \mathbf{y}(\tau)) \right] d\tau,$$

To see that $\mathbf{A} : \mathcal{B} \to \mathcal{B}$ notice that $\mathbf{y}$ continuous implies $\mathbf{A}(\mathbf{y})$ continuous, because $\mathbf{q}$ and $\mathbf{h}$ are continuous, and that

$$\begin{aligned} \|\mathbf{A}(\mathbf{y}) - \mathbf{y}_0\|_{C^0} &= \sup_{0 \leq t \leq T} \|\mathbf{A}(\mathbf{y})(t) - \mathbf{y}_0\| \\ &\leq \sup_{0 \leq t \leq T} \int_0^t \left(\|\mathbf{q}(\mathbf{y}(\tau))\| + \|\mathbf{h}(t, \tau, \mathbf{y}(\tau))\| \right) d\tau \\ &\leq (M_1 + M_2) T \\ &\leq b, \end{aligned}$$

where we have used (4.24), (4.29) and, in the last inequality, (4.34). To see that $\mathbf{A}$ is a contraction mapping, notice that if $\mathbf{y}_1$ and $\mathbf{y}_2 \in \mathcal{B}$ then

$$\begin{aligned} &\|\mathbf{A}(\mathbf{y}_1) - \mathbf{A}(\mathbf{y}_2)\|_{C^0} = \sup_{0 \leq t \leq T} \|\mathbf{A}(\mathbf{y}_1)(t) - \mathbf{A}(\mathbf{y}_2)(t)\| \\ &\leq \sup_{0 \leq t \leq T} \int_0^t \left(\|\mathbf{q}(\mathbf{y}_1(\tau)) - \mathbf{q}(\mathbf{y}_2(\tau))\| \right. \\ &+ \left. \int_\tau^t |C(s - \tau)| \, \|\mathbf{p}(s - \tau, \mathbf{y}_1(s), \mathbf{y}_1(\tau)) - \mathbf{p}(s - \tau, \mathbf{y}_2(s), \mathbf{y}_2(\tau))\| \right) ds \, d\tau \\ &\leq_{(4.30),(4.33)} \sup_{0 \leq t \leq T} \int_0^t \left[L_1 \|\mathbf{y}_1(\tau) - \mathbf{y}_2(\tau)\| + L_2 \int_\tau^t |C(s - \tau)| \sqrt{4D(s - \tau)} \right. \\ &\left. (\|\mathbf{y}_1(s) - \mathbf{y}_2(s)\| + \|\mathbf{y}_1(\tau) - \mathbf{y}_2(\tau)\|) \right] ds \, d\tau \\ &\leq L_1 T \|\mathbf{y}_1 - \mathbf{y}_2\|_{C^0} + 2L_2 \|\mathbf{y}_1 - \mathbf{y}_2\|_{C^0} \\ &\times \sup_{0 \leq t \leq T} \int_0^t \int_\tau^t |C(s - \tau)| \sqrt{4D(s - \tau)} \, ds \, d\tau \\ &= \left(L_1 T + 2L_2 \sup_{0 \leq t \leq T} \int_0^t \int_0^{t - \tau} |C(z)| \sqrt{4Dz} \, dz \, d\tau \right) \|\mathbf{y}_1 - \mathbf{y}_2\|_{C^0} \\ &\leq \left(L_1 T + 2L_2 \int_0^T \int_0^{+\infty} |C(z)| \sqrt{4Dz} \, dz \, d\tau \right) \|\mathbf{y}_1 - \mathbf{y}_2\|_{C^0} \\ &= (L_1 + 2L_2 M) T \|\mathbf{y}_1 - \mathbf{y}_2\|_{C^0}. \end{aligned}$$

From (4.34) the constant $(L_1 + 2L_2 M)T \in (0, 1)$. Definition 3 and Theorem 1 complete the proof.

4.4 Global existence and uniqueness of the solution

To obtain global existence and uniqueness for (4.22) we will use a principle of continuation of solutions. We will prove that bounded solutions can be continued to $t = +\infty$. Firstly, we recall the following

Lemma 1 (Gronwall's inequality) *Let u and v be continuous non-negative scalar functions on $[t_0, T)$ and let $K \geq 0$. If*

$$u(t) \leq K + \int_{t_0}^{t} v(s)u(s)\, ds$$

for $t_0 \leq t < T$, then

$$u(t) \leq K e^{\int_{t_0}^{t} v(s)\, ds}, \quad t_0 \leq t < T.$$

Moreover, if u is differentiable in $t_0 < t < T$ and satisfies

$$u'(t) \leq w(t)u(t), \quad t_0 < t < T,$$

with w continuous function on $[t_0, T)$, also negative, then

$$u(t) \leq u(t_0) e^{\int_{t_0}^{t} w(s)\, ds}, \quad t_0 \leq t < T.$$

The following general result, adapted for equation (4.22), provides a condition for the continuation of solutions.

Proposition 3 *Let $\mathbf{y}(t)$ be a solution of (4.22) on a interval $[0, T)$, if there is a constant P with $\|\mathbf{y} - \mathbf{y}_0\| \leq P$ on $[0, T)$, then there is a $\bar{T} > T$ such that $\mathbf{y}(t)$ can be continued to $[0, \bar{T}]$.*

Proof. We show that $\lim_{t \to T^-} \mathbf{y}(t)$ exists, so we can applied Theorem 2 starting at $t = T$, and this complete the proof.

Let t_n be a monotonic increasing sequence with limit T, and let

$$\bar{U} = \left\{(t, \tau, s, \mathbf{y}) : 0 \leq \tau \leq s \leq t \leq T,\ \|\mathbf{y} - \mathbf{y}_0\| \leq P\right\}.$$

We prove that $\{\mathbf{y}(t_n)\}$ is a Cauchy sequence. If $t_m > t_n$, from (4.22) we have

$$\begin{aligned}
\|\mathbf{y}(t_m) - \mathbf{y}(t_n)\| &= \bigg\| \int_0^{t_m} \left[\mathbf{q}(\mathbf{y}(\tau)) + \int_\tau^{t_m} C(s-\tau)\mathbf{p}(s-\tau, \mathbf{y}(s), \mathbf{y}(\tau))\, ds \right] d\tau \\
&\quad - \int_0^{t_n} \left[\mathbf{q}(\mathbf{y}(\tau)) + \int_\tau^{t_n} C(s-\tau)\mathbf{p}(s-\tau, \mathbf{y}(s), \mathbf{y}(\tau))\, ds \right] d\tau \bigg\| \\
&\le \int_0^{t_n} \bigg\| \int_\tau^{t_m} C(s-\tau)\mathbf{p}(s-\tau, \mathbf{y}(s), \mathbf{y}(\tau))\, ds \\
&\quad - \int_\tau^{t_n} C(s-\tau)\mathbf{p}(s-\tau, \mathbf{y}(s), \mathbf{y}(\tau))\, ds \bigg\|\, d\tau \\
&\quad + \bigg\| \int_{t_n}^{t_m} \left[\mathbf{q}(\mathbf{y}(\tau)) + \int_\tau^{t_m} C(s-\tau)\mathbf{p}(s-\tau, \mathbf{y}(s), \mathbf{y}(\tau))\, ds \right] d\tau \bigg\| \\
&\le \int_0^{t_n} \bigg\| \int_{t_n}^{t_m} C(s-\tau)\mathbf{p}(s-\tau, \mathbf{y}(s), \mathbf{y}(\tau))\, ds \bigg\|\, d\tau \\
&\quad + \bigg\| \int_{t_n}^{t_m} \int_\tau^{t_m} C(s-\tau)\mathbf{p}(s-\tau, \mathbf{y}(s), \mathbf{y}(\tau))\, ds\, d\tau \bigg\| \\
&\quad + \bigg\| \int_{t_n}^{t_m} \mathbf{q}(\mathbf{y}(\tau))\, d\tau \bigg\| \\
&\le \int_0^{t_n} \int_{t_n}^{t_m} \| C(s-\tau)\mathbf{p}(s-\tau, \mathbf{y}(s), \mathbf{y}(\tau)) \|\, ds\, d\tau \\
&\quad + \int_{t_n}^{t_m} \int_\tau^{t_m} \| C(s-\tau)\mathbf{p}(s-\tau, \mathbf{y}(s), \mathbf{y}(\tau)) \|\, ds\, d\tau \\
&\quad + \int_{t_n}^{t_m} \| \mathbf{q}(\mathbf{y}(\tau)) \|\, d\tau.
\end{aligned}$$

In the last inequality the third integral go to zero as $n, m \to +\infty$, because $\mathbf{q}$ is bounded on $\bar{U}$ and $t_m, t_n \to T$. Also the first two integral go to zero as $n, m \to +\infty$, because of (4.28). The proof is completed.

Now, from Proposition 3, we obtain the following

Theorem 3 *Equation* (4.23) *has a unique solution in all* $[0, +\infty)$

Proof. First, equations (4.16)–(4.19) implies

$$\begin{aligned}
|q_{1,i1}| &\le 2\beta ||\mathbf{y}||, \\
|q_{1,i2}| &\le 2\beta ||\mathbf{y}||, \\
|q_{2,i1}| &\le ||\mathbf{y}||, \\
|q_{2,i2}| &\le ||\mathbf{y}||,
\end{aligned}$$

so that

$$||\mathbf{q}|| \le \sqrt{2N(4\beta^2 + 1)}||\mathbf{y}||.$$

Then (4.27) establishes

$$\|\mathbf{p}(s-\tau, \mathbf{y}(s), \mathbf{y}(\tau))\| \le \bar{M}\sqrt{2N}\sqrt{4D(s-\tau)},$$

so from (4.22) we have

$$
\begin{aligned}
||\mathbf{y}|| \leq ||\mathbf{y}_0|| + \sqrt{2N(4\beta^2+1)} \int_0^t ||\mathbf{y}(\tau)||\, d\tau \\
+ \bar{M}\sqrt{2N} \int_0^t \int_\tau^t |C(s-\tau)| \sqrt{4D(s-\tau)}\, ds\, d\tau \\
= ||\mathbf{y}_0|| + \sqrt{2N(4\beta^2+1)} \int_0^t ||\mathbf{y}(\tau)||\, d\tau + \bar{M}\sqrt{2N} \int_0^t \int_0^{t-\tau} |C(z)| \sqrt{4Dz}\, dz\, d\tau \\
\leq ||\mathbf{y}_0|| + \sqrt{2N(4\beta^2+1)} \int_0^t ||\mathbf{y}(\tau)||\, d\tau + \bar{M}\sqrt{2N} \int_0^t \int_0^{+\infty} |C(z)| \sqrt{4Dz}\, dz\, d\tau \\
= ||\mathbf{y}_0|| + \sqrt{2N(4\beta^2+1)} \int_0^t ||\mathbf{y}(\tau)||\, d\tau + M\bar{M}\sqrt{2N}t,
\end{aligned}
$$

where we have set $z = s - \tau$, and M is given by (4.35).

Now, for each $0 \leq t < T$,

$$
||\mathbf{y}|| \leq \left(||\mathbf{y}_0|| + M\bar{M}\sqrt{2N}T\right) + \sqrt{2N(4\beta^2+1)} \int_0^t ||\mathbf{y}(\tau)||\, d\tau,
$$

so that

$$
||\mathbf{y}|| \leq \left(||\mathbf{y}_0|| + M\bar{M}\sqrt{2N}T\right) e^{t\sqrt{2N(4\beta^2+1)}},
$$

by Gronwall's inequality (Lemma 1). Since solution remains bounded, for Proposition 3, it is continuable to all $[0, +\infty)$.

4.5 Asymptotic properties on the linearized system

In this section we prove some asymptotic properties on the linearized form of system (4.15) that, for convenience we recall here:

$$\begin{cases} \dot{V}_{i1} &= \dfrac{\beta}{N}\displaystyle\sum_{j=1}^{N} \dfrac{1}{\left(1+\frac{\|\mathbf{X}_i-\mathbf{X}_j\|^2}{R^2}\right)^{\sigma}}(V_{j1}-V_{i1}) \\ & -\displaystyle\int_0^t C(t-\tau)\sum_{j=1}^{N}\int_{-R}^{+R} e^{-\frac{(X_{i2}(t)-X_{j2}(\tau)-\tilde{x}_2)^2}{4(t-\tau)D}}\left(e^{-\frac{\left(X_{i1}(t)-X_{j1}(\tau)-\sqrt{R^2-\tilde{x}_2^2}\right)^2}{4(t-\tau)D}}\right. \\ & \left. -e^{-\frac{\left(X_{i1}(t)-X_{j1}(\tau)+\sqrt{R^2-\tilde{x}_2^2}\right)^2}{4(t-\tau)D}}\right) d\tilde{x}_2\, d\tau, \\ \dot{V}_{i2} &= \dfrac{\beta}{N}\displaystyle\sum_{j=1}^{N} \dfrac{1}{\left(1+\frac{\|\mathbf{X}_i-\mathbf{X}_j\|^2}{R^2}\right)^{\sigma}}(V_{j2}-V_{i2}) \\ & -\displaystyle\int_0^t C(t-\tau)\sum_{j=1}^{N}\int_{-R}^{+R} e^{-\frac{(X_{i1}(t)-X_{j1}(\tau)-\tilde{x}_1)^2}{4(t-\tau)D}}\left(e^{-\frac{\left(X_{i2}(t)-X_{j2}(\tau)-\sqrt{R^2-\tilde{x}_1^2}\right)^2}{4(t-\tau)D}}\right. \\ & \left. -e^{-\frac{\left(X_{i2}(t)-X_{j2}(\tau)+\sqrt{R^2-\tilde{x}_1^2}\right)^2}{4(t-\tau)D}}\right) d\tilde{x}_1\, d\tau, \\ \dot{X}_{i1} &= V_{i1}, \\ \dot{X}_{i2} &= V_{i2}, \end{cases} \tag{4.36}$$

with

$$C(t-\tau) := \frac{\gamma\xi e^{-\eta(t-\tau)}}{4\pi(t-\tau)D}. \tag{4.37}$$

We are interested in the equilibrium points that satisfy the condition:

$$\begin{cases} \mathbf{X}_i(t) = \mathbf{X}_{\text{eq}}(t), & \forall i, \quad \forall t; \\ \mathbf{V}_i(t) = \mathbf{0}, & \forall i; \end{cases} \quad \Leftrightarrow \quad \mathbf{X}_i(t) = \mathbf{X}_{\text{eq}} = \text{constant}, \quad \forall i. \tag{4.38}$$

Equation (4.38) means that all particles are in a same position for all times. Now, to make a first-order approximation of (4.15), we consider the following Taylor expansions around points (4.38):

$$\frac{1}{\left(1+\frac{\|\mathbf{X}_j-\mathbf{X}_i\|^2}{R^2}\right)^{\sigma}}(V_{j1}-V_{i1}) = V_{j1}-V_{1i}+\rho_1(\mathbf{X}_j-\mathbf{X}_i, V_{j1}-V_{i1}), \tag{4.39}$$

$$\begin{aligned}
e^{-\frac{(X_{i2}(t)-X_{j2}(\tau)-\tilde{x}_2)^2}{4(t-\tau)D}} &= e^{-\frac{\tilde{x}_2^2}{4(t-\tau)D}} + e^{-\frac{\tilde{x}_2^2}{4(t-\tau)D}} \frac{\tilde{x}_2}{2(t-\tau)D}\,(X_{i2}(t)-X_{j2}(\tau)) \\
&\quad + \rho_2(t-\tau, X_{i2}(t)-X_{j2}(\tau), \tilde{x}_2), \qquad (4.40) \\
e^{-\frac{\left(X_{i1}(t)-X_{j1}(\tau)\pm\sqrt{R^2-\tilde{x}_2^2}\right)^2}{4(t-\tau)D}} &= e^{-\frac{R^2-\tilde{x}_2^2}{4(t-\tau)D}} \mp e^{-\frac{R^2-\tilde{x}_2^2}{4(t-\tau)D}} \frac{\sqrt{R^2-\tilde{x}_2^2}}{2(t-\tau)D}\,(X_{i1}(t)-X_{j1}(\tau)) \\
&\quad + \rho_3(t-\tau, X_{i1}(t)-X_{j1}(\tau), \tilde{x}_2), \qquad (4.41)
\end{aligned}$$

where the functions ρ_1, ρ_2 and ρ_3 contain the nonlinear terms. Similarly we can treat equation $(4.36)_2$.

From (4.39)–(4.41), we linearize equation $(4.36)_1$ in the form

$$\begin{aligned}
\dot{V_{i1}} &= \frac{\beta}{N}\sum_{j=1}^{N}(V_{j1}(t)-V_{i1}(t)) - \int_0^t \frac{C(t-\tau)}{2(t-\tau)D}\int_{-R}^{+R} e^{-\frac{\tilde{x}_2^2}{4(t-\tau)D}} e^{-\frac{R^2-\tilde{x}_2^2}{4(t-\tau)D}} \sqrt{R^2-\tilde{x}_2} \\
&\times \sum_{j=1}^{N}(X_{i1}(t)-X_{j1}(\tau)+X_{i1}(t)-X_{j1}(\tau))\,d\tilde{x}_2\,d\tau \\
&= \frac{\beta}{N}\sum_{j=1}^{N}(V_{j1}(t)-V_{i1}(t)) - \int_0^t \frac{C(t-\tau)e^{-\frac{R^2}{4(t-\tau)D}}}{(t-\tau)D}\int_{-R}^{+R}\sqrt{R^2-\tilde{x}_2^2}\,d\tilde{x}_2 \\
&\times \sum_{j=1}^{N}(X_{i1}(t)-X_{j1}(\tau))\,d\tau \\
&= \frac{\beta}{N}\sum_{j=1}^{N}(V_{j1}(t)-V_{i1}(t)) - \int_0^t \bar{C}(t-\tau)\sum_{j=1}^{N}(X_{i1}(t)-X_{j1}(\tau))\,d\tau,
\end{aligned}$$

with

$$\bar{C}(t-\tau) := \frac{\pi R^2 C(t-\tau)e^{-\frac{R^2}{4(t-\tau)D}}}{2(t-\tau)D}. \tag{4.42}$$

Similarly it can be done for $\dot{V_{i2}}$. Finally, we obtain

$$\begin{cases}
\dot{V_{i1}} &= \frac{\beta}{N}\sum_{j=1}^{N}(V_{j1}(t)-V_{i1}(t)) - \int_0^t \bar{C}(t-\tau)\sum_{j=1}^{N}(X_{i1}(t)-X_{j1}(\tau))\,d\tau, \\
\dot{V_{i2}} &= \frac{\beta}{N}\sum_{j=1}^{N}(V_{j2}(t)-V_{i2}(t)) - \int_0^t \bar{C}(t-\tau)\sum_{j=1}^{N}(X_{i2}(t)-X_{j2}(\tau))\,d\tau, \\
\dot{X_{i1}} &= V_{i1}, \\
\dot{X_{i2}} &= V_{i2}.
\end{cases} \tag{4.43}$$

First, we are interested to establish a time-asymptotic convergence property of all particles towards a same position and a same velocity. For this it is convenient to introduce the centre of mass system, in which equations (4.43) become a nonautonomous system of ordinary differential equation, decoupled with respect to the i-th particle and with respect to the two components of each position and velocity vector. Then the equation of the centre of mass can be studied apart.

We define position and velocity of the centre of mass of a system of N particles with same mass, as

$$\mathbf{X}_{\mathrm{CM}} := \frac{1}{N}\sum_{i=1}^{N}\mathbf{X}_i, \tag{4.44}$$

$$\mathbf{V}_{\mathrm{CM}} := \frac{1}{N}\sum_{i=1}^{N}\mathbf{V}_i, \tag{4.45}$$

and we consider the new variables

$$\bar{\mathbf{X}}_i := \mathbf{X}_i - \mathbf{X}_{\mathrm{CM}}, \tag{4.46}$$

$$\bar{\mathbf{V}}_i := \mathbf{V}_i - \mathbf{V}_{\mathrm{CM}}. \tag{4.47}$$

In variables (4.46)–(4.47) the equilibrium condition (4.38) becomes

$$(\bar{\mathbf{X}}_i, \bar{\mathbf{V}}_i) = (\mathbf{0}, \mathbf{0}), \quad \forall i = 1, \ldots, N, \tag{4.48}$$

moreover the following identities hold:

$$\sum_{i=1}^{N}\bar{\mathbf{X}}_i = \mathbf{0}, \tag{4.49}$$

$$\sum_{i=1}^{N}\bar{\mathbf{V}}_i = \mathbf{0}. \tag{4.50}$$

If $\mathbf{V}_{\mathrm{CM}} = (V_{\mathrm{CM}1}, V_{\mathrm{CM}2})$ and $\mathbf{X}_{\mathrm{CM}} = (X_{\mathrm{CM}1}, X_{\mathrm{CM}2})$, from (4.43) we have

$$\begin{aligned}
\dot{V}_{\mathrm{CM}1} &= \frac{1}{N}\sum_{i=1}^{N}\dot{V}_{i1} = \frac{1}{N}\frac{\beta}{N}\sum_{i=1}^{N}\sum_{j=1}^{N}(V_{j1}(t) - V_{i1}(t)) \\
&- \frac{1}{N}\int_0^t \bar{C}(t-\tau)\sum_{i=1}^{N}\sum_{j=1}^{N}\left(X_{i1}(t) - X_{j1}(\tau)\right)\, d\tau \\
&= \frac{1}{N}\frac{\beta}{N}\sum_{i=1}^{N}(NV_{\mathrm{CM}1}(t) - NV_{i1}(t)) \\
&- \frac{1}{N}\int_0^t \bar{C}(t-\tau)\sum_{i=1}^{N}\left(NX_{i1}(t) - NX_{\mathrm{CM}1}(\tau)\right)\, d\tau \\
&= \frac{1}{N}\frac{\beta}{N}(N^2V_{\mathrm{CM}1}(t) - N^2V_{\mathrm{CM}1}(t)) \\
&- \frac{1}{N}\int_0^t \bar{C}(t-\tau)\left(N^2X_{\mathrm{CM}1}(t) - N^2X_{\mathrm{CM}1}(\tau)\right)\, d\tau \\
&= -\int_0^t \bar{C}(t-\tau)\left(NX_{\mathrm{CM}1}(t) - NX_{\mathrm{CM}1}(\tau)\right)\, d\tau,
\end{aligned} \tag{4.51}$$

where we have used definitions (4.44)–(4.45). The same holds for $\dot{V}_{\mathrm{CM2}}$:

$$\dot{V}_{\mathrm{CM2}} = -\int_0^t \bar{C}(t-\tau)\,(NX_{\mathrm{CM2}}(t) - NX_{\mathrm{CM2}}(\tau))\;d\tau. \tag{4.52}$$

In the variables $(\bar{\mathbf{X}}_i, \bar{\mathbf{V}}_i)$, taking into account (4.51)–(4.52), equations $(4.43)_{1,3}$ become

$$\begin{aligned}
\dot{\bar{V}}_{i1} &= -\dot{V}_{\mathrm{CM1}} + \frac{\beta}{N}\sum_{j=1}^{N}(\bar{V}_{j1}(t) - \bar{V}_{i1}(t)) \\
&- \int_0^t \bar{C}(t-\tau)\sum_{j=1}^{N}\Big(\bar{X}_{i1}(t) - \bar{X}_{j1}(\tau) + X_{\mathrm{CM1}}(t) - X_{\mathrm{CM1}}(\tau)\Big)\;d\tau \\
&= \frac{\beta}{N}\left(\sum_{j=1}^{N}\bar{V}_{j1}(t) - \sum_{j=1}^{N}\bar{V}_{i1}(t)\right) \\
&- \int_0^t \bar{C}(t-\tau)(N\bar{X}_{i1}(t) - \sum_{j=1}^{N}\bar{X}_{j1}(\tau) + NX_{\mathrm{CM1}}(t) - NX_{\mathrm{CM1}}(\tau) \\
&- NX_{\mathrm{CM1}}(t) + NX_{\mathrm{CM1}}(\tau))\,d\tau \\
&= -\beta\bar{V}_{i1}(t) - N\left(\int_0^t \bar{C}(t-\tau)\,d\tau\right)\bar{X}_{i1}(t),
\end{aligned}$$

where we have used (4.49)–(4.50), and

$$\dot{\bar{X}}_{i1} = -\dot{X}_{\mathrm{CM1}} + \bar{V}_{i1} + V_{\mathrm{CM1}} = \bar{V}_{i1}.$$

Similarly for $\dot{\bar{V}}_{i2}$ and $\dot{\bar{X}}_{i2}$.

Finally, we can write the following system:

$$\begin{cases}
\dot{\bar{V}}_{i1} = -\beta\bar{V}_{i1}(t) - g(t)\bar{X}_{i1}(t), \\
\dot{\bar{V}}_{i2} = -\beta\bar{V}_{i2}(t) - g(t)\bar{X}_{i2}(t), \\
\dot{\bar{X}}_{i1} = \bar{V}_{i1}, \\
\dot{\bar{X}}_{i2} = \bar{V}_{i2},
\end{cases} \tag{4.53}$$

where

$$g(t) := N\int_0^t \bar{C}(t-\tau)\,d\tau.$$

Before establishing stability properties of equilibrium (4.48) for system (4.53), we recall some definitions.

Consider a system of ordinary differential equations

$$\dot{\mathbf{y}} = \mathbf{F}(t, \mathbf{y}(t)), \quad \mathbf{F}(t, \mathbf{0}) = \mathbf{0}, \tag{4.54}$$

in which $\mathbf{F} : [0, +\infty) \times U \to \mathbb{R}^n$ is continuous and U is an open set in $\mathbb{R}^n$ with $\mathbf{0}$ in U.

Definition 4 *The solution* $\mathbf{y}(t) = \mathbf{0}$ *of* (4.54) *is*

a) stable *if, for each* $\varepsilon > 0$ *and* $t_0 \geq 0$*, there is a* $\delta(\varepsilon, t_0) > 0$ *such that*

$$\|\mathbf{y}_0\| < \delta, \quad \textit{and} \quad t \geq t_0 \Rightarrow \|\mathbf{y}(t, t_0, \mathbf{y}_0)\| < \varepsilon;$$

b) uniformly stable *if it is stable and* δ *is independent of* $t_0 \geq 0$*;*

c) asymptotically stable *if it is stable and if, for each* $t_0 \geq 0$*, there is an* $\lambda(t_0) > 0$ *such that*

$$\|\mathbf{y}_0\| < \lambda \Rightarrow \|\mathbf{y}(t, t_0, \mathbf{y}_0)\| \to 0, \quad \textit{as } t \to +\infty,$$

(if, in addition, λ *can be made arbitrarily large, then* $\mathbf{y} = \mathbf{0}$ *is globally asymptotically stable);*

d) uniformly asymptotically stable *if it is stable and if there is a* $\lambda > 0$ *independent of* t_0 *such that, for all* $\|\mathbf{y}_0\| < \lambda$*,* $\|\mathbf{y}(t, t_0, \mathbf{y}_0)\| \to 0$ *as* $t \to +\infty$ *uniformly in* t_0*, that is for each* $\zeta > 0$*, there is a* $T(\zeta) > 0$ *such that*

$$\|\mathbf{y}_0\| < \lambda, \quad t_0 \geq 0, \quad \textit{and} \quad t \geq t_0 + T \Rightarrow \|\mathbf{y}(t, t_0, \mathbf{y}_0)\| < \zeta, \tag{4.55}$$

(if, in addition, λ *can be made arbitrarily large, then* $\mathbf{y} = \mathbf{0}$ *is globally uniformly asymptotically stable).*

Below we will prove the uniform asymptotic stability of equilibrium (4.48) providing a suitable Lyapunov function for system (4.53). For simplicity system (4.53) can be written, for each particle and for each component, as a planar system in the variable $\mathbf{y} = (V, X)$:

$$\begin{cases} \dot{V} = -\beta V - g(t) X, \\ \dot{X} = V, \end{cases} \tag{4.56}$$

with

$$g(t) := N \int_0^t \bar{C}(t - \tau)\, d\tau.$$

In relation to (4.56) we prove the following two theorems.

Theorem 4 *Fixed a* $\bar{t} > 0$*, the system* (4.56) *admits a Lyapunov function* $U(t, \mathbf{y})$ *with the properties:*

a)

$$U(t, \mathbf{y}) \leq k_1 \|\mathbf{y}\|^2, \quad \forall\, t \geq \bar{t}; \tag{4.57}$$

b)

$$U(t,\mathbf{y}) \geq k_2 \left\|\mathbf{y}\right\|^2, \quad \forall\, t \geq \bar{t}; \tag{4.58}$$

c)

$$\dot{U}(t,\mathbf{y}) = \frac{\partial U}{\partial t} + \frac{\partial U}{\partial V}\dot{V} + \frac{\partial U}{\partial X}\dot{X} \leq -k_3 \left\|\mathbf{y}\right\|^2, \quad \forall\, t \geq \bar{t}; \tag{4.59}$$

where k_1*,* k_2*,* k_3 *are positive constants.*

Proof. Let $\bar{t} > 0$, we define the Lyapunov function

$$U(t,V,X) := (V^2 + kXV + g(t)X^2)\psi(t),$$

where

$$\begin{aligned}
\psi(t) &:= e^{-\frac{g(t)}{\underline{g}}}, \\
\underline{g} &:= \inf_{t\geq\bar{t}} g(t) = N\int_0^{\bar{t}} \bar{C}(t-\tau)\,d\tau, \\
\bar{g} &:= \sup_{t\geq\bar{t}} g(t) = N\int_0^{+\infty} \bar{C}(t-\tau)\,d\tau, \\
\underline{\psi} &:= \inf_{t\geq\bar{t}} \psi = e^{-\frac{\bar{g}}{\underline{g}}}, \\
\overline{\psi} &:= \sup_{t\geq\bar{t}} \psi = e^{-1}, \\
\overline{\overline{\psi}} &:= \sup_{t\geq\bar{t}} |\dot{\psi}| = \sup_{t\geq\bar{t}} \frac{e^{-\frac{g(t)}{\underline{g}}}\dot{g}}{\underline{g}}, \\
k &:= \min\left\{ \frac{\underline{\psi}}{\overline{\overline{\psi}}}, \frac{\underline{g}\,\underline{\psi}}{\overline{\overline{\psi}}}, \frac{2\beta\underline{g}\,\underline{\psi}^2}{2\underline{g}\,\underline{\psi}\overline{\psi} + (\overline{\overline{\psi}} + \beta\overline{\psi})^2} \right\}.
\end{aligned} \tag{4.60}$$

In the following equations we consider the inequalities:

$$-\frac{X^2+V^2}{2} \leq XV \leq \frac{X^2+V^2}{2}.$$

Then, because of $g(t)$ is an increasing function, $\psi(t)$ is nonincreasing, so

$$\dot{\psi} \leq 0, \tag{4.61}$$

and finally

$$\begin{aligned}
\dot{\psi}g + \psi\dot{g} &= -e^{-\frac{g(t)}{\underline{g}}}\frac{\dot{g}}{\underline{g}}g + e^{-\frac{g(t)}{\underline{g}}}\dot{g} \\
&= \dot{g}e^{-\frac{g(t)}{\underline{g}}}\left(1 - \frac{g(t)}{\underline{g}}\right) \\
&\leq 0, \quad \forall\, t \geq \bar{t}.
\end{aligned} \tag{4.62}$$

To prove *a*) we consider the inequalities

$$\begin{aligned}U(t,V,X) &\leq \left(V^2 + k\frac{X^2+V^2}{2} + \overline{g}X^2\right)\overline{\psi}\\ &= \left[\left(1+\frac{k}{2}\right)V^2 + \left(\overline{g}+\frac{k}{2}\right)X^2\right]\overline{\psi}\\ &\leq k_1\left\|\mathbf{y}\right\|^2,\end{aligned}$$

where

$$k_1 := \max\left\{\left(1+\frac{k}{2}\right)\overline{\psi}, \left(\overline{g}+\frac{k}{2}\right)\overline{\psi}\right\}.$$

To prove *b*) we consider

$$\begin{aligned}U(t,V,X) &\geq \underline{\psi}V^2 + \underline{g}\,\underline{\psi}X^2 - k\overline{\psi}\frac{X^2+V^2}{2}\\ &= V^2\left(\underline{\psi} - \frac{k\overline{\psi}}{2}\right) + X^2\left(\underline{g}\,\underline{\psi} - \frac{k\overline{\psi}}{2}\right)\\ &\geq_{(4.60)} V^2\frac{\underline{\psi}}{2} + X^2\frac{\underline{g}\,\underline{\psi}}{2}\\ &\geq k_2\left\|\mathbf{y}\right\|^2,\end{aligned}$$

where

$$k_2 := \min\left\{\frac{\underline{\psi}}{2}, \frac{\underline{g}\,\underline{\psi}}{2}\right\}$$

To prove *c*) we consider the following inequalities:

$$\begin{aligned}\dot{U}(t,V,X) = {}&\dot{\psi}(V^2+kXV+gX^2) + \psi\Big[2V(-\beta V - gX) + kV^2\\ &+kX(-\beta V - gX) + \dot{g}X^2 + 2gXV\Big]\\ ={}&\left(\dot{\psi} - 2\beta\psi + k\psi\right)V^2 + \left(k\dot{\psi} - \beta k\psi\right)XV + \left(\dot{\psi}g + \psi\dot{g} - kg\psi\right)X^2\\ \leq_{(4.61),(4.62)}{}& \left(-2\beta\psi + k\psi\right)V^2 + \left(k\dot{\psi} - \beta k\psi\right)XV - kg\psi X^2\\ \leq{}& \left(-2\beta\psi + k\psi\right)V^2 + \left(k|\dot{\psi}| + \beta k\psi\right)|X||V| - kg\psi X^2\\ \leq{}& \left(-2\beta\underline{\psi} + k\overline{\psi}\right)V^2 + \left(k\overline{\overline{\psi}} + \beta k\overline{\psi}\right)|X||V| - k\underline{g}\,\underline{\psi}X^2\\ ={}& \left(-2\beta\underline{\psi} + k\overline{\psi}\right)V^2 - \frac{k\underline{g}\,\underline{\psi}}{2}\left[|X| - \frac{|V|\left(\overline{\overline{\psi}} + \beta\overline{\psi}\right)}{\underline{g}\,\underline{\psi}}\right]^2 - \frac{k\underline{g}\,\underline{\psi}}{2}X^2\\ &+\frac{k\left(\overline{\overline{\psi}} + \beta\overline{\psi}\right)^2}{2\underline{g}\,\underline{\psi}}V^2\end{aligned}$$

$$
\begin{aligned}
&\leq \left(-2\beta\underline{\psi} + k\overline{\psi} + \frac{k\left(\overline{\overline{\psi}} + \beta\overline{\psi}\right)^2}{2\underline{g}\,\underline{\psi}} \right) V^2 - \frac{k\underline{g}\,\underline{\psi}}{2} X^2 \\
&\leq_{(4.60)} -\left(\beta\underline{\psi} V^2 + \frac{k\underline{g}\,\underline{\psi}}{2} X^2 \right) \\
&\leq -k_3 \left\| \mathbf{y} \right\|^2,
\end{aligned}
$$

where

$$
k_3 := \min\left\{ \beta\underline{\psi}, \frac{k\underline{g}\,\underline{\psi}}{2} \right\}.
$$

This completes the proof.

Starting from Proposition 4 we can state

Theorem 5 *The equilibrium point* $(V, X) = (0, 0)$ *of* (4.56) *is globally uniformly asymptotically stable with exponential rate of convergence.*

Proof. Inequalities (4.59) and (4.57) imply that U satisfies the differential inequality

$$
\dot{U} \leq -\frac{k_3}{k_1} U, \quad \forall\, t \geq \bar{t}.
$$

By the Gronwall's inequality (Lemma 1),

$$
U(t, \mathbf{y}(t)) \leq U\left(\bar{t}, \mathbf{y}\left(\bar{t}\right)\right) e^{-(k_3/k_1)(t-\bar{t})}.
$$

Then, using (4.58) and again (4.57), we have

$$
\begin{aligned}
\|\mathbf{y}(t)\| &\leq \left(\frac{U(t, \mathbf{y}(t))}{k_2} \right)^{1/2} \\
&\leq \left(\frac{U\left(\bar{t}, \mathbf{y}\left(\bar{t}\right)\right) e^{-(k_3/k_1)(t-\bar{t})}}{k_2} \right)^{1/2} \\
&\leq \left(\frac{k_1 \left\|\mathbf{y}\left(\bar{t}\right)\right\|^2 e^{-(k_3/k_1)(t-\bar{t})}}{k_2} \right)^{1/2} \\
&= \left(\frac{k_1}{k_2} \right)^{1/2} \left\|\mathbf{y}\left(\bar{t}\right)\right\| e^{-(k_3/(2k_1))(t-\bar{t})}. \qquad (4.63)
\end{aligned}
$$

From (4.63) condition (4.55) is satisfied with exponential convergence. The proof is completed.

Returning to system (4.53), Theorem 5 can be applied for each particle and for each component of the position and velocity vectors. Reminding transformation (4.46)–(4.47), we can say that all agents converge, time-asymptotically, to the position and velocity of their centre of mass.

Now let us investigate equation (4.51) for the motion of the centre of mass. For convenience, we write it again for the first component, the second is similar:

$$\begin{cases} \dot{V}_{\mathrm{CM1}} = -N \displaystyle\int_0^t \bar{C}(t-\tau)\,(X_{\mathrm{CM},1}(t) - X_{\mathrm{CM1}}(\tau))\; d\tau, \\ \dot{X}_{\mathrm{CM1}} = V_{\mathrm{CM1}}, \end{cases} \tag{4.64}$$

with $\bar{C}(t-\tau)$ defined in (4.42) that, from (4.37), gives

$$\bar{C}(t-\tau) := \frac{\pi R^2 C(t-\tau) e^{-\frac{R^2}{4(t-\tau)D}}}{2(t-\tau)D} = \frac{\gamma \xi R^2 e^{-\frac{R^2}{4(t-\tau)D} - \eta(t-\tau)}}{8(t-\tau)^2 D^2}. \tag{4.65}$$

Then from system (4.64) we get the scalar equation

$$\dot{V}_{\mathrm{CM1}} = -N \int_0^t \bar{C}(t-\tau) \int_\tau^t V_{\mathrm{CM1}}(s)\, ds\, d\tau. \tag{4.66}$$

In order to establish the asymptotic behaviour of (4.66), we prove the following

Theorem 6 *Equation* (4.66)*, with initial datum* $V_{CM1}(t_0)$*, has a unique solution in* $[t_0, +\infty)$*.*

Proof. The existence of the solution is ensured by the existence of the solution proved for system (4.36).

Since the linearity of the equation it is sufficient to prove that the unique solution with zero initial datum is the constant zero solution. In fact, if we consider the case of nonzero initial datum and we suppose that there exist two solutions, $y(t)$ and $z(t)$, in correspondence of the same initial condition $y(t_0) = z(t_0)$, their difference $w(t) := y(t) - z(t)$ is also a solution with zero initial datum. If $w(t)$ must be necessarily the zero solution, then $y(t)$ and $z(t)$ have to coincide, ensuring the uniqueness.

First, we observe that $\bar{C}(t-\tau)$ in (4.65) is bounded, we say

$$0 < N\bar{C}(t-\tau) \le \nu,$$

with ν positive constant. Then, from (4.66) we write the inequalities

$$\begin{aligned} \frac{d\,|V_{\mathrm{CM1}}|}{dt} &\le \left| \frac{dV_{\mathrm{CM1}}}{dt} \right| \\ &\le \nu \int_0^t \int_\tau^t |V_{\mathrm{CM1}}(s)|\; ds\, d\tau \\ &= \nu \int_0^t s\, |V_{\mathrm{CM1}}(s)|\; ds, \end{aligned}$$

where we have changed the order of integration in the integral. Integrating both sides from t_0 to t, changing again the order of integration, and fixed a $T > t_0$, we state

$$\begin{aligned}
|V_{\mathrm{CM}1}(t)| &\leq |V_{\mathrm{CM}1}(t_0)| + \nu \int_{t_0}^{t} \int_{0}^{\tau} s\,|V_{\mathrm{CM}1}(s)|\, ds\, d\tau \\
&\leq |V_{\mathrm{CM}1}(t_0)| + \nu \int_{0}^{t} \int_{0}^{\tau} s\,|V_{\mathrm{CM}1}(s)|\, ds\, d\tau \\
&= |V_{\mathrm{CM}1}(t_0)| + \nu \int_{0}^{t} s(t-s)\,|V_{\mathrm{CM}1}(s)|\, ds \\
&\leq |V_{\mathrm{CM}1}(t_0)| + \nu T \int_{0}^{t} s\,|V_{\mathrm{CM}1}(s)|\, ds, \quad \forall t_0 \leq t < T.
\end{aligned}$$

By Gronwall's Lemma 1

$$|V_{\mathrm{CM}1}(t)| \leq |V_{\mathrm{CM}1}(t_0)|\, e^{\frac{\nu T t^2}{2}}, \quad \forall t_0 \leq t < T,$$

so that, due to the arbitrariness of T, if $V_{\mathrm{CM}1}(t_0) = 0$, $V_{\mathrm{CM}1}(t)$ will be the constant zero solution. This complete the proof.

From Theorem 6 descends

Theorem 7 *Each solution of equation* (4.66) *go to zero as* $t \to +\infty$.

Proof. If the initial datum is $V_{\mathrm{CM}1}(0) = 0$ the unique solution is the constant zero solution. We consider now $V_{\mathrm{CM}1}(0) > 0$. In this case the solution is greater or equal to zero in all $[0, +\infty)$. In fact, if there is a $\bar{t} > 0$ such that $V_{\mathrm{CM}1}(\bar{t}) = 0$, Theorem 6, applied at $t_0 = \bar{t}$, would give $V_{\mathrm{CM}1}(t) \equiv 0$ for all $t > \bar{t}$. Then the right hand side of (4.66) implies $\dot{V}_{\mathrm{CM}1} < 0$, so $V_{\mathrm{CM}1}(t)$ is a decreasing function on $[0, +\infty)$, and there exit its limit $0 \leq l < +\infty$, as $t \to +\infty$. Hence, since from (4.66) $\dot{V}_{\mathrm{CM}1}(t)$ is monotone and its limit exists, we have also $\lim_{t\to+\infty} \dot{V}_{\mathrm{CM}1}(t) = 0$. Now, if we suppose $l > 0$, $V_{\mathrm{CM}1}(t) > l$ for all $t \geq 0$, and from (4.66) holds

$$\begin{aligned}
\dot{V}_{\mathrm{CM}1} &< -Nl \int_{0}^{t} \bar{C}(t-\tau)(t-\tau)\, d\tau && (4.67)\\
&= -Nl \int_{0}^{t} z\bar{C}(z)\, dz, \quad \forall t \in [0, +\infty), && (4.68)
\end{aligned}$$

where we have performed the change of variables $z = t - \tau$. Taking the limit for $t \to +\infty$ on both side of (4.67) we would have the contradiction

$$0 = \lim_{t\to+\infty} \dot{V}_{\mathrm{CM}1}(t) \leq -\mu < 0,$$

where

$$\mu := Nl \int_{0}^{+\infty} z\bar{C}(z)\, dz.$$

So the only chance is $l = 0$.

The case $V_{\mathrm{CM}1}(0) < 0$ can be treated in a similar way. The proof is now completed.

Theorem 7 is valid also for the second velocity component $V_{\mathrm{CM}2}$, whose equation is analogous to (4.66).

Finally, returning to system (4.43), Theorems 7 and 5 ensure a condition of time-asymptotic flocking such as stated in Definition 2. Moreover, we have also the stronger condition that all particles converge asymptotically to their centre of mass and the velocity of the centre of mass decays to zero.

It is interesting to extend such result from the linear model to the fully nonlinear system, at least for “small” initial data. Numerical simulations, performed in the next section on the nonlinear system, suggest that such results could possibly be obtained.

4.6 Numerical simulations

In order to verify the analytical results presented in Section 4.5 for the nonlinear model, we perform several numerical simulation. Numerical results are shown in nondimensional form using the following dimensionless quantities:

$$t^* := t\eta, \quad \mathbf{X}^* := \frac{\mathbf{X}}{R}, \quad f^* := \frac{f}{f_{\max}}, \quad \beta^* := \frac{\beta}{\eta},$$
$$\gamma^* := \frac{\gamma f_{\max}}{R^2\eta^2}, \quad D^* := \frac{D}{R^2\eta}, \quad \xi^* := \frac{\xi}{f_{\max}\eta},$$

where $f_{\max}$ is the maximum concentration of signal f. With these definitions, system (4.7) can be written as

$$\begin{cases} \dot{\mathbf{V}}_i = \dfrac{\beta}{N}\displaystyle\sum_{j=1}^{N} \frac{1}{\left(1+\|\mathbf{X}_i-\mathbf{X}_j\|^2\right)^\sigma}(\mathbf{V}_j-\mathbf{V}_i) + \gamma\nabla f(\mathbf{X}_i), \\ \\ \dot{\mathbf{X}}_i = \mathbf{V}_i, \\ \\ \partial_t f = D\Delta f + \xi \displaystyle\sum_{j=1}^{N} \chi_{\mathbf{B}(\mathbf{X}_j,1)} - f, \end{cases} \tag{4.69}$$

where we have dropped, for simplicity, the asterisks for the nondimensional quantities. Notice that, due to the choice of R as characteristic length, the dimensionless particle ray turns out to be a unit value.

Numerical approximation

The numerical approximation scheme used here employs a 2D finite difference method, similar to which designed in Section 3.6. On the spatial domain $\Omega := [a,b] \times [c,d]$ we will assume periodic boundary conditions. If Δx and Δy are the spatial steps and Δt the time step, we define the grid points (x_m, y_n, t_k), where $x_m = m\Delta x$, $x_n = n\Delta y$ and $t_k = k\Delta t$. The notation $u^k_{m,n}$ will denote the approximation of a function $u(x,y,t)$ at the grid point (x_m, y_n, t_k).

For the parabolic equation $(4.69)_3$, in order to eliminate the stiff term $-f$ we perform the exponential transformation

$$f(\mathbf{x},t) = e^{-t}u(\mathbf{x},t),$$

where $u(\mathbf{x},t)$ satisfies the equation

$$\partial_t u = D\Delta u + e^t \xi \sum_{j=1}^{N} \chi_{\mathbf{B}(\mathbf{X}_j,1)}, \tag{4.70}$$

with initial condition

$$u(\mathbf{x},0) = 0,$$

and periodic boundary conditions.

Now, for (4.70) we apply a central difference scheme in space and the parabolic Crank-Nicolson scheme in time (Morton and Mayers, 2005; LeVeque, 2007). Namely we write

$$\begin{aligned}\frac{u_{m,n}^{k+1}-u_{m,n}^{k}}{\Delta t} &= \frac{D}{2}\left(D_x^2 u^{k+1} + D_y^2 u^{k+1}\right) + \frac{D}{2}\left(D_x^2 u^{k} + D_y^2 u^{k}\right)\\ &+ \frac{1}{2} e^{(k+1)\Delta t} \xi \sum_{j=1}^{N} \chi_{\mathbf{B}(\mathbf{X}_j^k,1)}\\ &+ \frac{1}{2} e^{k\Delta t} \xi \sum_{j=1}^{N} \chi_{\mathbf{B}(\mathbf{X}_j^k,1)},\end{aligned}$$

where

$$\begin{aligned} D_x^2 u^k &:= \frac{u_{m-1,n}^k - 2u_{m,n}^k + u_{m+1,n}^k}{\Delta x^2},\\ D_y^2 u^k &:= \frac{u_{m,n-1}^k - 2u_{m,n}^k + u_{m,n+1}^k}{\Delta y^2},\end{aligned} \tag{4.71}$$

and

$$\chi_{\mathbf{B}(\mathbf{X}_j^k,1)} = \begin{cases} 1, & \text{if} \quad (x_m,y_n) \in \mathbf{B}(\mathbf{X}_j^k,1);\\ 0, & \qquad \text{otherwise.}\end{cases}$$

For equations $(4.69)_1$ we adopt a one step IMEX method, putting in implicit the term depending on the velocities and in explicit the gradient term (Hundsdorfer and Verwer, 2003). The scheme reads:

$$\begin{cases} \dfrac{\mathbf{V}_i^{k+1}-\mathbf{V}_i^k}{\Delta t} &= \dfrac{\beta}{N}\displaystyle\sum_{j=1}^{N} \frac{1}{\left(1+\|\mathbf{X}_i^k-\mathbf{X}_j^k\|^2\right)^{\sigma}}(\mathbf{V}_j^{k+1}-\mathbf{V}_i^{k+1}) + \gamma \mathcal{I}_{\mathbf{X}_i^k}\left(\nabla_{m,n} f^k\right),\\ \dfrac{\mathbf{X}_i^{k+1}-\mathbf{X}_i^k}{\Delta t} &= \mathbf{V}_i^k,\end{cases} \tag{4.72}$$

where

$$\nabla_{m,n} f^k := \left(\frac{f_{m+1,n}^k - f_{m-1,n}^k}{2\Delta x}, \frac{f_{m,n+1}^k - f_{m,n-1}^k}{2\Delta y}\right),$$

and $\mathcal{I}_{\mathbf{X}_i^k}(\nabla_{m,n} f^k)$ represents an interpolation of the values $\nabla_{m,n} f^k$ on the grid points nearest to $\mathbf{X}_i^k$.

About the spatial and temporal steps employed in the simulations we chose $\Delta x = \Delta y$ and, in the first time steps, the parabolic CFL condition $\Delta t \sim \frac{\Delta x^2}{D}$ (Morton and Mayers, 2005), which has shown more stability in the numerical tests, taken into account in (4.70) the discontinuous source term and the value of $u(\mathbf{x}, t)$ initially near to zero. In practice, after few time steps, we have release the parabolic CFL in favor of $\Delta t \sim \Delta x$.

Numerical tests

In all the following numerical tests we set N particles in a spatial domain $\Omega = [0, 50] \times [0, 50]$ with periodic boundary conditions, and we chose a suitable time interval of observation $[0, T]$. For the initial data we fix

$$f(\mathbf{x}, 0) = 0,$$

and, for $i = 1, \dots, N$,

$$\begin{aligned} \mathbf{X}_i(0) &= \mathbf{X}_{i0}, \\ \mathbf{V}_i(0) &= \mathbf{V}_{i0}. \end{aligned}$$

In particular $\mathbf{X}_{i0}$ is chosen as a random vector, such that all the particles at $t = 0$ are contained in a suitable initial region, fixed in the domain. Then $\mathbf{V}_{i0} = (V_{i0} \cos \theta_i, V_{i0} \sin \theta_i)$ are chosen with V_{i0} random numbers in $[0, V_{0,\max}]$, and θ_i random numbers in $[0, 2\pi]$. Let us now describe some meaningful tests.

Test 1

In this test we set the parameters $\sigma = 0.5$, $\beta = 5$, $\gamma = 2 \times 10^2$, $D = 2 \times 10^2$, $\xi = 0.5$, $V_{0,\max} = 3$, and we consider $N = 10$ particles located in $\mathbf{X}_0$ as in Figure 4.1 (a). The time interval of observation is $[0, 500]$. Spatial and temporal discretizations are given respectively by $\Delta x = \Delta y = 0.25$ and $\Delta t = 10^{-4}$.

Figure 4.1 shows four time steps of the numerical simulation. Here and in the next tests for each time step we plot, on the left the chemoattractant concentration $f(\mathbf{x}, t)$, while on the right the positions and the velocities of the particles in the spatial domain. Red square at $t = 0$ is the region in which the initial positions are taken. Red marker indicates the centre of mass of the system, and the blue arrows are the velocity vectors. We observe an initial stage in which the particles tend to move somewhat aligned about until $t = 5$ (Figure 4.1 (b)), then they begin to converge to their centre of mass about at $t = 30$ (Figure 4.1 (c)), finally all particles stop in a same position (Figure 4.1 (d)).

In Figure 4.2 (a) is shown the spatial fluctuation around the centre of mass system

$$Fl_X(t) := \sum_{i=1}^{N} \left\| \mathbf{X}_i(t) - \mathbf{X}_{\mathrm{CM}}(t) \right\|^2,$$

as a function of the time. In Figure 4.2 (b) is shown the velocity fluctuation around the centre of mass

$$Fl_V(t) := \sum_{i=1}^{N} \|\mathbf{V}_i(t) - \mathbf{V}_{\mathrm{CM}}(t)\|^2 .$$

About for $t > 61$ $Fl_X(t)$ and $Fl_V(t)$ are less than 10^{-10}. Notice that the square root of $Fl_X(t)$ and $Fl_V(t)$ is proportional to the standard deviations of $\mathbf{X}_i(t)$ and $\mathbf{V}_i(t)$ with respect to the position and velocity of the centre of mass. Figure 4.2 (c) displays the norm of the velocity of the centre of mass $\|\mathbf{V}_{\mathrm{CM}}(t)\|$ versus time. About for $t > 52$ this velocity is less than 7.8×10^{-2}. The oscillating pattern, shown here and in the next tests, can be attributed to the numerical error, as it is confirmed using finer meshes for the discretization. Figure 4.2 (d) is obtained, for the same simulation, using a spatial and temporal steps respectively of $\Delta x = \Delta y = 0.0125$ and $\Delta t = 10^{-5}$. About for $t > 88$ $\|\mathbf{V}_{\mathrm{CM}}(t)\|$ is less than 2×10^{-2}. With smaller values of Δx, Δy, and Δt, lower values of $\|\mathbf{V}_{\mathrm{CM}}(t)\|$ are achieved (data not shown).

In the next two tests, starting from Test 1, we change only the two parameters related to the alignment and to the chemotaxis, in order to investigate the competition between these two effects.

Test 2

In this test we set $\beta = \gamma = 10$, while the other parameters are set as in Test 1. The time of observation is $[0, 3500]$.

Particles and chemotactic signal are not shown. In Figure 4.3 (a)–(b) we plot the spatial and the velocity fluctuations around the centre of mass system $Fl_X(t)$ and $Fl_V(t)$. About for $t > 1689$ $Fl_X(t)$ and $Fl_V(t)$ are less than 10^{-10}. Figure 4.3 (c) displays the quantity $\|\mathbf{V}_{\mathrm{CM}}(t)\|$ as a function of time. About for $t > 2134$ this value is less than 1.82×10^{-2}.

Test 3

In this test we set $\beta = 15$, $\gamma = 10$ and the other parameters are set as in Test 1. The time of observation is $[0, 3500]$.

The figures related to the particles and to the chemotactic signal are not shown, while in Figure 4.4 (a)–(b) we plot the spatial and the velocity fluctuations around the centre of mass system $Fl_X(t)$ and $Fl_V(t)$. About for $t > 3109$ we have values less than 10^{-10}. Figure 4.4 (c) displays the quantity $\|\mathbf{V}_{\mathrm{CM}}(t)\|$ versus time. About for $t > 2579$ this velocity is less than 1.87×10^{-2}.

In Table 4.1 we summarize the results of the first three tests. We can observe that increasing values of the ratio $\frac{\beta}{\gamma}$ imply a decreasing rate of convergence of the particles.

Test 4

In this simulation we fix the parameters as in Test 1, and we double the number of the interacting agents considering $N = 20$ cells as in Figure 4.5 (a). The time interval of observation is $[0, 500]$.

Table 4.1. Spatial and velocity fluctuations in the centre of mass system, and velocity of the centre of mass for different values of the parameters β and γ used in Tests 1–3.

Test	β	γ	Time after which $\max\{Fl_X, Fl_V\} < 10^{-10}$	Time after which $\|\mathbf{V}_{\text{CM}}(t)\| < 7.8 \times 10^{-2}$
1	5	2×10^2	61	52
2	10	10	1689	1021
3	15	10	3109	1554

In Figure 4.5 we can observe four different time steps of the numerical simulation showing the aggregation of the initial group and the convergence to zero of its velocity.

In Figures 4.6 (a)–(b) we plot, the quantities $Fl_X(t)$ and $Fl_V(t)$. Here, about for $t > 34$ we have values less than 10^{-10}. In Figure 4.6 (c) we show the quantity $\|\mathbf{V}_{\text{CM}}(t)\|$ versus time, with values smaller than 8.39×10^{-2} about for $t > 28$. Comparing the results of this test with those of Test 1 we can state that, with the same parameters, an increasing number of cells enhances the rate of convergence due to the greater amount of the expressed chemoattractant.

Test 5

In this test we consider a case in which, for the pure Cucker-Smale model (4.1), i.e. $\gamma = 0$ in our model, the flocking behaviour does not occur. We fix the other parameters $\sigma = 0.8$, $\beta = 5$, $D = 2 \times 10^2$, $\xi = 0.5$, $V_{0,\max} = 3$, and $\mathbf{X}_0$ as in Figure 4.7 (a). The time interval of observation is $[0, 15]$. Spatial and temporal discretizations are as in Test 1. Clearly in this case equations $(4.6)_{1,2}$ and $(4.6)_3$ are decoupled. Since $\sigma > 1/2$, and taking into account the initial data, according to the results in Ha and Liu (2009), the flocking of the system is not guaranteed.

Figure 4.7 shows our numerical simulation at three time steps. We can observe, in fact, a dispersion of the initial group of particles.

In the next test we will show that, adding the chemotactic effect, we can recover the time-asymptotic convergence of the migrating group.

Test 6

In this test we set the same parameters and initial data of Test 5, moreover we introduce a non zero value for the chemotactic effect: $\gamma = 10^2$. The interval of observation, spatial and temporal discretizations are fixed as in Test 1.

Figure 4.8 shows the numerical simulations at four different time steps. We can note that the initial group of particles does not disperse, but converge in position and velocity.

In Figures 4.9 (a)–(b) we plot, as in Test 1, respectively $Fl_X(t)$ and $Fl_V(t)$. About for $t > 107$ these quantities are less than 10^{-10}. Figure 4.9 (c) shows the quantity $\|\mathbf{V}_{\text{CM}}(t)\|$ versus time. About for $t > 65$ we have values smaller than 2.1×10^{-2}.

Test 7

Inspired by the mathematical model proposed in Chapter 3 for the zebrafish lateral line development, we consider a simulation in which two kinds of cells are involved: the *leaders* that produce the chemotactic signal and the *followers* that do not produce any signal, both subjected to the alignment effect and to the attraction of the chemical gradient.

For the numerical simulation set $\sigma = 0.5$, $\beta = 5$, $\gamma = 1.5 \times 10^2$, $D = 2 \times 10^2$, $\xi = 3$, $V_{0,\max} = 0.3$, and $\mathbf{X}_0$ as in Figure 4.10 (a). We consider a time interval of observation $[0, 500]$. Spatial and temporal discretizations are as in Test 1.

Figure 4.10 shows four time steps of our simulation. A single leader cell is marked in green colour, while the other follower cells are in red colour. Here the centre of mass is marked in blue. We observe, about at $t = 15$, that cells begin to be attracted toward the chemoattractant source (Figure 4.10 (b)). In the next time steps the cells tend to converge in the centre of mass and then they stop (Figure 4.10 (c)–(d)).

In Figures 4.11 (a)–(b) are shown the spatial and velocity fluctuations, $Fl_X(t)$ and $Fl_V(t)$, around the centre of mass system. About for $t > 131$ these quantities are less than 10^{-10}. Figure 4.11 (c) displays the quantity $\|\mathbf{V}_{\mathrm{CM}}(t)\|$. About for $t > 328$ we have values smaller than 5.3×10^{-2}.

Test 8

In this test we consider a case in which the particles have zero initial velocity. If we considered the pure Cucker-Smale model (4.1), we would have the particles constant in the initial position with zero velocity. Here we show that the chemotactic effect ensure the convergence of the group of particles. As in Test 7 we consider a single leader that produce the chemoattractant, and other followers that do not produce any signal, but they follow the gradient produced by the leader signal.

For the numerical simulation we set $\sigma = 0.6$, $\beta = 2$, $\gamma = 10^2$, $D = 2 \times 10^2$, $\xi = 3$, $V_{0,\max} = 0$, and $\mathbf{X}_0$ as in Figure 4.12 (a). The time interval of observation is the same as Test 5. Spatial and temporal discretizations are fixed as in Test 1.

Figure 4.12 shows four time steps of our simulation. Green colour marks the leader cell, while red colour is for the followers. The centre of mass is marked in blue. In early time steps we observe the velocity vectors that point the source of chemoattractant (Figure 4.12 (b)). In the next time steps all particles go to converge in position and velocity.

In Figures 4.13 (a)–(b) we plot respectively $Fl_X(t)$ and $Fl_V(t)$ versus time. About for $t > 67$ we obtain values less than 10^{-10}. In Figure 4.13 (c) is shown the quantity $\|\mathbf{V}_{\mathrm{CM}}(t)\|$ as a function of time. About for $t > 109$ we have values smaller than 4.3×10^{-2}.

Test 9

In this test we simulate the system only under the chemotactic effect, neglecting the alignment term, that is we set $\beta = 0$. The other parameters are $\gamma = 10^2$, $D = 2 \times 10^2$, $\xi = 1.5$, and the initial data $V_{0,\max} = 0.8$, $\mathbf{X}_0$ as in Figure 4.14 (a). The time interval of observation is $[0, 4000]$. Spatial and temporal discretizations are fixed as in Test 1.

In Figure 4.14 we plot four time steps. Although the initial group aggregates we do not observe, in our time of observation, a convergence of the particles, rather they show an oscillating behaviour around their centre of mass.

In Figures 4.15 (a)–(b) we plot respectively $Fl_X(t)$ and $Fl_V(t)$. In this case, the spatial and velocity fluctuations around the centre of mass remain bounded but do not converge to zero. In particular, in the time interval of observation, we have about $Fl_X(t) > 0.88$ and, if we consider a trend line, its slope seems to decreases monotonically approaching to zero. For example, in relation to Figure 4.15 (a), the slope of the linear fit on the values of $Fl_X(t)$, computed on the time intervals $[0, 800]$ and $[3200, 4000]$, changes from -1.46×10^{-1} to -1.84×10^{-4}. Moreover, we remark that in previous simulations, containing the alignment effect, on time intervals much smaller than this test we have obtained values of $Fl_X(t)$ less than 10^{-10}.

In Figure 4.15 (c) is shown $\|\mathbf{V}_{\mathrm{CM}}(t)\|$ as a function of time. About for $t > 254$ we have values smaller than 3.79×10^{-2}. Performing the same numerical test with the finer discretization $\Delta x = \Delta y = 1.25$ and $\Delta t = 10^{-5}$, we find that, about for $t > 120$, $\|\mathbf{V}_{\mathrm{CM}}(t)\|$ is smaller than 1.41×10^{-2}, see Figure 4.15 (d). From this we can deduce that the velocity of the centre of mass go to zero.

Our numerical results suggest that our model, in absence of alignment and with the only chemotactic effect, is unable to reproduce stationary patterns.

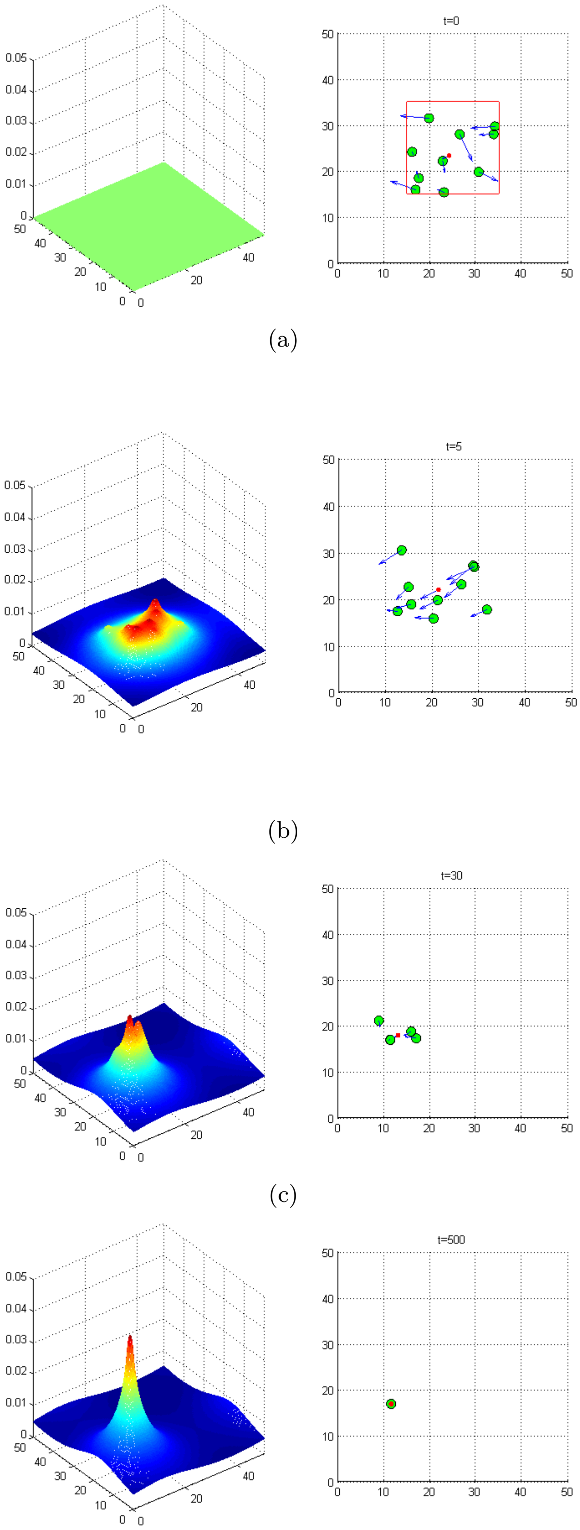

(a)

(b)

(c)

(d)

Figure 4.1. **Test 1**. Numerical simulation in a spatial domain $\Omega = [0, 50] \times [0, 50]$ with periodic boundary conditions, and in the time interval $[0, 500]$. The parameters values are $\sigma = 0.5$, $\beta = 5$, $\gamma = 2 \times 10^2$, $D = 2 \times 10^2$, $\xi = 0.5$, $V_{0,\max} = 3$, and $\mathbf{X}_0$ randomly taken in the red square shown in (a). Spatial and temporal discretizations are respectively $\Delta x = \Delta y = 0.25$ and $\Delta t = 10^{-4}$. The four plots are respectively at time steps $t = 0, 5, 30, 500$. On the left there is the chemoattractant concentration $f(\mathbf{x}, t)$, while on the right the positions and the velocities of the particles. Red marker indicates the centre of mass of the system, and the blue arrows are the velocity vectors.

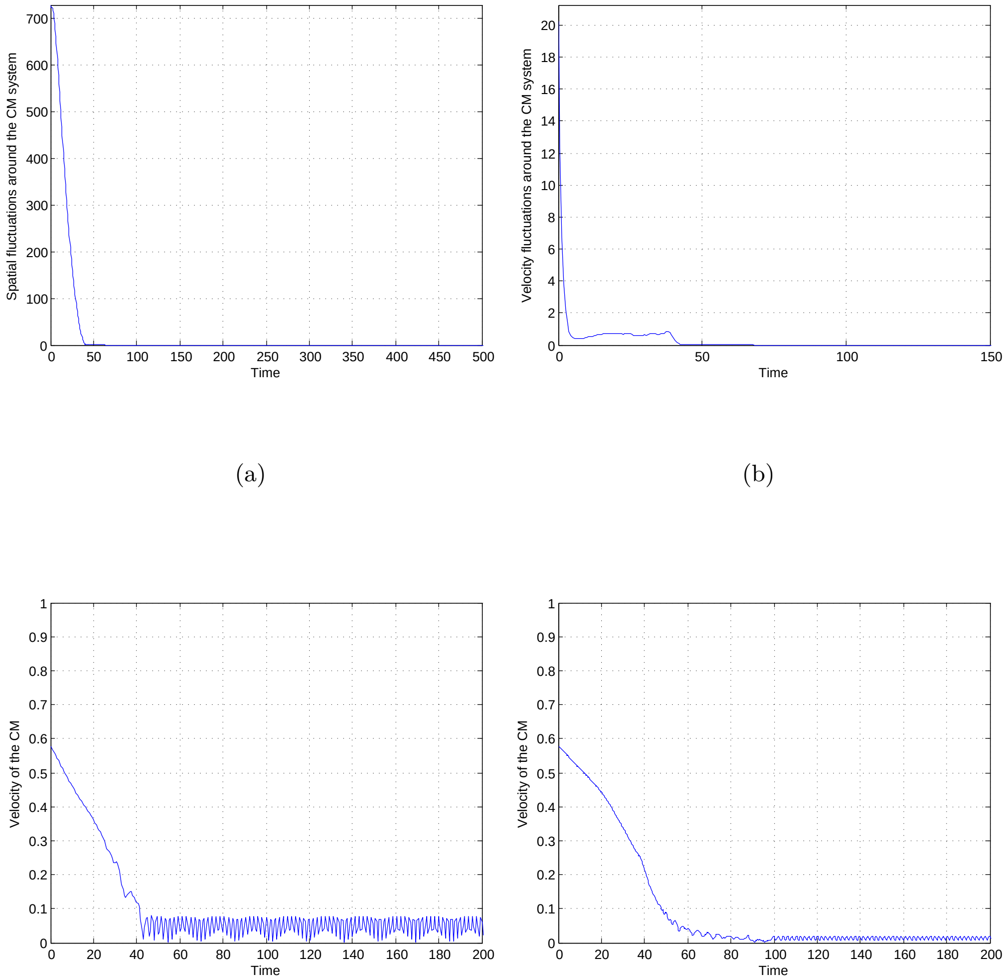

(a) (b)

(c) (d)

Figure 4.2. Test 1. (a) Spatial fluctuation around the centre of mass system $Fl_X(t) := \sum_{i=1}^{N} \|\mathbf{X}_i(t) - \mathbf{X}_{\mathrm{CM}}(t)\|^2$ as a function of the time. (b) Velocity fluctuation around the centre of mass system $Fl_V(t) := \sum_{i=1}^{N} \|\mathbf{V}_i(t) - \mathbf{V}_{\mathrm{CM}}(t)\|^2$ as a function of the time (x-axis shows only a part of the time domain). About for $t > 61$ $Fl_X(t)$ and $Fl_V(t)$ are less than 10^{-10}. (c) Norm of the velocity of the centre of mass $\|\mathbf{V}_{\mathrm{CM}}(t)\|$ versus time (only a part of the time interval is shown on the x-axis). About for $t > 52$ this velocity is less than 7.8×10^{-2}. The plot is related to a numerical simulation with spatial and temporal steps respectively of $\Delta x = \Delta y = 0.25$ and $\Delta t = 10^{-4}$. (d) With a finer mesh, $\Delta x = \Delta y = 0.125$ and $\Delta t = 10^{-5}$, smaller values of $\|\mathbf{V}_{\mathrm{CM}}(t)\|$ can be obtained: for $t > 88$ the maximum value in the plot is less than 2×10^{-2}. This confirm that the oscillating pattern shown in (c) can be attributed to a numerical error.

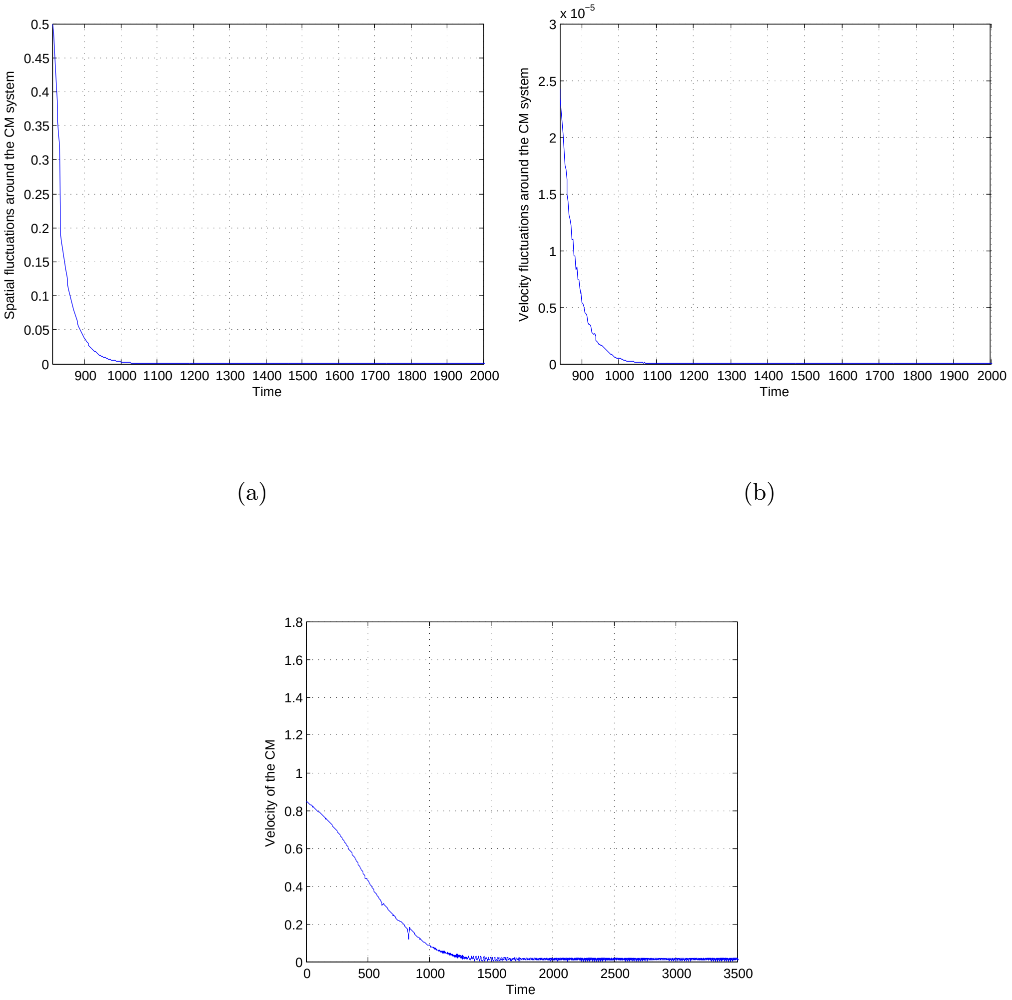

(a) (b)

(c)

Figure 4.3. Test 2. (a)-(b) Spatial and velocity fluctuations around the centre of mass system $Fl_X(t)$ and $Fl_V(t)$. About for $t > 1689$ $Fl_X(t)$ and $Fl_V(t)$ are less than 10^{-10} (on the x-axis only a part of the time domain is shown). (c) Norm of the velocity of the centre of mass $\|\mathbf{V}_{\mathrm{CM}}(t)\|$ versus time. About for $t > 2134$ this velocity is less than 1.82×10^{-2}.

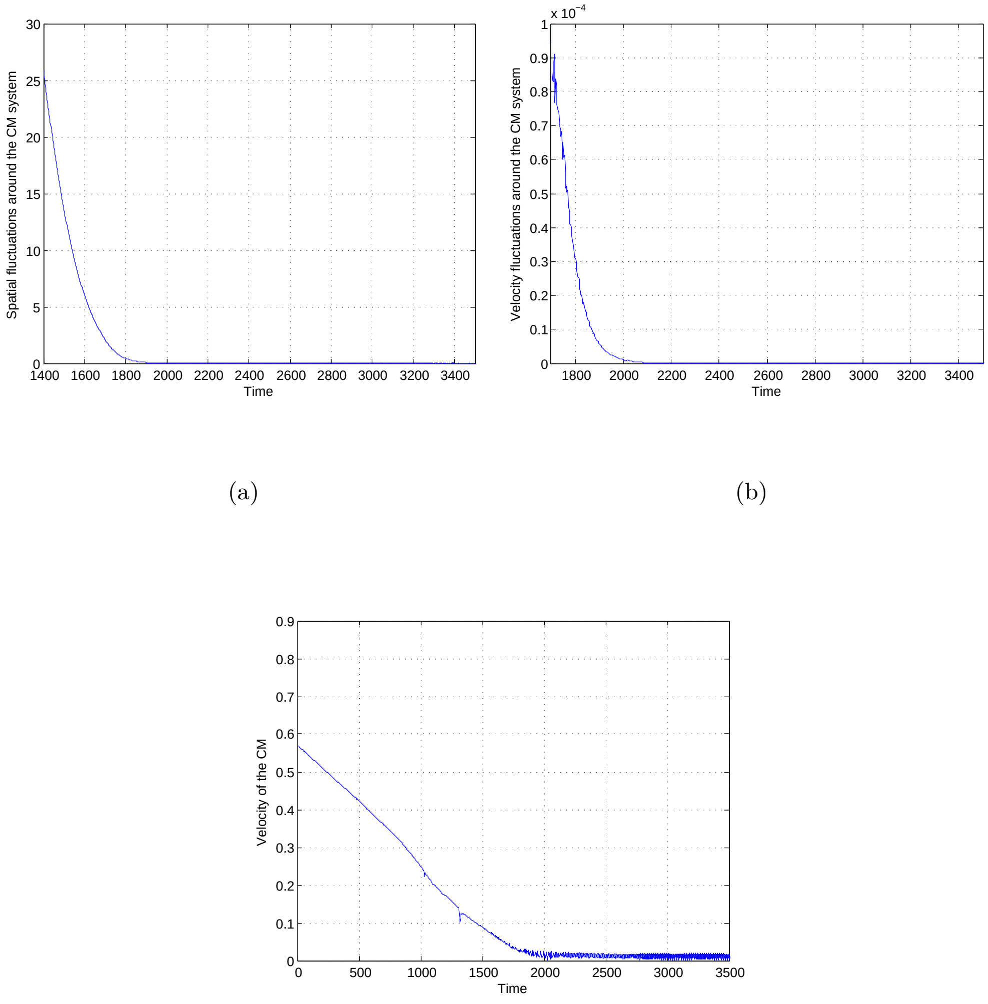

(a) (b)

(c)

Figure 4.4. Test 3. (a)-(b) Spatial and velocity fluctuations around the centre of mass system: $Fl_X(t)$ and $Fl_V(t)$. About for $t > 3109$ $Fl_X(t)$ and $Fl_V(t)$ are less than 10^{-10} (on the x-axis only a part of the time domain is shown). (c) Norm of the velocity of the centre of mass $\|\mathbf{V}_{\mathrm{CM}}(t)\|$ versus time. About for $t > 2579$ this velocity is less than 1.87×10^{-2}.

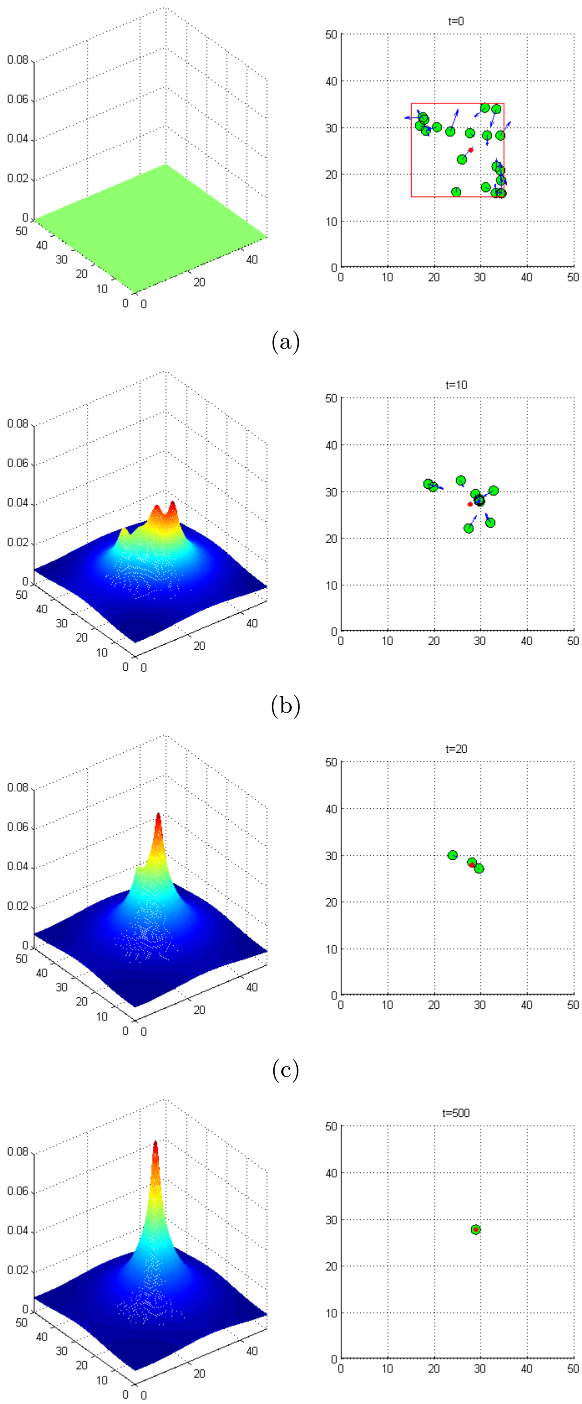

(a)

(b)

(c)

(d)

Figure 4.5. **Test 4**. Numerical simulation in a spatial domain $\Omega = [0, 50] \times [0, 50]$ with periodic boundary conditions, and in the time interval $[0, 500]$. The parameters values are $\sigma = 0.5$, $\beta = 5$, $\gamma = 2 \times 10^2$, $D = 2 \times 10^2$, $\xi = 0.5$, $V_{0,\max} = 3$, and $\mathbf{X}_0$ randomly taken in the red square shown in (a). Spatial and temporal discretizations are respectively $\Delta x = \Delta y = 0.25$ and $\Delta t = 10^{-4}$. The four plots are respectively at time steps $t = 0, 10, 30, 500$. The chemoattractant concentration $f(\mathbf{x}, t)$ is on the left, while on the right there is the positions and the velocities of the particles. Red marker marks the centre of mass of the system, and the blue arrows are the velocity vectors.

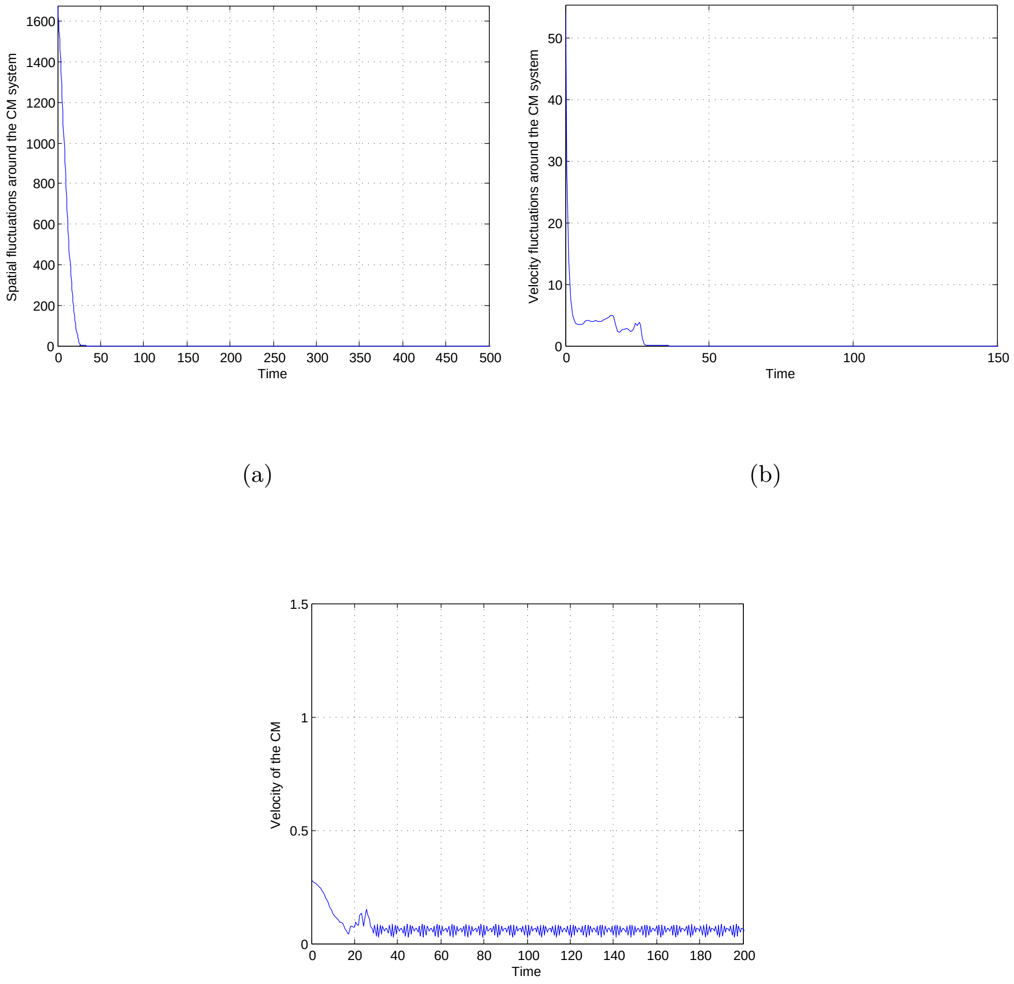

(a) (b)

(c)

Figure 4.6. Test 4. (a)–(b) Spatial and velocity fluctuations around the centre of mass system $Fl_X(t)$ and $Fl_V(t)$ (x-axis shows only a part of the time domain). About for $t > 34$ we have values less than 10^{-10}. (c) Norm of the velocity of the centre of mass $\|\mathbf{V}_{\mathrm{CM}}(t)\|$ versus time (only a part of the time interval is shown on the x-axis). About for $t > 28$ this velocity is less than 8.39×10^{-2}.

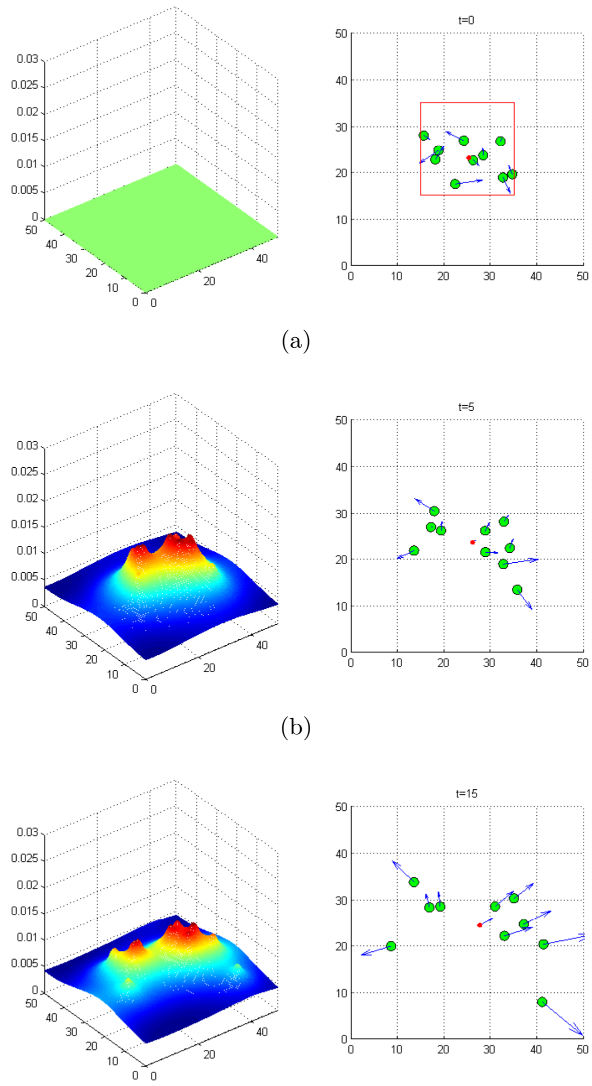

(a)

(b)

(c)

Figure 4.7. Test 5. Numerical simulation in a spatial domain $\Omega = [0, 50] \times [0, 50]$ with periodic boundary conditions, and in the time interval $[0, 15]$. The parameters values are $\sigma = 0.8$, $\beta = 5$, $\gamma = 0$, $D = 2 \times 10^2$, $\xi = 0.5$, $V_{0,\max} = 3$, and $\mathbf{X}_0$ randomly taken in the red square shown in (a). Spatial and temporal discretizations are respectively $\Delta x = \Delta y = 0.25$ and $\Delta t = 10^{-4}$. The red marker indicates the centre of mass of the system, and the blue arrows are the velocity vectors. On the left there is the chemoattractant concentration, while on the right the positions and the velocities of the particles. In this case the motion equations and the chemoattractant equation are decoupled and for the particles we simulate the pure Cucker-Smale model (4.1). Taken into account the parameters values and the initial data the flocking behaviour is not ensured by results in Ha and Liu (2009). In fact, from the three plots, taken respectively at time steps $t = 0, 5, 15$, we can observe a dispersion of the initial group.

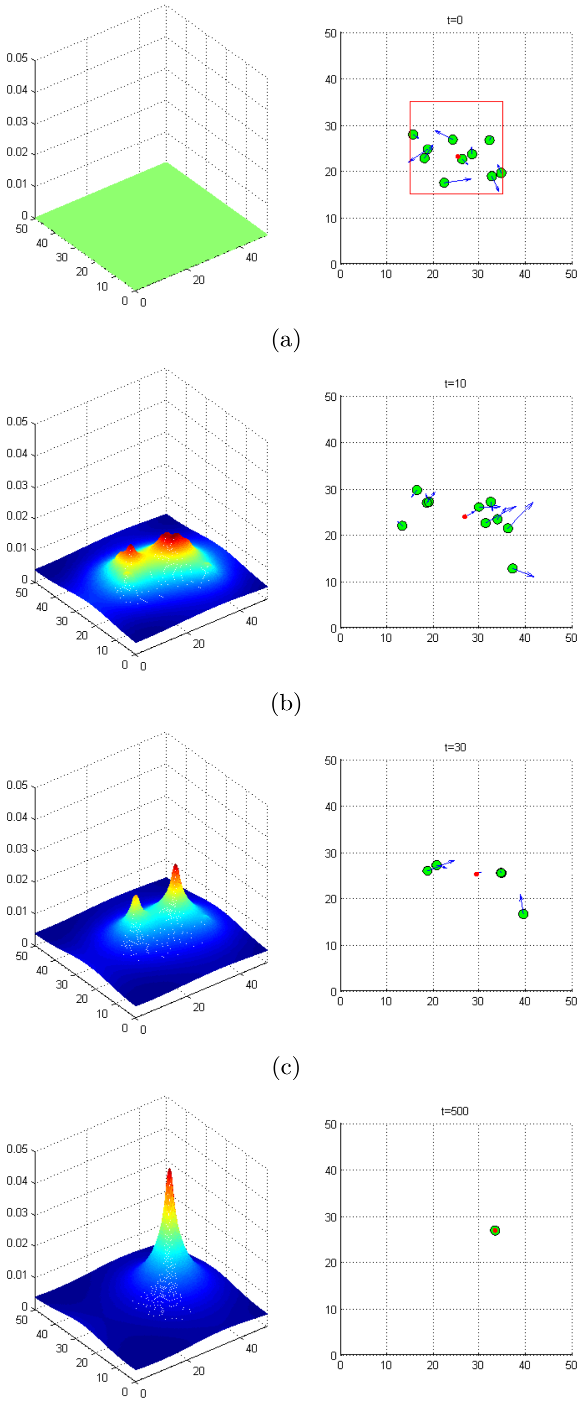

(a)

(b)

(c)

(d)

Figure 4.8. **Test 6**. Numerical simulation in a spatial domain $\Omega = [0, 50] \times [0, 50]$ with periodic boundary conditions, and in the time interval $[0, 500]$. The parameters values and the initial data are as in Figure 4.7: $\sigma = 0.8$, $\beta = 5$, $D = 10^2$, $\xi = 0.5$, $V_{0,\mathrm{max}} = 3$, and $\mathbf{X}_0$ as in Figure 4.7 (a). Then here a nonzero value for γ is chosen: $\gamma = 2 \times 10^2$. Spatial and temporal discretizations are $\Delta x = \Delta y = 0.25$ and $\Delta t = 10^{-4}$. The four plots are respectively at time steps $t = 0, 10, 30, 500$. On the left there is the chemoattractant concentration $f(\mathbf{x}, t)$, while on the right the positions and the velocities of the particles. The red marker is the centre of mass of the system, and the blue arrows are the velocity vectors. Comparing this figure with Figure 4.7, we observe that, introducing the chemotactic effect, the time-asymptotic convergence of the particles is recovered.

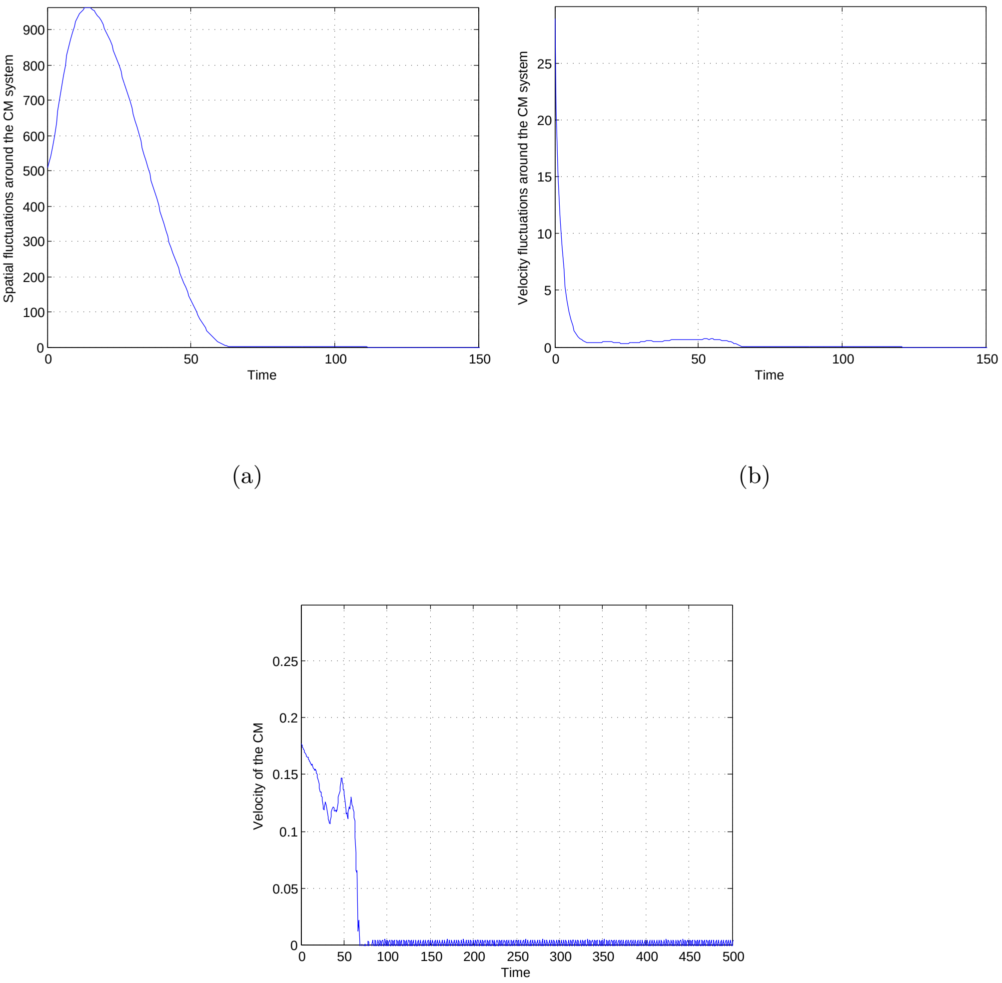

(a) (b)

(c)

Figure 4.9. Test 6. (a)-(b) Spatial fluctuation $Fl_X(t)$ and velocity fluctuation $Fl_V(t)$ around the centre of mass system as a function of the time (x-axis shows only a part of the time interval). About for $t > 107$ $Fl_X(t)$ and $Fl_V(t)$ are less than 10^{-10} (on the x-axis only a part of the time domain is shown). (c) Velocity of the centre of mass $\|\mathbf{V}_{\text{CM}}(t)\|$ versus time. About for $t > 65$ we have values smaller than 2.1×10^{-2}.

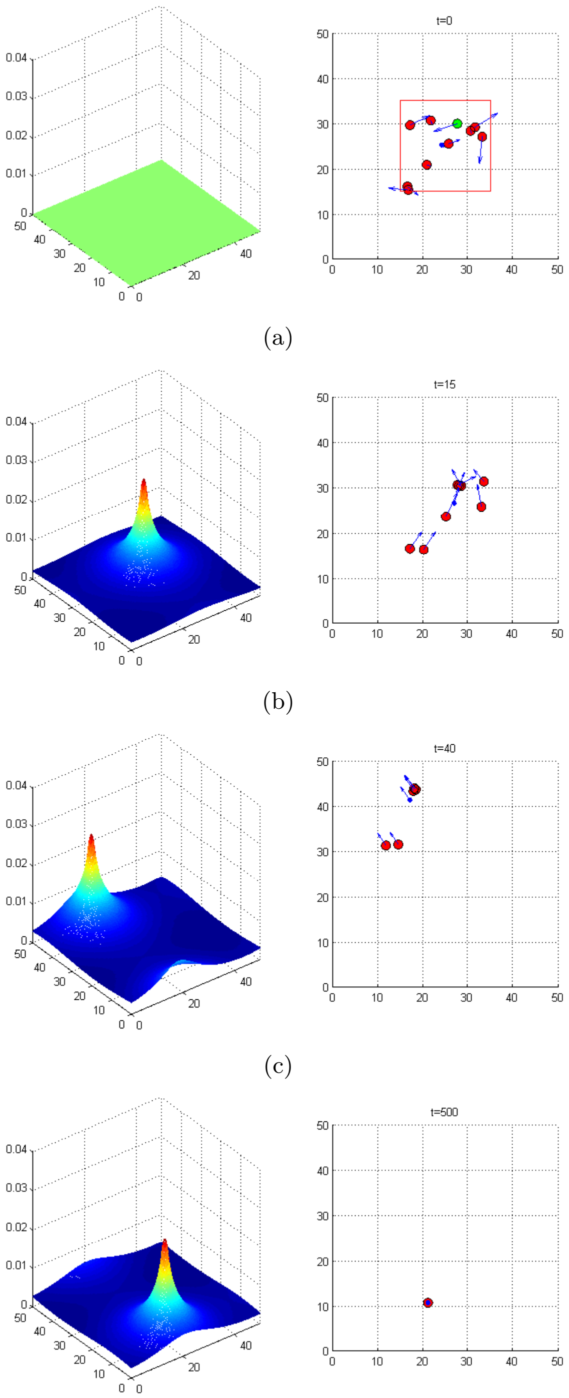

(a)

(b)

(c)

(d)

Figure 4.10. Test 7. Numerical simulation in a spatial domain $\Omega = [0, 50] \times [0, 50]$ with periodic boundary conditions, and in the time interval $[0, 500]$. The parameters values are $\sigma = 0.5$, $\beta = 5$, $\gamma = 1.5 \times 10^2$, $D = 2 \times 10^2$, $\xi = 3$, $V_{0,\max} = 0.3$, and $\mathbf{X}_0$ randomly taken in the red square shown in (a). Spatial and temporal discretizations are respectively $\Delta x = \Delta y = 0.25$ and $\Delta t = 10^{-4}$. The green cell marks a leader cell (●), that produce the chemical signal, while the other red cells are the followers (●), that do not produce any signal and follow the chemoattractant gradient. The blue marker is the centre of mass of the system, and the blue arrows are the velocity vectors. The four plots are respectively at time steps $t = 0, 15, 40, 500$. On the left there is the chemoattractant concentration, while on the right the positions and the velocities of the particles.

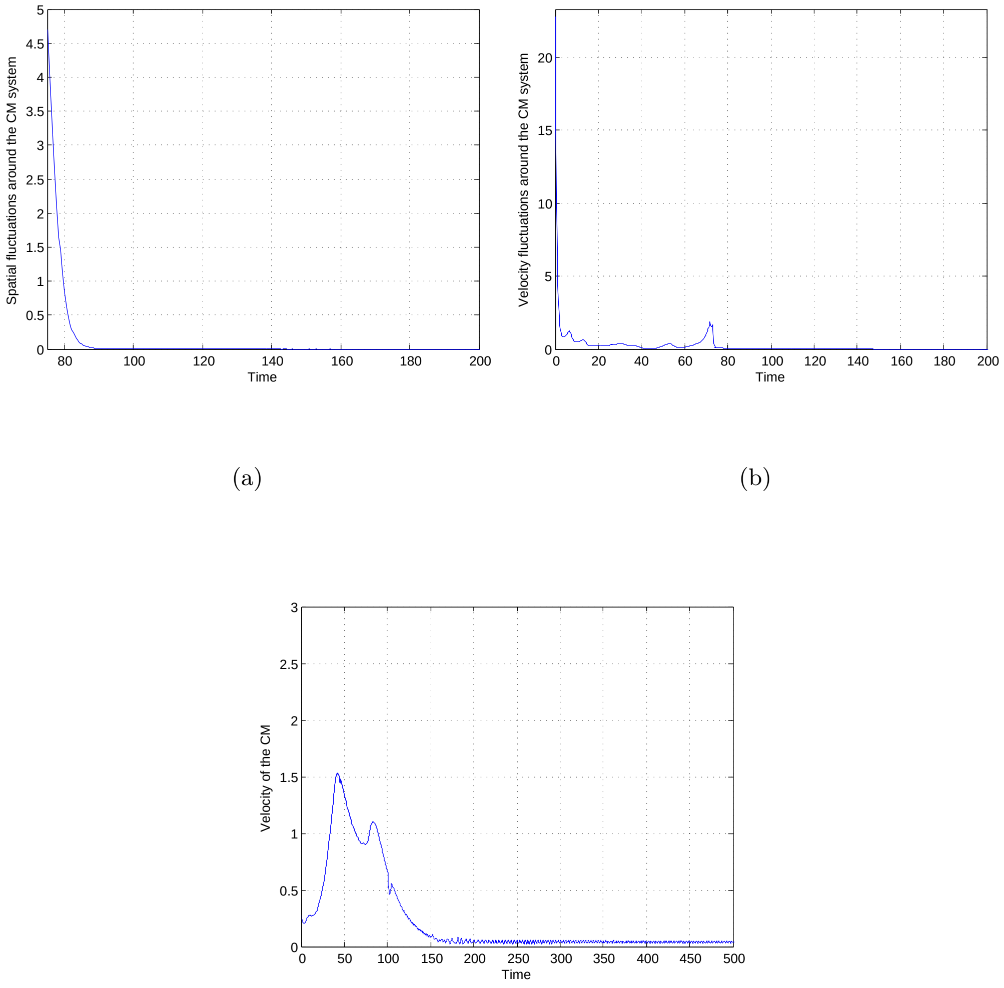

(a)

(b)

(c)

Figure 4.11. Test 7. (a)-(b) Spatial and velocity fluctuations, $Fl_X(t)$ and $Fl_V(t)$, around the centre of mass system (only a part of the time domain is shown on the x-axis). About for $t > 131$ $Fl_X(t)$ and $Fl_V(t)$ are less than 10^{-10}. (c) Velocity of the centre of mass $\|\mathbf{V}_{\mathrm{CM}}(t)\|$ as a function of the time. About for $t > 328$ we have values smaller than 5.3×10^{-2}.

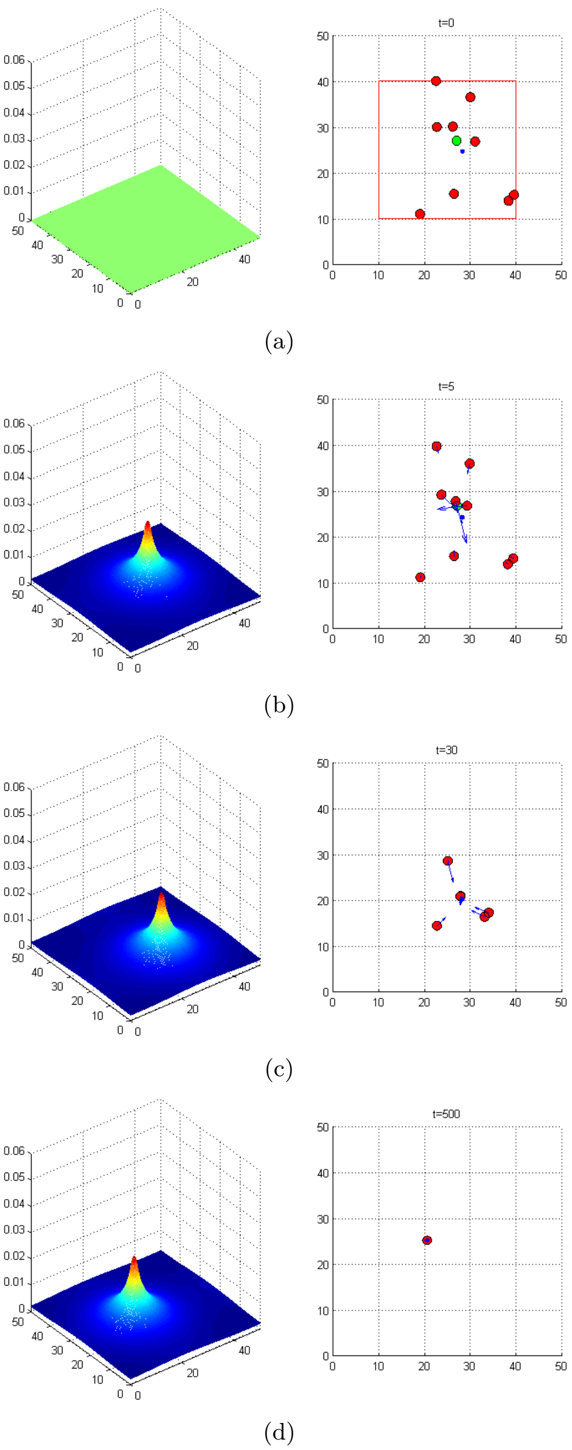

(a)

(b)

(c)

(d)

Figure 4.12. Test 8. Numerical simulation in a spatial domain $\Omega = [0, 50] \times [0, 50]$ with periodic boundary conditions, and in the time interval $[0, 500]$. Spatial and temporal discretizations are respectively $\Delta x = \Delta y = 0.25$ and $\Delta t = 10^{-4}$. In this case we fix a zero initial velocity, $V_{0,\max} = 0$, and the parameters $\sigma = 0.6$, $\beta = 2$, $\gamma = 10^2$, $D = 2 \times 10^2$, $\xi = 3$, and $\mathbf{X}_0$ randomly taken in the red square shown in (a). As in Figure 4.10 we consider a single leader cell (●) and other red follower cells (●). Because of the zero initial velocity, if we considered the pure Cucker-Smale (4.1), we would have all particles constant in time in the initial position. Conversely, in the four plots at time steps $t = 0, 5, 30, 500$ we observe the time-asymptotic convergence of the migrating group.

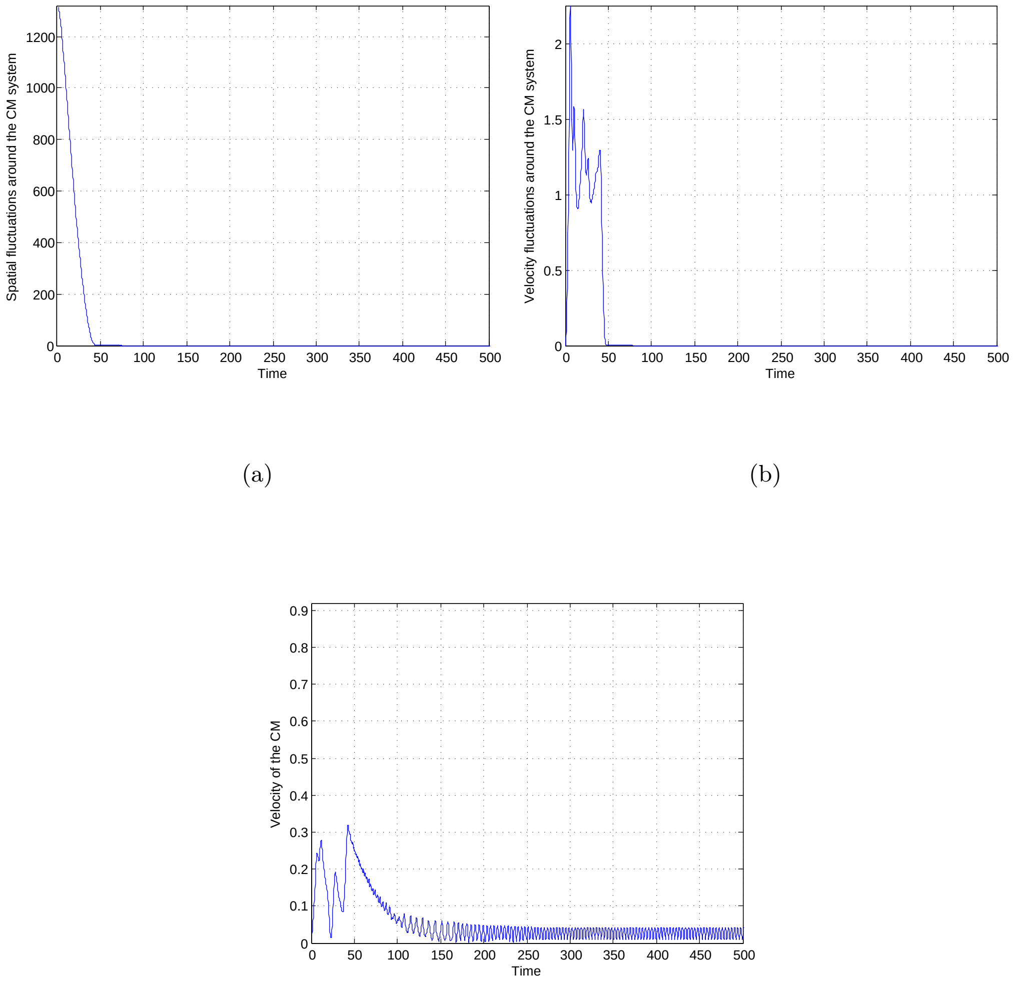

(a)

(b)

(c)

Figure 4.13. Test 8. (a)-(b) Spatial and velocity fluctuations around the centre of mass system as a function of the time: $Fl_X(t)$ and $Fl_V(t)$. About for $t > 67$ $Fl_X(t)$ and $Fl_V(t)$ are less than 10^{-10}. (c) Velocity of the centre of mass $\|\mathbf{V}_{\mathrm{CM}}(t)\|$ versus time. About for $t > 109$ this quantity is smaller than 4.3×10^{-2}.

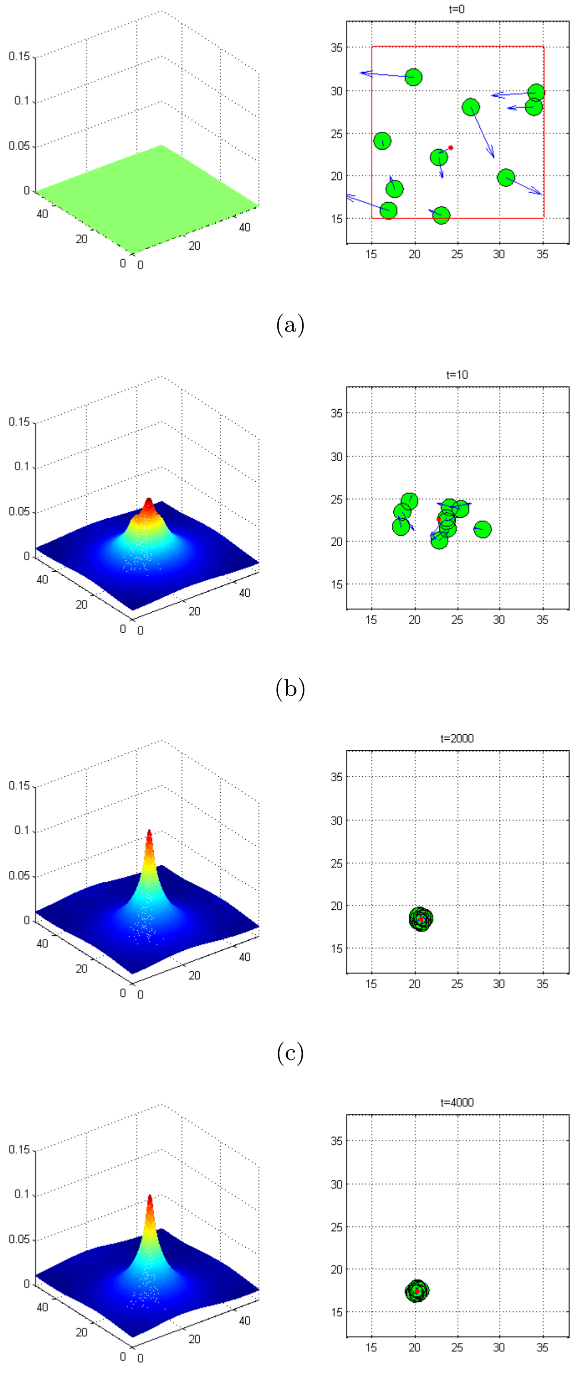

(a)

(b)

(c)

(d)

Figure 4.14. Test 9. Numerical simulation in a spatial domain $\Omega = [0, 50] \times [0, 50]$ with periodic boundary conditions, and in the time interval $[0, 4000]$ (plots on the right shown only a part of the spatial domain). Spatial and temporal discretizations are respectively $\Delta x = \Delta y = 0.25$ and $\Delta t = 10^{-4}$. In this test only the chemotactic force is considered, neglecting the alignment effect ($\beta = 0$). For the other values we fix $\gamma = 10^2$, $D = 2 \times 10^2$, $\xi = 1.5$, $V_{0,\max} = 0.8$, and $\mathbf{X}_0$ randomly taken in the red square shown in (a). The plots taken at time steps $t = 0, 10, 2000, 4000$ display the aggregation of the initial group of particles. In this case the convergence is not observed, but an oscillating behaviour around their centre of mass is shown.

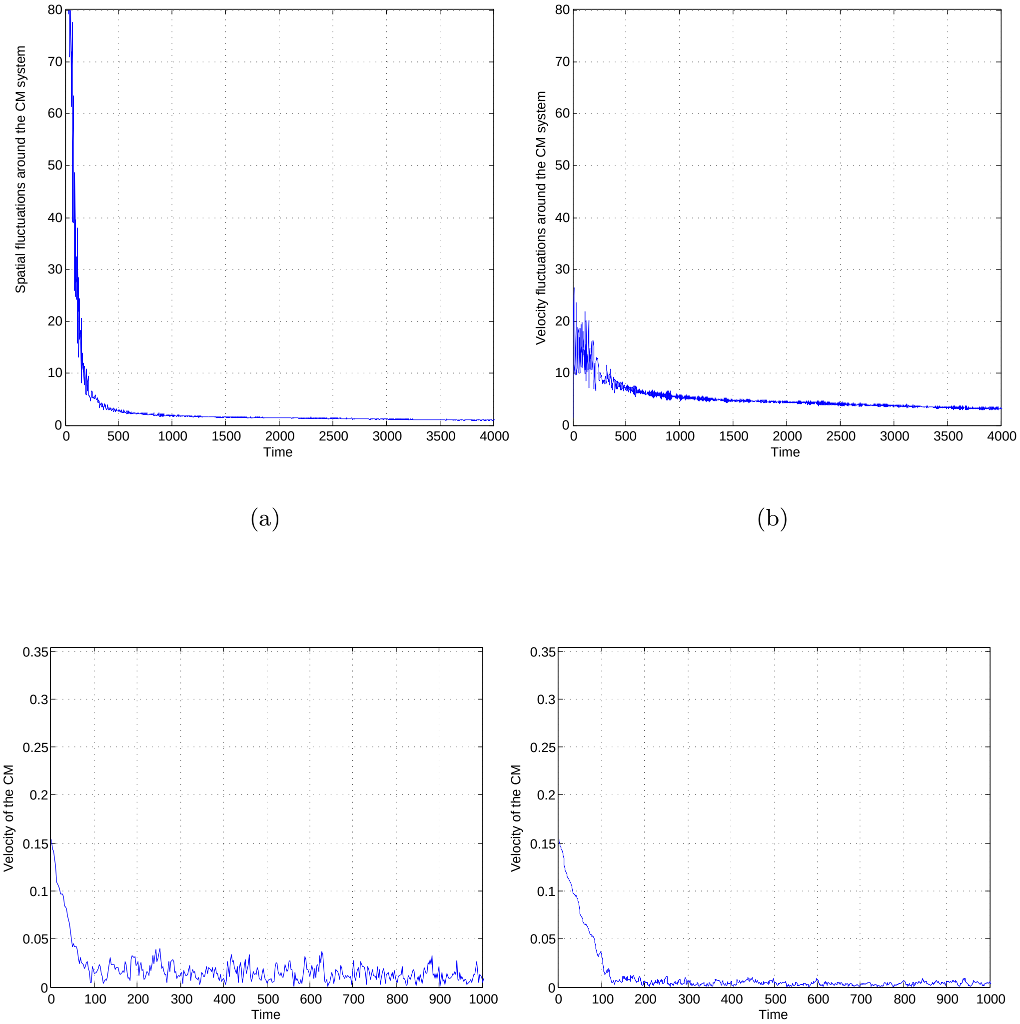

(a) (b)

(c) (d)

Figure 4.15. **Test 9**. (a)-(b) Spatial and velocity fluctuations, $Fl_X(t)$ and $Fl_V(t)$, around the centre of mass system versus time (only a part of the time domain is shown on the x-axis). In this case $Fl_X(t)$ and $Fl_V(t)$ remain bounded but do not converge to zero. In particular we have about $Fl_X(t) > 0.88$ and, if we consider a trend line, its slope seems to decrease monotonically. In particular in the time intervals $[0, 800]$ and $[3200, 4000]$, the slope of the fit line changes from -1.46×10^{-1} to -1.84×10^{-4}. (c) Velocity of the centre of mass $\|\mathbf{V}_{\text{CM}}(t)\|$ versus time, using a spatial and a temporal discretization given by $\Delta x = \Delta y = 2.5$ and $\Delta t = 10^{-4}$ (x-axis shows a part of the time interval). About for about $t > 254$ this quantity is smaller than 3.79×10^{-2}. (d) With a finer mesh, $\Delta x = \Delta y = 0.125$ and $\Delta t = 10^{-5}$, we obtain smaller values: about for $t > 120$ we have values less than 1.41×10^{-2}.

4.7 Conclusions

In this chapter we have proposed an extension of the Cucker-Smale model introducing a mathematical model for collective motion driven by an alignment and a chemotaxis effect. We have adopted a hybrid description, discrete for the particles and for the motion equations, and continuous for the molecular lever containing the equation for the chemical signal.

We have studied our model by both an analytical and a numerical point of view. By the analytical point of view, using a fixed–point theorem, we have proved local existence and uniqueness of the solution of the nonlinear system. Then, through a principle of continuation of solutions, we have extended such result proving global existence and uniqueness for all times. Moreover, we have investigated the asymptotic behaviour of particular equilibrium configurations, corresponding to a state in which all particles are located in a same position with zero velocity. On a linearized system around such configurations we have proved, using a Lyapunov functional approach, the asymptotic convergence of the particles in their centre of mass with same velocity. Then the velocity of the centre of mass is proved to go time-asymptotically to zero. By a numerical point of view this property has been tested on the nonlinear system, finding a complete concordance with the analytical results, and some numerical simulations have been proposed. Among these, we have discussed the competition between alignment and chemotactic effects varying the parameters of the system. We have found a decrease in the rate of convergence of the particles when the strength of the alignment term increases with respect to the chemotaxis. On the other hand, an increase in the rate of convergence can be found with the same parameters and with a greater number of interacting particles. Then we have considered the presence of two cell populations, as in the model of the lateral line proposed in Chapter 3, finding the convergence of cells towards the sources of chemical signal. Finally, the case of a pure chemotactic effect, without alignment, has been simulated. Numerical results have shown the absence of convergence in the migrating group, suggesting that our model, with the only chemotaxis mechanism, is not able to describe biological processes leading to stationary aggregates.

Future perspectives can concern the extension of the stability result, proved on the linearized system, to the full nonlinear model. Furthermore, other interactions could be taken into account in the collective motion, such as adhesion-repulsion, damping or lateral inhibition terms, similar to those introduced in Chapter 3. This would be interesting in view of studying, in an analytical framework, the morphogenetic process arising in the zebrafish lateral line, and establish results in relation to the rosette formation and the neuromast deposition.

Bibliography

Aguirre A, Rubio ME, Gallo V (2010) Notch and EGFR pathway interaction regulates neural stem cell number and self-renewal. Nature 467(7313):323–327

Alberts B, Bray D, Lewis J, Raff M, Roberts K, Watson JD (1994) Molecular Biology of The Cell (3rd edition). Garland

Albi G, Pareschi L (2013) Modeling self-organized systems interacting with few individuals: From microscopic to macroscopic dynamics. Appl Math Lett 26(4):397–401

Anderson ARA, Chaplain MAJ, Rejniak KA (2007) Single-cell-based models in biology and medicine. Springer

Anderson ARD, Chaplain MAJ (1998) Continuous and discrete mathematical models of tumor-induced angiogenesis. Bull Math Biol pp 857–899

Aoki I (1982) A simulation study on the schooling mechanism in fish. Bullettin Of The Japanese Society Scientific Fischeries 48(8):1081–1088

Arboleda-Estudillo Y, Krieg M, Stühmer J, Licata NA, Muller DJ, Heisenberg CP (2010) Movement Directionality in Collective Migration of Germ Layer Progenitors. Curr Biology 20:161–169

Armstrong NJ, Painter K, Sherrat JA (2009) Adding Adhesion to a Chemical Signaling Model for Somite Formation. Bullettin of Mathematical Biology 71:1–24

Ballerini M, Cabibbo N, Candelier R, Cavagna A, Cisbani E, Giardina I, Lecomte V, Orlandi A, Parisi G, Procaccini A, Viale M, Zdravkovic V (2008) Interaction ruling animal collective behavior depends on topological rather than metric distance: Evidence from a field study. P Natl Acad Sci USA 105(4):1232–1237

Bayly PV, Taber LA, Carlsson AE (2012) Damped and persistent oscillations in a simple model of cell crawling. J R Soc Interface 9(71):1241–1253

Beenken A, Mohammadi M (2009) The fgf family: biology, pathophysiology and therapy. Nat Rev Drug Discov 8(3):235–253

Bell GI, Dembo M, Bongrand P (1984) Cell adhesion. Competition between nonspecific repulsion and specific bonding. Biophys J 45(6):1051–1064

Bellomo N, Bellouquid A, Nieto J, Soler J, Maini PK (2007) Multicellular biological growing systems: Hyperbolic limits towards macroscopic description. Math Models Methods Appl Sci 17:1675–1692

Bellomo N, Piccoli B, Tosin A (2012) Modeling crowd dynamics from a complex viewpoint. Mathematical Models and Methods in Applied Sciences 22(2):1230004

Belmonte JM, Thomas GL, Brunnet LG, de Almeida RM, Chaté H (2008) Self-propelled particle model for cell-sorting phenomena. Phys Rev Lett 100(24):248702

Berec L (2002) Techniques of spatially explicit individual-based models: construction, simulation, and mean-field analysis. Ecological Modelling 150(1–2):55–81

Bolós V, Grego-Bessa J, de la Pompa JL (2007) Notch signaling in development and cancer. Endocr Rev 28(3):339–363

Böttcher RT, Niehrs C (2005) Fibroblast Growth Factor Signaling during Early Vertebrate Development. Endocr Rev 26(1):63–77

Bruno L, Tosin A, Tricerri P, Venuti F (2011) Non-local first-order modelling of crowd dynamics: A multidimensional framework with applications. Applied Mathematical Modelling 35:426–445

Burton TA (2005) Volterra Integral and Differential Equations. Second edition. Springer

Chaffer CL, Weinberg RA (2011) A perspective on cancer cell metastasis. Science 331:1559–1564

Chalub FACC, Markowich PA, Perthame B, Schmeiser C (2004) Kinetic models for chemotaxis and their drift-diffusion limits. Monatsh Math 142:123–141

Chaplain MA (2000) Mathematical modelling of angiogenesis. J Neurooncol 50(1–2):37–51

Chaplain MAJ, Singh GD, McLachlan JC (eds) (1999) On Growth and Form. Spatio-Temporal Pattern Formation in Biology. John Wiley

Chauviere A, Hille T, Preziosi L (2007) Modeling cell movement in anisotropic and heterogeneous network tissues. Netw Heterog Media 2:333–357

Chitnis AB, Nogare DD, Matsuda M (2012) Building the Posterior Lateral Line System in Zebrafish. Dev Neurobiol 72(3):234–255

Colin T, Durrieu MC, Joie J, Lei Y, Mammeri Y, Poignard C, Saut O (2013) Modeling of the migration of endothelial cells on bioactive micropatterned polymers. Math BioSci and Eng 10(4):997–1015

Colombi A, Scianna M, Tosin A (2014) Differentiated cell behavior: a multiscale approach using measure theory. J Math Biol DOI 10.1007/s00285-014-0846-z

Condeelis J, Singer RH, Segall JE (2005) The great escape: when cancer cells hijack the genes for chemotaxis andmotility. Annu Rev Cell Dev Biol 21:695–718

Coombs S, Netten SV (2005) The Hydrodynamics and Structural Mechanics of the Lateral Line System. Fish Physiology 23:103–139

Couzin ID, Krause J, James R, Ruxton GD, Franks NR (2002) Collective memory and spatial sorting in animal groups. J Theor Biol 71:1–11

Couzin ID, Krause J, Franks NR, Levin SA (2005) Effective leadership and decision-making in animal groups on the move. Nature 433:513–516

Cristiani E, Piccoli B, Tosin A (2010) Modeling self-organization in pedestrians and animal groups from macroscopic and microscopic viewpoints. In: Naldi G, Pareschi L, Toscani G (eds) Mathematical modeling of collective behavior in socio-economic and life-sciences, Modeling and Simulation in Science, Engineering, and Technology, Birkhäuser Boston, pp 337–364

Cristiani E, Frasca P, Piccoli B (2011a) Effects of anisotropic interactions on the structure of animal groups. J Math Biol 62:569–588

Cristiani E, Piccoli B, Tosin A (2011b) Multiscale modeling of granular flows with application to crowd dynamics. Multiscale Model Sim 9(1):155–182

Cristiani E, Piccoli B, Tosin A (2014) Multiscale Modeling of Pedestrian Dynamics, Modeling, Simulation and Applications, vol 12. Springer

Cristiani E, Priuli FS, Tosin A (2015) Modeling rationality to control self-organization of crowds: an environmental approach. SIAM J Appl Math

Cucker F, Dong JG (2010) Avoiding collisions in flocks. IEEE Transactions on Automatic Control 55:1238–1243

Cucker F, Dong JG (2011) A General Collision-Avoiding Flocking Framework. IEEE Transactions on Automatic Control 56(5):1124–1129

Cucker F, Huepe C (2008) Flocking with informed agents. MathematicS In Action 1:1–25

Cucker F, Mordecki E (2008) Flocking in noisy environments. J Math Pures Appl 89:278–296

Cucker F, Smale S (2007a) Emergent Behavior in Flocks. Ieee T Automat Contr 52(5):852–862

Cucker F, Smale S (2007b) On the mathematics of emergence. Japan J Math 2:197–227

Dahm R (2006) The Zebrafish Exposed. American Scientist 94(5):446–53

Dallon J, Othmer HG (2004) How cellular movement determines the collective force generated by the dictyostelium discoideum slug. J Theor Biol 231:203–222

Dambly-Chaudiére C, Cubedo N, Ghysen A (2007) Control of cell migration in the development of the posterior lateral line: antagonistic interactions between the chemokine receptors CXCR4 and CXCR7/RDC1. BMC Dev Biol 7(23)

Derzsi A, Szőlősi G, Vicsek T (2009) Most minimal spp model, URL `http://hal.elte.hu/~vicsek/`

Deutsch A (2004) Mathematical and Theoretical Biology: A European Perspective. Science Careers URL `http://sciencecareers.sciencemag.org/career_magazine/previous_issues/articles/2004_03_12/nodoi.10452093265631564779`

Di Russo C, Lagaert JB, Chapuisat G, Dronne MA (2010) A mathematical model of inflammation during ischemic stroke. ESAIM: Proceedings, CEMRACS 2009: Mathematical Modelling in Medicine 30

Dijkgraaf S (1989) A short personal review of the history of lateral line research. In: Coombs S, Gorner P, Munz H (eds) The Mechanosensory Lateral Line, Neurobiology and Evolution, Springer-Verlag, pp 7–14

Doitsidou M, Reichman-Fried M, Stebler J, Koprunner M, Dorries J, Meyer D, Esguerra C, Leung T, Raz E (2002) Guidance of primordial germ cell migration by the chemokine SDF-1. Cell 111:647–659

Donà E, Barry JD, Valentin G, Quirin C, Khmelinskii A, Kunze A, Durdu S, Newton LR, Fernandez-Minan A, Huber W, Knop M, Gilmour D (2013) Directional tissue migration through a self-generated chemokine gradient. Nature 503:285–289

Dormann D, Weijer CJ (2006) Chemotactic cell movement during dictyostelium development and gastrulation. Curr Opin Genet Dev 16(4):367–373

Dormann S, Deutsch A (2002) Modeling of self-organized avascular tumor growth with a hybrid cellular automaton. In Silico Biol 2:393–406

D'Orsogna MR, Chuang YL, Bertozzi AL, Chayes LS (2006) Self-Propelled Particles with Soft-Core Interactions: Patterns, Stability, and Collapse. Phys Rev Lett 96(10):104302

Draper BW, Morcos PA, Kimmel CB (2001) Inhibition of Zebrafish fgf8 Pre-mRNA Splicing With Morpholino Oligos: A Quantifiable Method for Gene Knockdown. Genesis 30:154–156

Drasdo D (2003) On selected individual-based approaches to the dynamics in multicellular systems. In: Alt W, Chaplain M, Griebel M, Lenz J (eds) Polymer and cell dynamics, Birkhäuser Verlag Basel, pp 169–204

Drasdo D (2005) Coarse graining in simulated cell populations. Advs Complex Syst 319

Drasdo D, Dormann S, Hoehme S, Deutsch A (2004) Cell-Based Models of Avascular Tumor Growth. In: Deutsch A, Falcke M, Howard J, Zimmermann W (eds) Function and Regulation of Cellular Systems: Experiments and Models, Birkhäuser Verlag Basel, pp 367–378

Drummond IA (2005) Kidney development and disease in the zebrafish. J Am Soc Nephrol 16(2):299–304

Eisenbach M, Lengeler JW (2004) Chemotaxis. Imperial College Press

Faria JJ, Dyer JRG, Tosh CR, Krause J (2010) Leadership and social information use in human crowds. Animal Behaviour 79(4):895–901

Ferreira SC, Martins ML, Vilela MJ (1998) A growth model for primary cancer. Physica A 261:569–580

Filion RJ, Popel AS (2005) Intracoronary administration of FGF-2: a computational model of myocardial deposition and retention. Am J Physiol Heart Circ Physiol 288(1):H263–H279

Fish FE (1995) Kinematics of ducklings swimming in formation: consequences of position. Journal of Experimental Zoology 273:1–11

Fournier MF, Sauser R, Ambrosi D, Meister JJ, Verkhovsky AB (2010) Force transmission in migrating cells. J Cell Biol 188(2):287–297

Friedl P, Gilmour D (2009) Collective cell migration in morphogenesis, regeneration and cancer. Nat Rev Mol Cell Biol 10:445–457

Fusi L (2009) Macroscopic models for fibroproliferative disorders: A review. Mathematical and Computer Modelling 50:1474–1494

Gaiano N, Fishell G (2002) The role of notch in promoting glial and neural stem cell fates. Annu Rev Neurosci 25(1):471–90

Galle J, Loeffler M, Drasdo D (2005) Modeling the effect of deregulated proliferation and apoptosis on the growth dynamics of epithelial cell populations in vitro. Biophys J 88:62–75

Ghysen A, Chaudière CD (2004) Development of the zebrafish lateral line. Curr Opin Neurobiol 14:67–73

Gilbert SF (2000) Developmental Biology. 6th Edition. Sunderland (MA): Sinauer Associates

Grego-Bessa J, Luna-Zurita L, del Monte G, Bolós V, Melgar P, Arandilla A, Garratt AN, Zang H, Mukouyama YS, Chen H, Shou W, Ballestar E, Esteller M, Rojas A, Pérez-Pomares JM, de la Pompa JL (2007) Notch signaling is essential for ventricular chamber development. Dev Cell 12(3):415–429

Grégoire G, Chaté (2004) Onset of collective and cohesive motion. Phys Rev Lett 92:025702

Grégoire G, Chaté H, Tu Y (2003) Moving and staying together without a leader. Physica D 181:157

Ha SY, Levy D (2009) Particle, kinetic and fluid models for phototaxis. Discrete and Continuous Dynamical Systems - Series B 12(1):77–108

Ha SY, Liu JG (2009) A simple proof of the Cucker-Smale flocking dynamics and mean-field limit. Commun Math Sci 7(2):297–325

Ha SY, Lee K, Levy D (2009) Emergence of time-asymptotic flocking in a stochastic Cucker-Smale system. Comm Math Sci 7(2):453–469

Haas P, Gilmour D (2006) Chemokine Signaling Mediates Self-Organizing Tissue Migration in the Zebrafish Lateral Line. Dev Cell 10:673–680

Haddon C, Smithers L, Schneider-Maunoury S, Coche T, Henrique D, Lewis J (1998) Multiple delta genes and lateral inhibition in zebrafish primary neurogenesis. Development 125:359–370

Hart A, Papadopoulou S, Edlund H (2003) Fgf10 Maintains Notch Activation, Stimulates Proliferation, and Blocks Differentiation of Pancreatic Epithelial Cells. Dev Dynam 228:185–193

Hatzikirou H, Deutsch A (2007) Collective guidance of collective cell migration. Curr Top Dev Biol 81:401–434

He L, Niemeyer B (2003) A Novel Correlation for Protein Diffusion Coefficients Based on Molecular Weight and Radius of Gyration. Biotechnol Prog 19:544–548

Helbing D, Schweitzer F, Keltsch J, Molnár P (1997) Active walker model for the formation of human and animal trail systems. Physical Review 56(3):2527–2539

Hemelrijk CK, Hildenbrandt H (2008) Self-organized shape and frontal density of fish schools. Ethology 114:245–254

Honda H, Tanemura M, Yoshida A (2000) Differentiation of wing epidermal scale cells in a butterfly under the lateral inhibition model–appearance of large cells in a polygonal pattern. Acta Biotheor 48(2):121–136

Horstmann D (2004) From 1970 until present: the Keller-Segel model in chemotaxis and its consequences. II. Jahresber Deutsch Math-Verein 106(2):51–69

Hunding A (1999) Turing structures of the second kind. In: Chaplain MAG, Singh GD, McLachlan JC (eds) On Growth and Form. Spatio-temporal Pattern Formation in Biology, Chapman & Hall/CRC Math. Biol. Med. Ser., John Wiley, pp 75–88

Hundsdorfer W, Verwer JG (2003) Numerical Solution of Time-Dependent Advection-Diffusion-Reaction Equations. Computational Mathematics, Springer

Huth A, Wissel C (1992) The simulation of the movement of fish schools. J Theor Biol 156:365–385

Ioannou CC, Tosh CR, Neville L, Krause J (2008) The confusion effect. from neural networks to reduced predation risk. Behavioral Ecology 19(1):126–130

Itoh M, Chitnis AB (2001) Expression of proneural and neurogenic genes in the zebrafish lateral line primordium correlates with selection of hair cell fate in neuromasts. Mech Develop 102:263–266

Jadbabaie A, Lin J, Morse A (2003) Coordination of groups of mobile autonomous agents using nearest neighbor rules. IEEE Trans Autom Control 48(6):988–1001

Joie J, Lei Y, Colin T, Durrieu MC, Poignard C, Saut O (2014) Modelling of migration and orientation of endothelial cells on micropatterned polymers. DCDS-B

Kansal AR, Torquato S, Harsh GR, Chiocca EA, Deisboeck TS (2000) Simulated brain tumor growth dynamics using a three-dimensional cellular automaton. J Theor Biol 203(4):367–382

Kauffman SA, Shymkoa R, Trabert K (1978) Control of sequential compartment in Drosophila. Science 199:259–270

Keller EF, Segel LA (1970) Initiation of slime mold aggregation viewed as an instability. J Theor Biol 26:399–415

Keller EF, Segel LA (1971) Travelling bands of chemotactic bacteria: a theoretical analysis. J Theor Biol 30:235–248

Kerstetter A, Azodi E, Marrs JA, Liu Q (2004) Cadherin-2 Function in the Cranial Ganglia and Lateral Line System of Developing Zebrafish. Dev Dynam 230:137–143

Kevin F (2008) Barrel Cortex. Cambridge University Press

Kirkpatrick B, Nguyen L, Kondrikova G, Herberg S, Hill WD (2010) Brief Technical Note: Stability of Human Stromal-Derived Factor-1α (CXCL12α) After Blood Sampling. Ann Clin Lab Sci 40(3):257–260

Knaut H, Werz C, Geisler R, Nusslein-Volhard C (2003) A zebrafish homologue of the chemokine receptor Cxcr4 is a germ-cell guidance receptor. Nature 421:279–282

Lai EC (2004) Notch signaling: control of cell communication and cell fate. Development 131(5):965–73

Landman KA, Pettet GJ, Newgreen DF (2003) Chemotactic cellularmigration: smooth and discontinuous travelling wave solutions. SIAM J Appl Math 63(5):1666–1681

Larrivee B, Karsan A (2000) Signaling pathways induced by vascular endothelial growth factor (review). Int J Mol Med 5(5):447–456

Lecaudey V, Akdogan GC, Norton WHJ, Gilmour D (2008) Dynamic fgf signaling couples morphogenesis and migration in the zebrafish lateral line primordium. Development 135:2695–2705, DOI 10.1242/dev.025981

Lee J, Blaber M (2010) Increased Functional Half-life of Fibroblast Growth Factor-1 by Recovering a Vestigial Disulfide Bond. Journal Of Proteins And Proteomics 1(2):37–42

LeVeque RJ (2007) Finite Difference Methods for Ordinary and Partial Differential Equations. Steady-State and Time-Dependent Problems. SIAM

Li B, Zheng YW, Sano Y, Taniguchi H (2011) Evidence for mesenchymal-epithelial transition associated with mouse hepatic stem cell differentiation. PLoS ONE 6(2):e17092

Li Q, Shirabe K, Kuwada JY (2004) Chemokine signaling regulates sensory cell migration in zebrafish. Dev Biol 269:123–136

Liu Q, Ensign RD, Azodi E (2003a) Cadherin-1, -2 and -4 expression in the cranial ganglia and lateral line system of developing zebrafish. Gene Expr Patterns 3:653–658

Liu Q, Dalman MR, Sarmah S, Chen S, Chen Y, Hurlbut AK, Spencer MA, L P, Marrs JA (2011) Cell Adhesion Molecule Cadherin-6 Function in Zebrafish Cranial and Lateral Line Ganglia Development. Dev Dynam 240:1716–1726

Liu S, Leach SD (2011) Zebrafish models for cancer. Annu Rev Pathol 6:71–93

Liu ZJ, Shirakawa T, Li Y, Soma A, Oka M, Dotto GP, Fairman RM, Velazquez OC, Herlyn M (2003b) Regulation of Notch1 and Dll4 by vascular endothelial growth factor in arterial endothelial cells: implications for modulating arteriogenesis and angiogenesis. Mol Cell Biol 23(1):14–25

Maini PK (1999) Some mathematical models for biological pattern formation. In: Chaplain MAG, Singh GD, McLachlan JC (eds) On Growth and Form. Spatio-temporal Pattern Formation in Biology, John Wiley, pp 111–128

Maini PK, Othmer HG (eds) (2000) Mathematical Models for Biological Pattern Formation. Springer-Verlag

Major RJ, Poss KD (2007) Zebrafish heart regeneration as a model for cardiac tissue repair. Drug Discovery Today: Disease Models 4(4):219–225

Mantzaris NV, Webb S, Othmer HG (2004) Mathematical modeling of tumor-induced angiogenesis. J Math Biol 49(2):111–187

Markus M, Boehm D, Schmick M (1999) Simulations of vessel morphogenesis using cellular automata. Mathematical Biosciences 156:191–206

Martin EA (1983) Dictionary of Life Sciences (2nd ed.). Macmillan Press

Matsuda M, Chitnis AB (2010) Atoh1a expression must be restricted by Notch signaling for effective morphogenesis of the posterior lateral line primordium in zebrafish. Development 137:3477–3487

Meeker ND, Trede NS (2008) Immunology and zebrafish: spawning new models of human disease. Dev Comp Immunol 32:745–757

Méhes E, Vicsek T (2014) Collective motion of cells: from experiments to models. Integr Biol 6(9):831–854

Meinhardt H (2000) Beyond spots and stripes: generation of more complex patterns and modifications and additions of the basic reaction. In: Maini PK, Othmer HG (eds) Mathematical Models for Biological Pattern Formation, Springer-Verlag, pp 143–164

Menzel R (1979) Spectral Sensitivity and Color Vision in Invertebrates. In: Autrum H (ed) Comparative Physiology and Evolution of Vision in Invertebrates - Invertebrate Photoreceptors, Handbook of Sensory Physiology VII/6A, Springer-Verlag, pp 503–580

Mertz AF, Che Y, Banerjee S, Goldstein J, Rosowski KR, Revilla SF, Niessen CM, Marchetti MC, Dufresne ER, Horsley V (2013) Cadherin-Based Intercellular Adhesions Organize Epithelial Cell-Matrix Traction Forces. P Natl Acad Sci USA 103(3):842–847

Mizoguchi T, Togawa S, Kawakami K, Itoh M (2011) Neuron and Sensory Epithelial Cell Fate Is Sequentially Determined by Notch Signaling in Zebrafish Lateral Line Development. J Neurosci 31(43):15,522–15,530

Morton KW, Mayers D (2005) Numerical Solution of Partial Differential Equations. Second edition. Cambrige University Press

Moussaïd M, Helbing D, Theraulaz G (2011) How simple rules determine pedestrian behavior and crowd disasters. Proceeding of the National Academy of Sciences of the United States of America 108:6884–6888

Muller A, Homey B, Soto H, Ge N, Catron D, Buchanan M, McClanahan T, Murphy E, Yuan W, Wagner S (2001) Involvement of chemokine receptors in breast cancer metastasis. Nature 410:50–56

Murray JD (1983) On a mechanical model for morphogenesis: Mesenchymal patterns. In: Jäger W, Murray JD (eds) Conference on: Modelling of Patterns in Space and Time, Heidelberg 1983, Lecture Notes in Biomathematics series, vol 55, Springer-Verlag, pp 279–291

Murray JD (2002) Mathematical biology I: An Introduction. Third edition. Springer

Murray JD (2003) Mathematical biology II: Spatial Models and Biomedical Applications. Third edition. Springer

Murray JD, Myerscough MR (1991) Pigmentation pattern formation on snakes. J Theor Biol 149(3):339–360

Murray JD, Oster GF (1984a) Cell traction models for generating pattern and form in morphogenesis. J Math Biol 19:265–279

Murray JD, Oster GF (1984b) Generation of biological pattern and form. IMA J Math Appl in Medic and Biol 1:51–75

Nakajima Y, Yamagishi T, Hokari S, Nakamura H (2000) Mechanisms involved in valvuloseptal endocardial cushion formation in early cardiogenesis: roles of transforming growth factor (TGF)-beta and bone morphogenetic protein (BMP). Anat Rec 258(2):119–127

Nakaya Y, Kuroda S, Katagiri YT, Kaibuchi K, Takahashi Y (2004) Mesenchymal-epithelial transition during somitic segmentation is regulated by differential roles of Cdc42 and Rac1. Dev Cell 7(3):425–438

Naldi G, Pareschi L, Toscani G (eds) (2010) Mathematical modeling of collective behavior in socio-economic and life-sciences. Modeling and Simulation in Science, Engineering, and Technology, Birkhäuser Boston

Nechiporuk A, Raible D (2008) FGF-Dependent Mechanosensory Organ Patterning in Zebrafish. Science 320:1774–1777

von Neumann J, Burks edit W (1966) Theory of self-reproducing automata, 1st edn. University of Illinois Press

Oster GF, Murray JD, Harris AK (1983) Mechanical aspects of mesenchymal morphogenesis. J Embryol Exp Morphol 78:83–125

Owen MR, Sherratt JA (1997) Pattern formation and spatiotemporal irregularity in a model for macrophage-tumour interactions. J Math Biol 189(1):63–80

Painter KJ, Maini PK, Othmer HG (2000) Development and applications of a model for cellular response to multiple chemotactic cues. J Math Biol 41(4):285–314

Palsson E, Othmer HG (2000) A model for individual and collective cell movement in Dictyostelium discoideum. Proc Natl Acad Sci USA 97(19):10,448–104,532

Papusheva E, Heisenberg CP (2010) Spatial organization of adhesion: force-dependent regulation and function in tissue morphogenesis. EMBO J 29:2753–2768

Patel AA, Gawlinski ET, Lemieux SK, Gatenby RA (2001) A cellular automaton model of early tumor growth and invasion. J Theor Biol 213(3):315–331

Perthame B (2007) Transport equations in biology. Birkhäuser

Perumpanani AJ, Sherratt JA, Norbury J, Byrne HM (1996) Biological inferences from a mathematical model for malignant invasion. Invas Metastas 16(4–5):209–221

Piccoli B, Tosin A (2009) Pedestrian flows in bounded domains with obstacles. Contin Mech Thermodyn 21(2):85–107

Piccoli B, Tosin A (2011) Time-evolving measures and macroscopic modeling of pedestrian flow. Arch Ration Mech Anal 199(3):707–738

Pitcher T, Magurran A, Winfield I (1982) Fish in larger shoals find food faster. Behav Ecol and Sociobiology 10(2)

Preziosi L, Tosin A (2009) Multiphase and Multiscale Trends in Cancer Modellings. Math Model Nat Phenom 4(3):1–11

Ramis-Conde I, Drasdo D, Anderson ARA, Chaplain MAJ (2008) Modeling the Influence of the E-Cadherin-β-Catenin Pathway in Cancer Cell Invasion: A Multiscale Approach. Phys Biol 95:155–165

Ramis-Conde I, Chaplain MAJ, Anderson ARA, Drasdo D, Ghysels P, Samaey G, Tijskens B, Van Liedekerke P, Ramon H, Roose D (2009) Multi-scale modelling of cancer cell intravasation: the role of cadherins in metastasis. Phys Biol 6:016008

Reece JB, Urry LA, Cain ML, Wasserman SA, Minorsky PV, Jackson RB (2013) Campbell Biology. 10th Edition. Benjamin Cummings

Reynolds CW (1987) Flocks, herds, and schools: A distributed behavioral model. Computer Graphics pp 25–34

Rorth P (2007) Collective guidance of collective cell migration. TRENDS in Cell Biology 17:575–579

Rubinstein B, Fournier MF, Jacobson K, Verkhovsky AB, Mogilner A (2009) Actin-Myosin Viscoelastic Flow in the Keratocyte Lamellipod. Biophys J 97:1853–1863

Sarrazin AF, Nuñez VA, Sapède D, Tassin V, Chaudière CD, A G (2010) Origin and Early Development of the Posterior Lateral Line System of Zebrafish. J Neurosci 30(24):8234–8244

Schaller G, Meyer-Hermann M (2005) Multicellular tumor spheroid in an off-lattice Voronoi-Delaunay cell model. Physical Review E 71:051910

Schaller G, Meyer-Hermann M (2006) Continuum versus discrete model: a comparison for multicellular tumour spheroids. Phil Trans R Soc A 364:1443–1464

Scherber C, Aranyosi AJ, Kulemann B, Thayer SP, Toner M, Iliopoulos O, Irimia D (2012) Epithelial cell guidance by self-generated EGF gradients. Integr Biol 4(3):259–269

Sepúlveda N, Petitjean L, Cochet O, Grasland-Mongrain E, Silberzan P, Hakim V (2013) Collective Cell Motion in an Epithelial Sheet Can Be Quantitatively Described by a Stochastic Interacting Particle Model. PLOS Computational Biology 9(3):e1002944

Shipley RJ, Jones GW, Dyson RJ, Sengers BG, Bailey CL, Catt CJ, Please CP, Malda J (2009) Design criteria for a printed tissue engineering construct: a mathematical homogenization approach. J Theor Biol 259(3):489–502

Stolarska AM, Kim Y, Othmer GH (2009) Multi-scale models of cell and tissue dynamics. Phil Trans R Soc A 367(1902):3525–3553

Streichan SJ, Velentin G, Gilmour D, Hufnagel L (2011) Collective cell migration guided by dynamically maintained gradients. Phys Biol 8:045004

Strömbom D (2011) Collective motion from local attraction. J Theor Biol 283:145–151

Sweet EM, Vemaraju S, Riley BB (2011) Sox2 and Fgf interact with atoh1 to promote sensory competence throughout the zebrafish inner ear. Dev Biol 358:113–121

Szabò B, Szöllösi GJ, Gönci B, Jurànyi Z, Selmeczi D, Vicsek T (2006) Phase transition in the collective migration of tissue cells: Experiment and model. Phys Rev E 74(6):061908

Tsitsiklis J (1984) Problems in decentralized decision making and computation. Ph.D. dissertation. Dept. EECS, MIT, Cambridge, MA

Turing AM (1952) TheChemical Basis of Morphogenesis. Philosophical Transactions of the Royal Society of London 237(641):37–72

Turner S, Sherratt JA (2002) Intercellular adhesion and cancer invasion: a discrete simulation using the extended potts model. J Theor Biol 216:85–100

Turner S, Sherratt JA, Painter KJ (2004) From a discrete to a continuous model of biological cell movement. Physical Review E 69:021910

Vicsek T, Zafeiris A (2012) Collective motion. Physics Reports 517(3):71–140

Vicsek T, Cziròk A, Ben-Jacob E, Cohen I, Shochet O (1995) Novel Type of Phase Transition in a System of Self-Driven Particles. Phys Rev Lett 75(6):1226–1229

Walbot V, Holder N (1987) Developmental Biology. Random House

Walshe J, Mason I (2003) Fgf signalling is required for formation of cartilage in the head. Dev Biol 264:522–536

Wootton JT (2001) Local interactions predict large-scale pattern in an empirically-derived cellular automata. Nature 413:841–843

Xiang J, Yang H, Che C, Zou H, Yang H, Wei Y, Quan J, Zhang H, et al (2009) Identifying Tumor Cell Growth Inhibitors by Combinatorial Chemistry and Zebrafish Assays. PLoS ONE 4(2):e4361

Yeh BK, Igarashi M, Eliseenkova AV, Plotnikov AN, Sher I, Ron D, Aaronson SA, Mohammadi M (2003) Structural basis by which alternative splicing confers specificity in fibroblast growth factor receptors. P Natl Acad Sci USA 100(5):2266–2271

Zheng H, Fu G, Dai T, Huang H (2007) Migration of endothelial progenitor cells mediated by stromal cell-derived factor-1alpha/CXCR4 via PI3K/Akt/eNOS signal transduction pathway. J Cardiovasc Pharmacol 50(3):274–280